

Nr. 351

Dominik Miller

Seismic noise analysis and isolation concepts  
for the ALPS II experiment at DESY



# Seismic noise analysis and isolation concepts for the ALPS II experiment at DESY

Von der Fakultät für Bauingenieurwesen und Geodäsie  
der Gottfried Wilhelm Leibniz Universität Hannover

zur Erlangung des Grades

**Doktor-Ingenieur (Dr.-Ing.)**

genehmigte Dissertation

von

**M. Sc. Wirt.-Ing. Dominik Miller**

geboren am 06.03.1991 in Hamburg

2019

Referent: Prof. Dr.-Ing. Jakob Flury  
Korreferenten: Prof. Dr.-Ing. Ingo Neumann  
Prof. Dr. rer. nat. Hartmut Grote  
Tag der Promotion: 22.05.2019

# Abstract

The ALPS II experiment at DESY is searching for new particles beyond the standard model of particle physics in a laboratory-based Light-Shining-through-a-Wall experiment, using high finesse optical resonators to reach the required sensitivity. The input and output mirrors on the optical tables have extremely accurate positioning and alignment requirements, for which the analysis of ground vibration and seismic noise is essential. This thesis, therefore, focuses on this analysis, its evaluation, and the development of future seismic isolations for the ALPS II and JURA experiments.

This work describes mechanical vibrations, seismic noise sources, seismic isolation principles, and also the seismic devices used to perform seismic noise analysis with their methods of measuring, calibrating, and analysing the acquired data. It summarises the seismic noise studies carried out in the ALPS II laboratories at HERA West as well as in the hall and tunnels of HERA North at DESY in Hamburg.

For a more accurate presentation of the prevailing noise frequencies a new method of the modal analysis, the MfwaFFT was developed. Here, a noise-independent procedure for more precise data analysis is implemented which accounts for the highly sensitive conditions on-site. Furthermore, a seismic isolation concept based on this analysis in connection with the ALPS II experiment is developed and presented.

**Keywords:** seismic noise analysis, modal analysis, seismic isolation concepts



# Kurzfassung

Das ALPS II Experiment am DESY forscht nach neuen Partikeln jenseits des Standardmodells der Teilchenphysik in einem laborgestützten „Licht-durch-die-Wand“ Experiment. Dafür werden optische Resonatoren mit sehr hoher Finesse verwendet, um die erforderliche Sensitivität zu erreichen. Die somit benötigten Ein- und Auskoppelspiegel, die sich auf optischen Tischen befinden, haben daher extrem genaue Positionierungs- und Ausrichtungsanforderungen, für die eine Analyse der Bodenvibration bzw. des seismischen Rauschens unerlässlich ist. Diese Doktorarbeit konzentriert sich daher auf diese Analyse, ihre Bewertung und die daraus resultierende Entwicklung zukünftiger seismischer Isolierungen für die ALPS II und JURA Experimente.

In dieser Arbeit werden mechanische Schwingungen, seismische Geräuschquellen, seismische Isolationsprinzipien sowie die zur Durchführung der seismischen Geräuschanalyse verwendeten seismischen Geräte mit ihren Verfahren zum Messen, Kalibrieren und Analysieren der erfassten Daten beschrieben. Es werden die seismischen Rauschstudien zusammengefasst, die in den ALPS II Laboratorien bei HERA West sowie in der Halle und den Tunneln von HERA North am DESY in Hamburg durchgeführt wurden. Um eine akkuratere Darstellung der vorhandenen Rauschfrequenzen herzustellen, wurde eine neue Methode der Modalanalyse, die MfwaFFT entwickelt, die eine von dem Rauschen unabhängige Vorgehensweise implementiert und den hochsensitiven Gegebenheiten vor Ort Rechnung trägt. Des Weiteren wird ein seismisches Isolierungskonzept in Zusammenhang mit dem ALPS II Experiment entwickelt.

**Stichworte:** Seismische Rauschanalyse, Modal Analyse, Seismische Isolierungskonzepte





# Table of Contents

<b>Abstract</b>	<b>v</b>
<b>Kurzfassung</b>	<b>vii</b>
<b>Table of Contents</b>	<b>ix</b>
<b>List of Figures</b>	<b>xiii</b>
<b>List of Tables</b>	<b>xxiii</b>
<b>Acronyms</b>	<b>xxv</b>
<b>Glossary</b>	<b>xxix</b>
<b>1. Introduction</b>	<b>1</b>
1.1. Motivations and background . . . . .	1
1.2. Research hypotheses and aims . . . . .	2
1.3. Outline of this work . . . . .	3
<b>2. Fundamentals and theory of seismic noise</b>	<b>5</b>
2.1. Fundamentals of mechanical vibration . . . . .	5
2.1.1. Theory of oscillation . . . . .	5
2.1.1.1. Oscillation and waves . . . . .	5
2.1.1.2. Standing waves and resonance . . . . .	7
2.1.1.3. Types of noise . . . . .	8
2.1.1.4. Signal-to-Noise Ratio . . . . .	9
2.1.2. The oscillatory systems . . . . .	9
2.1.2.1. Mass-Spring-Damper model . . . . .	11
2.1.2.2. Equation of motion . . . . .	12
2.1.2.3. Free damped oscillation . . . . .	12
2.1.2.4. Forced damped oscillation . . . . .	14
2.1.3. Modal analysis . . . . .	16
2.1.3.1. Fourier transform . . . . .	16
2.1.3.2. Windowing . . . . .	18
2.1.3.3. Averaging and overlapping . . . . .	21
2.1.4. Data evaluation . . . . .	23
2.1.4.1. Presenting spectra and spectral densities . . . . .	23

2.1.4.2.	RMS value in the frequency domain . . . . .	25
2.1.4.3.	Transfer function . . . . .	27
2.1.4.4.	Spectrogram . . . . .	30
2.2.	Seismic noise sources . . . . .	31
2.2.1.	Natural sources . . . . .	31
2.2.1.1.	Geodynamical aspects . . . . .	32
2.2.1.2.	Geological aspects at Hamburg, DESY . . . . .	32
2.2.2.	Human-made sources . . . . .	33
2.2.2.1.	Impact by stationary objects . . . . .	33
2.2.2.2.	Impact by traffic on site, machines and human work . . . . .	34
2.2.2.3.	Technical devices in the laboratory . . . . .	34
2.3.	Methods of seismic isolation . . . . .	34
2.3.1.	Passive constructions . . . . .	34
2.3.1.1.	Principle of a simple pendulum . . . . .	35
2.3.1.2.	Principle of a spring pendulum . . . . .	36
2.3.1.3.	The inverted pendulum concept . . . . .	37
2.3.1.4.	The anti-spring concept . . . . .	38
2.3.1.5.	The harmonic oscillator as transfer function . . . . .	39
2.3.2.	Control theory . . . . .	40
2.3.2.1.	Simple controller . . . . .	40
2.3.2.2.	Feed-forward controller . . . . .	41
2.3.2.3.	Feedback controller . . . . .	41
2.3.2.4.	Combined controller . . . . .	42
<b>3.</b>	<b>The Any Light Particle Search experiment</b>	<b>43</b>
3.1.	ALPS and its seismic noise requirements . . . . .	43
3.1.1.	The physics of ALPS . . . . .	45
3.1.2.	Optical resonators . . . . .	46
3.1.3.	Control loop design . . . . .	47
3.1.4.	Frequency region and absolute length requirements . . . . .	48
3.1.5.	Infrastructure and status . . . . .	49
3.2.	Tools and techniques used for seismic measurements, analyses, and isolations	50
3.2.1.	Seismic measuring instruments . . . . .	50
3.2.1.1.	Seismometers . . . . .	50
3.2.1.2.	Acquisition devices . . . . .	53
3.2.1.3.	Selected measurement chain . . . . .	53
3.2.2.	Data management and analyses . . . . .	54
3.2.2.1.	Notations for documentation . . . . .	54
3.2.2.2.	Analysing procedure . . . . .	54
3.2.3.	Finite Element Method simulation . . . . .	55
3.2.3.1.	Simple isolation simulations . . . . .	55
3.2.3.2.	Over-determined isolation systems . . . . .	55
3.2.3.3.	Selected FEM tools . . . . .	55

---

<b>4. Seismic noise analysis</b>	<b>57</b>
4.1. Method of frequency-weighted and averaged FFT	57
4.1.1. Problem definition and motivation	57
4.1.2. The solution approaches	59
4.1.2.1. Stitching	59
4.1.2.2. LPSD	60
4.1.2.3. New solution approach	61
4.1.3. The MfwaFFT algorithm	61
4.1.3.1. Data preparation	62
4.1.3.2. FFT generation	64
4.1.3.3. Windowing of the iteration steps	65
4.1.3.4. Weighting	67
4.1.3.5. Summing up	68
4.1.4. Advantages and disadvantages	70
4.1.5. Discussion in the field of geodesy	70
4.2. Measurement Preparation	71
4.2.1. Calibration of seismic devices	72
4.2.1.1. Single instruments	72
4.2.1.2. Cross-calibration	72
4.2.2. Accuracy analysis	76
4.2.2.1. Measuring device accuracy and precision	76
4.2.2.2. Digital uncertainties and errors	79
4.3. Seismic measurements on-site	80
4.3.1. On-site noise conditions (HERA)	80
4.3.1.1. ALPS IIa laboratory (HERA West)	81
4.3.1.2. ALPS IIc site (HERA North)	86
4.3.1.3. Reference (HERA South)	96
4.3.2. Optic-related components of the ALPS II experiment	96
4.3.2.1. Optical tables	97
4.3.2.2. CBB and mirror mountings	97
4.3.3. Associated noise sources	98
4.3.3.1. Dipole magnet girders	98
4.3.3.2. Filter Fan Units	99
4.4. Filtering of signal	101
4.4.1. Spatial transfer functions	101
4.4.2. Low-pass filter due to the cavity pole frequency	104
4.4.3. Filter by the control loop	105
4.5. Data evaluation	105
4.5.1. Specifications for the ALPS IIa isolation	106
4.5.2. Specifications for an ALPS IIc isolation	106
4.5.3. Specifications for a JURA isolation	108

---

<b>5. Development of seismic isolation systems</b>	<b>109</b>
5.1. Procedure for handling seismic noise and isolation problems . . . . .	109
5.2. State-of-the-art seismic isolation concepts . . . . .	111
5.2.1. The LIGO system . . . . .	111
5.2.2. The VIRGO system . . . . .	112
5.3. Development of a seismic isolation system . . . . .	114
5.3.1. CAD draft of a test model . . . . .	114
5.3.2. FEM simulations . . . . .	115
5.3.3. Design drawing . . . . .	121
5.3.4. Evaluation and validation . . . . .	122
5.4. Seismic isolation concept for ALPS IIc and JURA . . . . .	124
<b>6. Conclusion</b>	<b>129</b>
6.1. Summary . . . . .	129
6.2. Outlook . . . . .	130
<b>Appendices</b>	<b>131</b>
<b>A. Notation key for documentation</b>	<b>133</b>
<b>B. MATLAB code ‘Method of frequency-weighted and averaged FFT’</b>	<b>137</b>
<b>C. Calibration charts</b>	<b>141</b>
<b>D. Filter functions</b>	<b>145</b>
<b>E. FEM simulation</b>	<b>147</b>
<b>F. Technical drawings for SINUS</b>	<b>149</b>
<b>Bibliography</b>	<b>171</b>
<b>Acknowledgements</b>	<b>177</b>
<b>Lebenslauf</b>	<b>179</b>
<b>Eidesstattliche Erklärung</b>	<b>181</b>

# List of Figures

2.1. Power spectral densities and scatter plots of white, pink, and red noise [74].	9
2.2. Scheme of an oscillatory system including the interactions with and within the system, the system boundary, and its transfer function. . . . .	10
2.3. Scheme of mass-spring-damper model characteristics. . . . .	11
2.4. Scheme of a compounded mass-spring-damper model. . . . .	11
2.5. Displacement $x(t)$ against the time $t$ . The oscillation's amplitude $A(t)$ is damped according to equation (2.28) [26]. . . . .	13
2.6. Displacement $x(t)$ against the normalised time $t \cdot \omega_0/\text{rad}$ with different values for $\zeta$ . The oscillation is damped according to equation (2.31). . . .	14
2.7. Amplification ratio $\alpha$ for different $\zeta$ values plotted over $\eta$ – based on [54].	15
2.8. Transient and steady-state part of the general displacement $x(t)$ over the time $t$ for forced damped oscillations – left, $\omega \ll \Omega$ ; right, $\omega \gg \Omega$ [54]. . .	16
2.9. Sinusoidal 2 Hz signal in time domain transferred to a single peak in the frequency domain. . . . .	17
2.10. Aliasing effect in signal processing showing a wrongly interpreted signal. Here, a 1.1 Hz signal is sampled with 1 Hz and interpreted as an 10 Hz signal. . . . .	18
2.11. Imperfect sinusoidal 2.045 Hz signal with additional white noise with a variance of 2 in time domain with a sample rate of 100 Hz over 10 s transferred to a wide peak within in the frequency domain. . . . .	19
2.12. Hanning and Kaiser window functions in the time and frequency domain.	20
2.13. Segmentation of the time series with $M = 3$ separated windows. . . . .	21
2.14. Overlapping segmentation of the time series with $M = 5$ separated windows with 50% overlap. . . . .	21
2.15. Overlapping segmentation of the time series with $M = 5$ separated windows with 50% overlap of the Hanning window and the cumulative sum as a dashed line. . . . .	22
2.16. Hanning window characteristics: AF, OC and their difference over the overlap percentage $r$ . . . . .	23
2.17. Kaiser window characteristics: AF, OC and their difference over the overlap percentage $r$ . . . . .	23

2.18. FFTs of an imperfect sinusoidal 2.4 Hz signal with an amplitude of 0.8 V and additional white noise with a variance of 2 V. Simulated with a sample rate of 100 Hz over 100 s and 10 averages, resulting in a sample time of 10 s or frequency resolution of 0.1 Hz. Analysed with a Kaiser window with a beta factor of 2.5 and 20 % overlap. Upper left: power spectrum via equation (2.64); upper right: power spectral density via equation (2.65); lower left: linear spectrum via equation (2.66); lower right: linear spectral density via equation (2.67). . . . .	25
2.19. Imperfect sinusoidal 2.045 Hz signal with additional white noise with a variance of 2 V in time domain with a sample rate of 100 Hz over 10 s and an LSD with a RMS function in the frequency domain. . . . .	27
2.20. Scheme of a complex compounded mass-spring-damper model with a problematic connection between $m_2$ and $m_3$ . . . . .	28
2.21. Scheme of an enhanced, complex compounded mass-spring-damper model with object $m_4$ as an isolation. . . . .	29
2.22. Logarithmic LSDs & RMSs in units of length. Upper plot: excitation with sinusoidal signals at 4.045 Hz and 8.867 Hz and white noise with a variance of 2 m/s. Middle plot: system output of a mass-spring-damper with $\omega_d = 2$ Hz and $\zeta = 0.02$ . Lower plot: transfer function or amplification ratio of system output to excitation. . . . .	30
2.23. Spectrogram of a forced damped oscillation. System characteristics: natural frequency $f_0 = 12.67$ Hz, an initial amplitude $A_0 = 3$ and a decay rate $\beta = 0.2$ . Driving force characteristics: driving frequency $f_e = 378.73$ Hz and driving amplitude $A_e = 157$ . Analysing characteristics: 20 averages with a Kaiser window with a beta factor of 2.5 and an 20 % overlap. . . . .	31
2.24. Scheme of a simple pendulum. . . . .	35
2.25. Scheme of a spring pendulum (left) and a spring blade (right). . . . .	37
2.26. Scheme of an inverted pendulum – adapted from figure 5 of [32]. . . . .	38
2.27. Scheme of an anti-spring – adapted from figure 7 of [32]. . . . .	39
2.28. Transfer function of the harmonic oscillator $y/y_0$ over the frequency $f$ with different natural frequencies $f_0$ and a damping ratio of $\zeta = 0.02$ . . . . .	39
2.29. Scheme of an simple, open-loop controller acting on the input by steering the signal. . . . .	41
2.30. Scheme of a feed-forward controller using additional information to compensate disturbances. . . . .	41
2.31. Scheme of a closed-loop controller fed back the output to react on deviations. . . . .	42
2.32. Scheme of a combined feed-forward/feedback controller. . . . .	42
3.1. Schematic view of Primakoff Effect in an LSW set-up: photon conversion in a magnetic field (left), subsequent travel through a wall, and final photon regeneration in a magnetic field (right) [1]. . . . .	44
3.2. Schematic set-up of the ALPS IIc experiment with its optical resonators – taken from [43]. . . . .	44

---

3.3.	Photon to Axion or ALP coupling over its mass and projected coverage of ongoing and future experiments – taken from [19]. . . . .	46
3.4.	Schematic control loop design for the ALPS II experiment [66]. . . . .	48
3.5.	Schematic representation of a pure mechanical seismometer – taken from [23]. . . . .	51
4.1.	Section of an example time series with signals at 0.203 Hz, 20.17 Hz and 1,904.9 Hz with an amplitude of 1 V, additional white noise with a variance of 2 V, sampled with 5,000 Hz over 100 s. . . . .	58
4.2.	LSD of the example time series with 10 averages, a Kaiser window with a beta factor of 2.5, and 20 % overlap created with the <i>pwelch</i> function of MATLAB. . . . .	58
4.3.	LSDs of the example time series with 1, 10 and 100 averages, a Kaiser window with a beta factor of 2.5, and 20 % overlap; averaged over 100 s, 10 s, & 1 s. . . . .	59
4.4.	Stitched LSDs of the example time series with 1, 10, and 100 averages, a Kaiser window with a beta factor of 2.5, and 20 % overlap; averaged over 100 s, 10 s, & 1 s. . . . .	60
4.5.	Detailed semi-logarithmic view on stitched LSDs of the example time series with 1 and 10 averages, a Kaiser window with a beta factor of 2.5, and 20 % overlap; averaged over 10 s & 1 s. . . . .	60
4.6.	LSD from LPSD-function of the example time series with 10 averages, a Kaiser window with a beta factor equal to 2.5 ( $psll = 19$ ), and 20 % overlap; averaged over 10 s. . . . .	61
4.7.	LSDs of the example time series with 1, 40, and 1000 averages, a Kaiser window with a beta factor of 2.5, and 20 % overlap averaged over 100 s, 2.5 s, & 0.1 s. . . . .	65
4.8.	Window functions for LSD of the example time series over 100 s, sampled with 5,000 Hz, and calculated with the <i>pwelch</i> function of MATLAB, a Kaiser window with a beta factor of 2.5, and with 1, 40, & 1000 averages each over 100 s, 2.5 s, & 0.1 s. . . . .	67
4.9.	Frequency-weighted LSDs of the example time series with 1, 40, and 1000 averages, a Kaiser window with a beta factor of 2.5, and 20 % overlap averaged over 100 s, 2.5 s, & 0.1 s. . . . .	68
4.10.	Frequency-weighted and averaged LSD of the example time series with a Kaiser window with a beta factor of 2.5 and 20 % overlap averaged over and a <i>dod</i> of 3. . . . .	68
4.11.	Frequency-weighted and averaged LSD of the example time series with a Kaiser window with a beta factor of 2.5 and 20 % overlap averaged over and a <i>dod</i> of 16. . . . .	69
4.12.	Comparison of different analysing methods of the example time series with a Kaiser window with a beta factor of 2.5 and 20 % overlap: not averaged (blue), with 10 averages (red), and analysed with MfwaFFT with a <i>dod</i> of 3 (yellow) and with a <i>dod</i> of 16 (magenta). . . . .	69

4.13. Comparison of frequency-weighted and averaged LSDs of the example time series with a Kaiser window with a beta factor of 2.5 and 20 % overlap. Stitched (blue), LPSD-function (red), and analysed with MfwaFFT with a <i>dod</i> of 12 (yellow). . . . .	70
4.14. Calibration chart: differential displacement LSDs of optical table in longitudinal direction on 2019-01-30 at 11:12 UTC+1 with 731-207 accelerometers and the RC control signal. Analysing characteristics: Kaiser window with a beta factor of 2.5 and 20 % overlap; analysed with MfwaFFT with a <i>dod</i> of 12. . . . .	73
4.15. Calibration chart: single displacement LSDs of HERA North West Tunnel in longitudinal direction on 2018-11-22 at 12:24 UTC+1 with a 731-207 accelerometer and a Güralp seismometer. Analysing characteristics: Kaiser window with a beta factor of 2.5 and 20 % overlap; analysed with MfwaFFT with a <i>dod</i> of 16. . . . .	74
4.16. Calibration chart: single displacement LSDs of optical table horizontal on 2019-02-12 at 10:45 UTC+1 with a 731-207 accelerometer and a L-4C geophone. Analysing characteristics: Kaiser window with a beta factor of 2.5 and 20 % overlap; analysed with MfwaFFT with a <i>dod</i> of 12. . . . .	75
4.17. Calibration chart: single displacement LSDs of optical table vertical on 2019-02-12 at 10:45 UTC+1 with a 731-207 accelerometer and a L-22D geophone. Analysing characteristics: Kaiser window with a beta factor of 2.5 and 20 % overlap; analysed with MfwaFFT with a <i>dod</i> of 12. . . . .	75
4.18. Sensitivity measurement of 731-207 accelerometer with P702B power unit and amplifier – effect on the noise floor with a gain of 100 divided by a gain of 10 in vertical direction on 2018-09-17 at 11:16/11:27 UTC+2. Analysing characteristics: Kaiser window with a beta factor of 2.5 and 20 % overlap; analysed with MfwaFFT with a <i>dod</i> of 12. . . . .	76
4.19. Sensitivity measurement of 731-207 accelerometer with P702B power unit and amplifier – effect on measurement in VEL mode to ACC mode in longitudinal direction on 2017-06-13 UTC+2. Analysing characteristics: Kaiser window with a beta factor of 2.5 and 20 % overlap; analysed with MfwaFFT with a <i>dod</i> of 12. . . . .	77
4.20. Sensitivity measurement of 731-207 accelerometer with different mountings in longitudinal direction on 2018-12-06 11:33/11:55 UTC+1. Analysing characteristics: Kaiser window with a beta factor of 2.5 and 20 % overlap; analysed with MfwaFFT with a <i>dod</i> of 12. . . . .	77
4.21. Sensitivity measurement of Tektronix Digital Phosphor Oscilloscope DPO-7000 with different sample frequencies in longitudinal direction on 2018-11-22 12:00 UTC+1. Analysing characteristics: Kaiser window with a beta factor of 2.5 and 20 % overlap; analysed with MfwaFFT with a <i>dod</i> of 9. . . . .	78



---

4.22. Sensitivity measurement of Tektronix Digital Phosphor Oscilloscope DPO-7000 with different resolutions in longitudinal direction on 2018-12-06 11:40 UTC+1. Analysing characteristics: Kaiser window with a beta factor of 2.5 and 20 % overlap; analysed with MfwaFFT with a <i>dod</i> of 12. . . . .	79
4.23. Confidence intervals of single displacement LSDs of HERA North Hall in longitudinal direction on 2018-11-23 at 11:41 UTC+1. Analysing characteristics: Kaiser window with a beta factor of 2.5 and 20 % overlap; analysed with MfwaFFT with differnt averages and a <i>dod</i> of 12. . . . .	80
4.24. Single displacement LSDs & RMSs of HERA West ALPS Iia laboratory Central Table in longitudinal direction on 2019-01-30 at 11:03 UTC+1. Analysing characteristics: Kaiser window with a beta factor of 2.5 and 20 % overlap analysed; with MfwaFFT with a <i>dod</i> of 12. . . . .	82
4.25. Single displacement LSD & RMS of HERA West ALPS Iia laboratory Laser Table in longitudinal direction on 2019-01-30 at 11:03 UTC+1. Analysing characteristics: Kaiser window with a beta factor of 2.5 and 20 % overlap; analysed with MfwaFFT with a <i>dod</i> of 12. . . . .	82
4.26. Differential displacement LSDs & RMSs of HERA West ALPS Iia laboratory Laser to Central Table (PC) in longitudinal direction on 2019-01-30 at 11:03 UTC+1. Analysing characteristics: Kaiser window with a beta factor of 2.5 and 20 % overlap; analysed with MfwaFFT with a <i>dod</i> of 12. . . . .	83
4.27. Single displacement LSDs & RMSs of HERA West ALPS Iia laboratory End Table in longitudinal direction on 2019-01-30 at 11:12 UTC+1. Analysing characteristics: Kaiser window with a beta factor of 2.5 and 20 % overlap; analysed with MfwaFFT with a <i>dod</i> of 12. . . . .	84
4.28. Differential displacement LSDs & RMSs of HERA West ALPS Iia laboratory Central to End Table (RC) in longitudinal direction on 2019-01-30 at 11:12 UTC+1. Analysing characteristics: Kaiser window with a beta factor of 2.5 and 20 % overlap; analysed with MfwaFFT with a <i>dod</i> of 12. . . . .	85
4.29. Differential displacement LSDs & RMSs of HERA West ALPS Iia laboratory Production and Regeneration Cavity on 2019-01-30 UTC+1. Analysing characteristics: Kaiser window with a beta factor of 2.5 and 20 % overlap; analysed with MfwaFFT with a <i>dod</i> of 12. . . . .	85
4.30. Single displacement LSDs & RMSs of HERA North Hall in longitudinal direction on 2018-11-23 at 11:41 UTC+1. Analysing characteristics: Kaiser window with a beta factor of 2.5 and 20 % overlap; analysed with MfwaFFT with a <i>dod</i> of 12. . . . .	86
4.31. Single displacement LSDs & RMSs of HERA North West Tunnel in longitudinal direction on 2018-11-23 at 11:41 UTC+1. Analysing characteristics: Kaiser window with a beta factor of 2.5 and 20 % overlap; analysed with MfwaFFT with a <i>dod</i> of 12. . . . .	87
4.32. Differential displacement LSDs & RMSs of HERA North West Tunnel to Hall in longitudinal direction on 2018-11-23 at 11:41 UTC+1. Analysing characteristics: Kaiser window with a beta factor of 2.5 and 20 % overlap; analysed with MfwaFFT with a <i>dod</i> of 12. . . . .	88

4.33. Combined displacement LSDs & RMSs of HERA North, West Tunnel, Hall, and differential signal in longitudinal direction on 2018-11-23 at 11:41 UTC+1. Analysing characteristics: Kaiser window with a beta factor of 2.5 and 20 % overlap; analysed with MfwaFFT with a <i>dod</i> of 12. . . . .	89
4.34. Differential displacement LSDs & RMSs of HERA North Hall to East Tunnel in longitudinal direction on 2018-11-26 at 10:40 UTC+1. Analysing characteristics: Kaiser window with a beta factor of 2.5 and 20 % overlap; analysed with MfwaFFT with a <i>dod</i> of 12. . . . .	90
4.35. Differential displacement LSDs & RMSs of HERA North (ALPS IIc) Production and Regeneration Cavity on 2018-11-23 and 2018-11-26 UTC+1. Analysing characteristics: Kaiser window with a beta factor of 2.5 and 20 % overlap; analysed with MfwaFFT with a <i>dod</i> of 12. . . . .	90
4.36. Combined displacement LSDs & RMSs of HERA North Hall to West Tunnel in longitudinal direction on 2018-11-22 at 12:24 and 21:32 UTC+1. Analysing characteristics: Kaiser window with a beta factor of 2.5 and 20 % overlap; analysed over 100 averages. . . . .	91
4.37. Spectrogram of HERA North Hall to West Tunnel in longitudinal direction on 2018-11-23 UTC+1. Analysing characteristics: 1,440 averages (1 min) with a Kaiser window with a beta factor of 2.5 and 20 % overlap. . . . .	92
4.38. Spectrogram of HERA North Hall to West Tunnel in longitudinal direction on 2018-11-23 UTC+1. Analysing characteristics: 1,440 averages (1 min) with a Kaiser window with a beta factor of 2.5 and 20 % overlap. . . . .	92
4.39. Displacement RMS of HERA North, West Tunnel to Hall in longitudinal direction from 2018-11-22 at 10:40 UTC+1 to 2018-11-26 09:15 UTC+1. Analysing characteristics: 5676 averages (1 min) with Kaiser window with a beta factor of 2.5 and 20 % overlap. . . . .	93
4.40. Combined displacement LSDs & RMSs of HERA North, West Tunnel to Hall in three-dimensional direction on 2018-11-23 at 11:41/11:50/12:03 UTC+1. Analysing characteristics: Kaiser window with a beta factor of 2.5 and 20 % overlap; analysed with MfwaFFT with a <i>dod</i> of 12. . . . .	94
4.41. Single displacement LSDs & RMSs of HERA North Hall on concrete blocks and ground in longitudinal direction on 2018-11-22 at 16:20 UTC+1. Analysing characteristics: Kaiser window with a beta factor of 2.5 and 20 % overlap; analysed with MfwaFFT with a <i>dod</i> of 12. . . . .	95
4.42. Amplitude of transfer function of HERA North Hall on ground to concrete blocks in all three-dimensional directions on 2018-11-22 at 16:20/16:28/16:36 UTC+1. Analysing characteristics: Kaiser window with a beta factor of 2.5 and 20 % overlap; analysed with MfwaFFT with a <i>dod</i> of 12. . . . .	95
4.43. Amplitude of transfer function of HERA South Hall on ground to bridge construction in longitudinal and vertical direction on 2017-01-08 UTC+1. Analysing characteristics: Kaiser window with a beta factor of 2.5 and 20 % overlap; analysed with MfwaFFT with a <i>dod</i> of 12. . . . .	96

4.44. Amplitude of transfer function of HERA West ALPS IIa lab ground to optical tables in longitudinal direction on 2018-09-06 15:00/15:45/16:02 UTC+2. Analysing characteristics: Kaiser window with a beta factor of 2.5 and 20 % overlap; analysed with MfwaFFT with a *dod* of 12. . . . . 97

4.45. Amplitude of transfer function of OT to AP to CBB in longitudinal direction on 2017-09-18 11:42/11:56/12:08 UTC+2. Analysing characteristics: Kaiser window with a beta factor of 2.5 and 20 % overlap; analysed with MfwaFFT with a *dod* of 12. . . . . 98

4.46. Displacement LSDs & RMSs of dipole magnet and nearby ground powered and warm in longitudinal direction on 2017-11-21 15:17 UTC+1 and 2017-12-01 13:57 UTC+1. Analysing characteristics: Kaiser window with a beta factor of 2.5 and 20 % overlap; analysed with MfwaFFT with a *dod* of 12. . . . . 99

4.47. Displacement LSDs & RMSs of FFUs and a table inside the clean room in vertical direction on 2018-11-19 12:12/12:26 UTC+1. Analysing characteristics: Kaiser window with a beta factor of 2.5 and 20 % overlap; analysed with MfwaFFT with a *dod* of 12. . . . . 100

4.48. Displacement LSDs & RMSs of FFUs and a table inside the clean room in a horizontal direction on 2018-11-20 13:01/13:06 UTC+1. Analysing characteristics: Kaiser window with a beta factor of 2.5 and 20 % overlap; analysed with MfwaFFT with a *dod* of 12. . . . . 100

4.49. Filtering model: smoothed and averaged amplitude of transfer function of HERA West ALPS IIa lab ground to optical tables in longitudinal direction on 2018-09-06 15:00/15:45/16:02 UTC+2. Analysing characteristics: Kaiser window with a beta factor of 2.5 and 20 % overlap; analysed with MfwaFFT with a *dod* of 12. . . . . 102

4.50. Filtering model: smoothed amplitude of transfer function of optical table to CBB in longitudinal direction on 2017-09-18 12:08 UTC+2. Analysing characteristics: Kaiser window with a beta factor of 2.5 and 20 % overlap; analysed with MfwaFFT with a *dod* of 12. . . . . 102

4.51. Filtering model: smoothed amplitude of transfer function of stacked concrete blocks, bridge construction, and the case if the bridge is used instead of the blocks in longitudinal direction on 2017-01-08 and 2018-11-22 UTC+1. Analysing characteristics: Kaiser window with a beta factor of 2.5 and 20 % overlap; analysed with MfwaFFT with a *dod* of 12. . . . . 103

4.52. Suppression model: inverted absolute value of the low-pass filter of the ALPS II and JURA cavities. . . . . 104

4.53. Suppression model: inverted absolute value of the ALPS II control loop. . 105

4.54. Filtered differential displacement LSDs & RMSs of HERA West ALPS IIa laboratory Production and Regeneration Cavity on 2019-01-30 UTC+1. Analysing characteristics: Kaiser window with a beta factor of 2.5 and 20 % overlap; analysed with MfwaFFT with a <i>dod</i> of 12. Filter characteristics: attenuated by the cavities with $f_p = 1,018.32$ Hz for PC and $f_p = 67.89$ Hz for RC and by the control loop with a unity gain frequency of 4 kHz. . . . .	106
4.55. Filtered differential displacement LSDs & RMSs of HERA North (ALPS IIc) Production and Regeneration Cavity on 2018-11-23 and 2018-11-26 UTC+1. Analysing characteristics: Kaiser window with a beta factor of 2.5 and 20 % overlap; analysed with MfwaFFT with a <i>dod</i> of 12. Filter characteristics: attenuated by the cavities with $f_p = 74.95$ Hz for PC and $f_p = 5.00$ Hz for RC and by the control loop with a unity gain frequency of 4 kHz. . . . .	107
4.56. Filtered displacement RMS of HERA North, West Tunnel to Hall in longitudinal direction from 2018-11-22 at 10:40 UTC+1 to 2018-11-26 09:15 UTC+1. Analysing characteristics: 5676 averages (1 min) with Kaiser window with a beta factor of 2.5 and 20 % overlap. Filter characteristics: attenuated by the cavities with $f_p = 74.95$ Hz for PC and $f_p = 5.00$ Hz for RC and by the control loop with a unity gain frequency of 4 kHz. . . . .	107
4.57. Filtered differential displacement LSDs & RMSs of an assumption for JURA by the HERA North (ALPS IIc) Production and Regeneration Cavity data measured on 2018-11-23 and 2018-11-26 UTC+1. Analysing characteristics: Kaiser window with a beta factor of 2.5 and 20 % overlap; analysed with MfwaFFT with a <i>dod</i> of 12. Filter characteristics: attenuated by the cavities with $f_p = 11.99$ Hz for PC and $f_p = 0.50$ Hz for RC and by the control loop with a unity gain frequency of 4 kHz. . . . .	108
5.1. LIGO seismic isolation system at the example of the HAM camber – conceptual (a) and CAD (b) design – taken from [51]. . . . .	112
5.2. Schematic of the EIB-SAS with three inverted pendulums (1), GAS filters (2), a LVDT platform (3), a springbox (4), a top-plate (5), a optical bench (6), and a tilt stabiliser (7) for seismic noise suppression at low-frequencies [10]. . . . .	113
5.3. Strain noise LSD achieved at O2 observing run of LIGOs and VIRGO cavities – taken from [27]. . . . .	113
5.4. Schematic of the Spider with the blades mounted to the outside blocks without bending them. . . . .	115
5.5. Overview of steps of the FEM simulation carried out to define the optimal specifications for the Spider. . . . .	115
5.6. Geometry of Spider imported into ANSYS with an applied mesh. . . . .	116
5.7. “Static Structural” simulation of ANSYS showing the equivalent stress of the Spider with a blade thickness of 0.30 mm and a load of 2.3 kg. . . . .	117

5.8. “Modal” simulation of ANSYS showing the first mode of the Spider with a blade thickness of 0.30 mm and a load of 2.3 kg. . . . .	117
5.9. Frequency response in vertical direction with an excitation of 1 N at the baseplate and a decay rate of $\{\beta\} = 0.015$ as Bode plot of the Spider with a blade thickness of 0.30 mm and an applied load of 2.3 kg. . . . .	118
5.10. Parameter-based “Modal” simulation of ANSYS showing the first mode of the Spider with different blade thickness depending on the load from 0.3 kg to 6.4 kg (upper) and with different loads depending on the blade thickness from 0.18 mm to 0.40 mm (lower). . . . .	119
5.11. Parameter-based “Modal” simulation of ANSYS showing the first mode of the Spider with a blade thickness from 0.18 mm to 0.40 mm and an applied load from 0.3 kg to 6.4 kg with the red area indicating the system collapse. . . . .	119
5.12. “Response Spectrum” simulation of ANSYS showing the total displacement of the Spider with a blade thickness of 0.30 mm and an applied load of 2.3 kg with a measured excitation from the HERA North Hall applied. . . . .	120
5.13. Technical assembly drawing of Spider with base plate (10), keystone (20), angle brackets (30), tilttable blocks (40), wedges (50), spring blades (60), fixation plates (70), socket (80), and screws (90) – (110) with the blades mounted to keystone. . . . .	121
5.14. Photograph of the Spider including three spring blades. . . . .	122
5.15. Displacement LSDs & RMSs of Spider with 0.30 mm blades with different loads in vertical direction on 2018-07-10/13/23 and 09-10 at 15:31/13:21/11:28/11:21 UTC+2. Analysing characteristics: Kaiser window with a beta factor of 2.5 and 20 % overlap; analysed with MfwaFFT with a <i>dod</i> of 12. . . . .	123
5.16. Amplitude of transfer function of Spider with 0.30 mm blades with different loads in vertical direction on 2018-07-10/13/23 and 09-10 at 15:31/13:21/11:28/11:21 UTC+2. Analysing characteristics: Kaiser window with a beta factor of 2.5 and 20 % overlap; analysed with MfwaFFT with a <i>dod</i> of 12. . . . .	123
5.17. Technical assembly drawing of SINUS with base plate (10), inverted pendulums (20), upper plate (30), Spiders (40), swinging plate (50), and screws and nuts (60) to (90) – based on [10]. . . . .	124
5.18. Technical assembly drawing of Spider for SINUS with base plate (10), blocks (20), clamps (30), pre-load plates (40), keystone (50), spring blades (60), fixation plates (70), cylinder head screws (80) to (110), and knurled screw (120) – based on [10]. . . . .	125
5.19. Technical assembly drawing of IP for SINUS with foot (10), lower flex (20), tube connectors (30), tube (40), upper flex (50), wing screw (60) – based on [10]. . . . .	126
5.20. FEM analyses of ANSYS showing stress and main modes of the SINUS. . . . .	127

---

C.1. Calibration chart of the L-4C horizontal geophone – taken from the data sheet [47]. . . . .	141
C.2. Calibration chart of the L-22D vertical geophone – taken from the data sheet [64]. . . . .	141
C.3. Sensitivity measurement of 731-207 accelerometer with P702B power unit and amplifier – displacement LSDs of table measurements (single and differential) in vertical direction on 2018-09-17 at 11:16/11:27 UTC+2. Analysing characteristics: Kaiser window with a beta factor of 2.5 and 20 % overlap; analysed with MfwaFFT with a <i>dod</i> of 12. . . . .	142
C.4. Sensitivity measurement of 731-207 accelerometer with P702B power unit and amplifier – displacement LSDs of table measurements in longitudinal direction on 2017-06-13 UTC+2. Analysing characteristics: Kaiser window with a beta factor of 2.5 and 20 % overlap; analysed with MfwaFFT with a <i>dod</i> of 12. . . . .	142
C.5. Sensitivity measurement of 731-207 accelerometer with different mountings in longitudinal direction on 2018-12-06 11:33/11:55 UTC+1. Analysing characteristics: Kaiser window with a beta factor of 2.5 and 20 % overlap; analysed with MfwaFFT with a <i>dod</i> of 12. . . . .	143
D.1. Model of magnitude and phase for the ALPS II and JURA cavities. . . .	145
D.2. Model of magnitude and phase for the ALPS II and JURA cavities. . . .	145
D.3. Example showing the effect of several filters applied to the differential signal to attenuate the seismic noise and compare its RMS value to the given requirements. . . . .	146
E.1. “Modal” simulation of ANSYS showing the forth or fifth mode at 418 Hz of the Spider with a blade thickness of 0.30 mm and an applied load of 2.3 kg. . . . .	147
E.2. “Modal” simulation of ANSYS showing the sixth mode at 979 Hz of the Spider with a blade thickness of 0.30 mm and an applied load of 2.3 kg. . .	147

# List of Tables

2.1. Different damped systems depending on the damping ratio $\zeta$ [54]. . . . .	14
3.1. Requirements for the ALPS II and JURA cavities [6, 46]. . . . .	49
3.2. List of seismometers used in the ALPS II experiment to measure seismic noise data [29, 47, 64, 52, 53]. . . . .	52
3.3. List of devices used in the ALPS II experiment to acquire seismic noise data [67, 70, 3, 4]. . . . .	53
4.1. Overview of filters and transformations for adjusting the seismic noise data.	101





# Acronyms

A | C | D | E | F | G | H | I | J | L | M | N | O | P | Q | R | S | T | V | W

## A

<b>AC</b>	Alternating Current
<b>ACC</b>	ACceleration
<b>AF</b>	Amplitude Flatness
<b>ALP</b>	Axion-Like Particle
<b>ALPS</b>	Any Light Particle Search
<b>ANSYS</b>	ANalysis SYStem
<b>AOSEM</b>	Another Optical Sensor Electromagnetic Motor
<b>AP</b>	Alignment Plate
<b>AS</b>	Amplitude Spectrum
<b>ASD</b>	Amplitude Spectral Density

## C

<b>CAD</b>	Computer-Aided Design
<b>CBB</b>	Central Bread Board
<b>CP</b>	Charge and Parity
<b>CT</b>	Central Table

## D

<b>DC</b>	Direct Current
<b>DESY</b>	Deutsches Elektronen-SYnchrotron
<i>dod</i>	degree of detail
<b>DOF</b>	Degrees Of Freedom
<b>DWS</b>	Differential Wavefront Sensing

## E

<b>EGO</b>	European Gravitational Observatory
<b>EIB-SAS</b>	External Injection Bench Seismic Attenuation System
<b>eLISA</b>	evolved Laser Interferometry Space Antenna
<b>ENBW</b>	Effective Noise BandWidth
<b>ET</b>	End Table

## F

<b>FEM</b>	Finite Element Method
<b>FFT</b>	Fast Forurier Transform
<b>FFU</b>	Filter Fan Unit
<b>FSR</b>	Free Spectral Range
<b>G</b>	
<b>GAS</b>	Geometric Anti-Spring
<b>GIA</b>	Glacial Isostasy Adjustment
<b>H</b>	
<b>HAM</b>	Horizontal Access Modules
<b>HEPI</b>	Hydraulic External Pre-Isolator
<b>HERA</b>	Hadron-Elektron-Ring-Anlage
<b>HET</b>	HETrodyne sensing scheme
<b>I</b>	
<b>IP</b>	Inverted Pendulum
<b>ISI</b>	Internal Seismic Isolators
<b>J</b>	
<b>JURA</b>	Joint Undertaking Research for Axions
<b>L</b>	
<b>LIGO</b>	Laser Interferometer Gravitational-Wave Observatory
<b>LISA</b>	Laser Interferometry Space Antenna
<b>LPSD</b>	Logarithmic frequency axis Power Spectrum Density
<b>LS</b>	Linear Spectrum
<b>LSD</b>	Linear Spectral Density
<b>LSW</b>	Light-Shining-through-a-Wall
<b>LT</b>	Laser Table
<b>LTPDA</b>	LISA Technology Package Data Analysis
<b>LVDT</b>	Linear Variable Differential Transformer
<b>M</b>	
<b>MATLAB</b>	MATrix LABoratory
<b>MEA</b>	Maschinen- und ExperimenteAufbau
<b>MfwaFFT</b>	Method of frequency-weighted and averaged FFT
<b>N</b>	
<b>NENBW</b>	Normalised Equivalent Noise BandWidth

**O**

**OC**           Overlap Correlation  
**OT**           Optical Table

**P**

**PB**           Power Build-up  
**PC**           Production Cavity  
**PDH**         Pound-Drever-Hall  
**PF**           Power Flatness  
**PGR**         Post Glacial Rebound  
**PID**         Proportional Integral Derivative  
**PLL**         Phase-Lock Loop  
**PPKTP**       Periodically-Poled Potassium Titanyl Phosphate  
**PS**           Power Spectrum  
**PSD**         Power Spectral Density

**Q**

**QCD**         Quantum ChromoDynamics

**R**

**RC**           Regeneration Cavity  
**RMS**         Root Mean Square  
**RSTAB**       Räumliche STABwerke

**S**

**SHG**         Second Harmonic Generation  
**SINUS**       Seismic Isolation Non-Unified Systems  
**SNR**         Signal-to-Noise Ratio  
**SQUID**       Superconducting QUantum Interference Device

**T**

**TES**         Transition Edge Sensor

**V**

**VEL**         VELOCITY

**W**

**WISP**       Weakly Interacting Slim Particle



# Glossary

A | F | M | R | S | V

## A

**accelerance** Dynamic inertia of a system, defined by the second derivative of the system output divided by the excitation.

**ALAZAR** Named product by the Alazar Technologies Inc.

**aliasing** Effect of wrongly interpreting signals above the Nyquist frequency and therefore being indistinguishable from the real signals.

## F

**FFT** Here, the graph or plot in frequency domain.

## M

**mobility** Mechanical admittance of a system, defined by the first derivative of the system output divided by the excitation.

## R

**receptance** Dynamic resilience of a system, defined by the system output divided by the excitation.

## S

**seismometer** Device to detect seismic activities

## V

**Virgo** Large interferometer designed to detect gravitational waves, named after the Virgo cluster, a galaxy cluster in the constellation Virgo (latin for the virgin).



# 1. Introduction

In engineering science stepping beyond technical boundaries is always a difficult exercise. For example, measuring mechanical vibrations less than one thousandth of the diameter of an atom and even attempting to stabilise a system to this level, can be viewed as an enormous challenge. In general, people interact with mechanical vibrations even without being aware of them. This becomes even clearer when machines or vehicles are used that can produce, dampen, or compensate vibrations with complex control systems. The study of vibrations, their origin, and their propagation is useful to explore new technologies, as is the case of this thesis. In the following, the examined mechanical vibrations are defined as seismic noise, which in the narrower sense deals with earthquakes and the propagation of seismic waves through the earth, but in a broader sense observes any oscillation that can cause vibrations. This quickly leads to a complex and chaotic system, which arises from an almost infinite number of sources and generates an equal number of effects. Thus, even if it were possible to say that something is vibrating with a certain frequency and amplitude, it is difficult to determine what the source is. Conversely, it is often unknown what or to what extent a defined source of seismic noise would cause. The overall challenge for all these problems is to reduce or limit the causes of seismic noise to the specifications determined by relevant system requirements.

For scientific research and experiments, conditions are often not clearly defined in advance and circumstances can change continuously. The in Hamburg located Deutsches Elektronen-SYNchrotron (DESY) explores various areas of basic research in physics, including the search for new particles in high-energy physics. DESY has paved the way for innovative experiments such as Any Light Particle Search (ALPS) II with the Strategy 2030. This experiment requires the extremely precise alignment of optical components, for which seismic noise analysis is indispensable. This work therefore focuses on that analysis, its evaluation, and any seismic isolation that may be required for the ALPS II experiment.

## 1.1. Motivations and background

This work was written in the context of the ALPS group at DESY. In the group, scientists are working on a particle physics experiment, searching for particles beyond the standard model. More precisely, ALPS II is a laboratory-based experiment looking for axions and Axion-Like Particles (ALPs) that could explain unresolved physical phenomena. One theory assumes that the axion couples with a virtual photon in a magnetic field so that it can be converted into a photon. To prove this, ALPS II uses a Light-Shining-through-a-Wall (LSW) set-up in which photons are converted into axions, sent through a light-tight wall, and then reconverted to a photon with the same properties on the

other side. The experiment will be located in the former Hadron-Elektron-Ring-Anlage (HERA), an underground accelerator ring which passes through four large detector halls. Since the conversion probability is expected to be extremely low, ALPS II stores photons in a high finesse optical cavity inside a magnetic field, while attempting to convert as many photons into axions as possible. On the other side of the wall, the axions are reconverted to photons with a similar set-up using the reverse effect. To make this possible, the relative positions and movements of the mirrors of the optical resonators have to meet extreme requirements, since they are located on different optical tables. The two exterior mirrors are placed approximately 250 m opposite each other inside the HERA tunnel. The inner mirrors near the light-tight wall are mounted on one optical table within an experimental hall. The relative stability of all four mirrors in the longitudinal direction must be within half a picometre, which is the same as one millionth of the vibration that a human step normally triggers inside a building. Furthermore, the angular deviation of the mirrors has to be within a few microradians. In addition, stability must be maintained for the duration of the experiment. All these requirements are paramount as to why the seismic conditions have to be determined exceptionally precisely for the ALPS II experiment.

## 1.2. Research hypotheses and aims

To capture the whole extent of the problem, this thesis divides it into three research hypotheses. They focus on the acquisition and the post-processing of seismic noise data and its evaluation by merging them with the ALPS II requirements. Therefore, spectral data are examined in modal analyses to define critical frequencies or oscillating components. On this basis, an economic seismic test model should be built, which incorporates state-of-the-art concepts of seismic isolation to compensate for any critical vibrations that may occur. Building on this, a seismic isolation concept must be derived that meets the ALPS II requirements.

**Hypothesis 1:** — *Modal analysis can be extended with the ability to examine data over at least five orders of magnitude without the requirement of a priori information about the data, yielding valid, equally distributed, post-processable results, and subsequently resulting in an enhanced understanding of the seismic conditions.*

The first research hypothesis concentrates on result improvement of modal data analyses by extending the frequency range. The implementation of a modal analysis is always confronted with a trade-off in the validity of their individual results, which are influenced by subjective parameters. Therefore, a method should be developed to analyse data over at least five orders of magnitude of frequency. In addition, no a priori information about the data should have to be necessary. The result ought to be a continuous and differentiable spectrum or a spectral density with a known frequency bin size that can be intelligibly plotted across all frequencies and allows for frequency-dependent post-processing. Furthermore, frequency accuracy as well as data precision must be preserved throughout the frequency range to enable valid data interpretation.



**Hypothesis 2:** — *Modal data can be spatially transformed, including various conditions, by applying several filters according to the given circumstances, to determine specifications for a future ALPS IIc set-up from the existing ALPS IIa laboratory.*

If the first hypothesis is validated, an evaluation of the results must be made, since the measured data can not be compared directly to the given requirements. The second research hypothesis therefore focusses on the transformation of the analysed seismic data, which are performed on the basis of the current ALPS II set-up, in which they can be compared to the requirements determined by the laws of physics. In the case of not-yet existing objects, circumstances must be simulated or the measured position spatially converted to another. For this purpose, both the spectral and the cumulative (real movement over a specific period of time or frequency) results must be post-processed, i.e. multiple filters have to be defined and applied. First, as a projection onto the final location of the mirrors, then as a low-pass filter for the optical resonator itself, and finally as a high-pass filter of the downstream active control loop. The result will determine the respective specifications for the seismic isolation system.

**Hypothesis 3:** — *State-of-the-art, economical seismic isolation concepts can be used to develop a seismic isolation concept that meets the respective ALPS II requirements.*

While fulfilling the previously defined specifications, the last research hypothesis concerns itself with design, simulation, and validation of the seismic isolation system/concept. Therefore, the discrepancy between the respective requirements and the current realisations must be eliminated. Thus, simulations have to be compared and validated with real measurements on a passive construction in an iterative process to design a working isolation concept for the ALPS II experiment. Furthermore, additional active control systems for seismic isolation must be considered before the final concepts can be completed.

In summary, the aim of this work is a consistent execution of the above-mentioned research hypotheses, whereby the seismic noise analysis and the isolation concept are based on the requirements given by the ALPS II experiment.

### 1.3. Outline of this work

The dissertation is divided into six chapters to tackle the aforementioned research hypotheses. The reader will be guided from the basics of seismology over to the principles of the ALPS II experiment further on to the seismic noise analysis and the development of a seismic isolation system and finally to a conclusion of the research hypotheses.

For this, chapter 2 brings everyone to the same page by laying the theoretical foundation for the main chapters. The prime focus is on the fundamentals of mechanical vibrations, possible sources of seismic noise, and the conventional as well as state-of-the-art seismic isolation techniques. Chapter 3 outlines the fundamentals of the ALPS II experiment, the tools and techniques available, and the work procedures selected. Thus, it describes the problems and the necessity for this study.

The main part is divided into two chapters. The first, chapter 4, covers the entire seismic noise analysis done for the ALPS II experiment. Here, a new method is introduced to improve the results of modal analysis over large frequency ranges. The chapter also outlines the seismic measurements, the post-processing of the data and the evaluation carried out. The second component of the main part, chapter 5, focuses on seismic isolation systems related to the previous seismic noise analysis. Primarily, a developed approach is presented, which deals generally with seismic noise or seismic isolation problems. Subsequently, state-of-the-art concepts of seismic isolation are shown and a seismic isolation test model is described. The chapter concludes with a seismic isolation solutions, a concept for the Joint Undertaking Research for Axions (JURA)<sup>1</sup>.

The final chapter, chapter 6, summarises the study and the research hypotheses are validated. In addition, an outlook on possible future studies and follow-up tasks in this field is given.

---

<sup>1</sup>ALPS is now in his second phase, called ALPS II, where a possible follow-up experiment will be called JURA.

## 2. Fundamentals and theory of seismic noise

In order to properly perform seismic noise analysis, the concept of two primary pillars has to be understood. The first is formed by the fundamentals of mechanical vibrations, which are discussed in section 2.1 by outlining how seismic data can be analysed and evaluated in general after delineating the theoretical background of oscillation and mechanical systems. The second pillar is defined by its sources. Section 2.2 gives some examples relevant to this work by explaining where seismic noise or rather mechanical vibrations in the broader sense originate from and how they affect mechanical objects. Then, before going into seismic isolation concepts in chapter 5, it is essential to look at the methods of seismic isolation. Section 2.3 will introduce these methods by focussing on isolation techniques that are accurate enough to be useful for industry and experimental physics. This chapter will introduce the basic principles of seismology in order to understand the investigated problem and main work presented in the following chapters.

### 2.1. Fundamentals of mechanical vibration

This section provides a basic introduction to the fundamentals of mechanical vibration and represents the first pillar of understanding seismic noise analysis. It will handle the primary mechanics of oscillations in subsection 2.1.1, the background of mechanical systems in 2.1.2, followed by an outline about modal analysis in subsection 2.1.3, and concludes in 2.1.4 with an adequate way to visualise and present seismic data in the ALPS II experiment.

#### 2.1.1. Theory of oscillation

The theory of oscillation presents the baseline of working with (electronic) signals. From understanding harmonic oscillation to the derivation of a solution of the wave function up to the Signal-to-Noise Ratio (SNR), this subsection explains how a measured seismic time series can be understood and interpreted.

##### 2.1.1.1. Oscillation and waves

Oscillations are defined as repeated temporal fluctuations of state variables of a system, e.g. the movement of a simple pendulum in relation to its frame, the piston stroke in its cylinder of an engine, or the position of a satellite to the orbiting object. First, the most simple oscillation is known as a harmonic oscillation and is given by the following

equation:

$$x(t) = A_0 \cdot \sin(\omega t + \varphi) \quad (2.1)$$

where  $x(t)$  is the position  $x$  at the time  $t$ ,  $A_0$  is the maximum amplitude,  $\varphi$  is the phase, and  $\omega$  the angular frequency defined by:

$$\omega = 2\pi f \quad (2.2)$$

with  $f$  being the frequency. Hence, a harmonic oscillation can be described with a single sine wave. In fact, most oscillations are a composite of an arbitrary number of sine waves. Thus, they are not harmonic but periodic. They satisfy [34]:

$$x(t) = x(t + T) \quad (2.3)$$

where  $T$  is the oscillation period. Furthermore, a periodic oscillation can always be represented via the sum of harmonic oscillations as a Fourier series analysis [34]:

$$x(t) = \frac{a_0}{2} + \sum_{n=1}^{\infty} (a_n \cdot \cos(n\omega_0 t) + b_n \cdot \sin(n\omega_0 t)) \quad (2.4)$$

$$\begin{aligned} \text{with } a_0 &= \frac{2}{T} \int_0^T x(t) dt \\ a_n &= \frac{2}{T} \int_0^T x(t) \cos(n\omega_0 t) dt \\ b_n &= \frac{2}{T} \int_0^T x(t) \sin(n\omega_0 t) dt \end{aligned}$$

If the equation for harmonic oscillation (2.1) is modified to become spatially dependent, it will represent a solution of the wave function  $\psi$  via:

$$\psi(t, x) = A_0 \cdot \sin(\omega t + \varphi(x)) \quad (2.5)$$

Defining  $\omega$  from equation (2.2) as:

$$\omega = 2\pi f = 2\pi \frac{1}{T} \quad (2.6)$$

and the phase  $\varphi(x)$  as:

$$\varphi(x) = \frac{2\pi \cdot x}{v \cdot T} = \frac{2\pi \cdot x}{\lambda} \quad (2.7)$$

with  $v$  as the wave propagation velocity and  $\lambda$  as the wave length, a new wave function can be written from equation (2.5) as:

$$\psi(t, x) = A_0 \cdot \sin\left(2\pi \cdot \left(\frac{t}{T} - \frac{x}{\lambda}\right)\right) \quad (2.8)$$

In this notation, the time  $t$  depends linearly on the period of oscillation  $T$  and the position  $x$  on the wavelength  $\lambda$ , whereby their influences become clear [54].

### 2.1.1.2. Standing waves and resonance

Waves (here, seismic waves) can enter or exit mechanical objects (rather mechanical systems - see 2.1.2) and thereby be transmitted, absorbed, or reflected at every discontinuity. Always, each effect will occur with different characteristics. Reflections for instance can produce a wave in the opposite direction. Even within the object, reflections can occur due to different materials, their processing, temperature and pressure fluctuations, or even at grain boundaries – summarised with each density change. All these effects produce various directional (seismic) waves that oscillate within the object. The wave function from equation (2.8) must therefore be rewritten, with the position  $x$  being a directional path  $\vec{p}$  and  $\vec{k}$  the wave vector, where  $\vec{k}$  is a vector that is perpendicular to the wave front of a wave:

$$|\vec{k}| = \frac{2\pi}{\lambda} \quad (2.9)$$

$$\psi(t, \vec{p}) = A_0 \cdot \sin\left(\frac{2\pi \cdot t}{T} - \vec{p} \cdot \vec{k}\right) \quad (2.10)$$

$$\text{with } \vec{p} = x \cdot \vec{e} \quad (2.11)$$

where  $\vec{e}$  is the unit vector. The total wave function  $\Psi$  then is the sum of all individual waves as:

$$\Psi(t, \vec{p}) = \sum_{i=1}^n \psi_i(t, \vec{p}_i) \quad (2.12)$$

If waves of the same frequency or wavelength, but propagating in opposite directions superpose each other, standing waves will occur. The resulting wave oscillates in time, but does not move in space and therefore has a fixed location with minimum amplitude, 'nodes', and equivalent with maximum amplitude, 'antinodes' [34]. Imagine two waves with the same amplitude, oscillation period, and wavelength as follows:

$$\psi_1(t, \vec{p}_1) = A_0 \cdot \sin\left(\frac{2\pi \cdot t}{T} - \vec{p}_1 \cdot \vec{k}\right) \quad (2.13)$$

$$\text{with } \vec{p}_1 = x \cdot \begin{pmatrix} 1 \\ 0 \\ 0 \end{pmatrix} \quad (2.14)$$

$$\psi_2(t, \vec{p}_2) = A_0 \cdot \sin\left(\frac{2\pi \cdot t}{T} - \vec{p}_2 \cdot \vec{k}\right) \quad (2.15)$$

$$\text{with } \vec{p}_2 = x \cdot \begin{pmatrix} -1 \\ 0 \\ 0 \end{pmatrix} \quad (2.16)$$

By adding  $\psi_1$  and  $\psi_2$  the resulting standing wave follows with the addition theorem as [56]:

$$\psi_s(t, \vec{p}) = 2A_0 \cdot \sin\left(2\pi \cdot \frac{t}{T}\right) \cdot \cos(\vec{p} \cdot \vec{k}) \quad (2.17)$$

As  $\vec{p}$  from equations (2.14) and (2.16) indicates, standing waves also can be multidimensional, meaning that they propagate in a plane or in space, e.g. inside a mechanical object. Here, the possibility of having a standing wave creates natural frequencies  $\omega_0$  or  $f_0$  which then allows resonances<sup>1</sup>. That is, at this frequency, the system amplifies the excitation, which can be desired, e.g. in musical instruments or on a swing, but can also damage a machine or object if it is not. In this case, attenuation methods have to be implemented to reduce the amplitudes or to shift the natural frequencies in other, more workable, frequency ranges (see 2.1.2). From the perspective of mechanical vibrations resonances are of importance. They have to be estimated accurately and depending on the given specifications eliminated or enhanced as well as possible (compare section 3.1).

In summary, an oscillation caused by any (seismic) noise source (explained in section 2.2) propagates as a wave through an object where it will be reflected and might produce a standing wave. If this frequency coincides with a natural frequency of the object, it is defined as resonance.

### 2.1.1.3. Types of noise

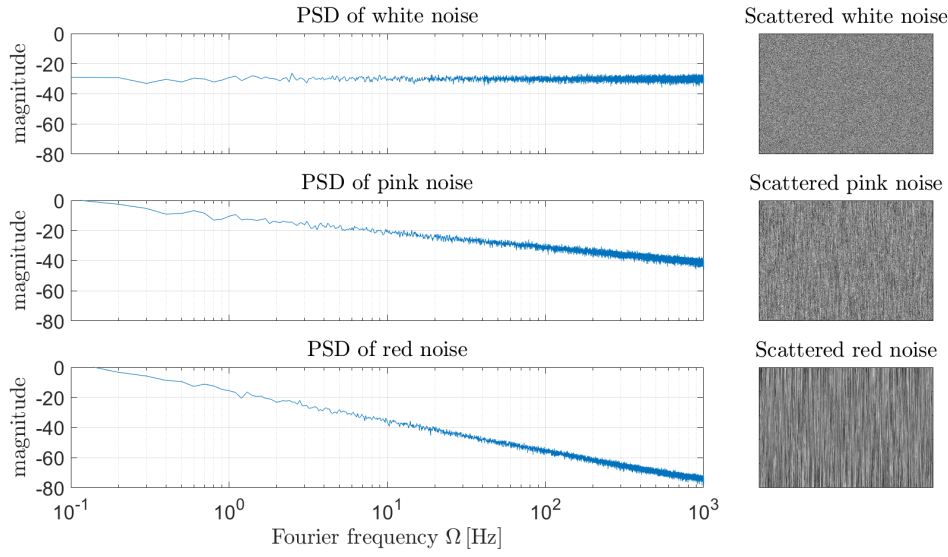
The term 'noise' in general can be defined as the occurrence of statistical fluctuations in an (electronic) measurement. The noise can occur at one or more frequencies or over the entire frequency range. Thus, the noise is frequency dependent. In signal processing, the background noise can be categorised by the colour analogy of its energy into following categories: white noise, pink noise, and red noise. The colours refer to the exponent of the frequency in the denominator. Here and in the following, noise as a function of the frequency with negative exponents, such as blue or violet noise will not be taken into consideration as they are not seismologically significant.

Figure 2.1 shows three different types of noise. First, white noise, also called thermal, Johnson, Nyquist, or Johnson-Nyquist noise, is a random signal with equal intensity over all frequencies. Therefore, it has constant power throughout the frequency spectrum (see upper plots in figure 2.1). If the Direct Current (DC) value is of no interest, white noise occurring before digitising the data with a zero mean can be averaged out before implementing a modal analysis. In contrast pink noise, also known as Flicker or  $1/f$  noise, is inversely proportional to the frequency  $f$  (see figure 2.1). Pink noise typically occurs in biological systems and within almost every electronic device. Therefore, it can become problematic in measurement chains. In some cases, it can be reduced by applying oversampling (see subsection 3.2.1.3). Lastly, red noise, also Brownian, brown, or  $1/f^2$  noise, can be seen as twice integrated white noise or "random walk" (see lower plots in figure 2.1). Among other things, it is the result of the Brownian particle motion.

One crucial aspect to consider is the noise level. It defines the minimum under which a signal can no longer be detected. Therefore, it must be determined before a measurement can be performed (see 3.2.1.3 and 4.2.2). In fact, in reality, a number of noise-coupling phenomena can affect the signal and thus change the noise level. This can be due

---

<sup>1</sup>Resonance is a phenomenon in which an oscillatory system (see 2.1.2) is excited by an external force that frequency  $\Omega$  coincides with a natural frequency (here: resonance frequency)  $\omega_0$  of the system.



**Figure 2.1.:** Power spectral densities and scatter plots of white, pink, and red noise [74].

to charging effects, inductance, frequency modulation, interference, atmospheric noise, correlations, and others.

#### 2.1.1.4. Signal-to-Noise Ratio

Besides the noise level or noise floor, the SNR is of importance. It easily can be defined as the signal power divided by the noise power as equation (2.18) shows. Other possible forms of presenting the SNR is via the ratio of the squared variances or the square of the ratio of the amplitudes:

$$SNR = \frac{P_{signal}}{P_{noise}} = \frac{\sigma_{signal}^2}{\sigma_{noise}^2} = \left( \frac{A_{signal}}{A_{noise}} \right)^2 \quad (2.18)$$

The SNR is dimensionless and can be calculated based on the time or frequency. Because of the wide dynamic range signals, and so noise, often are expressed in a logarithmic decibel scale as:

$$SNR = 10 \log_{10} \frac{P_{signal}}{P_{noise}} db \quad (2.19)$$

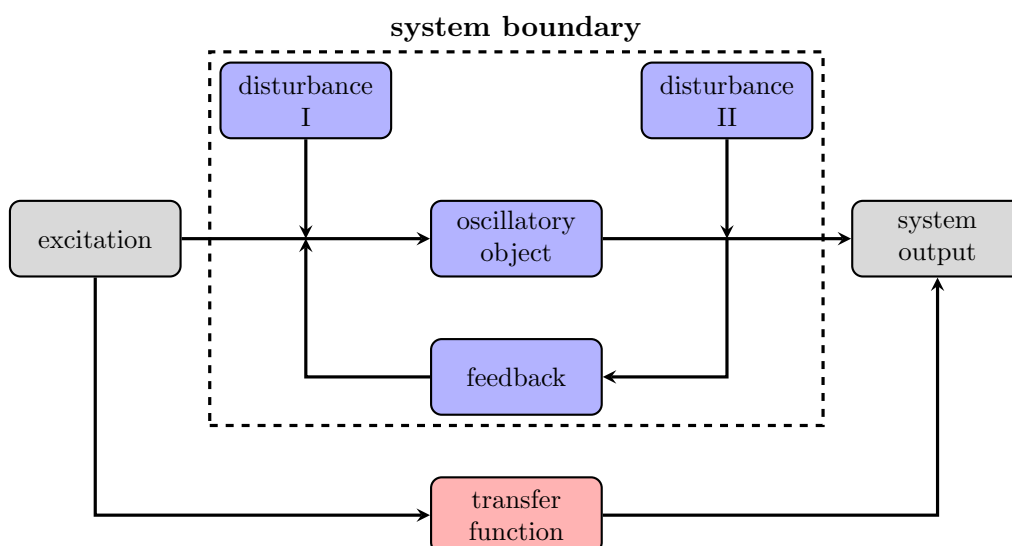
The SNR thus defines the quality of a measurement, an instrument, or a measurement chain. Together with the noise level, it is used as the lower limit in the accuracy analysis (see subsection 4.2.2).

### 2.1.2. The oscillatory systems

Each system described below consists of physical objects that can be considered as a mechanical system. Furthermore, each of these mechanical systems has the ability to

oscillate and therefore is defined as an oscillatory system. In fact, every physical body can be defined as an oscillatory system! The ability to oscillate is identified by three parameters that are explained later in 2.1.2.1. Depending on their specifications or their ratio to each other, the system is generally determined as an oscillatory system. Hence, every physical body has the capacity to resonate!

Figure 2.2 shows a sketch of an oscillatory system including the interactions with and within the system. It illustrates the response (or system output) to any excitation (or system input) applied to the oscillatory object. All boxes inside the dotted system boundary, coloured in blue, define the oscillatory system that is not accessible and therefore has to be considered as an unchangeable black box. Each oscillatory object has its own feedback loop, e.g. an elastic behaviour or a thermal capacity effect. Besides its feedback, there are two types of disturbances. First, affecting the signal before entering the object, e.g. as a background noise undistinguishable from the original signal. Second, directly after leaving the object, e.g. an electrical noise affecting the measuring devices. Both are undesirable but can not be avoided and may also interact with the internal feedback. In addition, the figure shows the alternative characterisation of the system by using a transfer function as a bypass (compare with 2.1.4.3).



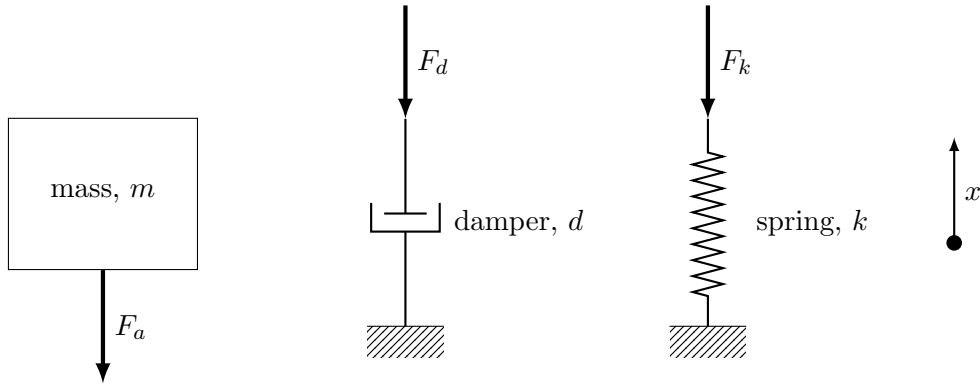
**Figure 2.2.:** Scheme of an oscillatory system including the interactions with and within the system, the system boundary, and its transfer function.

The functionality of an oscillatory system will be explained by using the model of a mass-spring-damper and the equation of motion. Afterwards, the basics and definitions of damping will be explained, which is split into free and forced damped systems. The usage of the transfer function is explained later in 2.1.4.3.



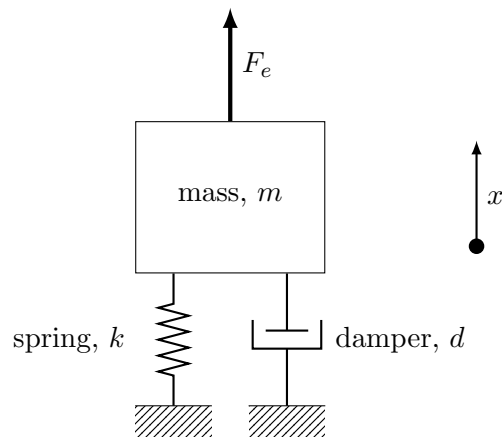
### 2.1.2.1. Mass-Spring-Damper model

As mentioned above, every physical body has the ability to oscillate. This strongly depends on the characteristics of the mass  $m$ , the damping constant  $d$ , and the spring constant  $k$ . Figure 2.3 illustrates these three attributes with their linked forces, where  $F_a$  is the inertia force,  $F_d$  the dampening force, and  $F_k$  is the restoring force. Here, all forces are defined as vectors acting in the opposite direction of the  $x$ -axis.



**Figure 2.3.:** Scheme of mass-spring-damper model characteristics.

Uniting all components creates the mass-spring-damper model as presented in figure 2.4. Here, the external force  $F_e$  is defined in the direction of the  $x$ -axis and opposite to the other forces. As before, the direction of the arrow is shown for better visualisation; same as in the arrangement of the components. This set-up can reflect any physical body as an oscillating system and leads to the equation of motion, which is described in the following paragraphs.



**Figure 2.4.:** Scheme of a compounded mass-spring-damper model.

### 2.1.2.2. Equation of motion

According to Newton's laws all forces within a system have to equalise themselves, which here refers to all forces from figures 2.3 and 2.4.

$$\sum \vec{F} = \vec{F}_e + \vec{F}_a + \vec{F}_d + \vec{F}_k = 0 \quad (2.20)$$

$$\text{with } \vec{F}_a(t) = m \cdot \frac{d^2}{dt^2}(\vec{x}) \quad (2.21)$$

$$\vec{F}_d(t) = d \cdot \frac{d}{dt}(\vec{x}) \quad (2.22)$$

$$\vec{F}_k(t) = k \cdot \vec{x} \quad (2.23)$$

With these equations every oscillatory system can be determined. The equation of motion is mostly represented as a simplified, linear second order derivative equation, when it is one-dimensional as visualised above:

$$F_e(t) = m \cdot \ddot{x} + d \cdot \dot{x} + k \cdot x \quad (2.24)$$

$F_e(t)$  is the external force acting on the system, or referring to figure 2.2 the excitation. If it equals 0, the system is referred to as a "free damped system" (see 2.1.2.3), otherwise as a "forced damped system" (see 2.1.2.4).

### 2.1.2.3. Free damped oscillation

The free (damped) oscillation is defined to have no external force so that the equation (2.24) is modified as follows:

$$0 = m \cdot \ddot{x} + d \cdot \dot{x} + k \cdot x \quad (2.25)$$

The term damping is defined as the conversion of oscillation energy into other forms of energy, usually heat. A damped free oscillatory system therefore reduces its displacement amplitude over time without an external force. It is determined by an exponential function with negative exponent consisting of the decay rate (damping coefficient)  $\beta$  and the time  $t$ . The correlation of the decay rate  $\beta$  and the damping constant  $d$  mentioned in the equation of motion (2.24) takes place via the mass of the system  $m$ . This is effecting the amplitude  $A_0$  so that it becomes time dependent:

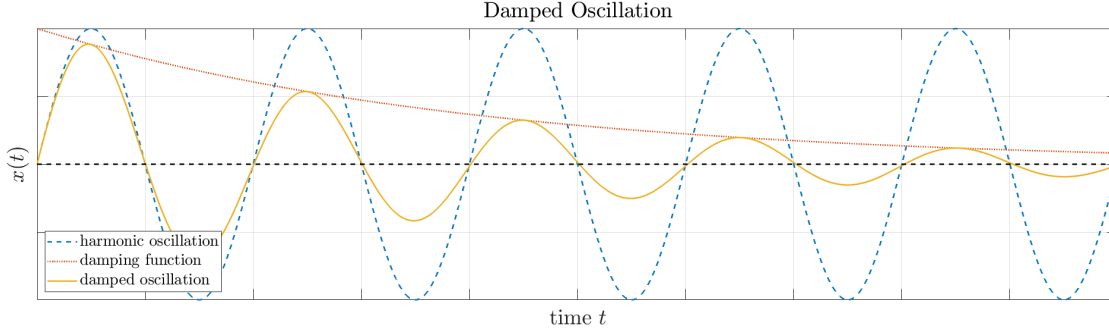
$$A(t) = A_0 \cdot e^{-\beta t} \quad (2.26)$$

$$\text{with } \beta = \frac{d}{2m} \quad (2.27)$$

Together with the equation for a free harmonic oscillation with constant phase  $\varphi_0$  from equation (2.1), this results in the equation of the free damped oscillation for the displacement:

$$x(t) = A_0 \cdot e^{-\beta t} \cdot \sin(\omega t + \varphi_0) \quad (2.28)$$

Figure 2.5 shows a damped oscillation in which the displacement  $x(t)$  is plotted against the time  $t$  as in equation (2.28). The red dotted line symbolises the decay function according to equation (2.26) with decreasing amplitude  $A(t)$  and the blue dashed line the case of a harmonic oscillation.



**Figure 2.5.:** Displacement  $x(t)$  against the time  $t$ . The oscillation's amplitude  $A(t)$  is damped according to equation (2.28) [26].

The natural frequency  $f_0$  or the natural angular frequency  $\omega_0$  is defined as the frequency at which the object or system tends to oscillate. Accordingly to the decay rate  $\beta$ , the damping ratio  $\zeta$  is used, which defines the stability of a damped system. It is defined as the decay rate  $\beta$  divided by the natural angular frequency  $\omega_0$ :

$$\zeta = \frac{\beta}{\omega_0} = \frac{d}{2m\omega_0} = \frac{d}{d_c} \quad (2.29)$$

$$\text{with } d_c = 2m\omega_0 \quad (2.30)$$

where  $d_c$  is defined as the critical damping constant. With equations (2.28) and (2.29) the displacement  $x(t)$  can be represented with  $\zeta$  as:

$$x(t) = A_0 \cdot e^{-\omega_0 \cdot \zeta t} \cdot \sin(\omega t + \varphi_0) \quad (2.31)$$

There are different types of damped systems which are classified depending on the value of the damping ratio  $\zeta$  as shown in table 2.1.

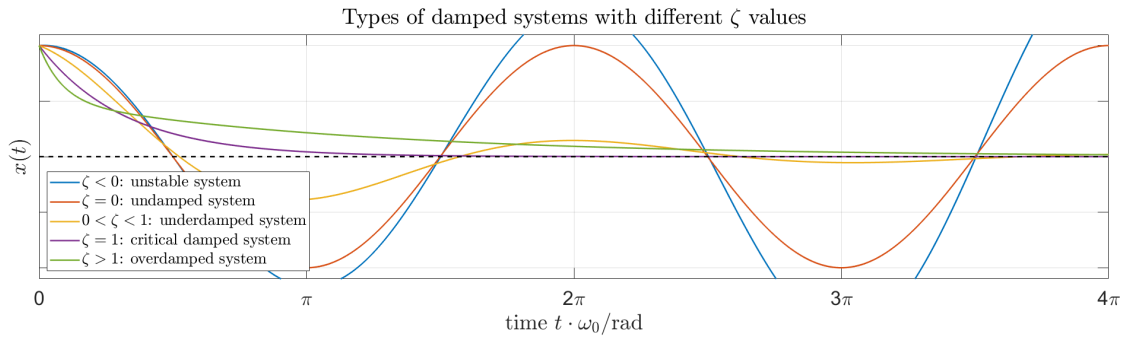
The desired or optimal case for a well damped system is the critical one, where  $\zeta$  equals 1. This ideal case requires tuning of  $k$ ,  $m$ , and  $d$ , which is not always possible. Figure 2.6 illustrates all cases named in table 2.1 with their displacement amplitude  $x(t)$  over the normalised time  $t \cdot \omega_0 / \text{rad}$ . The violet graph refers to the critical damped case.

Furthermore, there is a difference in  $\omega$  from the equation of the free harmonic oscillation (2.1)  $\omega = \omega_0$  and the damped oscillations (2.28) and (2.31)  $\omega = \omega_d$ . Their relation can be calculated with  $\zeta$  as follows:

$$\omega_d = \omega_0 \cdot \sqrt{1 - \zeta^2} \quad (2.32)$$

**Table 2.1.:** Different damped systems depending on the damping ratio  $\zeta$  [54].

Damping ratio $\zeta$	Type of system	Description
$\zeta < 0$	excited, unstable	Self-excited, oscillation system whose amplitude raises with time.
$\zeta = 0$	undamped, quasi stable	Equals the harmonic oscillator without damping.
$0 < \zeta < 1$	underdamped	Damping with oscillation around equilibrium.
$\zeta = 1$	critically damped	Aperiodic limit case; fastest damping to equilibrium.
$\zeta > 1$	overdamped	Slow, aperiodic damping also known as creeping.

**Figure 2.6.:** Displacement  $x(t)$  against the normalised time  $t \cdot \omega_0/\text{rad}$  with different values for  $\zeta$ . The oscillation is damped according to equation (2.31).

#### 2.1.2.4. Forced damped oscillation

In contrast to free oscillation, when applying an external force to the system, the term is defined as forced damped oscillation and affects equation (2.24) as follows [54]:

$$F_0 \cdot \cos(\Omega t + \varphi_e) = m \cdot \ddot{x} + d \cdot \dot{x} + k \cdot x \quad (2.33)$$

$$\text{with } F_e(t) = F_0 \cdot \cos(\Omega t + \varphi_e) \quad (2.34)$$

where  $F_0$  is the maximum force acting on the system,  $\Omega$  the external angular frequency, and  $\varphi_e$  the phase shift to the system's phase. A forced damped oscillatory system has a transient part before the system reaches its equilibrium state. Therefore, the equation for the general displacement  $x(t)$  is split into a transient  $x_t(t)$  and a steady-state  $x_s(t)$  solution [57]:

$$x(t) = x_t(t) + x_s(t) \quad (2.35)$$

The transient part  $x_t(t)$  is equal to the solution of the free damped oscillation, equation (2.31), but will be negligible after some time. The steady-state part  $x_s(t)$  describes the stationary solution at which the system converges as pictured in figure 2.8. It is proportional to the external, driving force  $F_e$  with a phase change  $\varphi$  as described in equation (2.34). An important indicator is the quotient of the driving frequency  $\Omega$  and the natural frequency  $\omega_0$ , which is defined as the frequency ratio  $\eta$ .

$$\eta = \frac{\Omega}{\omega_0} \quad (2.36)$$

An amplification ratio  $\alpha$  as derived in [54] dependent on the frequency ratio  $\eta$  can be used to calculate the frequency dependent effect on the amplitude. It is defined as follows:

$$\alpha = \frac{1}{\sqrt{(1 - \eta^2)^2 + 4\zeta^2\eta^2}} \quad (2.37)$$

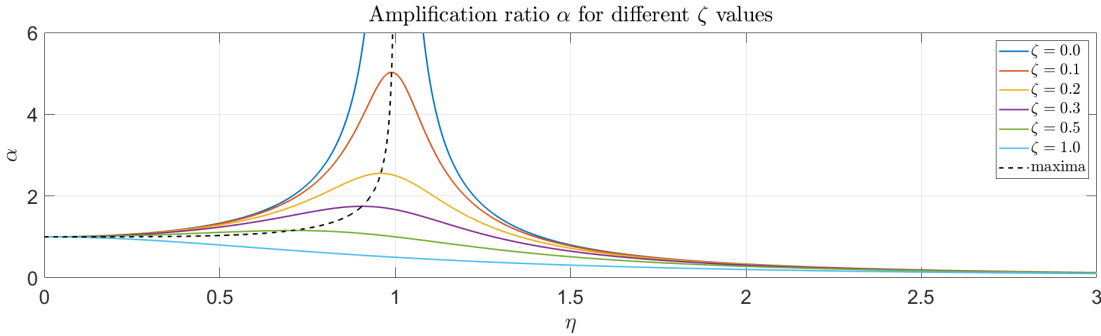
If  $\Omega$  equals the damped natural frequency  $\omega_d$ , that in turn results in resonance of the system. The frequency at that point is defined as resonance frequency  $\omega_r$  (compare with 2.1.1.2):

$$\omega_r \equiv \omega_d = \Omega \quad (2.38)$$

The resonance amplification ratio  $\alpha_r$ , i.e. the maximum amplification dependent on  $\zeta$  at  $\omega_r$  is described by the following equation:

$$\alpha_r = \frac{1}{\sqrt{1 - \eta^4}} \quad (2.39)$$

Figure 2.7 shows the amplification ratio  $\alpha$  for different damping ratios  $\zeta$  over the frequency ratio  $\eta$  [33, 28]. The resonance case is marked with a dashed line. Here, all graphs can be seen as damping quality for the given system over all frequencies.



**Figure 2.7.:** Amplification ratio  $\alpha$  for different  $\zeta$  values plotted over  $\eta$  – based on [54].

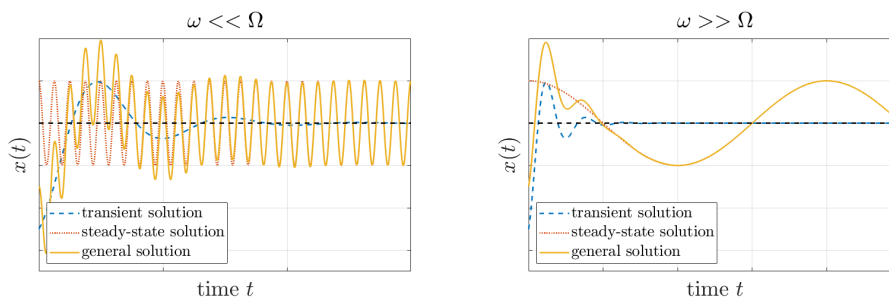
The steady-state solution  $x_s(t)$  has to include the amplification ratio  $\alpha$  from equation (2.37) into the driving force from equation (2.34) with a phase shift  $\varphi$  as follows:

$$x_s(t) = A_e \cdot \frac{1}{\sqrt{(1 - \eta^2)^2 + 4\zeta^2\eta^2}} \cdot \sin(\Omega t - \varphi) \quad (2.40)$$

The general solution for a forced damped oscillation from equation (2.33) therefore can be written as:

$$x(t) = A_0 \cdot e^{-\omega_0 \zeta t} \cdot \sin(\omega_d t + \varphi_0) + A_e \cdot \frac{1}{\sqrt{(1 - \eta^2)^2 + 4\zeta^2 \eta^2}} \cdot \sin(\Omega t - \varphi) \quad (2.41)$$

Figure 2.8 shows two possible appearances of  $x_t(t)$ ,  $x_s(t)$ , and  $x(t)$ . First, if the natural frequency  $\omega$  is much smaller than the driving frequency  $\Omega$  (left graph) and second vice versa (right graph).



**Figure 2.8.:** Transient and steady-state part of the general displacement  $x(t)$  over the time  $t$  for forced damped oscillations – left,  $\omega \ll \Omega$ ; right,  $\omega \gg \Omega$  [54].

With equation (2.41) any movement of a mechanical object that is excited by an external force  $F_e(t)$  can be specified. Therefore, this equation together with the figure 2.7 are essentially for characterising and rating mechanical systems like possible isolation systems for the ALPS II and JURA experiments.

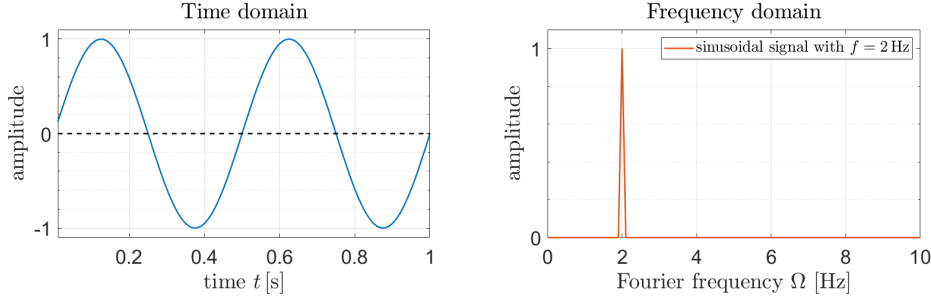
### 2.1.3. Modal analysis

Modal analyses examine systems in the frequency domain according to their dynamic properties as described in subsections 2.1.1 and 2.1.2. This is done by the study of time-dependent measurements and their derived spectra. The next paragraphs explain how a modal analysis can be done and which methods are mostly used to enhance its value. The following is based on the Fourier Theory, which cycles through a time series for each frequency to obtain a frequency-dependent spectrum. The method developed on this is defined as Fourier transform or its algorithm as Fast Fourier Transform (FFT).

#### 2.1.3.1. Fourier transform

The Fourier transform was developed by the French mathematician Jean Baptiste Joseph Fourier in 1822. Using a Fourier analysis is a method to break periodic or aperiodic signals down from the time to the frequency domain. The reverse process is named Fourier synthesis or inverse Fourier transform. Figure 2.9 shows the conversion of a single sinusoidal signal to a fine peak in the frequency domain.

The Fourier analysis uses the following equations, where the different options (1), (2), or (3) are made due to different norming issues or depend on a specific software tool



**Figure 2.9.:** Sinusoidal 2 Hz signal in time domain transferred to a single peak in the frequency domain.

that is used [31]:

$$y_m^{(1)} = \sum_{k=0}^{N-1} x_k e^{-2\pi i \frac{mk}{N}} \quad \text{with } m = 0, \dots, N-1 \quad (2.42)$$

$$y_m^{(2)} = \frac{1}{\sqrt{N}} \cdot y_m^{(1)} \quad (2.43)$$

$$y_m^{(3)} = \frac{1}{N} \cdot y_m^{(1)} \quad (2.44)$$

where  $x_k$  is the time dependent data point out of the vector  $X$  and  $N$  the number of data points determined by the sample rate  $f_s$  and the measuring duration  $T$ .

$$X = \begin{pmatrix} x_1 \\ x_2 \\ \vdots \\ x_N \end{pmatrix} \quad (2.45)$$

$$\text{where } N = T \cdot f_s \quad (2.46)$$

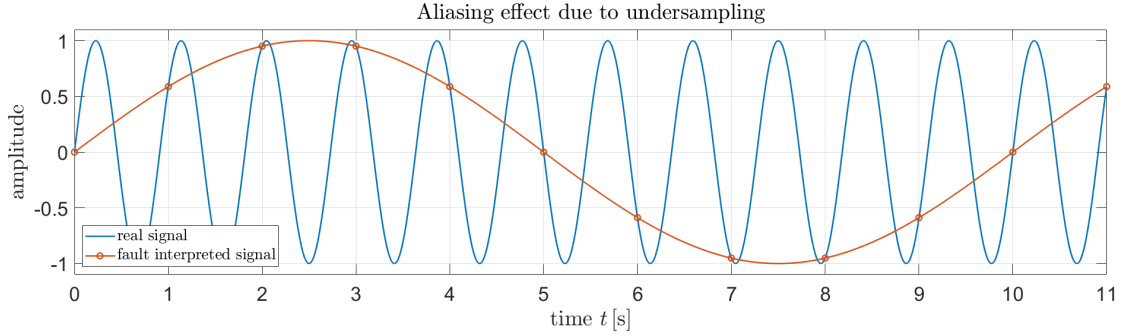
The maximum frequency possible to resolve  $f_{max}$  is determined by the Nyquist theorem or the Nyquist frequency  $f_{Ny}$  via:

$$f_{max} \equiv f_{Ny} = \frac{f_s}{2} \quad (2.47)$$

The theorem prevents aliasing, an effect caused, inter alia, by the fact that signals above the Nyquist frequency  $f_{Ny}$  are erroneously interpreted as low-frequency signals and therefore not distinguishable from the real signals. This is visualised in figure 2.10, where the red line represents the faulty interpreted signal. Aliasing can also occur if a noisy signal contains frequencies above the Nyquist frequency  $f_{Ny}$ . Implementing a low-pass, here anti-aliasing, filter can reduce the problem (see subsection 4.4.2).

In contrast, the lowest frequency possible to dissolve  $f_{min}$  is determined by the inverse of the duration of the measurement  $T$ :

$$f_{min} = T^{-1} = \frac{f_s}{N} \quad (2.48)$$



**Figure 2.10.:** Aliasing effect in signal processing showing a wrongly interpreted signal. Here, a 1.1 Hz signal is sampled with 1 Hz and interpreted as an 10 Hz signal.

Due to insufficient data points in the low frequency region often ten times the value of  $f_{min}$  is assumed to get the reliable lowest frequency possible to dissolve  $f_{min}^*$ :

$$f_{min}^* = 10 \cdot f_{min} = 10 \cdot T^{-1} \quad (2.49)$$

The values  $f_{min}$  or  $f_{min}^*$  and  $f_{max}$  define the frequency range that is accessible to analyse. Within a FFT also the frequency resolution  $f_{res}$  is of importance. It is a measure of precision and determined by the quotient of the sampling rate  $f_s$  and the amount of data points taken for the analysis  $N_{sample}$ :

$$f_{res} = \frac{f_s}{N_{sample}} \quad (2.50)$$

If the entire measurement is taken, it is equal to the lowest frequency possible to dissolve  $f_{min}$ , but this does not have to be the case (see 2.1.3.3). Data points produced by the FFT are frequency dependent and their ordinates are called Fourier frequencies  $f_m$ .

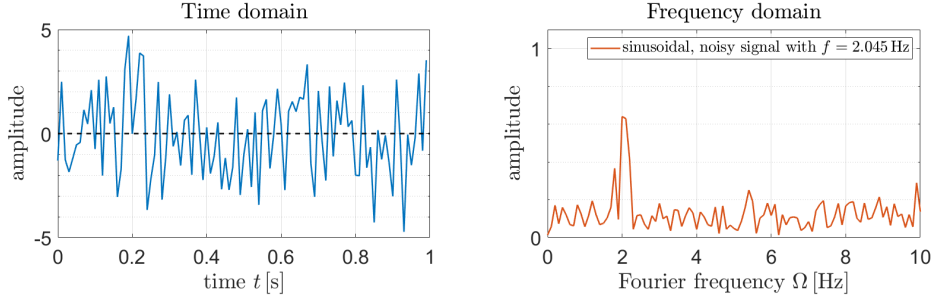
$$f_m = m \cdot f_{res} \quad \text{with } m = 0, \dots, \frac{N_{sample}}{2} \quad (2.51)$$

With all the above mentioned variables a frequency spectrum can be formed. In most cases further tunings and adjustments are made to reduce noise (see 2.1.1.3), enhance the SNR (see 2.1.1.4), or enable better data interpretation.

### 2.1.3.2. Windowing

One method of improving the quality of the FFT is to apply a window. That is because only an infinite periodic and perfect sinusoidal signal would create a fine peak in the frequency domain through the FFT. In reality this is rarely the case. Therefore, any imperfection would result in a wide peak as figure 2.11 visualises. Note that the quality of the FFT strongly depends on the sampling rate  $f_s$  and the measured time  $T$ . They should be at least as high as their requirements from equations (2.47) to (2.49) to define their needs and if possible, as high as the data capacity of the processing allows.





**Figure 2.11.:** Imperfect sinusoidal 2.045 Hz signal with additional white noise with a variance of 2 in time domain with a sample rate of 100 Hz over 10 s transferred to a wide peak within in the frequency domain.

To counteract the effect a window function is used for weighting the time series and thereby attenuating the undesired sidebands. There are a variety of different window functions used for FFT that all have their maximum in the centre and decrease to the sides towards zero. Furthermore, window functions usually apply zero padding [31]. In the following, two different window functions will be surveyed. First, the Hanning window  $w_H$  which is commonly used in signal processing. It is defined by:

$$w(t)_{H,j} = \frac{1}{2} \left( 1 - \cos \left( \frac{2\pi \cdot j}{N} \right) \right) \quad \text{with } 0 \leq j \leq N - 1 \quad (2.52)$$

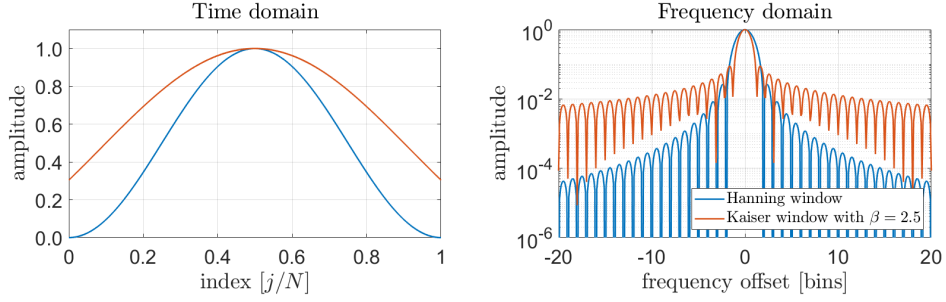
Second, the Kaiser window  $w_K$ , which is used to generate the spectra in chapter 4, because it has a better representation of the real seismic conditions due to its lower suppression on the sides. The function is defined by:

$$w(t)_{K,j} = \frac{I_0 \left( \beta \sqrt{1 - \left( \frac{j - N/2}{N/2} \right)^2} \right)}{I_0(\beta)} \quad \text{with } 0 \leq j \leq N - 1 \quad (2.53)$$

where  $\beta$  is a non-negative, real shape variable that is proportional to the attenuation and  $I_0$  is the zeroth order modified Bessel function of the first kind [31]:

$$I_0(x) = \sum_{k=0}^{\infty} \left( \frac{(x/2)^k}{k!} \right)^2 \quad (2.54)$$

Figure 2.12 visualises the two window functions, where the left side of figure 2.12 shows a Hanning window  $w(t)_H$  in blue and a Kaiser window  $w(t)_K$  with a beta coefficient of 2.5 in red over the index  $j/N$  that refers to the time  $t$  as examples. The right side represents the response of the window functions with a fictitious sinusoidal signal over an offset of  $f_m$  frequency bins. It shows the main, desired peak and the surrounding, so called, 'sidelobes'. The window function should attenuate them as much as possible while preserving the main signal as sharp as possible. The beta coefficient of 2.5 was chosen for its sufficient sidelobe suppression and at the same time preserving sharpness.



**Figure 2.12.:** Hanning and Kaiser window functions in the time and frequency domain.

The frequency dependent window responses on the right side of figure 2.12 are representing the noise suppression in the frequency domain. They are calculated with their real and imaginary parts defined as follows [31]:

$$a_r(f) = \sum_{j=0}^{N-1} w_j \cdot \cos\left(2\pi f \cdot \frac{j}{N}\right) \quad \leftarrow \text{real part} \quad (2.55)$$

$$a_i(f) = \sum_{j=0}^{N-1} w_j \cdot \sin\left(2\pi f \cdot \frac{j}{N}\right) \quad \leftarrow \text{imaginary part} \quad (2.56)$$

$$a(f) = \frac{\sqrt{a_r^2 + a_i^2}}{S_1} \quad (2.57)$$

Finally, to obtain a spectrum which is not affected by the window function and to be able to use any factor in the window that is suitable, the following two sums are defined for reasons of normalisation [31]:

$$S_1 = \sum_{j=0}^{N-1} w_j \quad (2.58)$$

$$S_2 = \sum_{j=0}^{N-1} w_j^2 \quad (2.59)$$

With  $S_1$  and  $S_2$  the Normalised Equivalent Noise BandWidth (NENBW), an index number of the window function, can be determined. It specifies the width of a rectangle that contains the same total power as the entire window in the frequency domain [31]:

$$NENBW = N \cdot \frac{S_2}{(S_1)^2} \quad (2.60)$$

Multiplying it with the frequency resolution  $f_{res}$  in equation (2.50) will result in the Effective Noise BandWidth (ENBW) in units of frequency [31]:

$$ENBW = NENBW \cdot f_{res} = NENBW \cdot \frac{f_s}{N} = f_s \cdot \frac{S_2}{(S_1)^2} \quad (2.61)$$

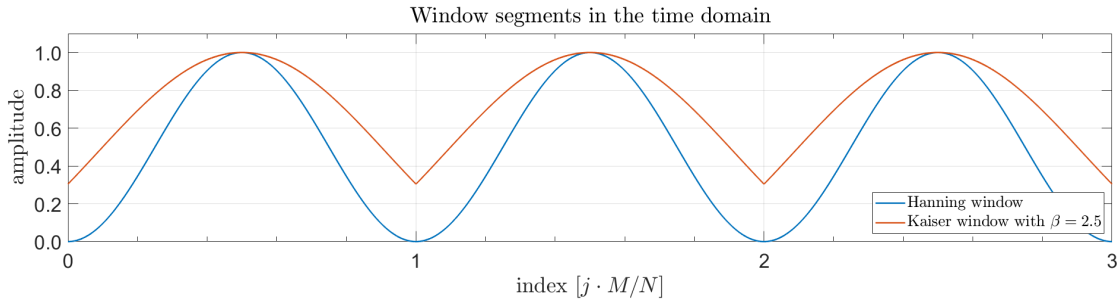
These factors will be used to scale and norm the data, e.g. for spectral densities (compare with 2.1.4.1).

Window functions are applied in the time domain before using the FFT operator to reduce the noise of an imperfect signal. Multiplying each component of the time series vector  $x(t)$  with those from the window function vector  $w(t)$  obtains the weighted time series vector  $x(t)_w$ :

$$x(t)_w = x(t) \circ w(t) \tag{2.62}$$

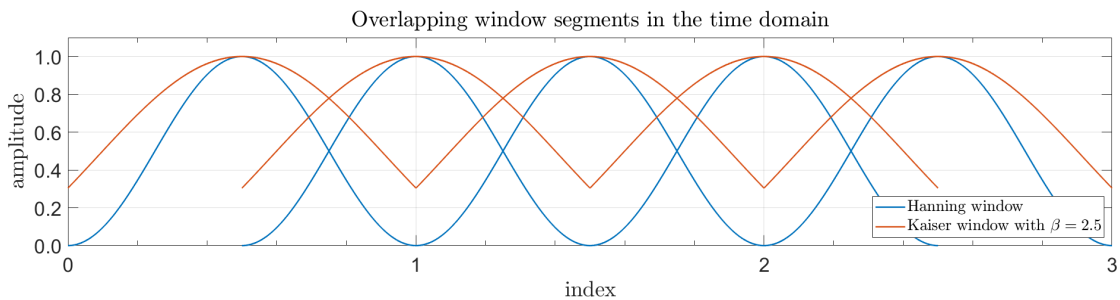
### 2.1.3.3. Averaging and overlapping

Even after applying a suitable window function to the time series before using the FFT algorithm, spectra can appear noisy. A solution is to take the average of  $M$  measurements. This will improve the SNR (see 2.1.1.4) by a factor of  $1/\sqrt{M}$  [31]. Therefore, the time series will be split into several segments, that are then analysed independently. Figure 2.13 visualises this effect based on an example with three segments of the Hanning and the Kaiser window.



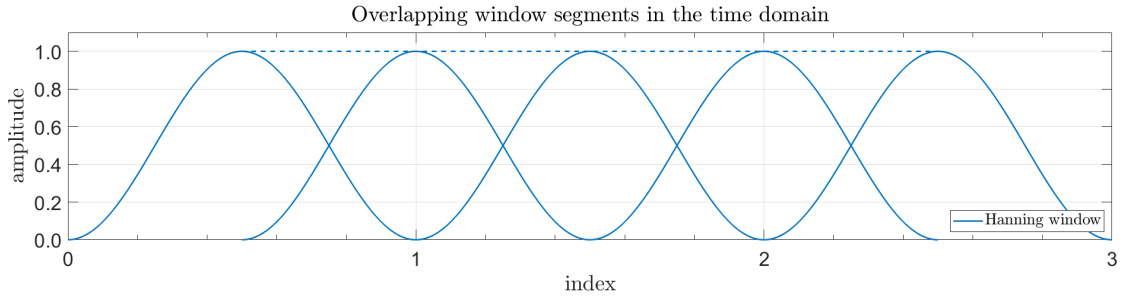
**Figure 2.13.:** Segmentation of the time series with  $M = 3$  separated windows.

As clearly seen in the graph, a large amount of data is lost at the boundaries of each segment. To counteract this, the segments can be overlapped [31]. This is pictured in figure 2.14 with an example of 50% overlap.



**Figure 2.14.:** Overlapping segmentation of the time series with  $M = 5$  separated windows with 50% overlap.

The optimal amount of overlap depends on the individual window function represented by two indicators: the Amplitude Flatness (AF) and the Overlap Correlation (OC). The AF is the ratio of the minimal to the maximal weight that the window function applies between the first and the last maximum [31]. An example is shown in figure 2.15, where the Hanning window shows a perfect flat amplitude (with  $AF = 1$ ) with an overlap of 50%, that is desirable. The dashed line represents the cumulative sum of all windows.



**Figure 2.15.:** Overlapping segmentation of the time series with  $M = 5$  separated windows with 50% overlap of the Hanning window and the cumulative sum as a dashed line.

There is an alternative to the AF, which is called the Power Flatness (PF). It uses the ratio of the minimum and maximum of the quadratically summed up window values. It is used if incoherent data such as white noise must be examined. Thus, it is not considered in the following.

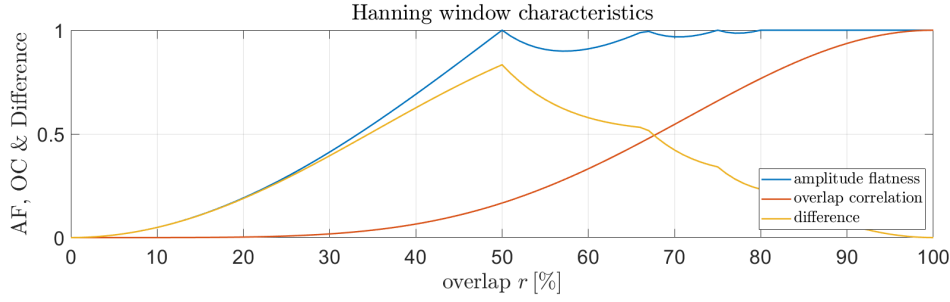
The OC represents the amount of data that is redundantly analysed. It expresses the unnecessary computation time and therefore should be as low as possible. It is defined as follows [30, 31]:

$$OC(r) = \frac{\sum_{j=0}^{rN-1} w_j w_{j+(1-r)N}}{\sum_{j=0}^{N-1} w_j^2} \quad (2.63)$$

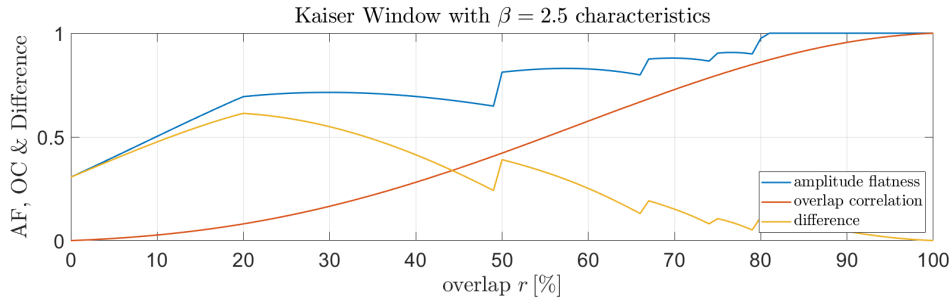
with  $r$  being the overlap percentage.

The optimal overlap  $r$  is defined by the point where the difference between the AF and the OC is the highest [31]. Figures 2.16 and 2.17 define AF, OC, and their difference over the overlap percentage  $r$  for the Hanning and the Kaiser (with  $\beta = 2.5$ ) windows.

As mentioned before, the Hanning window reaches its optimal point at 50% overlap, where the Kaiser window with  $\beta = 2.5$  at exactly 20%. These values will be used for later analyses (see chapter 4).



**Figure 2.16.:** Hanning window characteristics: AF, OC and their difference over the overlap percentage  $r$ .



**Figure 2.17.:** Kaiser window characteristics: AF, OC and their difference over the overlap percentage  $r$ .

### 2.1.4. Data evaluation

This subsection about data evaluation will introduce possibilities to present the data generated from the modal analysis (see subsection 2.1.3) to extract more information in the given context or rather about the oscillations (see subsection 2.1.1) in the examined system (see subsection 2.1.2). Except for the spectrogram – which will be explained in the last paragraph – only the modal data, meaning the data in the frequency domain, is of interest. That means, if this is not desired, the time series, which occupies a large amount of memory, can be deleted after the result is obtained.

#### 2.1.4.1. Presenting spectra and spectral densities

Using the FFT algorithm from equation (2.42) on the time series, equation (2.45), which is already multiplied with the desired window function, e.g. equation (2.53), will result in a real-to-complex FFT [31]. The time series is assumed to be calibrated correctly (see subsection 4.2.1) – here, in units of Volts. It then has to be normalised by the factors defined in equations (2.58) to (2.61). To receive an interpretable spectrum, it can be expressed as a Power Spectrum (PS) in units of  $V_{rms}^2$  (see 2.1.4.2) by [31]:

$$PS_{rms}(f_m) = \frac{2 \cdot |y_m|^2}{S_1^2} \quad \text{with} \quad m = 0, \dots, \frac{N}{2} \quad (2.64)$$

The PS takes the number of data points, the window function and any desired factor into account. Here, the factor of 2 refers to the single sided spectrum [31]. An alternative visualisation is the Power Spectral Density (PSD) in units of  $V_{rms}^2/\text{Hz}$  that is defined by PS divided by the ENBW from equation (2.61) [31]:

$$PSD_{rms}(f_m) = \frac{PS_{rms}(f_m)}{ENBW} = \frac{2 \cdot |y_m|^2}{f_s \cdot S_2} \quad \text{with } m = 0, \dots, \frac{N}{2} \quad (2.65)$$

It is very important to mention that the PS, unlike the PSD, does not vary by the number of data points  $N$ , since both the frequency resolution  $f_{res}$  and the ENBW are inversely proportional to  $N$ . Increasing  $N$  in a PS will show a constant peak height, while the noise level decreases proportional due to the changing frequency resolution  $f_{res}$  as less noise power falls into each frequency bin. The PSD compensates for this at the expense of amplitude accuracy [31]. The appropriate visualisation depends on the problem being investigated.

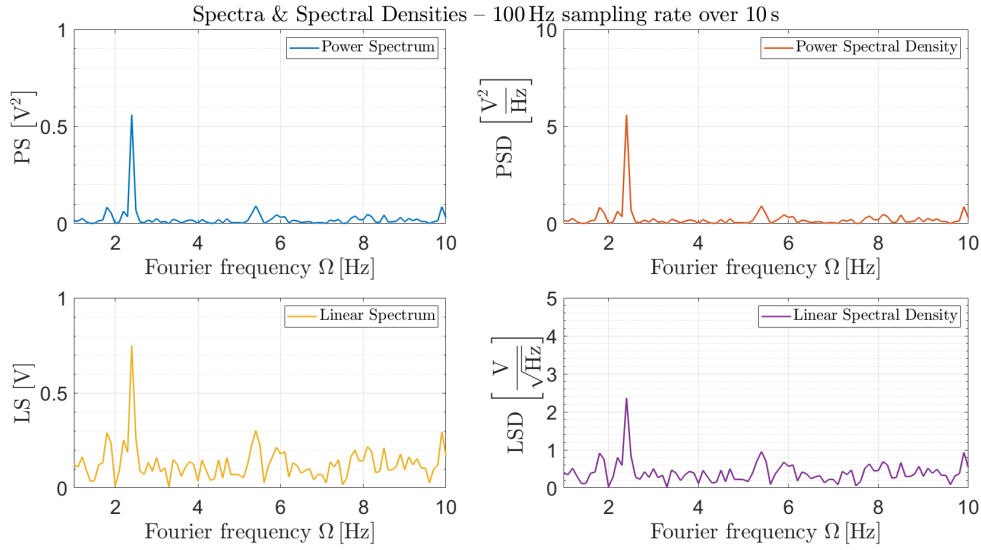
Both possibilities can be expressed as Linear Spectrum (LS) in units of  $V_{rms}$  or Linear Spectral Density (LSD) in units of  $V_{rms}/\sqrt{\text{Hz}}$  (also named Amplitude Spectrum (AS) or Amplitude Spectral Density (ASD)) to reflect its amplitude by:

$$LS_{rms}(f_m) = \sqrt{PS_{rms}(f_m)} \quad (2.66)$$

$$LSD_{rms}(f_m) = \sqrt{PSD_{rms}(f_m)} \quad (2.67)$$

For the ALPS II experiment, the LSD is preferred because of its better representation of the SNR and the overall real displacement (see 3.2.2.2). All described possible spectra and spectral densities are plotted in figure 2.18. Here, an imperfect sinusoidal signal at 2.4 Hz with an amplitude of 0.8 V and additional white noise with a variance of 2 V is simulated with a sample rate of 100 Hz over 100 s. This is averaged by 10, resulting in a sample time of 10 s or respectively a frequency resolution of 0.1 Hz. The FFT is analysed with a Kaiser window with a beta factor of 2.5 and 20% overlap. Note the different y-axis units and scaling.

The PS represents the power of the signal being equal to the square of the amplitude. The LS shows the (nearly) correct amplitude of 0.8 V. Both the densities show values that depend on the frequency resolution,  $f_{res} = 0.1 \text{ Hz}$ , and can be converted to units of V by multiplying them by 0.1 Hz for the PSD or  $\sqrt{0.1 \text{ Hz}}$  for the LSD. In summary, the spectra focus on the real amplitude accuracy and the spectral densities on the normalized noise level. The latter is therefore desirable when examining signals with low amplitudes, as is the case with this thesis (see chapter 4).



**Figure 2.18.:** FFTs of an imperfect sinusoidal 2.4 Hz signal with an amplitude of 0.8 V and additional white noise with a variance of 2 V. Simulated with a sample rate of 100 Hz over 100 s and 10 averages, resulting in a sample time of 10 s or frequency resolution of 0.1 Hz. Analysed with a Kaiser window with a beta factor of 2.5 and 20% overlap. Upper left: power spectrum via equation (2.64); upper right: power spectral density via equation (2.65); lower left: linear spectrum via equation (2.66); lower right: linear spectral density via equation (2.67).

#### 2.1.4.2. RMS value in the frequency domain

The Root Mean Square (RMS) value, commonly known from electronics, can be seen as the 'real' value of an oscillating signal. The easiest determination is dividing the peak signal  $V_{pk}$  by the factor  $\sqrt{2}$  [31]:

$$V_{rms} = \frac{V_{pk}}{\sqrt{2}} \quad (2.68)$$

Since it is usually not trivial for time series, the RMS value is generally defined as the square root of the sum over the quadratic times  $x_i$  times the distance of the measuring points  $\Delta t$  divided by the measuring period  $T$ :

$$X_{RMS} = \sqrt{\frac{1}{T} \sum_{i=1}^T x_i^2 \Delta t_i} \quad (2.69)$$

If calibrated correctly, the RMS value can represent the total displacement of the measured object over the measuring period. Accordingly, the RMS value in the frequency domain is defined as the square root of the sum over the quadratic bins, e.g. LSD from

equation (2.67), multiplied by ENBW [31]:

$$Y_{RMS} = \sqrt{ENBW \sum_{f_m=0}^{f_{Ny}} LSD_{rms}^2(f_m)} = \sqrt{\frac{2}{S_1^2} \sum_{m=0}^{N/2} y_m^2} \quad (2.70)$$

$$(2.71)$$

Both equations will produce the same total RMS value, except for small transformation and windowing errors.

$$X_{RMS} \simeq Y_{RMS} \quad (2.72)$$

By selecting a frequency interval  $F_m$  as:

$$F_m = [F_{start} F_{end}] \quad (2.73)$$

the RMS value can be specified and represents only the accumulated value, e.g. displacement, caused by defined frequencies.

$$Y_{RMS, F_m} = \sqrt{ENBW \sum_{f=F_{start}}^{F_{end}} LSD_{rms}^2(f_m)} \quad (2.74)$$

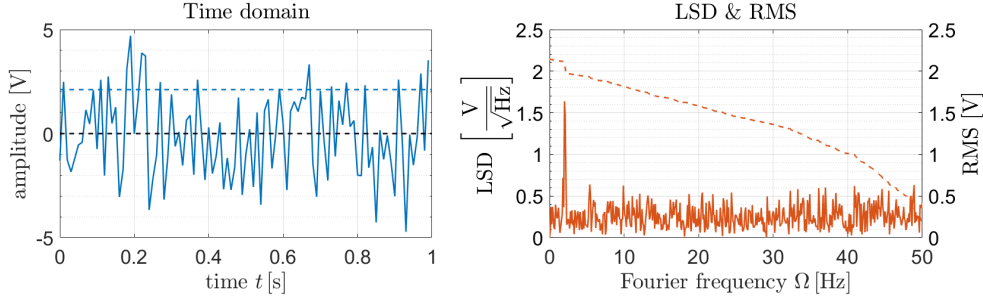
In addition, using its inversion  $F'_m$  and making the  $Y_{RMS}$  dependent of the frequency bins of the interval  $F_m$ , will calculate a cumulative RMS vector from the upper limit down to the index.

$$Y_{RMS}(F'_m) = \sqrt{ENBW \sum_{f_m=F_{end}}^{F'_m} LSD_{rms}^2(f_m)} \quad (2.75)$$

$$\text{with } F'_m = F_{end}, \dots, F_{start} \quad (2.76)$$

This can be used for a graphical representation of the RMS value in the frequency domain to express the rising significance with smaller frequencies! Figure 2.19 visualises the time series with its fixed RMS value from equation (2.69) on the left side. The right side shows an LSD from equations (2.67) and (2.65) with its RMS function from equation (2.75).





**Figure 2.19.:** Imperfect sinusoidal 2.045 Hz signal with additional white noise with a variance of 2 V in time domain with a sample rate of 100 Hz over 10 s and an LSD with a RMS function in the frequency domain.

### 2.1.4.3. Transfer function

The transfer function  $H$  can be determined using modal analysis, as indicated in subsection 2.1.3, by taking the ratio of the system output to the excitation (see figure 2.2).

$$\text{transfer function} = \frac{\text{system output}}{\text{excitation}} \quad (2.77)$$

On the other hand, if the transfer function is known, it can be used to determine one of the other components. The transfer function of a system or its resulting conversion therefore is either used to simulate the output with a defined input signal that might not be applicable to the system or to determine the excitation when the system output is known. Further, the transfer function can also be set as a requirement for defining a system used as isolation or as amplification. In particular, the direct transfer function is the ratio of the output  $y(f)$  to the input spectrum  $p(f)$  [42]:

$$H_{yp}(f) = \frac{y(f)}{p(f)} \quad \text{'receptance'} \quad (2.78)$$

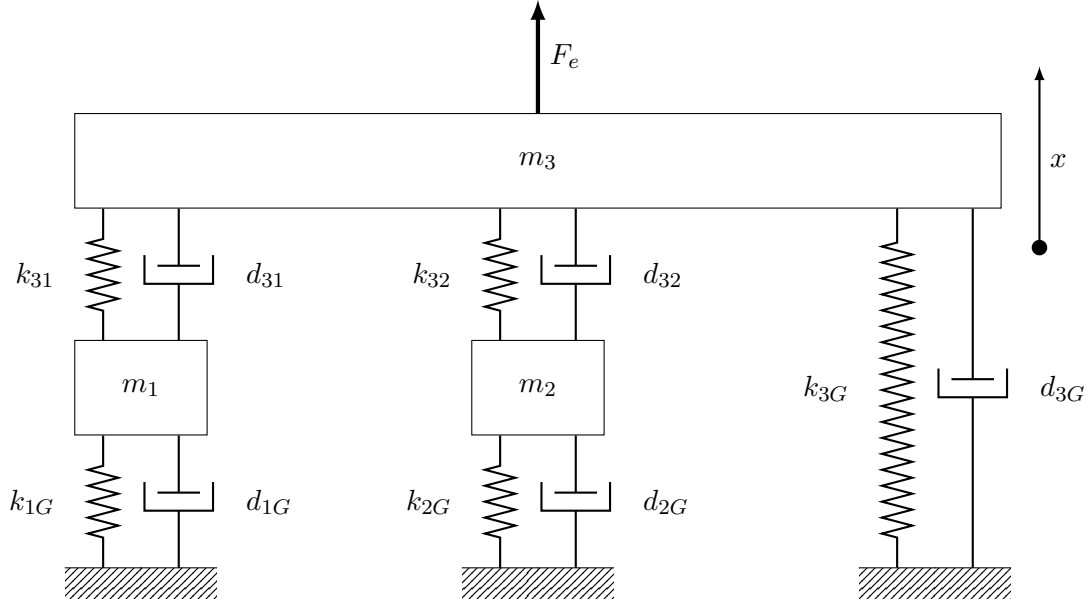
This transfer function reflects the dynamic resilience, which is also known as receptance. There are two more definitions by using the derivatives of the system output. With its first derivative it is known as the mechanical admittance or the mobility of the system and with its second derivative referring to the dynamic inertia of the system which is the accelerance [37]. In the following the term transfer function is used synonymously for receptance [42].

$$H_{\dot{y}p}(f) = \frac{\dot{y}(f)}{p(f)} \quad \text{'mobility'} \quad (2.79)$$

$$H_{\ddot{y}p}(f) = \frac{\ddot{y}(f)}{p(f)} \quad \text{'accelerance'} \quad (2.80)$$

Note that  $y(f)$  and  $p(f)$  have to be calculated from spectra from time series that have been measured at the same time with the same or synchronised instruments. Essential

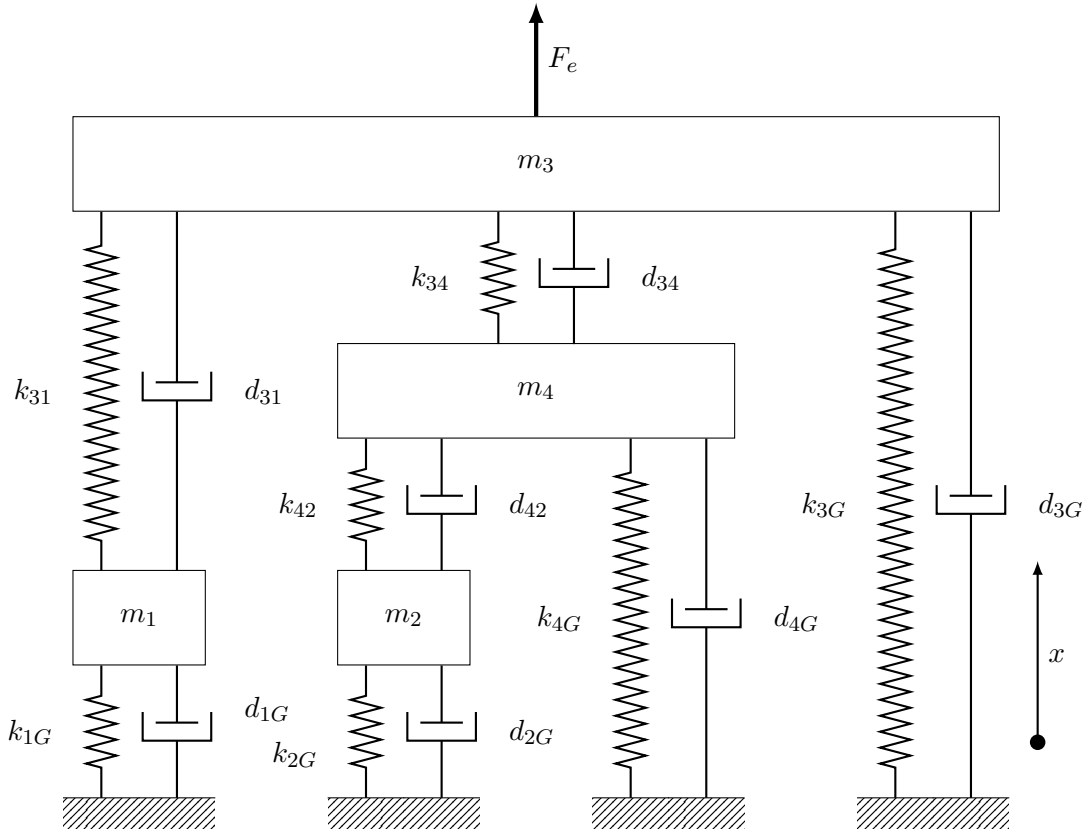
is the direct link between the signal peaks and the noise. Otherwise, the result is just a ratio between two spectra. Transfer functions can be used to simulate more-component systems by multiplying the known individual transfer functions for each stage. Figure 2.20 shows an example with two consecutive, chained stages.



**Figure 2.20.:** Scheme of a complex compounded mass-spring-damper model with a problematic connection between  $m_2$  and  $m_3$ .

The pictured system consists of three objects  $m_1, m_2$  &  $m_3$ , where  $m_1$  &  $m_2$  are mounted to the ground and  $m_3$  as well to  $m_1$  &  $m_2$ . Each mass-spring-damper has a transfer function, e.g.  $H_{1G}$  between object  $m_1$  and the ground  $G$ . For compound systems such as object  $m_3$  there is more than one transfer function, one to each subsystem, here  $H_{31}$ ,  $H_{32}$  and  $H_{3G}$ . The individual transfer function can refer to a main part of the system, a necessary, noisy system, or a damping system. As an example, assuming object  $m_3$  being the working stage with a seismic requirement that has to be fulfilled and object  $m_2$  being a noise source, e.g. a vacuum pump, with a direct and problematic connection to  $m_3$  that creates resonances. Therefore, an enhanced model with an additional isolation system is designed and illustrated in figure 2.21. It should solve the described problem by using different methods of seismic isolation (see section 2.3).

Here, the ground noise as well as the transfer functions of  $H_{1G}$ ,  $H_{2G}$ ,  $H_{3G}$ , and  $H_{31}$  are known from the old system. The connection to object  $m_2$ , thus  $H_{42}$ , will not be sufficient to reach the requirements, because it will depict the same problems as in the previous set-up. Also, due to stability reasons, it is not possible to implement object  $m_3$  without an additional ground connection. Hence,  $H_{43}$  must be designed to capture the noise introduced by  $m_2$ . The designing procedure will be discussed in chapter 5. Note, that any disturbance in the data that is used to determine the transfer function will influence all further results! Therefore, it must be confirmed that the data is valid

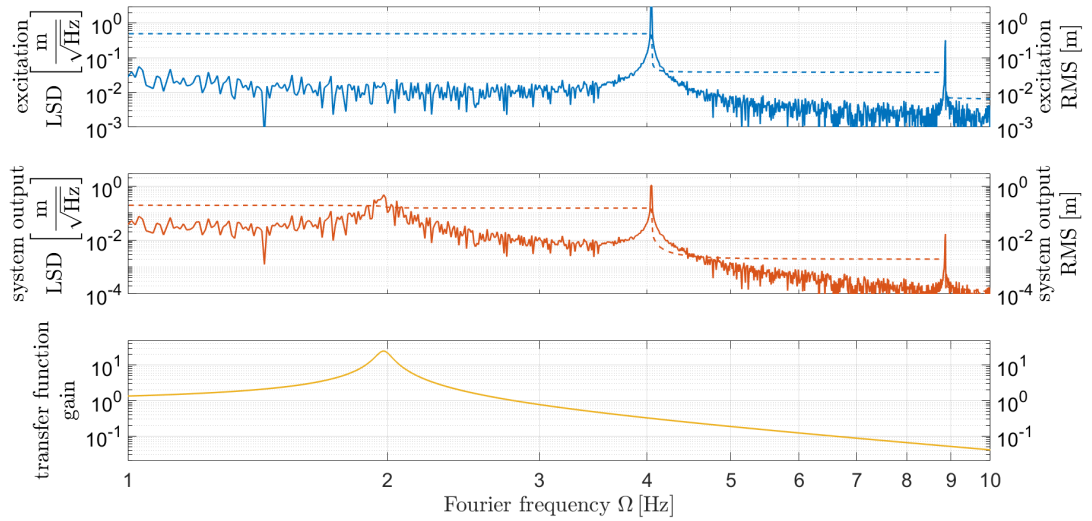


**Figure 2.21.:** Scheme of an enhanced, complex compounded mass-spring-damper model with object  $m_4$  as an isolation.

(see subsection 4.2.2 and section 4.4).

Figure 2.22 shows a transfer function, calculated according to equation (2.78), of two simultaneous LSDs, here as an example of a simple, compounded mass-spring-damper (see figure 2.4) with a damped natural frequency  $\omega_d$  of 1.98 Hz and a damping ratio  $\zeta$  of 0.02. The upper graph represents the LSD of the ground reference and refers to the excitation with sinusoidal signals at 4.045 Hz and 8.867 Hz and white noise with a variance of 2 m/s, whereas the middle graph shows the LSD of the investigated object and refers to the system output. The transfer function is then plotted in the lower graph by visualising the gain of its amplitude on the y-axis.

The middle plot illustrates a wide peak just below 2 Hz that reflects the resonance of the mass-spring-damper. The drop above 2 Hz shows the desired damping. Here, the RMS graph visualises a drop in the frequencies, where a signal peak occurs. Furthermore, the total RMS value (compare equation (2.70)) is below that of the excitation, which means that the mass-spring-damper also reduces the vibration in total. Even if that would not be the case, a shift of the seismic energy to other frequencies can meet the requirements.



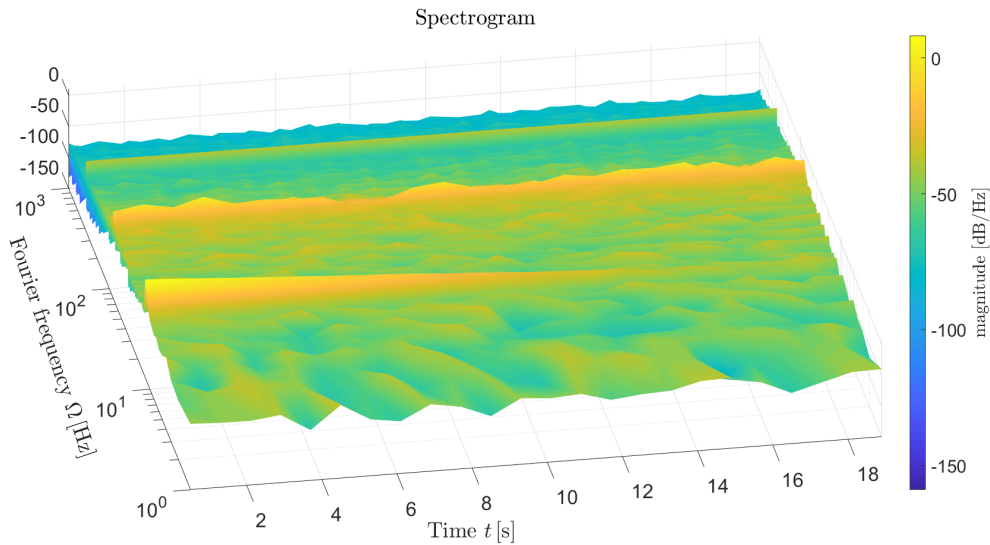
**Figure 2.22.:** Logarithmic LSDs & RMSs in units of length. Upper plot: excitation with sinusoidal signals at 4.045 Hz and 8.867 Hz and white noise with a variance of 2 m/s. Middle plot: system output of a mass-spring-damper with  $\omega_d = 2$  Hz and  $\zeta = 0.02$ . Lower plot: transfer function or amplification ratio of system output to excitation.

#### 2.1.4.4. Spectrogram

A spectrogram is a two-dimensional plot of seismic data, equivalent to a time and frequency dependent visualisation of a seismic noise measurement. Usually, the time  $t$  is plotted on the x-axis, the Fourier frequencies  $\Omega$  on the y-axis, and the magnitude of the spectrum or spectral density on the z-axis or as colour indicated in a two-dimensional plot. This is visualised with a simulated signal in figure 2.23.

The figure shows a systems output of a forced damped oscillation simulated with a sample frequency of  $f_s = 2$  kHz over  $T = 20$  s and is calculated with equation (2.41). The system has a natural frequency at  $f_0 = 12.67$  Hz, an initial amplitude of  $A_0 = 3$  and a decay rate of  $\beta = 0.2$ . This leads to  $\zeta = 0.0025$ , a damped angular frequency of  $\omega_d = 79.61$  Hz and shows the fall over time in the front ‘wall’ by visualising the transient part. The driving force has a frequency of  $f_e = 378.73$  Hz and an amplitude of  $A_e = 157$ , which results in a frequency ratio of  $\eta = 29.89$  and amplification ratio  $\alpha(29.89) = 0.0011$ . This attenuates the driving force, here the back ‘wall’, so that it becomes much lower than the initial amplitude. Additionally, a white noise with a variance of 2 is applied over all frequencies  $\Omega$  from 1 Hz to 1 kHz and folded with the amplification ratio  $\alpha(\eta)$ . This attenuates the noise except at the resonance frequency at  $\omega_r = 79.61$  Hz, which is visualised by the middle ‘wall’.

Spectrograms are mostly used for long-term measurements to estimate time-varying frequencies. As seen in the example only an approximate estimation of the effects is feasible, because of its rough level of detail. Nevertheless, it is a useful tool for pre-analysis of data to get an overview of the given conditions by avoiding long computation



**Figure 2.23.:** Spectrogram of a forced damped oscillation. System characteristics: natural frequency  $f_0 = 12.67$  Hz, an initial amplitude  $A_0 = 3$  and a decay rate  $\beta = 0.2$ . Driving force characteristics: driving frequency  $f_e = 378.73$  Hz and driving amplitude  $A_e = 157$ . Analysing characteristics: 20 averages with a Kaiser window with a beta factor of 2.5 and an 20% overlap.

times and the processing of large amounts of data. However, a subsequent analysis of the lessons learned will be necessary in the most cases.

## 2.2. Seismic noise sources

As defined in chapter 1, seismic noise is broadly defined as the observation of any oscillation that can cause mechanical vibration. Therefore, noise in general is understood as statistical fluctuations of any (electronic) signal. It can be the result of measuring uncertainties and errors of the used devices (compare with 2.1.1.3) or background conditions like those presented in the following. The uncertainties and errors will be determined in an accuracy analysis in subsection 4.2.2, whereas the background conditions however are essential to take into account. They let objects vibrate, which can become critical and thus have a scientific value. Their origin is defined as seismic noise sources, in which the seismic noise is white noise proportional to the force of a seismic wave (compare with 2.1.1.3). For relevance, only seismic noise sources in a frequency range between 10 mHz and 2 kHz (see subsection 3.1.4) are presented. In the following, they are separated into natural (see subsection 2.2.1) and human-made sources (see subsection 2.2.2).

### 2.2.1. Natural sources

Natural sources are inherent and accordingly have to be accepted as being present and not avoidable for humans. Whereas depending on the interfering system their vibrations

may be attenuated or the frequencies shifted so that the undesired effect is no longer critical. Most natural seismic noise sources have very low frequencies  $< 1$  mHz compared to the human-made sources and therefore are not usually of interest in physics or commercial use. Some ultra accurate production steps or experiments such as ALPS II nevertheless do have to take them into account, as their amplitudes could be exceed the dynamic range of the control system (see subsection 3.1.3). Thus natural phenomena like micro- and macro-seismic noise resulting from oceanic and atmospheric activities [68] have to be analysed in detail. In the following, it is distinguished between two different kinds of natural seismic noise sources. The first are caused by a force (see 2.2.1.1) and the second by the geological environment (see 2.2.1.2).

### **2.2.1.1. Geodynamical aspects**

In a broad sense all processes or forces within the earth that cause seismic noise are geodynamic seismic noise sources. The most tangible effect clearly is an earthquake resulting from plate tectonics. Their frequencies commonly lie below 1 Hz [54] with the possibility of very high amplitudes depending on the distance to the epicentre, e.g. up to 0.1 m at a distance of 100 km with a value of 5 on the Richter scale [39]. Usually, earthquakes exceed the acceptable limits of sensitive experiments but only for a short time. In science the normal procedure is not to use the data taken during that time and additionally have a safety system to prevent all devices from damage. It is therefore advisable to choose a location with acceptable seismic hazard if continuous data taking is required.

Also periodic effects, like tidal forces mainly from the moon and the sun, noise will have an influence on sensitive experiments. They directly change the gravity potential through a multitude of waves (semi-diurnal, diurnal, semi-monthly, monthly, semi-annual). Although their amplitudes can reach large values, their frequencies are far below 1 mHz and therefore are not of interest for this work.

Additionally, atmospheric convection, mainly winds, rains and their effects, have to be discussed. Winds can resonate (see 2.1.1.2) with surface objects such as trees and buildings (see 2.2.2.1) or directly change the regional pressure, which causes new convections [8]. In that, the seismic noise induced by winds is strongly related to its speed as well as the resonant frequencies of the surface objects. Here frequencies between 1 Hz to 60 Hz were observed [73]. Rains vary over the year and can change the ground water level, that influences heights, soil densities and damping factors. This will be described in the following passages.

### **2.2.1.2. Geological aspects at Hamburg, DESY**

The geological environment or rather the ground conditions at a specific place have a constant influence on the seismic noise at the location. As DESY is located in Hamburg, approximately 100 km from the North Sea coast, here, two effects have to be taken into account. First, global effects on a region have to be considered, which the Glacial Isostasy Adjustment (GIA) theory is examining in the Post Glacial Rebound (PGR) effect. This

describes the land uplift as well as its resulting gravity changes. GIA data specifies a vertical crustal motion from  $-6$  mm/a to  $18$  mm/a [63], where a positive value is defined as an uplift. Second, the soil composition around or the basement of a building working in has to be taken into account. For the HERA North Hall this would mean considering a single concrete foundation floating on the groundwater surface. A tilting to the tunnels over a long-term period is possible. Moreover, it is necessary to take a closer look at the loading effect resulting from the tides. With a tidal height at the North Sea of  $1$  m, the elastic tidal loading effect is on average  $-24$  mm at its centre,  $-16$  mm at its coast, and  $-4$  mm  $200$  km inland [63]. If the tilting of the hall exceeds the dynamic range of the actuators, this becomes critical even at very low frequencies.

All listed sources above have to be accepted as they are. Considering a counteraction would require a seismic isolation system, which is discussed in chapter 5. Below, seismic noise sources are listed, that are human-made and therefore more simple to manage.

### 2.2.2. Human-made sources

This type of seismic noise sources is directly or indirectly caused by humans, their machines, or other artificial objects. The frequencies they cause are usually more critical to scientific experiments than those from natural sources 2.2.1. This fact is owing to the risk of resonance (see 2.1.1.2) with other non-natural devices. Three different kinds are presented, which are subdivided into their duration of occurrence: stationary objects in 2.2.2.1, traffic on site, machines, and human work in 2.2.2.2, and technical devices in the laboratory in 2.2.2.3.

#### 2.2.2.1. Impact by stationary objects

A stationary object is primarily not a source of noise, but it can channel vibration caused by other origins. More precisely, surface objects can transform oscillations into vibrations (subsection 2.1.1), which can then be measured as seismic noise, e.g. wind will act as a driving force on a building and create resonances (see 2.2.1.1). This effect is especially noticeable when the objects are stiff, strongly shaped in one dimension, and free-standing, e.g. wind turbines, chimneys, or bridges (subsection 2.1.2). These resonances have to be minimised in the process of designing surface objects.

A second indirect effect can be induced by heavy or highly dense, nearby objects by provoking a gravity anomaly and setting an offset to the gravity potential. The gravitational acceleration caused by an object  $a$  is calculated by the following equation [22]:

$$a = \frac{GM}{r^2} \quad \text{with} \quad G = 6.67408 \cdot 10^{-11} \frac{\text{m}^3}{\text{kg} \cdot \text{s}^2} \quad (2.81)$$

where  $G$  is the gravitational constant,  $M$  the mass of the interfered object, and  $r$  the distance to the point to be examined. Assuming a worst case with a mass of  $1$  t in a distance of  $1$  m, this will affect the acceleration by  $66.74 \mu\text{m}/\text{s}^2$ . Further worth mentioning is that the gravity disturbance of a heavy, stationary object will only cause a vibration when it is moved.

### 2.2.2.2. Impact by traffic on site, machines and human work

In contrast to the indirect effects mentioned above, moving masses, machines, or humans themselves will produce vibrations. Their frequencies usually range between 0.1 Hz and 20 Hz [54], whilst their amplitudes depend on the specific case. Trains, trucks, and heavy machines with low resonances will produce the highest amplitudes, but mostly below 1 Hz. In contrast, pumps, drills, working machines, and humans create oscillations above 1 Hz up to several kHz [54]. Their amplitudes decrease with increasing frequency. Due to the daily working hours, their appearances are day-night dependent.

These oscillations cause the greatest challenges, because their frequency range as well as their amplitudes are crucial to most experiments or industry. Seismic isolation methods have to be implemented to avoid peaks or resonances of the examined objects (see section 2.3).

### 2.2.2.3. Technical devices in the laboratory

In addition, electro-magnetic oscillations arising from the Alternating Current (AC) power supply frequency of 50 Hz (in some countries 60 Hz, e.g. Brazil, Canada, USA, and most countries in South America) have to be regarded. This noise peak and its harmonics will occur in all signals produced, processed, or converted by an electrical device connected to the network. Furthermore, it is stimulated with each additional device in the measurement or production chain. Highly sensitive devices therefore use additional DC power supply. Thus, according to the power supply frequency at 50 Hz (or 60 Hz), the frequency must be closely monitored and the cooperating devices need to be non-resonant. If necessary, devices with critical noise can be isolated using simple dampers.

## 2.3. Methods of seismic isolation

Seismic isolation is the attenuation of seismic noise, e.g. for a seismic noise source as explained in section 2.2. Here, seismic noise is understood to mean a three-dimensional wave (see subsection 2.1.1) which must be adequately passively damped or actively controlled over all resulting frequencies.

Since there are many different methods for seismic isolation, in this work only isolations useful for high-accurate structures are of interest, i.e. isolations that have a clean damping ratio and few natural frequencies. Furthermore, this section is divided into passive constructions, illustrated in subsection 2.3.1 and active control loops, see 2.3.2. The former focuses on smart designs to achieve attenuation, while the latter works through electronic control schemes with sensors and actuators.

### 2.3.1. Passive constructions

As described in 2.1.2.1, every object is a damper as defined by the mass-spring-damper. The goal of effective passive seismic isolation is to dampen the unwanted frequencies and

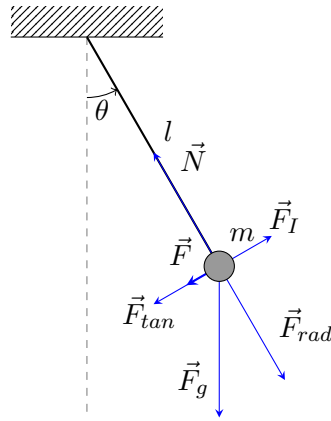


define the natural frequencies in a non-critical frequency range. In other words, to shift the energy of the vibration so that it does not affect the isolated object.

Since the seismic noise is a three-dimensional disturbance and due to the orientation of gravity, the horizontal (longitudinal and transversal) and vertical isolation methods differ slightly and therefore are considered separately. The horizontal, passive isolations are based on simple pendulums and the verticals on spring pendulums. Their principles are explained in the paragraphs 2.3.1.1 and 2.3.1.2. Subsequently, more advanced concepts of an inverted pendulum and of an anti-spring are presented in the paragraphs 2.3.1.3 and 2.3.1.4 respectively. In addition, horizontal springs, elastomer supports, or gels could be used, but are not discussed here because of the given requirements (compare section 3.1). After specifying all methods, the last paragraph explains their effect on seismic noise in 2.3.1.5.

### 2.3.1.1. Principle of a simple pendulum

The most trivial pendulum is the mathematical, also simple pendulum, with a point mass  $m$ , on a massless rod with the length  $l$  which swings frictionless. Figure 2.24 visualises this at an angle  $\theta$  with all interfering forces  $F$ .



**Figure 2.24.:** Scheme of a simple pendulum.

Here,  $\vec{F}_g$  is defined as the gravitational force,  $\vec{F}_{tan}$  as the tangential force,  $\vec{F}_{rad}$  as the radial force points in the same direction as the rod,  $\vec{N}$  as the normal force,  $\vec{F}_I$  as the inertia, and  $\vec{F}$  the resulting restoring force. Since  $\vec{N}$  and  $\vec{F}_{rad}$  stabilise the pendulum in equilibrium and if the rod is not elastic, only the tangential force and the inertia are causing the motion of the pendulum via the restoring force  $\vec{F}(t)$ :

$$\vec{F}(t) = \vec{F}_I(t) + \vec{F}_{tan}(t) \quad (2.82)$$

It also can be expressed as a second order derivative equation of motion via:

$$0 = m \cdot a(t) + m \cdot g \cdot \sin(\theta(t)) \quad (2.83)$$

where  $g$  is the gravitational acceleration and  $a(t)$  is the tangential acceleration as:

$$a(t) = l \cdot \ddot{\theta}(t) \quad (2.84)$$

With this, equation (2.83) can be more simplified to:

$$0 = \ddot{\theta}(t) + \frac{g}{l} \cdot \sin(\theta(t)) \quad (2.85)$$

Assuming very small angles, the sine of  $\theta$  is approximately  $\theta$ .

$$\sin(\theta) \approx \theta \quad \text{if } |\theta| \ll 1 \quad (2.86)$$

Then, equation (2.85) can be simplified to:

$$0 = \ddot{\theta}(t) + \frac{g}{l} \cdot \theta(t) \quad (2.87)$$

$$\text{with } \theta(t) = \hat{\theta} \cdot \sin\left(\sqrt{\frac{g}{l}} \cdot t + \theta_0\right) \quad (2.88)$$

where  $\hat{\theta}$  is the maximal amplitude and  $\theta_0$  the phase shift. According to the equations (2.1) and (2.2) the natural frequencies  $\omega_0$  and  $f_0$  for a simple pendulum are:

$$\omega_0 = \sqrt{\frac{g}{l}} \quad (2.89)$$

$$f_0 = \frac{1}{2\pi} \cdot \sqrt{\frac{g}{l}} \quad (2.90)$$

Since the vertical axis is defined in the direction of gravity, pendulums can not be used to attenuate vertical vibrations. The following paragraph explains the methods for resolving this problem.

### 2.3.1.2. Principle of a spring pendulum

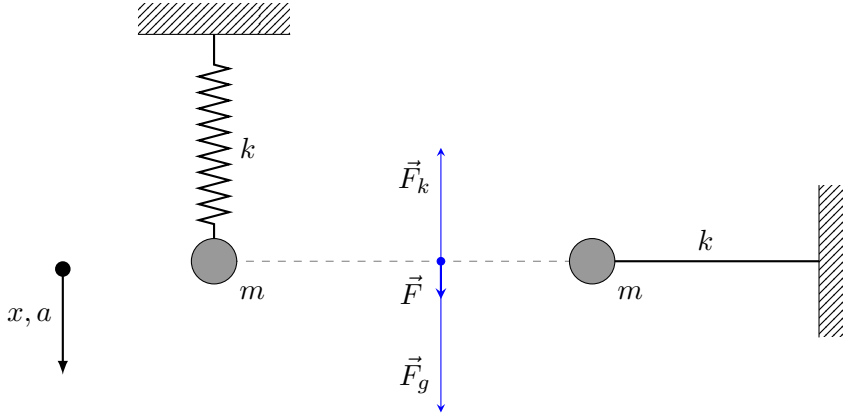
In addition to the usage of simple dampers, spring pendulums or spring blades are the most common way to attenuate vertical vibrations. The former usually is mounted vertically from the ceiling, where the latter can be fixed horizontally from the sides. Figure 2.25 shows the spring pendulum on the left, the spring blade on the right side, and the referring forces in the middle.

Both sketches consider a point mass  $m$  that is effected by gravity and a spring constant  $k$  that will induce a force counteracting the displacement. The resulting force  $\vec{F}$  is defined as follows:

$$\vec{F}(t) = \vec{F}_g(t) + \vec{F}_k(t) \quad (2.91)$$

According to the simple pendulum, it can be expressed as the second order derivative equation of motion as in:

$$0 = m \cdot g - k \cdot x(t) \quad (2.92)$$



**Figure 2.25.:** Scheme of a spring pendulum (left) and a spring blade (right).

where  $x(t)$  is the downward displacement. Expressing  $g$  by  $\ddot{x}$  results in:

$$0 = \ddot{x}(t) - \frac{k}{m} \cdot x(t) \quad (2.93)$$

The natural frequencies  $\omega_0$  and  $f_0$  are defined according to the equations (2.89) and (2.90) as follows:

$$\omega_0 = \sqrt{\frac{k}{m}} \quad (2.94)$$

$$f_0 = \frac{1}{2\pi} \cdot \sqrt{\frac{k}{m}} \quad (2.95)$$

In summary, the natural frequency  $f_0$  of the simple pendulum depends on the length  $l$ , whereas the spring pendulum depends on the spring constant  $k$  and the mass  $m$ .

### 2.3.1.3. The inverted pendulum concept

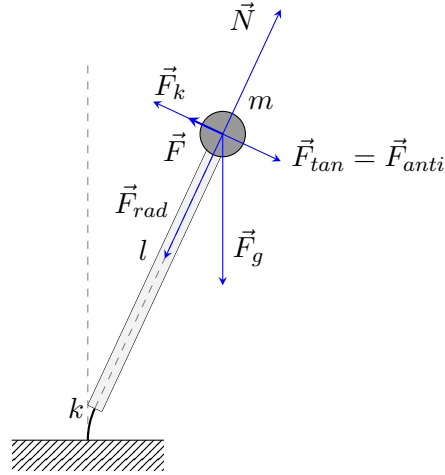
To achieve a lower natural frequency, the inverted pendulum concept was developed [32]. Here, the idea is to apply a mass  $m$  on the end of a stiff rod with the length  $l$  that has an elastic flexure as a pivot point with a spring constant  $k$  and therefore combining a simple pendulum with a spring blade. Figure 2.26 visualises the inverted pendulum with its interfering forces.

The resulting force  $\vec{F}$  is defined by the restoring force of the flexure  $\vec{F}_k$  and the tangential (or anti-spring) force  $\vec{F}_{anti}$  as follows [32]:

$$\vec{F} = \vec{F}_k + \vec{F}_{anti} = - \left( k - \frac{mg}{l} \right) \cdot x \quad (2.96)$$

where  $x$  is the horizontal distance to the equilibrium. The natural frequency  $f_0$  then is defined as:

$$f_0 = \frac{1}{2\pi} \cdot \sqrt{\frac{k}{m} - \frac{g}{l}} \quad (2.97)$$



**Figure 2.26.:** Scheme of an inverted pendulum – adapted from figure 5 of [32].

The dependency on  $k$  and  $m$  due to the flexure causes an anti-spring effect [32]. For this reason, the natural frequency can be tuned close to zero; in practice  $f_0 = 0.05$  Hz has been achieved [32]. The equivalent length of a simple pendulum would be 100 m.

#### 2.3.1.4. The anti-spring concept

The same anti-spring effect can be used in the vertical dimension for the anti-spring concept. Here, the spring pendulum is combined with two horizontally compressed springs, which apply a force that balances in the equilibrium and amplifies the displacement [32]. Thus, the stiffness or natural frequency will be reduced. This is shown in figure 2.27, where  $\vec{F}_{k2}$  are the compression forces and  $d$  is the distance from the sides to the suspended mass.

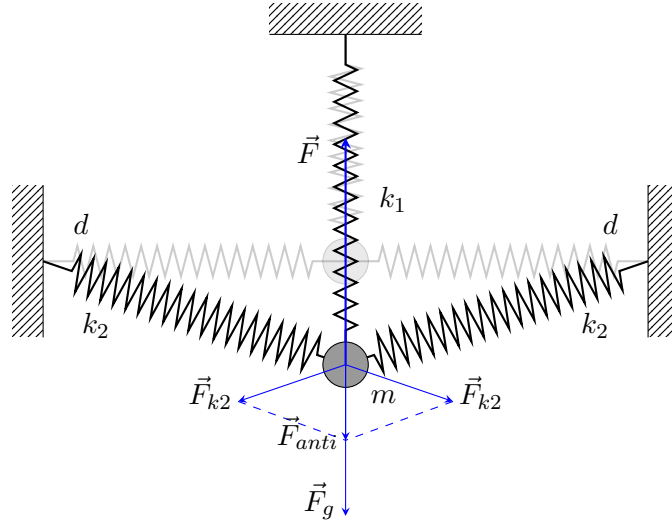
In a normal spring pendulum,  $\vec{F}_g$  and  $\vec{F}_{k1}$  are balanced, where here  $\vec{F}_{anti}$  will induce an additional load on the vertical spring that results in an increase in the restoring force by  $\Delta\vec{F}$ . For small displacements  $x$  the restoring force  $\vec{F}$  is defined as follows [32]:

$$\vec{F} = \Delta\vec{F} + \vec{F}_{anti} = - \left( k_1 - \frac{2\vec{F}_{k2}}{d} \right) \cdot x \quad (2.98)$$

As with the inverted pendulum, here, the compression forces create the anti-spring effect. Consequently, the natural frequency can be tuned close to zero via [32]:

$$f_0 = \frac{1}{2\pi} \cdot \sqrt{\frac{k_1 - \frac{2\vec{F}_{k2}}{d}}{m}} \quad (2.99)$$

In practice a value of  $f_0 = 0.15$  Hz has been reached [32].



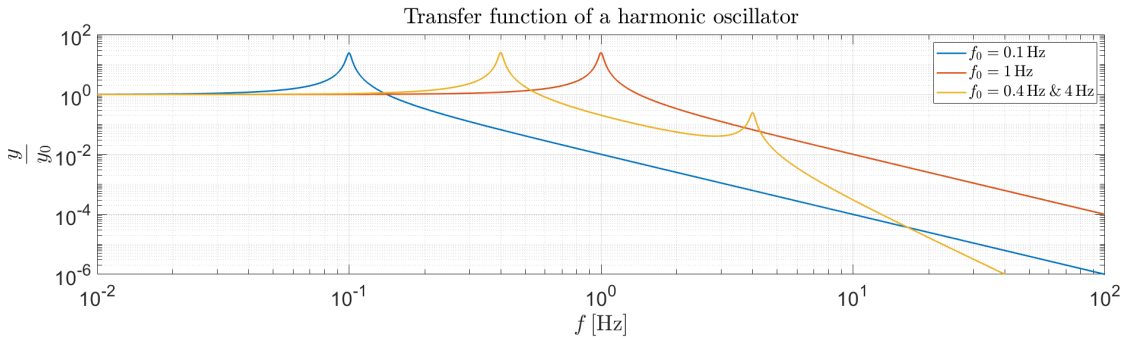
**Figure 2.27.:** Scheme of an anti-spring – adapted from figure 7 of [32].

### 2.3.1.5. The harmonic oscillator as transfer function

Pendulum structures act as low-pass filters to the input signal. The equation for the transfer function of the harmonic oscillator  $H_H$  can be derived with the equation of the amplification ratio (2.37) from the forced damped oscillation (see 2.1.2.4), that is a low-pass filter, as follows:

$$H_H = \frac{y}{y_0} = \frac{1}{\sqrt{(1 - \eta^2)^2 + 4\zeta^2\eta^2}} \quad (2.100)$$

where  $y_0$  is the excitation and  $y$  the output signal in the frequency domain. Figure 2.28 plots  $y/y_0$  over the frequency  $f$  with different natural frequencies  $f_0$  and a damping ratio of  $\zeta = 0.02$ .



**Figure 2.28.:** Transfer function of the harmonic oscillator  $y/y_0$  over the frequency  $f$  with different natural frequencies  $f_0$  and a damping ratio of  $\zeta = 0.02$ .

Since the natural frequency defines the resonance and also the beginning of the attenuation (compare also figure 2.22 in 2.1.4.3), it should be set as low as possible. The

attenuation falls proportional to  $1/f^2$  due the derivative of second order of the equation of motion. With a pendulum length  $l$  of 25 cm a natural frequency of 1 Hz can be achieved, resulting in an attenuation of 100 at 10 Hz and 10,000 at 100 Hz (compare red graph in figure 2.28). Owing to the resonance around 1 Hz (see section 2.2), this will not be sufficient. If larger scales are not possible, e.g. an inverted pendulum or anti-spring can be used (e.g. expressed by the blue graph).

The attenuation can be further improved by using a cascade of  $N$  oscillators. With each step, the slope becomes steeper. Above the last resonance, it is proportional to [32]:

$$\sim \frac{1}{f^{2N}} \quad (2.101)$$

The last (yellow) graph (see figure 2.28) visualises a two staged pendulum with natural frequencies at 0.4 Hz and 4 Hz. For high frequencies, it falls proportional to  $1/f^4$ . Note that each resonance causes an amplification of the input signal around it. Therefore, it has to be ensured that it does not coincide with any noise peak. Hence, it can be more sufficient to use fewer stages with lower resonances or combine the isolation with a control loop (see subsection 2.3.2).

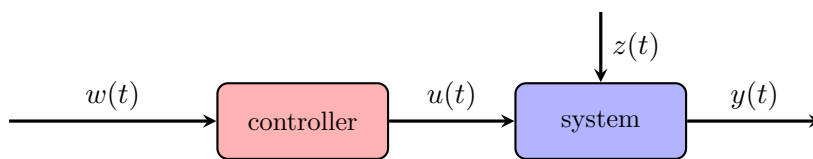
### 2.3.2. Control theory

The concept of control loops utilises sensors, actuators, as well as control circuits and is based on control theory. Here, control is defined as the targeted influence of a managed input variable of a system so that the output variable reaches a desired value as quickly and accurately as possible by ensuring a stability criterion [11]. Controllers can be distinguished between simple (see 2.3.2.1), feed-forward (see 2.3.2.2), and feedback controllers (see 2.3.2.3). Also, their combination is possible and described in 2.3.2.4. Any named controller unit here, can be considered as a Proportional Integral Derivative (PID) controller.

#### 2.3.2.1. Simple controller

The simple controller (also called open-loop controller) uses steering to apply an actuation  $u(t)$  to the reference variable  $w(t)$  to appropriately affect the output  $y(t)$  [12]. Since the output information is not used to act on the controller, it is independent of the result. Therefore, this scheme is used when only minor disturbances  $z(t)$  occur or when the output is not of interest, e.g. when heating a boiler with a timer for a set interval. Figure 2.29 visualises a scheme of a simple, open-loop controller.

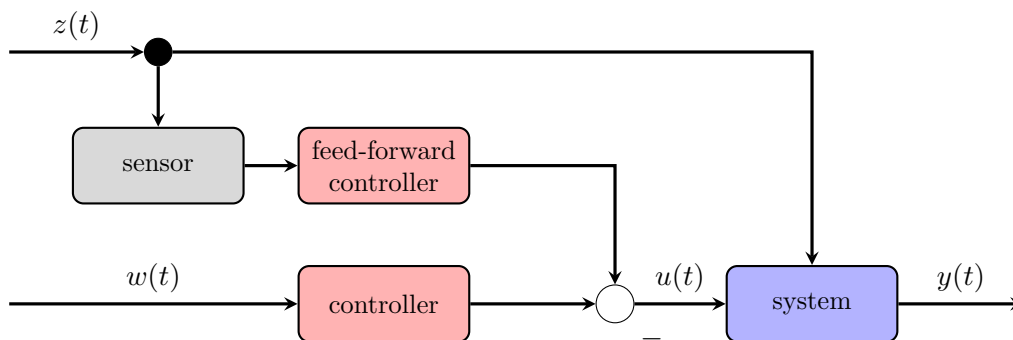
On the one hand, the advantages of a simple, open-loop controller are its simplicity, speed, and low costs. On the other hand, it can not react to disturbances and therefore easily run into a bias. Therefore, the feed-forward scheme is introduced.



**Figure 2.29.:** Scheme of an simple, open-loop controller acting on the input by steering the signal.

### 2.3.2.2. Feed-forward controller

The feed-forward control scheme measures additional information, e.g. the disturbances  $z(t)$  to predict their impact on the system. The information obtained is used by a feed-forward controller to generate a signal which is combined with the control signal of the simple controller to obtain a corrected actuation  $u(t)$  to be applied to the system [12]. Figure 2.30 illustrates a scheme of a feed-forward controller.



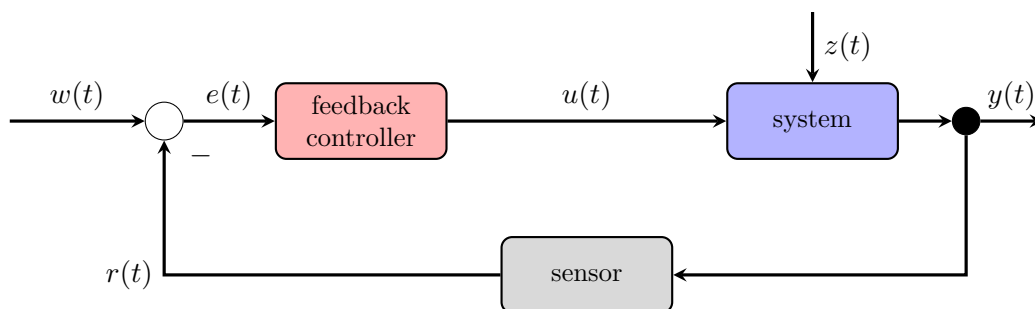
**Figure 2.30.:** Scheme of a feed-forward controller using additional information to compensate disturbances.

This control scheme is able to compensate disturbances very quickly. Nevertheless, no information about the output is known, which still can cause drifts. For more stable systems a feedback controller is needed.

### 2.3.2.3. Feedback controller

Unlike the above described controllers, the feedback controller uses output information to respond to deviations occurring in the process. Hence, it is also called a closed-loop controller. The output signal  $y(t)$  is measured by a sensor and the returning signal  $r(t)$  is subtracted from the input  $w(t)$  to create an error signal  $e(t)$  [12]. This again affects the process until the set-point has been reached satisfactorily. Therefore, a stability criterion needs to be met that requires the sensor, the actuator and the loop to be fast enough. Figure 2.31 shows a scheme of a feedback controller.

Feedback systems can control complex systems more accurately than feed-forward or open-loop systems, but are usually slower and rely on compliance with the stability

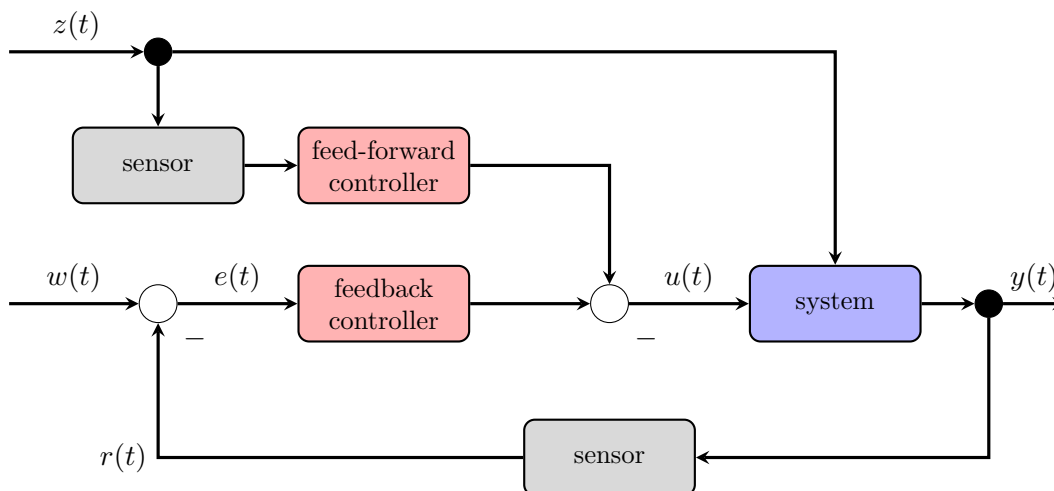


**Figure 2.31.:** Scheme of a closed-loop controller fed back the output to react on deviations.

criterion. If the criterion is not fulfilled, the system can oscillate or drive off the set point (compare with 2.1.2).

#### 2.3.2.4. Combined controller

To improve the performance of a controller, a feed-forward element can be combined with a feedback system. The feed-forward component speeds-up reaching the set-point, and since this controller is independent of the output, the system will not oscillate. Whereas, the feedback controller responds to the disturbances to ensure an accurate and stable output [12]. Figure 2.32 visualises a scheme of a combined feed-forward/feedback controller.



**Figure 2.32.:** Scheme of a combined feed-forward/feedback controller.

In practice, with complex systems usually a combination of feed-forward and feed-back controllers is used. In the context of ALPS, a feedback controller is used and its implementation presented in the chapter of the seismic noise analysis in section 4.4. A combined controller could be an improvement to the existing control loop.



# 3. The Any Light Particle Search experiment

The aim of the ALPS research group is find answers to long-standing questions in particle physics and cosmology by searching for new particles in the field of particle physics. In contrast to the usual approaches of high-energy experiments at large accelerators, ALPS is looking for ultra-light and very weakly interacting particles beyond the Standard Model, the so-called Weakly Interacting Slim Particles (WISPs). A candidate for a WISP would be the Axion postulated in the 1970s to resolve the strong Charge and Parity (CP) problem in Quantum ChromoDynamics (QCD). It could be an important component of Dark Matter in the universe. From various theories and studies, however, there might be Axion-Like Particles (ALPs). Apart from providing a possible explanation for Dark Matter, these ALPs could also deliver explanation regarding hints on the anomalous star cooling.

The first section 3.1 describes the ALPS II experiment with its motivation in physics, its optical set-up, and its experimental requirements. The technical conditions, available tools, and techniques used for seismic measurements, analyses, and isolations are outlined in section 3.2. Here, the selection of the instruments and tools for best data acquisition and analysis to meet the ALPS II requirements is delineated. The section thus defines the technical boundaries for this work.

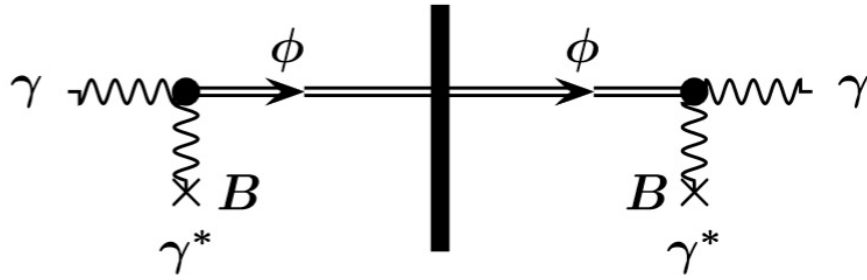
## 3.1. ALPS and its seismic noise requirements

The ALPS I experiment, which was based at DESY in Hamburg, carried out the search for ALPs with a Light-Shining-through-a-Wall (LSW) set-up from 2007 to 2010. It was pioneer work that set new limits for laboratory-based ALP experiments [72]. After its success in 2010 [20, 21], the next generation of LSW experiments was launched with ALPS II. The experiments are based on the Primakoff Effect, where two photons  $\gamma$  interact with each other to generate an ALP<sup>1</sup>  $\phi$  or, conversely, an ALP scatters with a photon to create a photon. The effect further predicts that the interacting photon can be replaced by a magnetic field  $B$  that can be seen as a source of virtual photons. Figure 3.1 visualises the Primakoff Effect in an LSW experiment.

The basic idea is to inject photons into an area with a strong magnetic field, possibly to convert them into ALPs. If an ALP is produced, it passes a fully opaque wall and enters another magnetic field behind the wall, where it can regenerate to a photon, both via the Primakoff Effect. Since the probability for a single photon-ALP conversion is

---

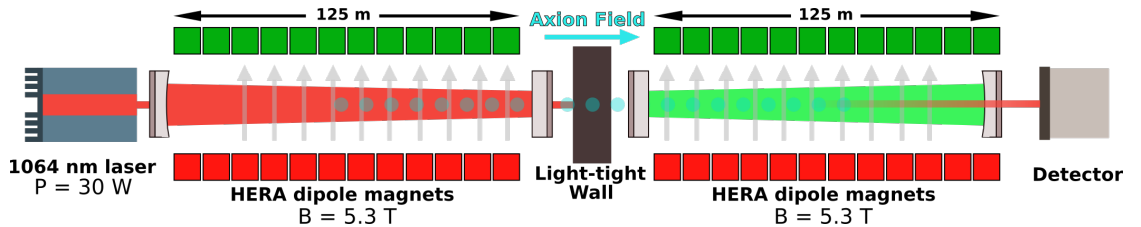
<sup>1</sup>Here, a generalised scalar or pseudo-scalar particle  $\phi$  is used as an example for an Axion or ALP.



**Figure 3.1.:** Schematic view of Primakoff Effect in an LSW set-up: photon conversion in a magnetic field (left), subsequent travel through a wall, and final photon regeneration in a magnetic field (right) [1].

extremely low (see subsection 3.1.1), the ALPS II experiment enhances the probabilities with long baseline, high-finesse optical resonators (see subsection 3.1.2) [72, 13].

The experiment is divided into ALPS IIa and ALPS IIc<sup>2</sup> [6]. ALPS IIa is designed to test and demonstrate the optical set-up, the control design, and the detection scheme in a 20 m long laboratory with 9.2 m long resonators, located in the HERA West Hall at DESY. ALPS IIc is planned to be the final stage with over 250 m in length with at least twenty four 8.8 m long 5.3 T dipole magnets and 125 m long optical resonators, located in the straight tunnel section in HERA North at DESY. Figure 3.2 represents a schematic set-up of the ALPS IIc experiment, with a 30 W 1064 nm continuous wave laser as the light source on the left side, the opaque wall in the experimental hall, in the middle, and a high-sensitive detector on the right side.



**Figure 3.2.:** Schematic set-up of the ALPS IIc experiment with its optical resonators – taken from [43].

Since the probability for detecting a regenerated photon is very low, the sensor has to be sensitive for a photon rate of  $2 \cdot 10^{-5}$  Hz [59]. Two detection schemes are developed simultaneously. First, the Transition Edge Sensor (TES), a cryogenic superconducting single photon detector, and second the HETrodyne sensing scheme (HET), a technique for weak-field detection. The former works as a cryogenic calorimeter and makes use of the dependence of electrical resistance of a material on the temperature at the superconducting edge. It applies a Superconducting QUantum Interference Device (SQUID) [7] read-out system to measure the change in the conductivity. The latter detection scheme

<sup>2</sup>ALPS IIb was originally planned, but was abandoned for time and cost reasons.

depends on the interference between the local oscillator and the regenerated field with an offset frequency of several megahertz. The resulting beat frequency is demodulated and integrated over long-term measurements to allow measurements at fundamental, shot noise limit [44, 58].

The overall goal for the ALPS II experiment is defined as:

“A sensitivity of experiment for scalar and pseudo-scalar particles with 95 % confidence level at  $g_{a\gamma\gamma} = 2 \cdot 10^{-11} \text{ GeV}^{-1}$  for an integration time of 12 days” – [59].

From this, further top-level requirements can be derived. Since the thesis focusses on seismic noise, which induces vibrations on the optical components of the ALPS II set up, this section will concentrate to the requirements for the optical set-up. The following subsections include the theoretical background, the optical resonators, the necessary dual resonance condition, the control loop design, the actual requirements, and the current status of the infrastructure.

#### 3.1.1. The physics of ALPS

Figure 3.3 visualises the Axion- or the ALP-photon coupling  $g_{a\gamma\gamma}$  over the Axion mass  $m_a$  and estimates the limits for current and future experiments. ALPS IIc can explore areas of the hitherto unexplored ALP parameter space with a sensitivity up to  $2 \cdot 10^{-11} \text{ GeV}$  in photon coupling strength for masses below  $10^{-4} \text{ eV}$ . The figure also shows current and future sensitivities of other Axion experiments using different detection methods relying on astrophysical models of axion sources. The yellow area indicates the region where the QCD-Axion can be found.

As mentioned above, the Axion or the ALPs could solve a multitude of fundamental problems in modern physics if their existence can be proven [61, 19]. The probability of converting a photon  $\gamma$  into an Axion  $\phi$  and back into a photon  $P_{\gamma \rightarrow \phi \rightarrow \gamma}$  in an LSW experiment, as the ALPS II experiment, is defined by the Power Build-up (PB) factors of the optical resonators with  $PB_{PC} = 5,000$  for the first and  $PB_{RC} = 40,000$  for the second resonator [6], the ALP-photon coupling  $g_{a\gamma\gamma}$ , the magnetic field strength  $B$ , and the length of the resonators  $l$  [25].

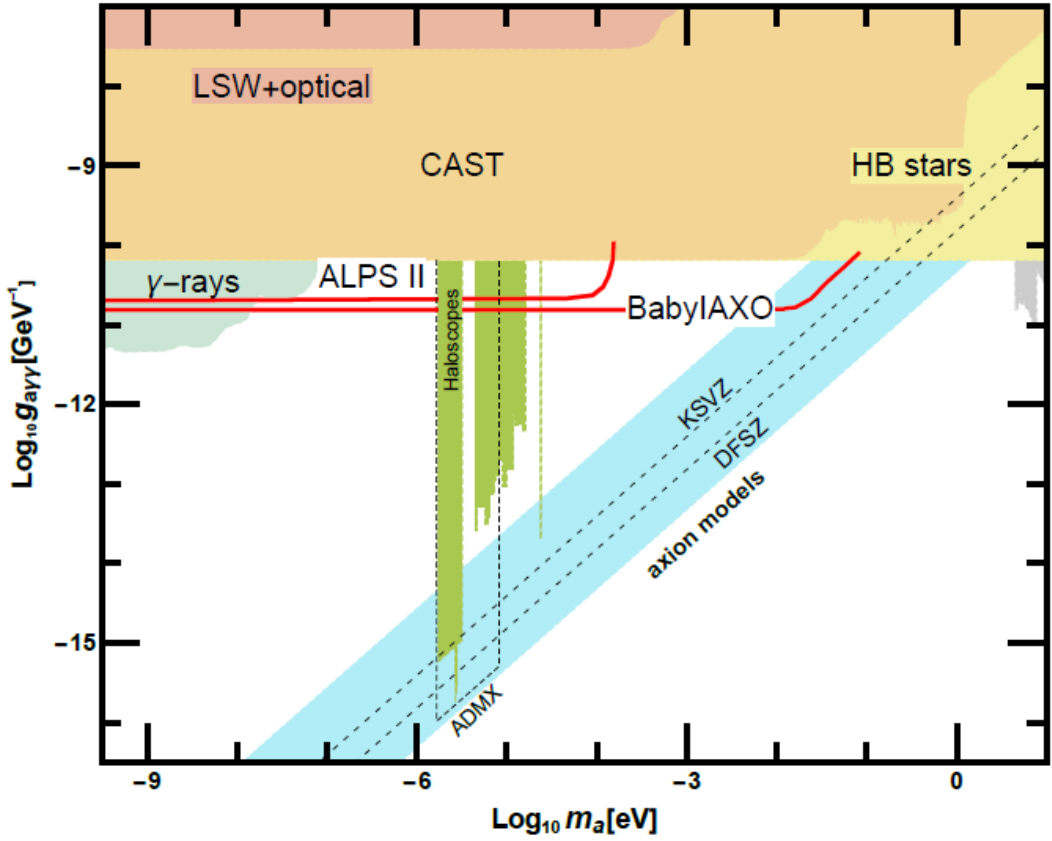
$$P_{\gamma \rightarrow \phi \rightarrow \gamma} = \frac{1}{16} \cdot PB_{PC} \cdot PB_{RC} \cdot (g_{a\gamma\gamma} B l)^4 \quad (3.1)$$

$$= 6 \cdot 10^{-34} \cdot 5,000 \cdot 40,000 \cdot \left( \frac{2 \cdot 10^{-11} \text{ GeV}^{-1} \cdot 5.3 \text{ T} \cdot 105.6 \text{ m}}{10^{-10} \text{ GeV}^{-1} \cdot 1 \text{ T} \cdot 100 \text{ m}} \right)^4$$

$$\approx 1.88 \cdot 10^{-25}$$

$$\text{with } g_{a\gamma\gamma} = 2 \cdot 10^{-11} \text{ GeV}^{-1} \quad (3.2)$$

The factor of  $6 \cdot 10^{-34}$  results of dimensional analysis. Since the ALP-photon coupling  $g_{a\gamma\gamma}$  is fixed, the probability clearly depends on the PB and the magnetic field times the resonator length  $Bl$ , where the latter weights with an exponent of 4. The resonator length is limited by the length and aperture of the magnets and its magnetic field strength more



**Figure 3.3.:** Photon to Axion or ALP coupling over its mass and projected coverage of ongoing and future experiments – taken from [19].

by technical restrictions. The PB depends on the arrangements of the optical resonators, which are explained in the next subsection.

### 3.1.2. Optical resonators

An optical resonator, also called a cavity, is a space in which light is reflected back and forth multiple times to create a standing light wave. If the optical path length of the resonator is a multiple of half the wavelength of the injected light, a standing wave is formed due to interference in the resonator (compare with 2.1.1.2). The difference between two subsequent resonant frequencies is defined as Free Spectral Range (FSR). In terms of frequency  $f_{FSR}$ , it is defined as follows [45]:

$$f_{FSR} = \frac{c}{l_{rt}} \quad (3.3)$$

where  $c$  is the speed of light and  $l_{rt}$  its round trip length inside the resonator. Since the ALPS II experiment uses linear cavities, two times the length of the physical resonator

is set:

$$f_{FSR} = \frac{c}{2l} \quad \text{with} \quad l_{rt} = 2l \quad (3.4)$$

As both cavities are high-finesse Fabry-Prot resonators, the line width can be assumed to be as follows [45]:

$$f_{LW} \approx \frac{f_{FSR}}{\mathcal{F}} \quad (3.5)$$

with  $\mathcal{F}$  being the finesse of the optical cavity, depending only on the reflectivity of the mirrors  $r_1$  (for the inner mirrors) and  $r_2$  (for the outer mirrors) [45]:

$$\mathcal{F} = \frac{\pi \sqrt[4]{r_1 \cdot r_2}}{1 - \sqrt{r_1 \cdot r_2}} \quad \text{if} \quad r \approx 1 \quad (3.6)$$

Since the first cavity is used to produce Axions, it is called the Production Cavity (PC), whereas the second will regenerate photons, it is therefore called the Regeneration Cavity (RC). The ALPS II experiment cavities are defined with a finesse of 8,000 for the PC and 120,000 for the RC, both with a length of 125 m [6]. To reach the goal of the ALPS II experiment the PC is defined to store 150 kW of circulating power in the fundamental mode, linearly polarised at 1,064 nm [59].

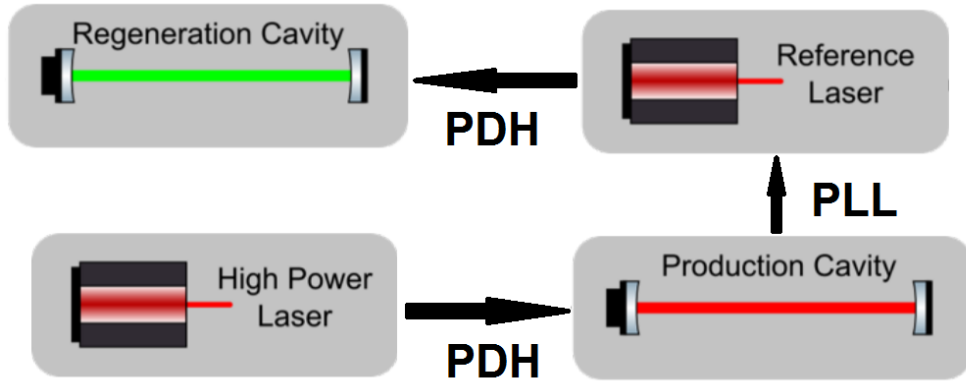
With respect to the overall goal, the photon component of the Axion- or ALP-field generated in the PC has to experience resonant enhancement in the RC, which is defined as dual resonance condition. Here, a half-confocal cavity design is used, which means the outer mirrors are curved and would form a confocal cavity with the inner mirrors inserted being flat, as shown in figure 3.2. The spatial overlap  $\eta$  between the ALP-field and the RC fundamental mode is defined as [59].

$$\eta = 0.95 \quad (3.7)$$

This determines the frequency and length requirements for the cavities (see subsection 3.1.4) and also affects some specifications for the control loop design.

#### 3.1.3. Control loop design

To maintain the dual resonance condition and ensure the field overlap  $\eta$ , seismic noise occurring, must be compensated. Therefore, the control scheme shown in figure 3.4 is used to attenuate mechanical vibrations. Due to the smaller line width of the ALPS IIc RC  $f_{LW}(RC) = 10$  Hz, compare equation (3.5), the control design is built from the rear. To achieve fast actuation a Pound-Drever-Hall (PDH) locking scheme was chosen to lock the RC with a reference laser and the PC to the high-power laser [9]. Here, a piezo-element acts on the laser crystal to tune its frequency. Subsequently, both cavities are locked towards each other with a Phase-Lock Loop (PLL). Thus, as both lasers are controlled, the length of a cavity must be adjusted by acting on one cavity mirror. Due to the fact that the PDH loops are faster and more broadband control, they can be used



**Figure 3.4.:** Schematic control loop design for the ALPS II experiment [66].

to pre-lock the cavities before aiming for the dual resonance requirement with the PLL. To observe and actuate on the angular pointing of the mirrors, a Differential Wavefront Sensing (DWS) scheme is used via quad-photo diodes [44, 66, 58].

The light circulating in the RC must have a different frequency than the high power light in the PC in order to distinguish their photons. The TES detection method uses a non-linear Periodically-Poled Potassium Titanyl Phosphate (PPKTP) crystal for Second Harmonic Generation (SHG) to create frequency doubled 532 nm green light to compensate for any (seismic) noise misaligning the mirrors. In the HET method, the megahertz offset light used to generate the beat signal is the same light used to lock the cavity [44, 58].

### 3.1.4. Frequency region and absolute length requirements

The ratio of the transmission  $T$  to the maximum transmission  $T_{max}$  is determined as being the maximal allowed frequency or length fluctuation between the PC circulating field and the RC length. This can be expressed via the Lorentzian equation of power transmission with a small frequency approximation [65]:

$$\frac{T}{T_{max}} = \frac{1}{1 + \left(\frac{\Delta f}{f_p}\right)^2} \equiv 0.95 \quad (3.8)$$

with the pole frequency  $f_p$  being the half of the line width  $f_{LW}$  from equation (3.5):

$$f_p = \frac{f_{LW}}{2} \approx \frac{f_{FSR}}{2\mathcal{F}} = \frac{c}{4\mathcal{F} \cdot l} \quad (3.9)$$

and  $\Delta f \equiv \Delta f_{0.95}$  being the maximal permissible frequency fluctuation to preserve 95% of power. Converting equation (3.8) to  $\Delta f_{0.95}$  as follows:

$$\Delta f_{0.95} = \sqrt{\frac{1}{0.95} - 1} \cdot f_p \quad (3.10)$$

The absolute length requirement is limited by the differential length  $\Delta l$  and can be derived from the linear relationship of the frequency to the length in optical resonators as follows:

$$\frac{\Delta l}{l} = \frac{\Delta f}{f} \quad (3.11)$$

with  $f$  being the laser frequency of  $282 \cdot 10^{12}$  Hz and  $l$  the length of the resonator,  $\Delta l$  follows as:

$$\Delta l = \Delta f \cdot \frac{l}{282 \cdot 10^{12} \text{ Hz}} \quad (3.12)$$

With the equations (3.8) to (3.12) the absolute length limit  $\Delta l_{0.95}$  can be derived. Table 3.1 lists the resonator length  $l$ , its finesse  $\mathcal{F}$ , as well as the cavity pole frequency  $f_p$  derived from equation (3.9), the maximal permissible frequency fluctuation  $\Delta f_{0.95}$ , and the maximal length fluctuation  $\Delta l_{0.95}$  to preserve 95 % of the power.

**Table 3.1.:** Requirements for the ALPS II and JURA cavities [6, 46].

Cavity	ALPS IIa	ALPS IIc	JURA
<b>PC</b>	$l = 9.2 \text{ m}$	$l = 125 \text{ m}$	$l = 500 \text{ m}$
	$\mathcal{F} = 8,000$	$\mathcal{F} = 8,000$	$\mathcal{F} = 12,500$
	$f_p = 1,018.32 \text{ Hz}$	$f_p = 74.95 \text{ Hz}$	$f_p = 11.99 \text{ Hz}$
	$\Delta f_{0.95} = 233.62 \text{ Hz}$	$\Delta f_{0.95} = 17.19 \text{ Hz}$	$\Delta f_{0.95} = 2.75 \text{ Hz}$
	$\Delta l_{0.95} = 7.622 \text{ pm}$	$\Delta l_{0.95} = 7.622 \text{ pm}$	$\Delta l_{0.95} = 4.878 \text{ pm}$
<b>RC</b>	$l = 9.2 \text{ m}$	$l = 125 \text{ m}$	$l = 500 \text{ m}$
	$\mathcal{F} = 120,000$	$\mathcal{F} = 120,000$	$\mathcal{F} = 300,000$
	$f_p = 67.89 \text{ Hz}$	$f_p = 5.00 \text{ Hz}$	$f_p = 0.50 \text{ Hz}$
	$\Delta f_{0.95} = 15.57 \text{ Hz}$	$\Delta f_{0.95} = 1.15 \text{ Hz}$	$\Delta f_{0.95} = 0.11 \text{ Hz}$
	$\Delta l_{0.95} = 0.508 \text{ pm}$	$\Delta l_{0.95} = 0.508 \text{ pm}$	$\Delta l_{0.95} = 0.203 \text{ pm}$

Since the pole frequency of the cavities acts as a natural low-pass filter (see subsection 4.4.2), frequencies above a few kHz are not of interest. Furthermore, the expected common mode of the optical tables is a lower limit for the frequency to be examined by a few mHz (see subsection 4.3.1). This range can be defined even more narrowly by the suppression of the control loop (see subsection 4.4.3). Therefore, based on the requirements and experience with vibrations and earlier measurements at DESY [2], a frequency range between 10 mHz and 2 kHz can be defined and investigated!

### 3.1.5. Infrastructure and status

In the current state, the ALPS II experiment starts the construction of ALPS IIc in the HERA tunnel. Testing and demonstration of the optical set-up is almost finished

and ready for implementation. The deconstruction and clearing of the old HERA accelerator components is completed. For the connection of the tunnel entrances in the HERA North Hall, radiation protective concrete blocks are stacked to the appropriate height that are supported by a steel structure. Old HERA dipole magnets are reused by straightening. At the moment most of them are tested and ready for installation. After their deformation, the HERA dipole magnets fulfil the yoke aperture requirement of 50 mm [6]. Its magnetic field times the length constitutes 560 Tm before and after the the wall [59]. The clean room design is in progress and they are planned to be mounted rigidly on the concrete base in the tunnels or the hall. The cavities will have a vacuum of  $10^{-8}$  mbar inside the vessels [6] where the cavity mirrors are located on bezel mounts. The inner ones are fixed on a Central Bread Board (CBB) that is mounted on the central optical table, which allows high stability for the detection schemes.

## **3.2. Tools and techniques used for seismic measurements, analyses, and isolations**

The following section presents the tools and techniques available for the ALPS II experiment, that are used to determine the seismic noise present in HERA at DESY. First, the instruments to measure and acquire seismic data are specified in subsection 3.2.1. Subsequently, the data management notations and the procedure of performing the seismic noise analysis are presented in 3.2.2. Finally in this section, the possibilities of the Finite Element Method (FEM) at DESY are shown in 3.2.3.

### **3.2.1. Seismic measuring instruments**

The ALPS collaboration uses several instruments to measure seismic noise at DESY. The next paragraphs present all the different instruments to measure and to acquire seismic data available within the ALPS II experiment. For that purpose, the instruments' advantages and disadvantages are pointed out and the specifications are summarised in tables 3.2 and 3.3.

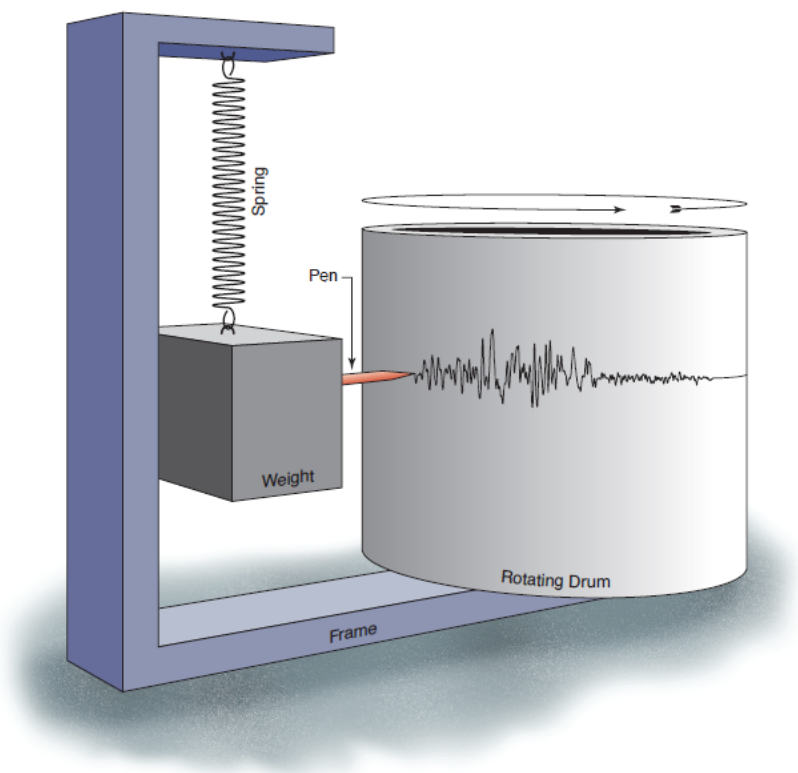
#### **3.2.1.1. Seismometers**

The term seismometer is defined as a device which registers seismic activities. The functionality of a seismometer can vary from optical to mechanical and electronic sensors. In the ALPS II collaboration, all three kinds are used. In addition, there is research into an optomechanical acceleration sensor with high dynamic range, high bandwidth, and low read-out noise levels [24]. It would allow measurements directly on the mirror surface via an interferometric system. As described above, the ALPS II experiment itself works with an optical resonator including an error and control signal (compare section 3.1). Thus, the ALPS IIa cavities are the most suitable devices to detect seismic noise for the given requirements. However, it should be noted that their signal is also mixed with other types of noise such as laser noise, thermal noise, and noise of components that may not be installed in the final set-up (ALPS IIc) [38]. The control signals of the cavities



are used as an upper limit for the frequency range in which the seismic noise dominates (see 4.2.1.2).

The mechanical and electronic seismometers are classic sensors used in geophysics. The Maschinen- und ExperimenteAufbau (MEA) group at DESY has high-end three-dimensional seismometers from Güralp Systems Limited [29] for broadband, low-frequency seismic noise detection with an integrated software running on a connected computer, which were available for the ALPS group. It uses a moving mass inside a coil that generate a voltage proportional to the velocity of the ground movement. It is well known at DESY and has been used for many years. It needs a fair amount of expertise to operate and also, together with its readout, it is unwieldy. Therefore, it was designated to register low-frequency data and to cross-check the calibration of other devices (see subsection 4.2.1). In the following, the two seismometers used are named after their internal numbers *S6* and *S7*. Also, one-dimensional horizontal geophones from Mark Products [47] and a vertical geophone from Sercel [64] are available within the ALPS collaboration. Geophones are relatively heavy but are stand-alone devices that do not require a power supply to operate. They contain a freely oscillating mass within a coil like the seismometer, which induces a voltage by movement that can then be read out. The basic principle is presented in figure 3.5.



**Figure 3.5.:** Schematic representation of a pure mechanical seismometer – taken from [23].

In general, geophones measure the velocity of the ground movement. For that pur-

pose, they must be firmly mounted or fixed in their angular rotation. Otherwise, a reproducible result can not be achieved. Thus, they are easy to use, but due to their moving mass also unhandy and easy to damage. For operation, broadband seismometers and geophones can be placed on the ground. However, to achieve a better connection with the measurement object, e.g. with an optical table, they should be clamped or screwed on it. The ALPS collaboration additionally uses Wilcoxon Research model 731-207 low-frequency accelerometers [52]. These utilise the piezoelectric effect to convert pressure into voltage. Since pressure is related to a force and is proportional to the acceleration, these devices measure the acceleration of the ground movement. An accelerometer requires a preload force and is therefore bolted to a metal block in this case. This allows a three-dimensional reattachment via a grub screw and can then be mounted onto the optical table or placed on the floor. Since they actually only measure the change in resistance of the piezoelectric material, they need a power supply to operate. Here, the Wilcoxon Research model P702B power unit and amplifier is used. It is a power supply, an analogue integrator, and an amplifier at the same time. The use of the internal integrator is called the VELOCITY (VEL) mode. If it is not integrated, it is called ACCeleration (ACC) mode. When the accelerometer is not connected to a power supply, it is robust and can be easily transported.

Note, that the term “low-”, “middle-”, or ”high-frequency” strongly depends on the kind of device or the problem under investigation! A broadband seismometer can measure frequencies down to some mHz and up to several hundred Hz, whereas the sensitivity of an accelerometer is usually between around one Hz but up to several kHz. The geophones fit mostly somewhere in between, but with a narrower frequency range. All seismometers used and their specifications are listed in table 3.2.

**Table 3.2.:** List of seismometers used in the ALPS II experiment to measure seismic noise data [29, 47, 64, 52, 53].

Type	Description
ALPS IIa cavity	The control signal of the cavity itself could be used to measure the frequency noise of the optical resonators.
Güralp CMG-6TD seismometer	Broadband seismometer Frequency response from 0.033 Hz to 100 Hz
L-4C horizontal geophone	Natural response at 1 Hz Frequency response from 0.5 Hz to 20 Hz
L-22D vertical geophone	Natural response at 2 Hz Frequency response from 0.1 Hz to 1,000 Hz
Wilcoxon Research model 731-207 accelerometer	Natural response at 2,400 Hz Frequency response from 0.2 Hz to 1,300 Hz
Wilcoxon Research model P702B power unit/amplifier	Power supply, Gain at 1, 10, or 100 Integrator to convert acceleration in velocity

### 3.2.1.2. Acquisition devices

To acquire the measured data, i.e. to digitally convert and store the data, three different instruments are available. First, the Stanford Research Systems SR785 Spectrum Analyzer to directly convert the signal in the frequency domain. Here, the results can be presented as PS, PSD, LS, LSD, or as coherence plots. For this purpose the data is compressed to a maximum of 800 bins, i.e. depending on the frequency range desired, e.g. 0 Hz to 400 Hz, the frequency resolution is downsized to 0.5 Hz. In exchange, the data is immediately visualised and the resulting files are comparatively small [67]. Second, the Tektronix Digital Phosphor Oscilloscope DPO7000 is used, which digitises and records the time series simultaneously at 8-bit. This device can sample on four channels with a maximum frequency of 20 MHz. The advantage of obtaining a time series is the option of post-processing and easily analysing the data afterwards. Unfortunately, the internal memory of the device only holds a maximum of 500 s at 50 kHz with 2 channels [70]. The last acquiring device is a high-speed waveform digitaliser card from AlazarTech. The ALPS collaboration uses two different versions. One, the 14-bit ATS9416 with a sample rate of 100 MHz, 16 channels, and  $\pm 1$  V input range is dedicated for the cavity data readout [3]. Two, a 16-bit ATS9626 with a sample rate of 250 MHz, 2 channels, and  $\pm 1.25$  V input range is used for the readout of the TES detector data [4]. The ALAZAR cards are very convenient to use due to their computer integration, but can not be moved without the computer. All acquiring devices and their specifications are listed in table 3.3.

**Table 3.3.:** List of devices used in the ALPS II experiment to acquire seismic noise data [67, 70, 3, 4].

Type	Description
Stanford Research Systems SR785 Spectrum Analyzer	Generate spectra (e.g. LSD) with maximal 800 bins from 0 Hz to 102.4 kHz
Tektronix Digital Phosphor Oscilloscope DPO7000	Samples up to 20 MHz with 4 channels with 8 bit resolution ( $> 11$ bit with Hi Res)
ALAZAR ATS9416	16 channels with 14 bit resolution and 100 MHz and $\pm 1$ V input range
ALAZAR ATS9626	2 channels with 16 bit resolution and 250 MHz and $\pm 1.25$ V input range

### 3.2.1.3. Selected measurement chain

In order to ensure an efficient and comparable analysis, the measurement chain described in the following was selected. Due to the required broadband frequency response in combination with its relatively high sensitivity, the 731-207 accelerometer, along with the P702B power unit and amplifier, is used in most cases to measure the seismic noise. When regarding frequencies below 0.1 Hz, the Güralp seismometers are additionally included into the measurement chain. The result must then be obtained from the combi-

nation of the spectral data of both sensors (see 4.3.1.2).

Due to the necessity for calibrations and adjustments, a time series is required for acquisition. Since the ALAZAR cards currently are in use and therefore can not be brought to HERA North, the Oscilloscope DPO7000 was used for all measurements to ensure comparability. To achieve a good SNR, the oscilloscope must be set to the finest possible resolution and the highest possible sampling frequency (compare subsection 2.1.3). Otherwise, the analogue-to-digital conversion induces a quantisation error that is higher than the actual seismic signal measured. Consequently, the resolution is fixed to 40 mV/div or lower and the sampling frequency to at least 50 kHz. Since 2,000 Hz is the highest frequency valid for the accelerometer (see 4.2.1.2), this is an oversampling by a factor of 12.5 – note the Nyquist criterion. Furthermore, the measurement time  $T$  for normal measurements is set to 100s to enable a modal analysis down to a minimum of 0.01 Hz. In all cases, the signal is transmitted from the seismometer via coaxial cable to the oscilloscope to provide the best possible protection against noise, e.g. pink noise (compare with 2.1.1.3).

### 3.2.2. Data management and analyses

Since the acquisition of seismic noise data is a continuous dynamic process, data management and organisation as well as its understanding are of importance. The following paragraph therefore explains the necessity and convention of the documentation of the acquired data in 3.2.2.1. Furthermore, the analysing procedure is explained in 3.2.2.2.

#### 3.2.2.1. Notations for documentation

All measured seismic data of the analyses presented in chapter 4 and additional acquired in the past are stored for future research. For the sake of clarity and retrievability, a naming scheme was defined for all raw data files. This notation is defined as follows:

*[acquisition device]\_[seismometer (+specs)]\_[location (+specs)]\_[date]\_[time]\_[sample rate]\_[measurement time]\_[additional information]*

The key to decode the notation is explained in appendix A.

#### 3.2.2.2. Analysing procedure

After the data acquisition it has to be analysed by a script that performs the modal analysis and generates charts from the time series. Therefore, the script calculates an LSD by applying an FFT, a window function, as well as an adequate averaging and overlapping as described in subsection 2.1.3. The LSD was chosen as the form of representation, since in the ALPS II experiment the detection of a seismic noise signal and the overall RMS are more important than the correct amplitude accuracy or the exact representation of a single peak (compare with 2.1.4.1). For implementing the FFT a newly developed method is used, which is explained in detail in section 4.1. Furthermore, the script has to perform the instrument-dependent calibration as fully described in subsection 4.2.1. The result is then visualised as a time series, LSD, or

spectrogram as detailed in subsection 2.1.4. In addition, the RMS value is added to the LSD diagram to get a direct connection to the ALPS II length stability requirements (compare with subsection 3.1.4).

The spectral diagrams are shown in a double logarithmic scale. For the x-axis, the reason is the more descriptive representation of all frequency ranges. For the y-axis, it is because seismic noise is white noise that is proportional to the force of the seismic wave (compare section 2.2). By integrating twice for displacement, this would become red noise falling  $1/f^2$ . Therefore, to visualise the spectra are shown in logarithmic scale.

Furthermore, the script allows the user to customise the settings of the analysis. This refers, for example, to the selected data set, the corresponding calibration, and the desired presentation. To list all possible settings would go beyond the scope in this context. All the coding was done with MATrix LABoratory (MATLAB) [50] available at DESY.

### 3.2.3. Finite Element Method simulation

This subsection specifies the requirements for FEM to simulate a seismic isolation model to damp seismic noise in critical frequency ranges, as discussed in subsection 5.3.2. Therefore, the following paragraphs explain the approach on how to simulate the effect of a pendulum structure (compare subsection 2.3.1) or an entire isolation system with the measured seismic noise. In addition, the tool with which this simulation is executed is specified.

#### 3.2.3.1. Simple isolation simulations

In order to understand and to learn the tools, an elementary isolation principle such as a simple or spring pendulum was investigated (compare subsection 2.3.1). For this, one dimensional horizontal and vertical constructions are modelled in order to study bending effects and to observe their modes, damping factors, and transfer functions.

#### 3.2.3.2. Over-determined isolation systems

Subsequently, a fine mesh was applied to accurately study the effects of gravity and measured seismic noise on an over-determined isolation system which might be implemented in the ALPS II or JURA experiments. Furthermore, a detailed Computer-Aided Design (CAD) model of the isolation system with technical drawings will have to be made for the manufacturing (see chapter 5).

#### 3.2.3.3. Selected FEM tools

To model sufficient seismic isolation, a CAD and an FEM tool must be used. At DESY, NX 10 is used as a CAD design tool. In addition, two FEM programs are available. First, ANalysis SYStem (ANSYS), a tool for linear and non-linear problems in different areas of mechanics [40], and second, Räumliche STABwerke (RSTAB), a static 3D program that is suitable for the calculation of trusses, which usually serve as supporting

structures. The software is not able to define prestressing forces required to implement the anti-spring concept (compare with 2.3.1.4), which is why ANSYS has been selected. Nevertheless, a manufactured model must be used to validate critical over-determined system parameters (see chapter 5).

## 4. Seismic noise analysis

This chapter expounds the seismic noise analysis that was done in HERA at DESY for the ALPS II experiment from 2016 to 2018. For that reason, a new FFT analysing method was developed, which enhances the resolution over a wide frequency range called the "Method of frequency-weighted and averaged FFT (MfwaFFT)". The first section 4.1 introduces this new method by explaining its algorithm with a given example and demonstrates its advantages over existing methods.

Subsequently, the seismic measurement preparation will be explained in section 4.2 by stating the calibration of the instruments as well as executing an accuracy analysis. The next section then presents the given ground conditions of HERA and the existing (optical) components of the ALPS II experiment in 4.3. Afterwards, the data post-processing given by the different filtering possibilities is specified in 4.4. The chapter closes with the evaluation of the results and the determination of the requirements for the optics in 4.5, which can be used for further interpretations and future research.

### 4.1. Method of frequency-weighted and averaged FFT

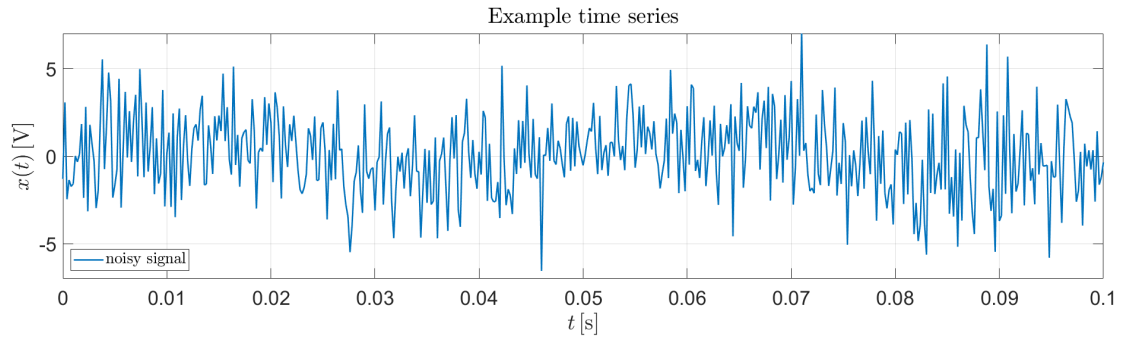
As lined out in 2.1.3 an FFT is always a trade-off between frequency resolution, amplitude accuracy, and suppression of frequency dispersion [55]. The developed MfwaFFT faces this trilemma by analysing a time series over a wide frequency range. A normal distribution of acquired data is assumed as no further information is available. Furthermore, no damping is used in the analysis to ensure data integrity. These assumptions improve the significance of the results generated. All representations in the following show an LSD since the detection of a low-amplitude signal is more important than absolute amplitude accuracy.

The next subsections sketch the problem and present motivations for the development in 4.1.1, introduce solution approaches in 4.1.2, explain the algorithm in 4.1.3 and point out the advantages as well as some disadvantages of the new method in 4.1.4.

#### 4.1.1. Problem definition and motivation

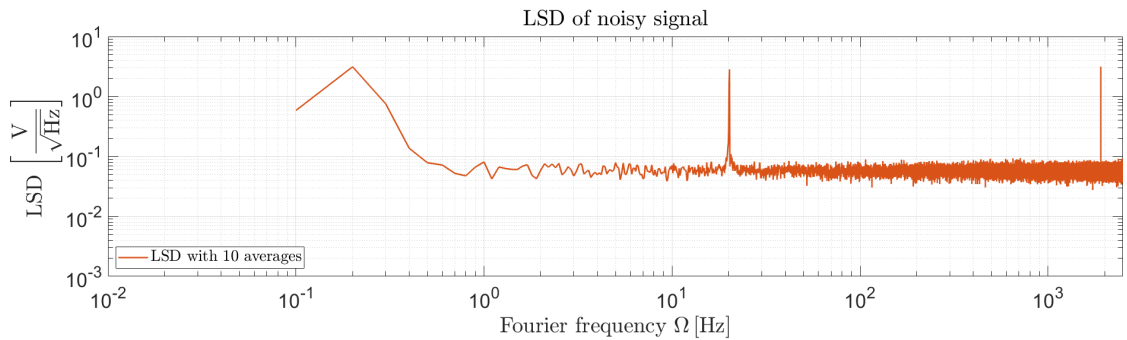
The stated trilemma can be minimised in a defined (small) frequency range by modal analysis techniques, which use windowing and averaging as instruments to reduce noise and aliasing effects [31]. Although, an always present challenge is to choose the fitting window function and the right amount of averages for the FFT. The latter depends on the to-be-examined frequency range, the FFT function used and the nature of the noise source. Hence, it is not simply possible to achieve a satisfying result for all aspects. In practice, depending on the field of work, several methods exist to avoid losses.

In the following a simple example is used to explain the trilemma and approaches to the solution. For this, a time series with sinusoidal signals at 0.203 Hz, 20.17 Hz, as well as 1,904.9 Hz, all with an amplitude of 1 V, and additional white noise with a variance of 2 V sampled with 5,000 Hz over 100 s is used. The imperfect frequencies have been chosen to avoid harmonic as well as aliasing effects and represent the reality. A section of the time series of that noisy signal is shown in figure 4.1.



**Figure 4.1.:** Section of an example time series with signals at 0.203 Hz, 20.17 Hz and 1,904.9 Hz with an amplitude of 1 V, additional white noise with a variance of 2 V, sampled with 5,000 Hz over 100 s.

Considering the length of the time series and the Nyquist criteria, all three signals should be represented in the spectrum. With the given techniques from 2.1.3 an LSD was computed with the *pwelch*<sup>1</sup> function (explained below in 4.1.3.2) of the Signal Processing Toolbox of MATLAB with 10 averages, a Kaiser window with a beta factor of 2.5, and 20 % overlap as it is optimal (compare subsection 2.1.3). This is plotted in figure 4.2.



**Figure 4.2.:** LSD of the example time series with 10 averages, a Kaiser window with a beta factor of 2.5, and 20 % overlap created with the *pwelch* function of MATLAB.

Here, the trilemma is visualised: all three signals are represented, but with different qualities. The first at 0.203 Hz is shown as a wide frequency peak due to insufficient frequency resolution and frequency dispersion. This is a result of taking 10 averages

<sup>1</sup>Detailed information about the syntax can be found on MathWorks: <https://de.mathworks.com/help/signal/ref/pwelch.html>



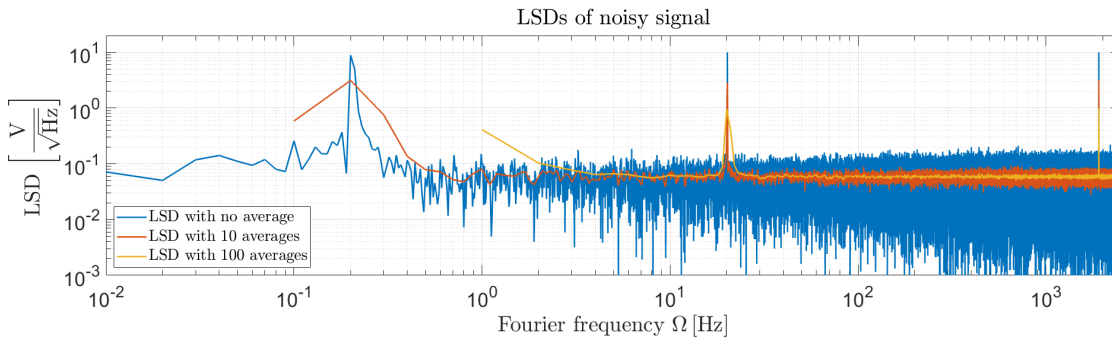
and therefore minimising the sample length to 10 s per average or inversely the resolution to 0.1 Hz. The middle signal at 20.17 Hz is represented adequately. The last at 1,904.9 Hz is plotted correctly but with a very high white noise level. As a result, a signal with a smaller amplitude would not be visible. Therefore, the resulting rendering is unsatisfactory for the desired level of detail.

### 4.1.2. The solution approaches

In the next paragraphs two different state of the art methods as well as the newly developed method are introduced, which all handle the indicated problem of analysing time series over a wide frequency range. The first is stitching, used in electronic signal processing. The second, called Logarithmic frequency axis Power Spectrum Density (LPSD) [36] developed by the "Laser Zentrum Hannover e.V." in cooperation with the "Max-Planck-Institut für Gravitationsphysik (Albert-Einstein-Institut)" both located in Hanover, Germany, to optimise the frequency resolution on a logarithmic scale. Last, the MfwaFFT that uses existing techniques to improve the result by averaging different frequency-weighted iteration steps.

#### 4.1.2.1. Stitching

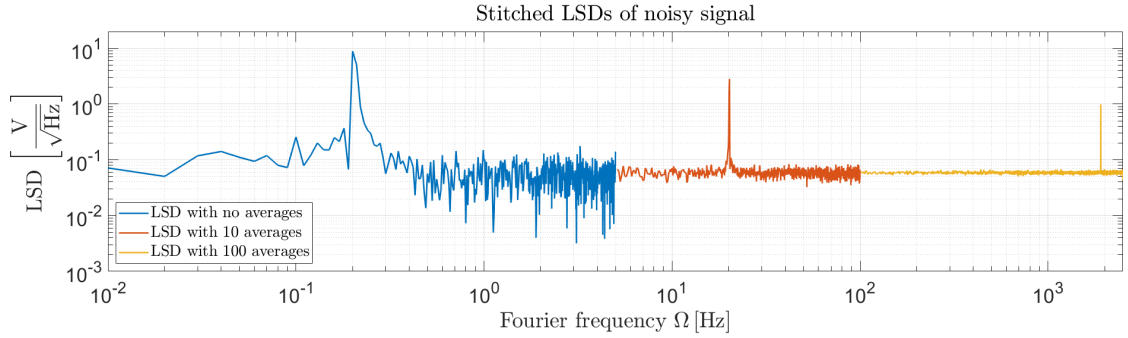
In signal processing the method of stitching adequate FFTs to each other is adopted. This method takes different amount of averages over a time series or rather the window size, that the FFT function uses. Figure 4.3 shows three LSDs with 1, 10, and 100 averages each over 100 s, 10 s, and 1 s, respectively.



**Figure 4.3.:** LSDs of the example time series with 1, 10 and 100 averages, a Kaiser window with a beta factor of 2.5, and 20% overlap; averaged over 100 s, 10 s, & 1 s.

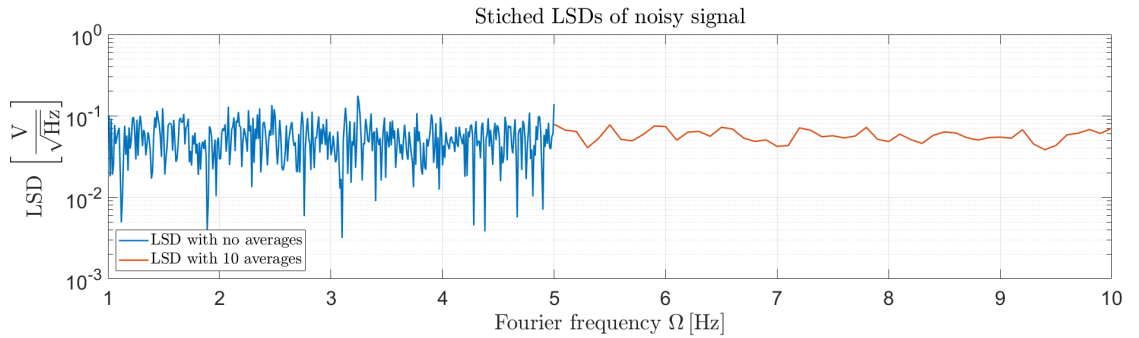
Stitching means to (manually) choose suitable frequency separations, where one graph should end and an other should start. The example in figure 4.3 shows this at, e.g. 5 Hz and 100 Hz (coinciding with the adjacent graph and not affected by the inaccuracy due to the low frequency resolution). The resulting data – stitched together – will give the the final FFT, which is plotted in figure 4.4.

A significant decrease in the amplitudes due to the different frequency resolutions  $f_{res}$  is visible. A closer look at the transitions, here at 5 Hz, illustrates the effect of the



**Figure 4.4.:** Stitched LSDs of the example time series with 1, 10, and 100 averages, a Kaiser window with a beta factor of 2.5, and 20% overlap; averaged over 100 s, 10 s, & 1 s.

different frequency resolutions  $f_{res}$  on the quality of the data. Because the resolution is proportional to the number of selected averages, it has a decisive effect on the data accuracy. Since the example is an LSD with normalised noise level, it remains constant. This is shown in figure 4.5.



**Figure 4.5.:** Detailed semi-logarithmic view on stitched LSDs of the example time series with 1 and 10 averages, a Kaiser window with a beta factor of 2.5, and 20% overlap; averaged over 10 s & 1 s.

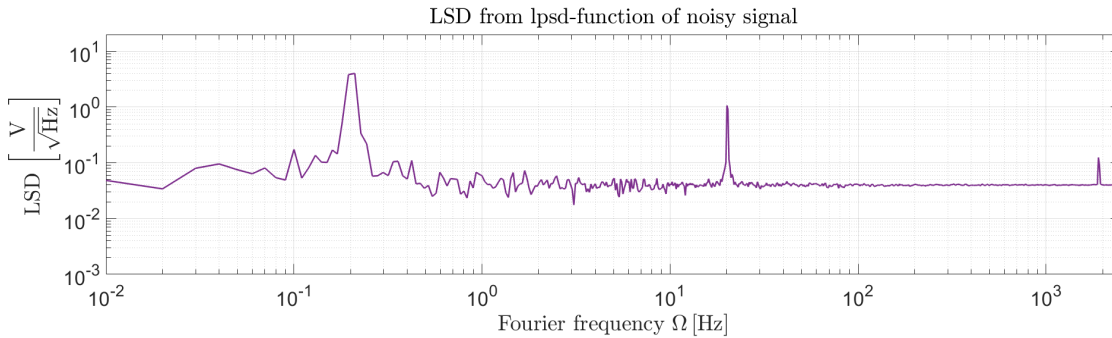
The method can be applied and carried out very quickly and easily. However, the frequency resolution differs between the individual parts, which can hinder third-person interpretation and therefore makes it difficult for further analyses and examinations.

#### 4.1.2.2. LPSD

The Laser Interferometry Space Antenna (LISA) project needed to analyse data over a wide frequency range. Therefore, the LPSD-method was developed, which is an algorithm used in the LISA Technology Package Data Analysis (LTPDA) toolbox<sup>2</sup> of

<sup>2</sup>Detailed information about the LTPDA toolbox and its functions can be found at the evolved Laser Interferometry Space Antenna (eLISA) website: <https://www.elisascience.org/ltpda/usermanual/usermanual.html>

MATLAB [5]. Applied to the exemplary time series, the spectral density is shown in figure 4.6.



**Figure 4.6.:** LSD from LPSD-function of the example time series with 10 averages, a Kaiser window with a beta factor equal to 2.5 ( $psll = 19$ ), and 20% overlap; averaged over 10 s.

The LPSD calculates the FFT over logarithmically spaced frequencies [36]. As a result, the same number of frequency bins are available over the entire (logarithmic) frequency range. Its advantages is shown by plotting the result in a double logarithmic scale. The white noise level in the higher frequency range is significantly minimised without losing information in the lower regions. Furthermore, the amount of data is significantly minimised, resulting in faster data processing and less storage space. The disadvantage, however, is the loss of amplitude accuracy with increasing frequency even stronger than in stitching and the very strong and not always desired smoothing of the graph.

#### 4.1.2.3. New solution approach

The idea of the MfwaFFT is simple: the algorithm creates a specified number of differently averaged FFTs continuously over all possible frequencies with a corresponding and differentiable window function as weight. This works similar to a multiband compression [41], but without the need for a priori information of the seismic noise. The particular weight will focus the FFT in its most valid frequency range. In the end, all averages will be summed up and normed to one final continuous FFT. Therefore, it uses frequency dependent weightings that are averaged over several iteration steps. The next subsection explains this method in detail.

#### 4.1.3. The MfwaFFT algorithm

The code enables the above-described method to process a time series vector  $X$  with a given sample rate  $f_s$  via MATLAB. The full code can be found in appendix B. In the following, all steps from the “data preparation” to the “summing up” of the iteration steps are explained.

#### 4.1.3.1. Data preparation

The time series vector  $X$  has a length of  $N$ , which is defined as the duration in seconds  $T$  multiplied by the sample rate  $f_s$  (compare to equations (2.45) and (2.46)).

$$X = \begin{pmatrix} x_1 \\ x_2 \\ \vdots \\ x_N \end{pmatrix} \quad (4.1)$$

$$\text{where } N = T \cdot f_s \quad (4.2)$$

Before operating the FFT function, the code calculates all suitable divisors  $D$  of  $T$  with the maximal number of different averages possible defined by  $\delta \rightarrow \delta(T)$ .

$$D = \begin{pmatrix} d_1 \\ \vdots \\ d_\delta \end{pmatrix} \quad (4.3)$$

In principal, every divisor of  $T$  is possible, but including them all would also increase the computation time, while not necessarily showing better results. Therefore, two adjustments are made. On the one hand, only natural divisors are allowed. On the other hand, a factor  $p$  is introduced, which is multiplied by the measurement duration  $T$ . This causes natural divisors of  $p$  times  $T$ . In this work, the data should be analysed in detail up to several kHz with a measuring time of 100 s. This results in  $p$  being equal to 10, since then a suitable averaging of the high frequencies is carried out:

$$p \equiv 10 \quad (4.4)$$

Thus,  $d_1 = 1$  and  $d_\delta$  is equal ten times  $T$ .

$$d_\delta = 10 \cdot |T| \quad (4.5)$$

With  $j$  being the control variable of the number of divisors  $d_j$  in general determines the duration of one generated sample piece by  $\tau_j \rightarrow \tau_j(d_j)$  and hence determines the frequency resolution  $f_{j,res}$  dependent on the sample frequency  $f_s$  (compare equation (2.50)).

$$\tau_j = \frac{T}{d_j} \quad (4.6)$$

$$f_{j,res} = \frac{1}{\tau_j} \quad (4.7)$$

E.g. with  $T = 10$  s and  $f_s = 5,000$  Hz:

$$\delta(10 \text{ s}) = 9$$

$$D(10 \text{ s}) = [1, 2, 4, 5, 10, 20, 25, 50, 100]$$

$$\text{e.g. } \tau_6 = 0.5 \text{ s}$$

$$f_{6,res} = 2 \text{ Hz}$$

As some numbers have way more possible natural divisors as desired, the user can specify a degree of detail (*dod*) which limits the amount of divisors and equally distributes the remaining, thus  $\delta(T)$  is equal to *dod*, e.g.:

$$\begin{aligned} T &= 36 \text{ s} \\ \delta(36 \text{ s}) &= 24 \\ D(36 \text{ s}) &= [1, 2, 3, 4, 5, 6, 8, 9, 10, 12, 15, 18, 20, 24, \\ &\quad 30, 36, 40, 45, 60, 72, 90, 120, 180, 360] \end{aligned}$$

$$\begin{aligned} T &= 36 \text{ s} \\ \textit{dod} &= 5 \\ D_5(36 \text{ s}) &= [1, 8, 20, 45, 360] \end{aligned}$$

Whereas, if  $p$  times  $T$  is not a good dividend, the user has to trim the data to an adequate length to receive more possible averages or change the value of  $p$ . Here from  $T = 59 \text{ s}$  to  $T_{trim} = 56 \text{ s}$ :

$$\begin{aligned} T &= 5.9 \text{ s} \\ \delta(59 \text{ s}) &= 2 \\ D(5.9 \text{ s}) &= [1, 59] \end{aligned}$$

$$\begin{aligned} T_{trim} &= 5.6 \text{ s} \\ \delta(5.6 \text{ s}) &= 8 \\ D(5.6 \text{ s}) &= [1, 2, 4, 7, 8, 14, 28, 56] \end{aligned}$$

The data preparation generates following specifications for the above example:

$$\begin{aligned} T &= 100 \text{ s} \\ f_s &= 5,000 \text{ Hz} \\ \textit{dod} &= 3 \\ D_3(100 \text{ s}) &= [1, 40, 1000] \\ f_{res} &= [0.01 \text{ Hz}, 0.4 \text{ Hz}, 10 \text{ Hz}] \end{aligned}$$

These calculated values will be used to generate the FFT.

### 4.1.3.2. FFT generation

To generate multiple FFTs, the time series vector is reshaped iteratively for every averaging step  $j$  into a  $(m \times n)$  time series matrix  $M_j$ .

$$M_{j,(m \times n)} = \begin{pmatrix} x_{1,1} & \cdots & x_{1,d_j} \\ x_{2,1} & \cdots & x_{2,d_j} \\ \vdots & \ddots & \vdots \\ x_{\frac{N}{d_j},1} & \cdots & x_{\frac{N}{d_j},d_j} \end{pmatrix} \quad (4.8)$$

$$\begin{aligned} \text{with } m &= 1, 2, \dots, \frac{N}{d_j} \\ n &= 1, \dots, d_j \\ j &= 1, \dots, \delta \end{aligned}$$

The  $M_j$  matrices then are inserted as  $x$  variables into the *pwelch* function to calculate the FFTs [31].

$$[Pxx, f] = \text{pwelch}(x, nwin, noverlap, nfft, fs)$$

The setting for the other variables are as follows: *nwin* to a Kaiser window with the length of  $m$ , *noverlap* to a fifth of the window length, *nfft* to the window length, and *fs* is set to the sample rate  $f_s$ , which will generate a Kaiser window with 20% overlap and an FFT length equivalent to that of the window. The calculated  $Pxx$  reflects the PSD where  $f$  corresponds to the Fourier frequencies  $\Omega$  [31]. As the *pwelch* function is operated with the  $M_{j,(m \times n)}$  for every iteration step  $j$ ,  $Pxx$  will produce a  $(f_m \times n)$  matrix for all  $\delta$  iteration steps  $j$ :

$$Pxx_{j,(f_m \times n)} = \begin{pmatrix} pxx_{f_0,1} & \cdots & pxx_{f_0,d_j} \\ \vdots & \ddots & \vdots \\ pxx_{f_{Ny},1} & \cdots & pxx_{f_{Ny},d_j} \end{pmatrix} \quad (4.9)$$

$$\text{with } f_m = m \cdot f_{res} \quad (4.10)$$

$$m = 0, \dots, \frac{N}{2 \cdot d_j}$$

$$f_{Ny} = \frac{N}{2 \cdot d_j} \cdot f_{res} \quad (4.11)$$

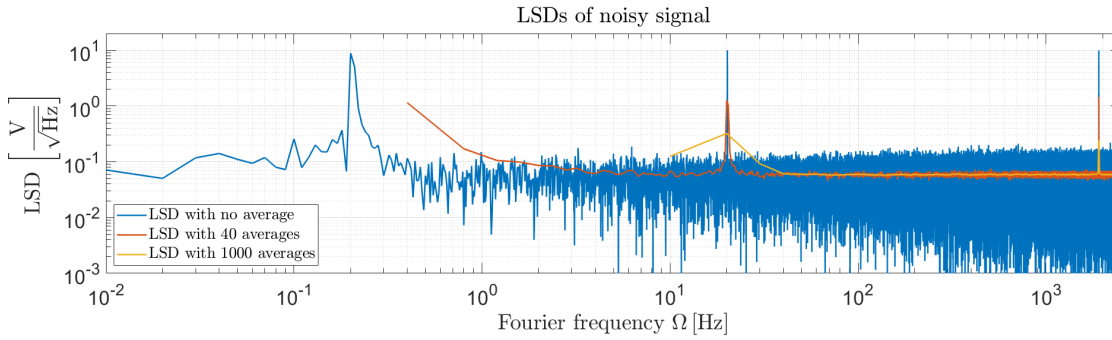
The data then has to be processed to an LSD as introduced in subsection 2.1.4  $Lxx_{j,(f_m \times n)}$ :

$$Lxx_{j,(f_m \times n)} = \begin{pmatrix} lxx_{f_0,1} & \cdots & lxx_{f_0,d_j} \\ \vdots & \ddots & \vdots \\ lxx_{f_{Ny},1} & \cdots & lxx_{f_{Ny},d_j} \end{pmatrix} \quad (4.12)$$

This will subsequently be averaged over the second dimension to an averaged LSD vector  $Lxx_{j,(f_m \times n),avg}$ :

$$Lxx_{j,(f_m \times 1),avg} = \begin{pmatrix} lxx_{f_0} \\ \vdots \\ lxx_{f_{N_y}} \end{pmatrix} \quad (4.13)$$

This is shown in figure 4.7 with three different numbers of averages. The first iteration step, always being  $(f_m \times 1)$  – here, the blue line – expresses an FFT over the full time series without any average, where the last iteration step with  $(f_m \times d_\delta)$  – here the yellow line – refers to an FFT with one average per 0.1 s, as  $d_\delta = 1000$ . Regarding the predominant trilemma and the effect of averaging data for a modal analysis as explained in subsection 2.1.3, the first iteration step yields the best results to the lower frequency region, whereas the last iteration is best in the higher region. Note: Beside the specifications of the instruments, the quality of the information strongly depends on  $T$  and  $f_s$ . Therefore, a sample rate at least twice the Nyquist frequency and a sample time ten times longer than the reciprocal lowest frequency examined should be used (compare with 2.1.3.1).



**Figure 4.7.:** LSDs of the example time series with 1, 40, and 1000 averages, a Kaiser window with a beta factor of 2.5, and 20% overlap averaged over 100 s, 2.5 s, & 0.1 s.

#### 4.1.3.3. Windowing of the iteration steps

To concentrate the iteration steps in their most valid frequency range, a weighting through a window function is applied. Note that the following window function is completely independent of the one used in the *pwelch* algorithm or described in 2.1.3.2! Also consider that in the following all  $Lxx$  are averaged vectors with the dimensions  $(f_m \times 1)$  as follows:

$$Lxx_j \equiv Lxx_{j,(f_m \times 1),avg} \quad (4.14)$$

The requirement for the weighting of the  $Lxx_j$  vectors relies on the quality of each vector, or more specifically, to its FFT data points. The quality is specified in relation

to all vectors produced by the iteration with the idea that massively averaged data may accidentally level-out signal peaks in low-frequency region due to the short effective time, whereas lightly averaged data is dominated by white noise in the high-frequency zone (compare figure 4.3). These aspects are solved by using a modified Tukey window<sup>3</sup>. The modification made is such that only the rising part of the also-called ‘tapered cosine window function’ is used to apply the weightings. Then it does not fall off again, because the information contained up to the Nyquist frequency has a better frequency resolution than that of the following, which are used for noise reduction. The function consists of three components: a preceding, a rising, and a subsequent part, which are controlled by a section start  $S$  and a safety factor  $\alpha$  as follows:

$$window_j(f_m) = \begin{cases} 0 & \text{if } f_m \leq \alpha \cdot S_j \\ r(f_m) & \text{if } \alpha \cdot S_j \leq f_m \leq 2\alpha \cdot S_j \\ 1 & \text{if } 2\alpha \cdot S_j < f_m \end{cases} \quad (4.15)$$

$$\begin{aligned} \text{with } j &= 1, \dots, \delta \\ \alpha &\equiv 10 \end{aligned} \quad (4.16)$$

where  $S_j$  is defined as the reciprocal of the duration  $T$  divided by the number of iterations  $D$  from equation (4.3):

$$S_j = \left(\frac{T}{D}\right)^{-1} \quad (4.17)$$

The rising part is given by the following  $r$  function as shown:

$$r(f_m) = 0.5 \cdot \left(1 - \cos\left(\pi \cdot \left(\frac{f_m}{\alpha \cdot S_j} - 1\right)\right)\right) \quad (4.18)$$

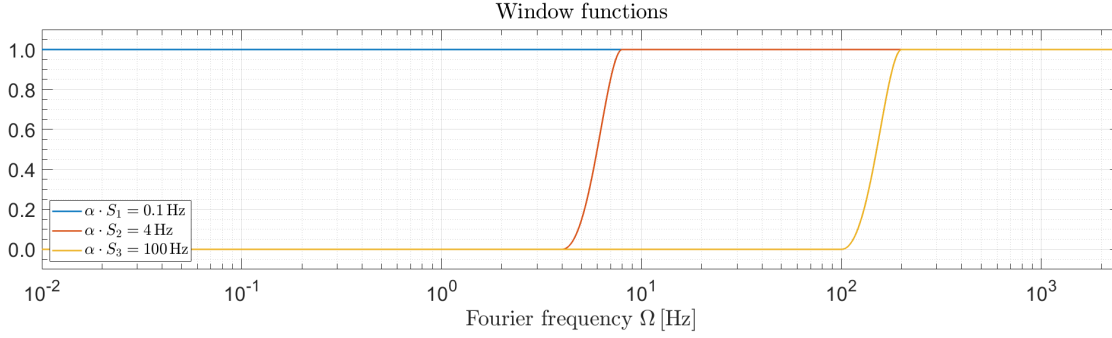
As equation (4.15) implies, the subsequent part of the window always equals 1, whereas the preceding part always equals 0 with the exception of the first iteration step which always equals 1. With  $\alpha$  defined as 10 an adequate area of the low-frequency range will be neglected due to insufficient data points (compare to equation (2.49)). Because of the modification to the Tukey window made in equation (4.15), the three parts are not equally distributed over the full window length. Taking equations (4.15) to (4.18) into account the resulting weighting window vector is defined as follows:

$$window_j(f_m) = \begin{pmatrix} w_{f_0} \\ \vdots \\ w_{f_{Ny}} \end{pmatrix} \quad (4.19)$$

Figure 4.8 plots the window functions  $window_j$  over  $f_m$  for the same data set used in the previous figures. The rising part starts at  $\alpha$  times  $S_j$  or in other words at  $\alpha$  times  $f_{j,res}$  (compare specifications in 4.1.3.1).

<sup>3</sup>Detailed information about the original *tukeywin* function syntax of MATLAB can be found on MathWorks: <https://de.mathworks.com/help/signal/ref/tukeywin.html>





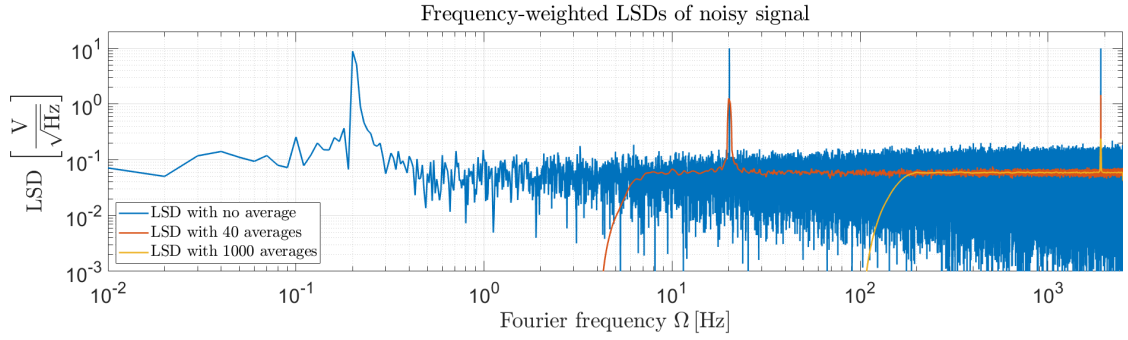
**Figure 4.8.:** Window functions for LSD of the example time series over 100 s, sampled with 5,000 Hz, and calculated with the *pwelch* function of MATLAB, a Kaiser window with a beta factor of 2.5, and with 1, 40, & 1000 averages each over 100 s, 2.5 s, & 0.1 s.

#### 4.1.3.4. Weighting

Before the data is weighted all  $Lxx_j$  vectors from equation (4.13) and the corresponding  $window_j$  vectors from equation (4.19) have to be interpolated to the same size ( $f_k \times 1$ ). Therefore, the  $f_m$  vector with the highest frequency resolution possible,  $j = 1$ , is used. It is worth noting that high frequency resolutions can produce very large matrices, which as a result can require immense computing power. Subsequently, the  $Lxx_j$  matrices can be convolved with the corresponding window function  $window_j$ . This means multiplying each element of the  $Lxx_{j,(f_k \times 1)}$  matrices by the corresponding element of the  $window_{j,(f_k \times 1)}$  matrices to receive weighted LSD matrices as follows:

$$\begin{aligned} Lxx_{j,(f_k \times 1),w} &= Lxx_{j,(f_k \times 1)} \circ window_{j,(f_k \times 1)} \\ &= \begin{pmatrix} lxx_{f_0} \\ \vdots \\ lxx_{f_{N_y}} \end{pmatrix} \circ \begin{pmatrix} w_{f_0} \\ \vdots \\ w_{f_{N_y}} \end{pmatrix} \end{aligned} \quad (4.20)$$

The result is shown in figure 4.9. Here, the first iteration step is executed completely, where the latter ones are only applied to the higher frequency. As figure 4.7 showed the information value of the each iteration step is now used in its most representative frequency region.



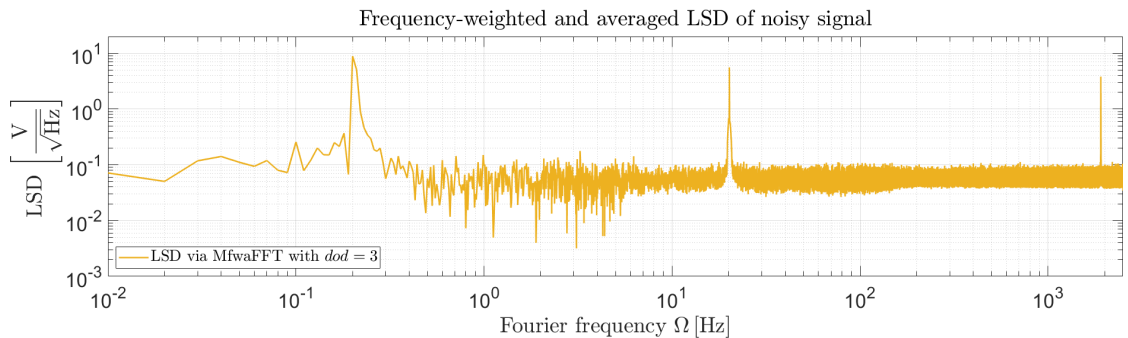
**Figure 4.9.:** Frequency-weighted LSDs of the example time series with 1, 40, and 1000 averages, a Kaiser window with a beta factor of 2.5, and 20% overlap averaged over 100 s, 2.5 s, & 0.1 s.

#### 4.1.3.5. Summing up

The last step to receive the final frequency-weighted and averaged continuous FFT is to sum up all iteration steps. Therefore all weighted LSD matrices are added to each other and afterwards divided by the sum of the window functions.

$$Lxx_{(f_k \times 1),w} = \sum_{j=1}^{\delta} Lxx_{j,(f_k \times 1),w} \circ \left( \sum_{j=1}^{\delta} window_{j,(f_k \times 1)} \right)^{-1} \quad (4.21)$$

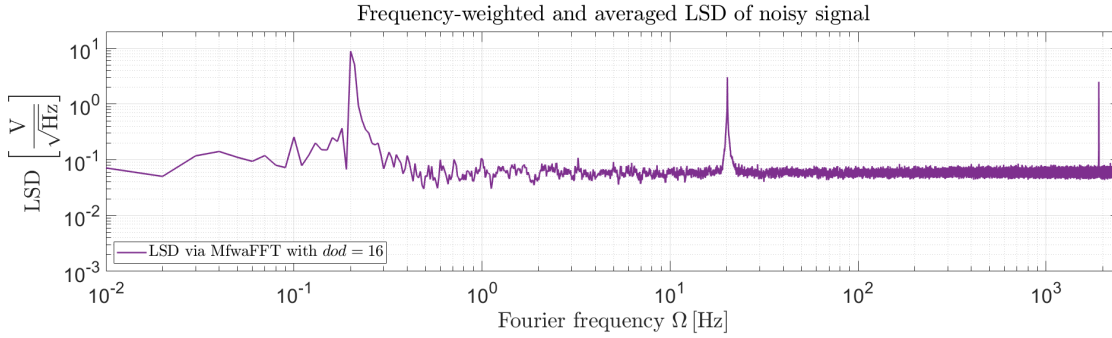
The result is shown in figure 4.10. Thus, the frequency resolution of the finest single FFT can be used, with the amplitude accuracy and suppression of frequency dispersion of each iteration step by reducing the white noise via averaging the data without levelling out signal peaks.



**Figure 4.10.:** Frequency-weighted and averaged LSD of the example time series with a Kaiser window with a beta factor of 2.5 and 20% overlap averaged over and a *dod* of 3.

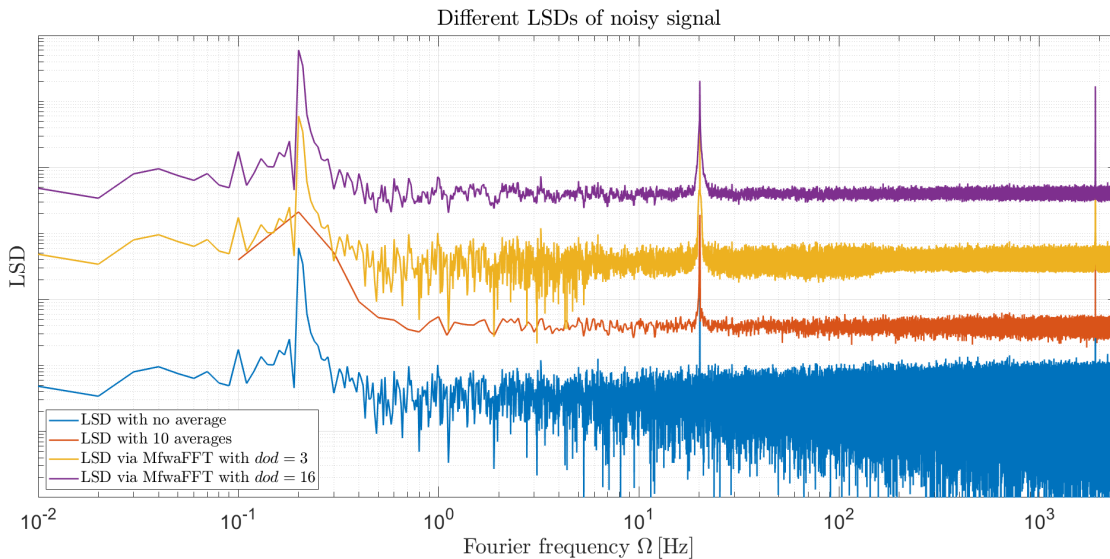
Figure 4.10 and the example described above only uses a *dod* of 3, which results in a very rough weighting. Figure 4.11 shows an FFT with a *dod* of 16. The resulting graph has much smoother transitions and a better white noise attenuation while only losing a factor of approximately 3 in the amplitude accuracy over four orders of magnitude.

#### 4.1. Method of frequency-weighted and averaged FFT



**Figure 4.11.:** Frequency-weighted and averaged LSD of the example time series with a Kaiser window with a beta factor of 2.5 and 20% overlap averaged over and a *dod* of 16.

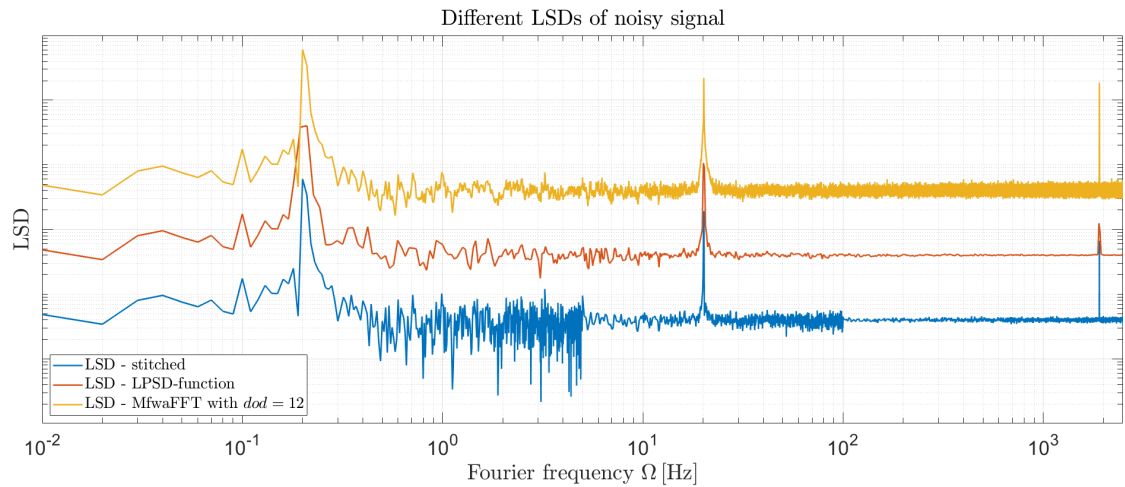
To distinguish the effect of the MfwaFFT and the *dod*, figure 4.12 shows four FFTs. The blue graph shows a FFT without any averages. The second, in red, has 10 averages that are each over a period of 10s as in figure 4.2. The last two are made with the MfwaFFT – here in yellow and magenta. The yellow one uses a *dod* of 3 and is the same as the graph from figure 4.10, where the magenta one uses the highest *dod* possible – here 16. The latter will increase the frequency accuracy over the broadband frequency range. For better visualisation, the FFTs are shifted so that they are displayed apart from each other by a factor of 10 on the y-axis.



**Figure 4.12.:** Comparison of different analysing methods of the example time series with a Kaiser window with a beta factor of 2.5 and 20% overlap: not averaged (blue), with 10 averages (red), and analysed with MfwaFFT with a *dod* of 3 (yellow) and with a *dod* of 16 (magenta).

To compare the different analysing methods, figure 4.13 presents the resulting LSDs of all three methods. In blue, the method of stitching adequate FFTs is shown (see

figure 4.4), in red the LPSD-function (see figure 4.6), and in yellow the MfwaFFT with a *dod* of 12, which is most suitable at 100 s from 0.01 Hz to 2,500 Hz.



**Figure 4.13.:** Comparison of frequency-weighted and averaged LSDs of the example time series with a Kaiser window with a beta factor of 2.5 and 20% overlap. Stitched (blue), LPSD-function (red), and analysed with MfwaFFT with a *dod* of 12 (yellow).

#### 4.1.4. Advantages and disadvantages

Obviously, there are quite some advantages in using the MfwaFFT opposed to stitching several FFTs to each other. First, there will be no change in the frequency resolution over the Fourier frequency indicated by the constant noise level of the LSD (compare with 2.1.4.1). This is clearly seen by comparing figures 4.4 to figures 4.10 to 4.13. Second, there are no jumps in the suppression of the white noise due to the different number of averages made over the FFT, that can cause errors in the subsequent analysis and interpretation. Last and most important is the gained objectivity in choosing the correct number of averages for the specific frequency range. Compared to the LPSD the retained amplitude accuracy and precision is also superior (compare figures 4.6 and 4.11 and figure 4.13).

As mentioned, the required higher power and the longer time needed for computing the FFT are the drawbacks. In summary, the MfwaFFT might not be a universal solution for all problems, but the easy adjustability and increase in value of the analysis performed outweigh the additional computation time needed. Standing to reason therefore, it is used in the analyses below.

#### 4.1.5. Discussion in the field of geodesy

The following literature provides background information for time series analysis in geodesy [35]. It deals with the ways how a time series can be represented in the time and frequency domain for data analyses. Furthermore it gives examples of how filters can

be set to a time series and it discusses the representation in the time-frequency domain (spectrogram). More specifically, amongst other things, it describes the basis of a spectral analysis similar to subsections 2.1.3 and 2.1.4. Here, the wavelet transformation is introduced, which uses time-localised waves in contrast to the Fourier transform. This allows the representation in the time-frequency domain with less computation power when examining known, non-sinusoidally shaped signals [35]. In real life though, the array of signals affecting an analysis can obscure the data set. The signals can be overlaid by unwanted frequencies and noise. This has already been discussed in the sections above. Though, a method was introduced by Ronald R. Yager, which provides estimates from existing measurements, which can be used as preliminary information for further analysis to reduce this problem [60] but nonetheless cannot completely dissipate all uncertainties as to how “clean” the analysed data is.

For more recent scientific findings, consult the “Journal of Time Series Analysis” [69] or via “International conference on Time Series Analysis and Forecasting” [62]. There are already quite a number of publications which describe advanced methods for pre-processing time series data. Some suggest using a Bayesian approach for clustering the data [71], other articles opt for utilising the Deep Learning [17] or the concept of the Mother Signal [14] in order to detect anomalies in the time series. Still others apply the usage of statistical methods to improve the output value, e.g. [75] with a class of spectral density kernel estimators based on the notion of a flattop kernel. As shown there are already quite a number of methods which have been developed and could be used to enhance time series analysis in general and some could even contribute to the MfwaFFT, though specific methods would need further scrutiny.

However, the application of a time series analysis over several orders of magnitude of the frequency spectrum as in MfwaFFT has not yet been carried out and published. Further advantages of this way of converting signals became apparent when the data was analysed. This is described in a previous subsection, 4.1.2, compare to the method of stitching and the LPSD algorithm [36]. In view of the conference program of the International Conference on Time Series and Forecasting (ITISE-2019) in September 2019, in addition to updates of existing studies, advanced methods and on-line learning in time series analysis with computational intelligence and Multiscaling with Complex/Big Data will be presented. These methods together with the ongoing advancement of computational power could further complement the MfwaFFT.

## 4.2. Measurement Preparation

This section describes the measurement preparations based on the selected measurement chain described in 3.2.1.3. Therefore, the (cross-)calibration of the seismic instruments stated in 3.2.1 will be presented in 4.2.1. Subsequently, an accuracy analysis is explained, which confirms the frequencies and amplitudes examined in 4.2.2 that were defined in 3.1.4.

### 4.2.1. Calibration of seismic devices

The following paragraphs contain the calibration settings for the seismometers as well as for the acquisition instruments which have been made for this study. The focus is on the Wilcoxon Research 731-207 accelerometer and the Tektronix Digital Phosphor Oscilloscope DPO7000, as these were selected as the most suitable devices (compare with 3.2.1.3.). The Güralp seismometers are not included in this section, as it is maintained and calibrated by the MEA group and in the following used for low-frequency measurements. Also not included is the ALPS II control signal, as it is well defined by the optics experts. Both sensors therefore are used to cross-calibrate the others listed in table 3.2 (see 4.2.1.2). The goal is to make the process more tangible and to convert all data in the right format to allow comparisons with older data<sup>4</sup>.

#### 4.2.1.1. Single instruments

First, each seismometer has to be calibrated into units of displacement. Therefore, the information from table 3.2 was used along with the specific calibration constant or curve of the respective data sheet.

The L-4C horizontal geophone is a velocity sensor as described in 3.2.1.1, which converts vibrations into an output signal in V proportional to the velocity of the ground movement. To get the correct calibration in units of velocity, it must be divided by the calibration curve in units of V/in/s. Figure C.1 in appendix C shows calibration curves for different impedance settings. For the measurements done within the ALPS II experiment curve A must be used. In order to obtain comparable data, it must be converted in m/s and then integrated to receive a displacement. The L-22D vertical geophone is also a velocity sensor as described in 3.2.1.1. For the correct velocity the data has to be divided by the transfer function in terms of V/m/s. Figure C.2 shows two calibration curves, here, the open (purple) curve must be used.

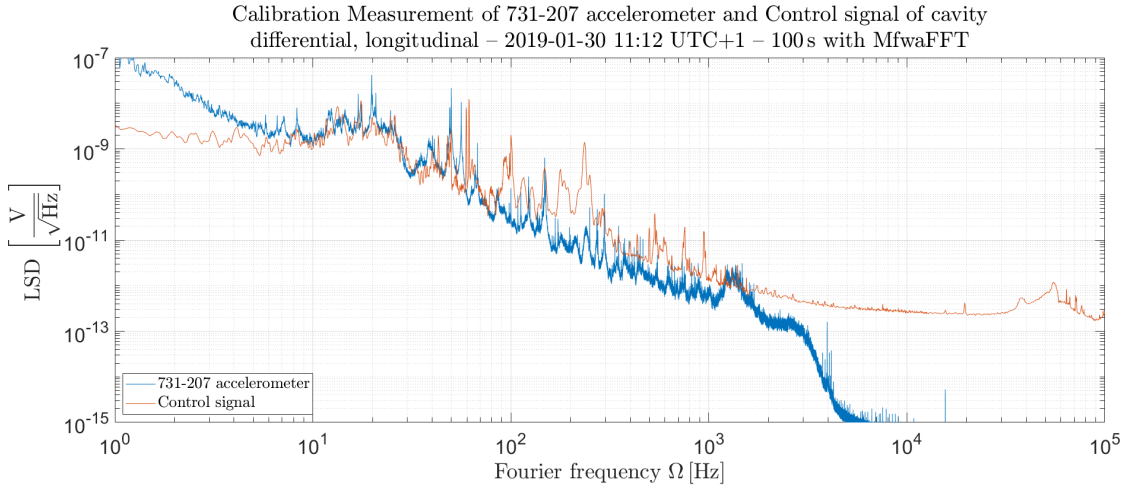
The Wilcoxon Research model 731-207 accelerometer measures the acceleration of a vibration with a sensitivity of 10 V/g [52]. As described in 3.2.1.1 it uses the Wilcoxon Research model P702B power unit and amplifier. To correctly measure the seismic noise, the data has to be divided by the set gain 1, 10, or 100 as well as the sensitivity of 10 V and multiplied by  $g = 9.81 \text{ m/s}^2$ . The signal is then present in units of acceleration in  $\text{m/s}^2$ . The conversion into displacement requires two integrations, with the amplifier being able to execute one integration using an internal integrator stage. This internally introduces an additional factor of 386.2, which results from the gravitational acceleration and the conversion from in to m [53].

#### 4.2.1.2. Cross-calibration

The following diagrams each show a cross-calibration of the selected 731-207 accelerometer with another seismometer (compare with 3.2.1.3). Figure 4.14 visualises a measurement of the RC with the blue line referring to a differential measurement with two

<sup>4</sup>e.g. seismic analysis made for the HERA ring accelerator since 2002: <http://vibration.desy.de/>.

731-207 accelerometers on the optical tables and the red being the control signal of the electronic set-up.



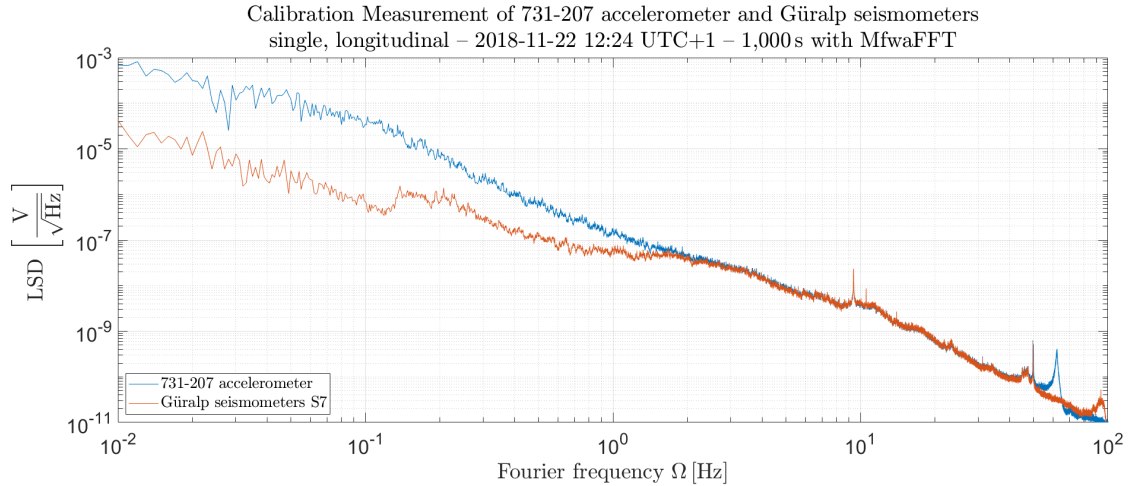
**Figure 4.14.:** Calibration chart: differential displacement LSDs of optical table in longitudinal direction on 2019-01-30 at 11:12 UTC+1 with 731-207 accelerometers and the RC control signal. Analysing characteristics: Kaiser window with a beta factor of 2.5 and 20% overlap; analysed with MfwaFFT with a *dod* of 12.

Since the control signal is closest to the actual displacement of the cavities, it is set as a reference value. However, it is only dominated by seismic noise in the lower frequency range. Above a frequency of 100 Hz further disturbances (electronic and laser noise) are included, which can not show up in the pure seismic signal (compare with 3.2.1.1). Thus, assuming that the mirror mountings do not attenuate the vibration, the control signal must be higher than the pure seismic noise. This is only true up to 100 Hz due to the fact that the control signal is already subject to filtering (see subsection 4.4.2).

Considering the differences of both sensors, figure 4.14 still illustrates the overlaying in the frequency range from 10 Hz to 100 Hz. Above 2,000 Hz the natural response falsifies the result of the accelerometer. Between 100 Hz and 2,000 Hz the difference is explainable by the above mentioned additional disturbances in the control signal. Due to the similarity, the accelerometer signal will be used up to 2,000 Hz.

Next, the lower frequency limit will be examined. Hence, a comparison to a Gralp seismometer is made. Figure 4.15 shows a simultaneous measurement of both sensors (blue: accelerometer; red: seismometer) from 0.01 Hz up to 100 Hz for a measurement time of 1,000s. The measurement was carried out in the HERA North West Tunnel on the concrete tunnel elements. Therefore, it was not possible to ensure adequate mounting for the acceleration sensor, which means that the data has an upper bound of approximately 100 Hz (see 4.2.2.1).

The figure shows congruent results between the frequencies of 2 Hz and 50 Hz. The peak around 60 Hz is assumed to be a real signal that the seismometer for some reason



**Figure 4.15.:** Calibration chart: single displacement LSDs of HERA North West Tunnel in longitudinal direction on 2018-11-22 at 12:24 UTC+1 with a 731-207 accelerometer and a Güralp seismometer. Analysing characteristics: Kaiser window with a beta factor of 2.5 and 20% overlap; analysed with MfwaFFT with a *dod* of 16.

did not pick up<sup>5</sup>. Thus, the independent measurement chains are validated and the instruments are cross-calibrated. The lower limit of the accelerometer therefore can be set to 2 Hz.

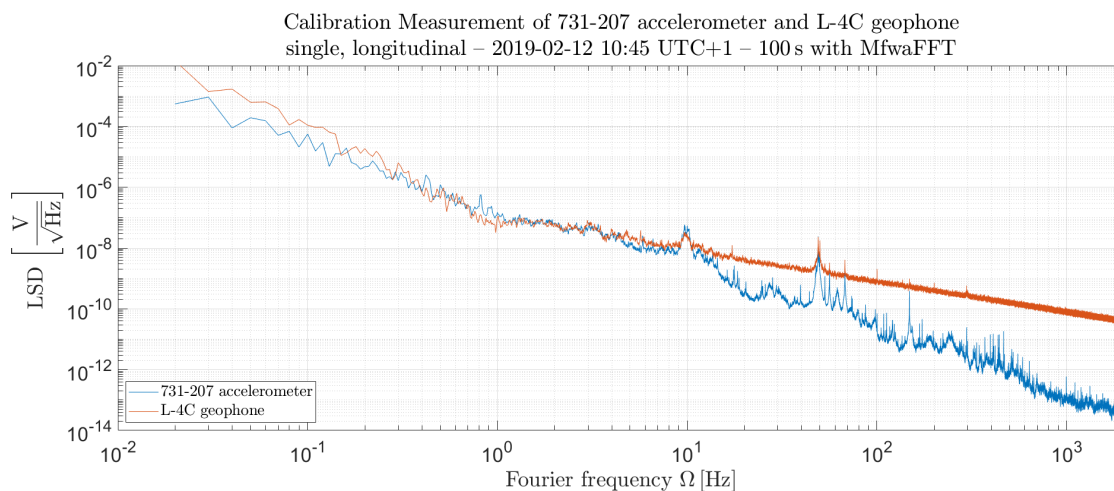
In addition, two cross-calibrations with the geophones were made. Figure 4.16 presents a simultaneous measurement of the accelerometer with the L-4C horizontal and figure 4.17 with the L-22D vertical geophone. Both diagrams show the accelerometer in blue and the geophone in red.

For both geophones, the overlaying part with the accelerometer is comparatively small. The geophones show similar results as the accelerometer between 0.1 Hz and 10 Hz. Below 1 Hz, the data is not valid due to the low sensitivity of the sensors. Since the SNR of the geophones is very low, signals above 10 Hz are only visible if they are well pronounced, e.g. the 50 Hz peak.

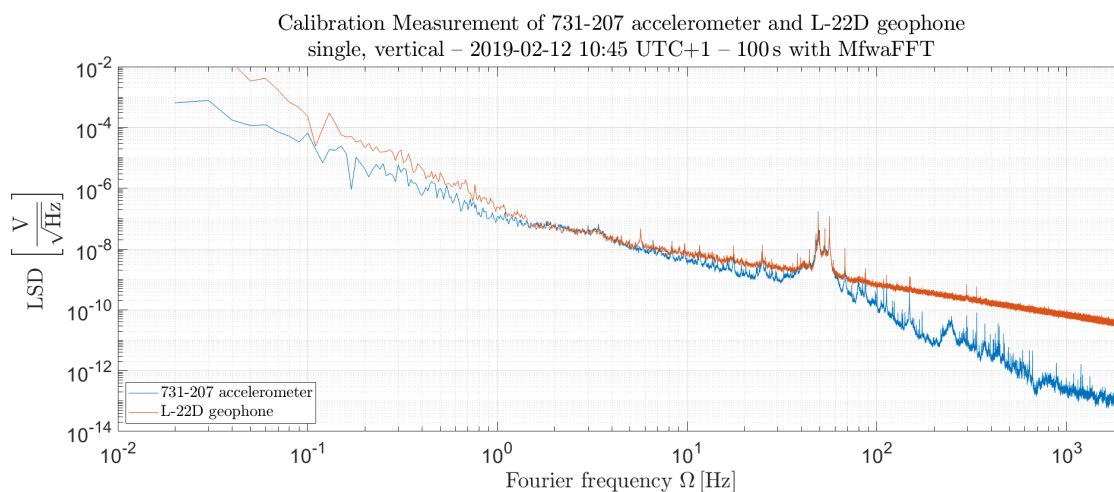
<sup>5</sup>MEA often sees a natural response around 80 Hz, even if the sensor should be valid up to 100 Hz



## 4.2. Measurement Preparation



**Figure 4.16.:** Calibration chart: single displacement LSDs of optical table horizontal on 2019-02-12 at 10:45 UTC+1 with a 731-207 accelerometer and a L-4C geophone. Analysing characteristics: Kaiser window with a beta factor of 2.5 and 20 % overlap; analysed with MfwaFFT with a *dod* of 12.



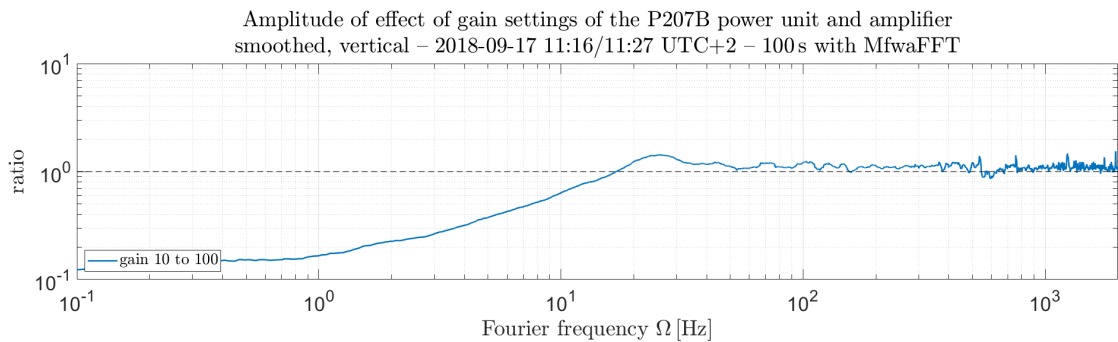
**Figure 4.17.:** Calibration chart: single displacement LSDs of optical table vertical on 2019-02-12 at 10:45 UTC+1 with a 731-207 accelerometer and a L-22D geophone. Analysing characteristics: Kaiser window with a beta factor of 2.5 and 20 % overlap; analysed with MfwaFFT with a *dod* of 12.

## 4.2.2. Accuracy analysis

As described in the subsection above (compare subsection 4.2.1), the in subsection 3.1.4 required frequency range can be detected with the selected measurement chain from 3.2.1.3. The following paragraphs discuss the validity of the data acquired and analysed. Therefore, the accuracy and precision of the measuring devices used, will be investigated in 4.2.2.1 and the digital uncertainties and errors occurring from the analysis in 4.2.2.2.

### 4.2.2.1. Measuring device accuracy and precision

Based on the results of the cross-calibration (compare subsection 4.2.1), the sensitivity of the 731-207 accelerometer is examined. For this purpose, two measurements were carried out with two accelerometers screwed onto an optical table, once with a gain setting of the P207B power unit of 100 and once with 10. To examine the noise floor the differential signals of the simultaneous measured time series are compared to each other. The resulting analysed spectra are presented in figure C.3 in appendix C. More of interest is the effect on the noise floor depending on the gain setting. Since the differential signal of the simultaneously used accelerometers next to each other represent the noise floor of the devices, figure 4.18 shows a smoothed ratio of the differential signal with a gain of 10 to the one with a gain of 100.

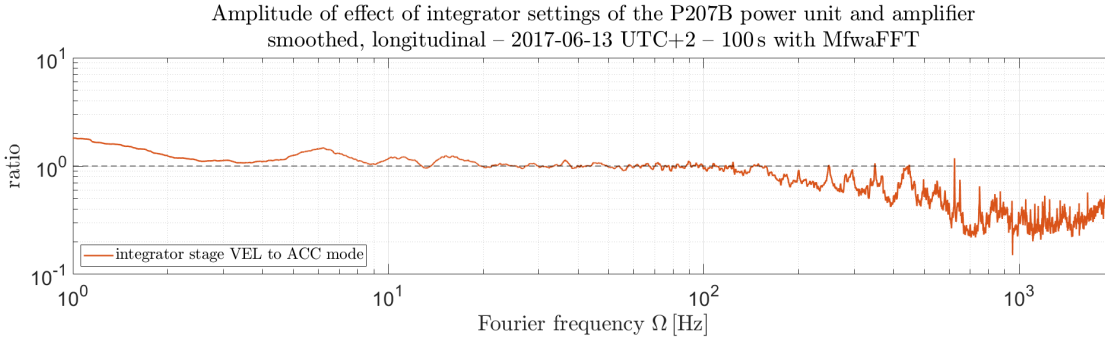


**Figure 4.18.:** Sensitivity measurement of 731-207 accelerometer with P702B power unit and amplifier – effect on the noise floor with a gain of 100 divided by a gain of 10 in vertical direction on 2018-09-17 at 11:16/11:27 UTC+2. Analysing characteristics: Kaiser window with a beta factor of 2.5 and 20 % overlap; analysed with MfwaFFT with a *dod* of 12.

The line begins to decrease below 20 Hz, which means that the noise floor is higher when a lower gain setting is used, and stagnates under 1 Hz, where other effects play a role. Hence, in the following a high gain setting is desirable. Note that it is limited by the input range of the acquisition device.

Furthermore, the integrator stage of the P207B power unit and amplifier was investigated. Therefore, a simultaneous measurement with one accelerometer in ACC mode and another in VEL mode was performed. The result is shown in figure C.4 in appendix C. The effect of not using the integrator stage, meaning acquiring the signal in units of acceleration, instead of applying it, is presented in figure 4.19 by plotting the ratio of the signal in VEL mode to the signal on ACC mode.

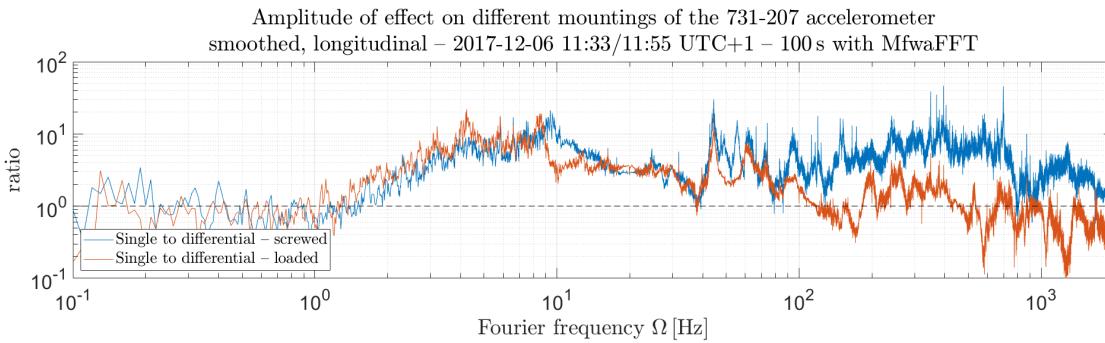
## 4.2. Measurement Preparation



**Figure 4.19.:** Sensitivity measurement of 731-207 accelerometer with P702B power unit and amplifier – effect on measurement in VEL mode to ACC mode in longitudinal direction on 2017-06-13 UTC+2. Analysing characteristics: Kaiser window with a beta factor of 2.5 and 20 % overlap; analysed with MfwaFFT with a *dod* of 12.

The graph shows a value higher than 1 in the frequency region below 2 Hz, which refers to a higher SNR when the integrator is not used, whereas the value decreases above 100 Hz, which refers to a lower SNR. Consequently, the integrator stage should be used if frequencies under 1 Hz are investigated and not if frequencies over 100 Hz are of interest.

In addition, the 731-207 accelerometer was expected to require a fixed mount to perform well at high frequencies. To examine the effect, a measurement with two accelerometers one screwed and one loaded with weights onto an optical table was carried out. The resulting spectra are shown in figure C.5 in appendix C. Again, since the differential signal of the simultaneously used accelerometers next to each other represents the noise floor, plotting the transfer function of a single measurement to the differential one shows the distance from the signal to the noise floor. This is visualised in figure 4.20, with the blue line referring to the accelerometers being screwed onto the optical table and the red line to the devices being loaded by the weights.

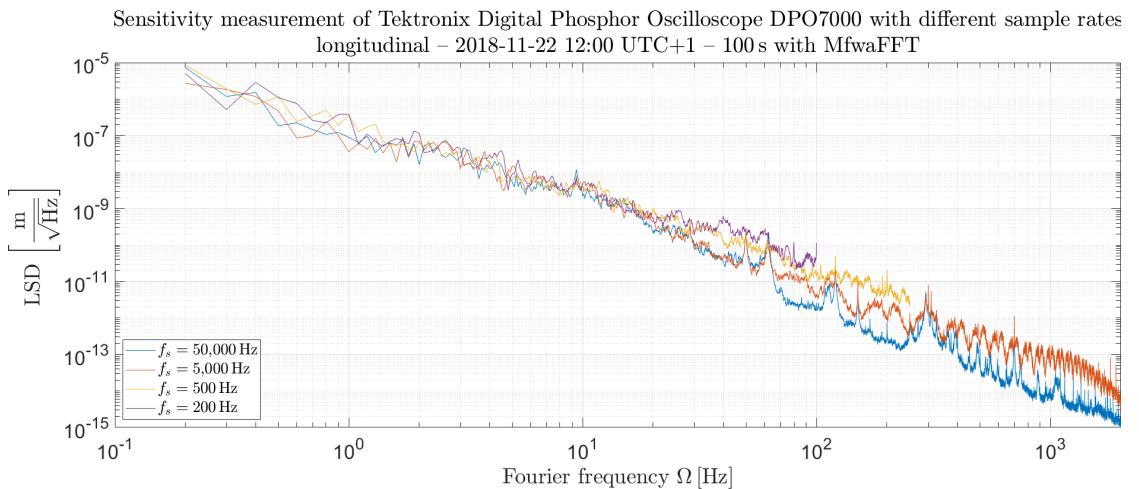


**Figure 4.20.:** Sensitivity measurement of 731-207 accelerometer with different mountings in longitudinal direction on 2018-12-06 11:33/11:55 UTC+1. Analysing characteristics: Kaiser window with a beta factor of 2.5 and 20 % overlap; analysed with MfwaFFT with a *dod* of 12.

Apart from small deviations and a significant anomaly at 10 Hz due to temporary

running pumps, the red line shows a drop in the sensitivity above 100 Hz. This can be explained by the effect of introducing resonances due to the non-rigid mounting (compare with 2.1.1.2). Thus, the device should always be correctly mounted onto the object that is examined.

Besides the seismometers, the acquisition devices can influence the signal as well. Therefore, the digitalisation and quantisation errors of the Tektronix Digital Phosphor Oscilloscope DPO7000 were examined. These are two effects, which depend on the one hand on the selected sampling frequency and on the other hand on the bit resolution chosen. First, the sampling frequency is investigated. Therefore, a measurement with a 731-207 accelerometer was acquired with four different sample frequencies from 200 Hz to 50 kHz. This is shown in figure 4.21.



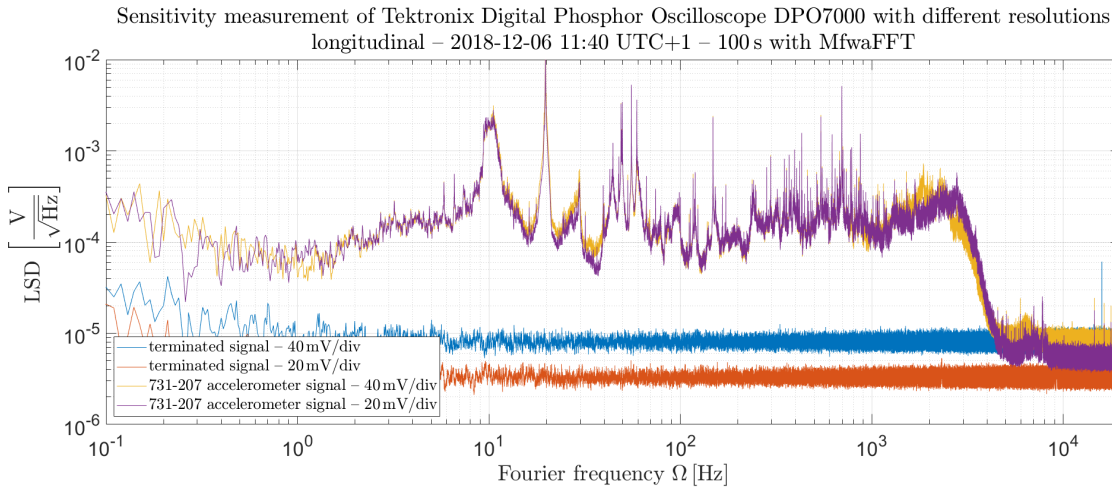
**Figure 4.21.:** Sensitivity measurement of Tektronix Digital Phosphor Oscilloscope DPO7000 with different sample frequencies in longitudinal direction on 2018-11-22 12:00 UTC+1. Analysing characteristics: Kaiser window with a beta factor of 2.5 and 20 % overlap; analysed with MfwaFFT with a *dod* of 9.

Apart from the high frequency cut at the Nyquist frequency (compare with 2.1.3.1), a decrease in sensitivity and the occurrence of aliasing effects are visible with decreasing sampling rates. This effect is called digitalisation error. Therefore, a sample frequency as high as necessary without wasting memory should be used. In the specific case, 50 kHz is a good compromise for investigating frequencies above 50 Hz.

The second effect referring to the resolution chosen is directly connected to the SNR, but bound to the amplitudes of the signal. With a high resolution, e.g. 20 m/div (small number per division), a finer classification of the signal can be made. However, noise spikes are faster outside the measurement range, which should be prevented to avoid aliasing effects. Therefore, depending on the prevailing seismic noise, the resolution should be as low as possible. Figure 4.22 shows two signals terminated by a 50  $\Omega$  resistor. The blue line was acquired with a resolution of 40 mV/div and the red with 20 mV/div. Corresponding signals detected with a 731-207 accelerometer are visualised in yellow and magenta. To enable the comparison to the terminated signals, the data is not calibrated

## 4.2. Measurement Preparation

in terms of  $V/\sqrt{\text{Hz}}$  on the y-axis.



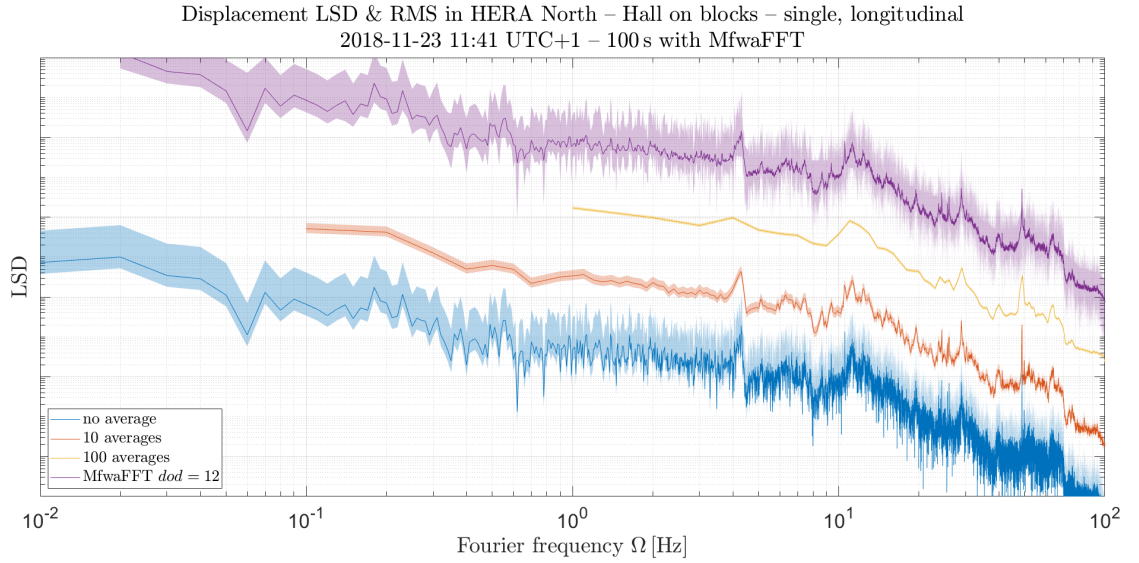
**Figure 4.22.:** Sensitivity measurement of Tektronix Digital Phosphor Oscilloscope DPO7000 with different resolutions in longitudinal direction on 2018-12-06 11:40 UTC+1. Analysing characteristics: Kaiser window with a beta factor of 2.5 and 20% overlap; analysed with MfwaFFT with a *dod* of 12.

The difference between the blue and the red line indicates the different sensitivity due to the resolution. The effect is called quantisation error. With a dominant signal as shown in the figure, the effect becomes critical only at very high frequencies. However, the resolution of the oscilloscope with the gain of the amplifier must be adjusted to the given seismic noise and always set as high as possible.

### 4.2.2.2. Digital uncertainties and errors

As shown in subsection 2.1.3 and section 4.1 an FFT always introduces a trade-off between the correct frequency resolution, amplitude accuracy, and suppression of frequency dispersion. This effect was already explained and sufficiently resolved by using the MfwaFFT. In addition, as using the *pwelch* function of MATLAB a confidence interval of the generated spectrum can be calculated. Figure 4.23 shows confidence intervals of 95% of an example measurement with three different averages and one with the MfwaFFT applied (magenta). For better visualisation, the FFTs are shifted so that they are displayed apart from each other by a factor of 10 on the y-axis.

The coloured areas indicate the confidence intervals of 95%. Since MfwaFFT also uses the data from the non-averaged LSD, its variance is similarly high, while it decreases linearly with the number of averages. The confidence interval extends over an order of magnitude, which makes the RMS more critical.



**Figure 4.23.:** Confidence intervals of single displacement LSDs of HERA North Hall in longitudinal direction on 2018-11-23 at 11:41 UTC+1. Analysing characteristics: Kaiser window with a beta factor of 2.5 and 20% overlap; analysed with MfwaFFT with different averages and a *dod* of 12.

### 4.3. Seismic measurements on-site

In the next section, the seismic noise measurements are described in the manner indicated above, which are necessary for the ALPS II experiment to meet the requirements outlined in subsection 3.1.4. Hence, the measurement results are presented by splitting them into on-site ground conditions in 4.3.1, optic-related components of ALPS II in 4.3.2, and associated noise sources in 4.3.3.

#### 4.3.1. On-site noise conditions (HERA)

Since ALPS II is or will be located in the HERA hall and tunnel, this subsection examines the seismic noise present there. HERA was the largest particle storage ring accelerator at DESY and also the largest research instrument in Germany with over 6.2 km in total length. From 1992 until 2007 it was used to study electron-proton collisions. It has an almost circular-shaped form with four approximately 300 m long straight sections, each with an experimental hall in the middle. These halls are named after their cardinal directions. The ALPS IIa laboratory for example is located in the HERA West Hall, where the ALPS IIc experiment will be situated in the straight section of HERA North. Therefore, these two locations will be examined below. In addition, HERA South is used as a reference, since it already has a stable construction between the two tunnel entrances that could possibly be used in HERA North for ALPS IIc.

All spectral plots below are calibrated measurements and represent the displacement in a double logarithmic scale with the LSD on the left y-axis in  $\text{m}/\sqrt{\text{Hz}}$ , the RMS on

the right y-axis in m, and the Fourier frequency  $\Omega$  on the x-axis in Hz as described in 3.2.2.2 and 4.2.1. Here, the solid line refers to the LSD and the dashed to the RMS. The most precise and accurate results were achieved with a Kaiser window with a beta factor of 2.5 and 20 % overlap as described in subsection 2.1.3. These settings were used predominantly. In addition, MfwaFFT was used to analyse the data over its broadband frequency range as explained in section 4.1. Further information about location, measurement time, sample frequency, instruments used, and specifications of the analysis will be explained in the text or can be found in the specific figure caption.

All measurements describe the conditions at the locations in their current state. To compare the measurements from ALPS IIa to ALPS IIc, adjustments will be made based on further analyses. These are done on the optical tables, the magnet girders, and on the Filter Fan Units (FFUs) and are described in subsection 4.3.2. Afterwards, transfer functions are generated and folded into the measured signals in section 4.4.

#### 4.3.1.1. ALPS IIa laboratory (HERA West)

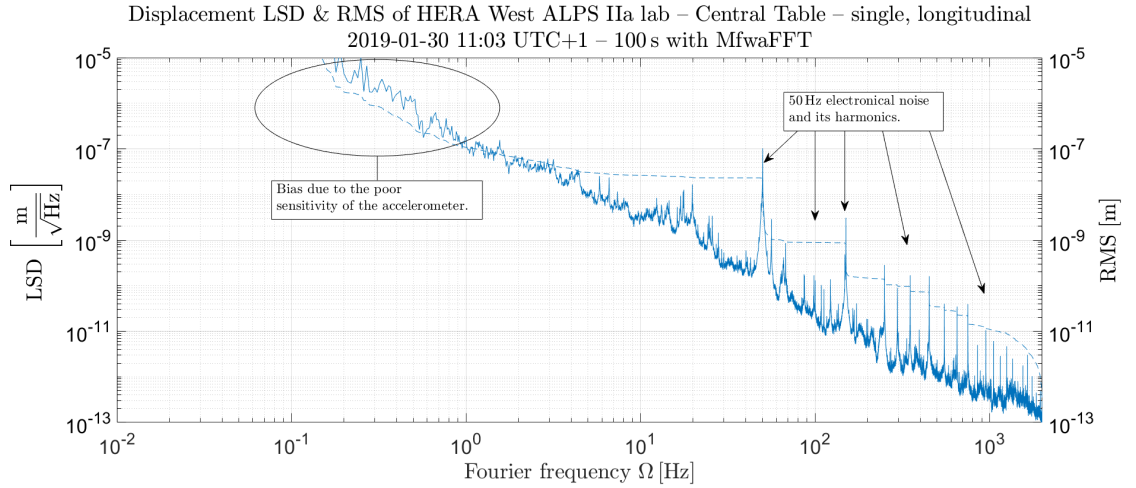
This paragraph describes the seismic noise conditions of the ALPS IIa laboratory in its current state. The measurements shown below were carried out with the 731-207 accelerometer on ACC mode with an amplification of 10 and were acquired with the Tektronix Digital Phosphor Oscilloscope DPO7000 with a resolution of 40 mV/div (compare section 3.2). To achieve the best fitting result for the future ALPS IIc set-up, the measurements were taken on the optical tables as close as possible to the cavity mirrors.

Therefore, all three tables were investigated in the longitudinal direction, as this is the most critical (compare section 3.1). The sensors were placed next to the vacuum tank where the mirror is located with the flow boxes turned off, since they produce noise that will not be present in the final design (see 4.3.3.2). For the central measurement, the sensor had to be placed on the central table where the CBB is mounted on, as this is not accessible (compare with 3.1.5).

Figure 4.24 presents a single measurement in the HERA West Hall in the ALPS IIa laboratory on the Central Table in longitudinal direction referring to the CBB. The measurement was acquired with the oscilloscope set to 50 kHz sampling frequency over 100 s. Afterwards, it was analysed with MfwaFFT with a Kaiser window with a beta factor of 2.5 and 20 % overlap.

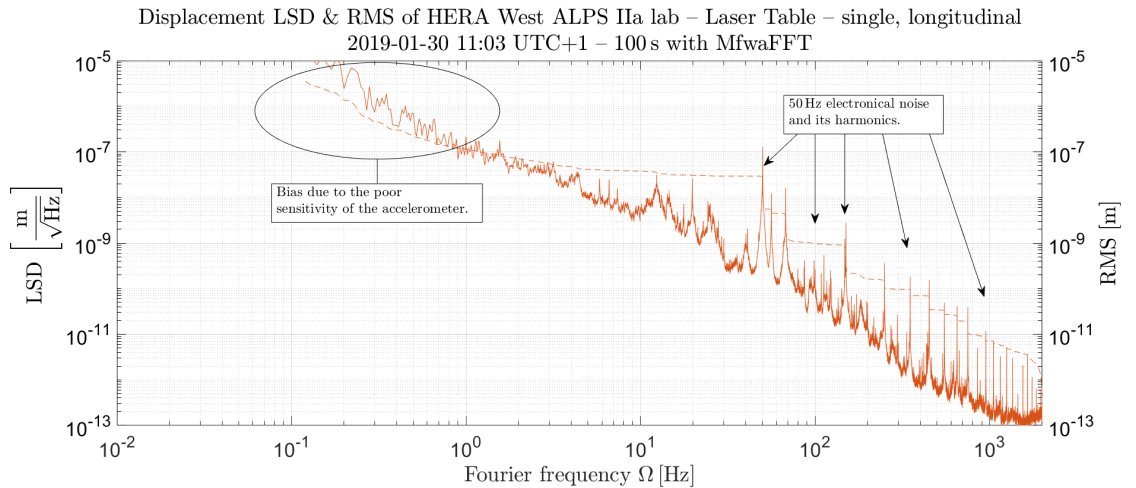
Three features are visible in the plot. First, the line shows a bias in the low-frequency region below 2 Hz. This is in contrast to the valid frequency range given in table 3.2 from the data sheet. Owing to the low signal or the low sensitivity of the sensor (compare with 4.2.1.2), the result is limited to frequencies above 2 Hz. Second, there are fine peaks starting at 50 Hz due to the power supply frequency and its harmonics (compare with 2.2.2.3). Third, all wide peaks, especially between 1 Hz and 100 Hz, are attributable to the table, instruments on it, or machines within the building (compare with 2.2.2.2). These are vibrations that need to be investigated.

To obtain a signal such as an optical resonator could detect, the seismic noise of the other tables had to be considered as well. Therefore, a simultaneous measurement of the longitudinal displacement with the same settings on the Laser Table was carried out.



**Figure 4.24.:** Single displacement LSDs & RMSs of HERA West ALPS IIa laboratory Central Table in longitudinal direction on 2019-01-30 at 11:03 UTC+1. Analysing characteristics: Kaiser window with a beta factor of 2.5 and 20% overlap analysed; with MfwaFFT with a *dod* of 12.

The resulting LSD and RMS are visualised in figure 4.25.

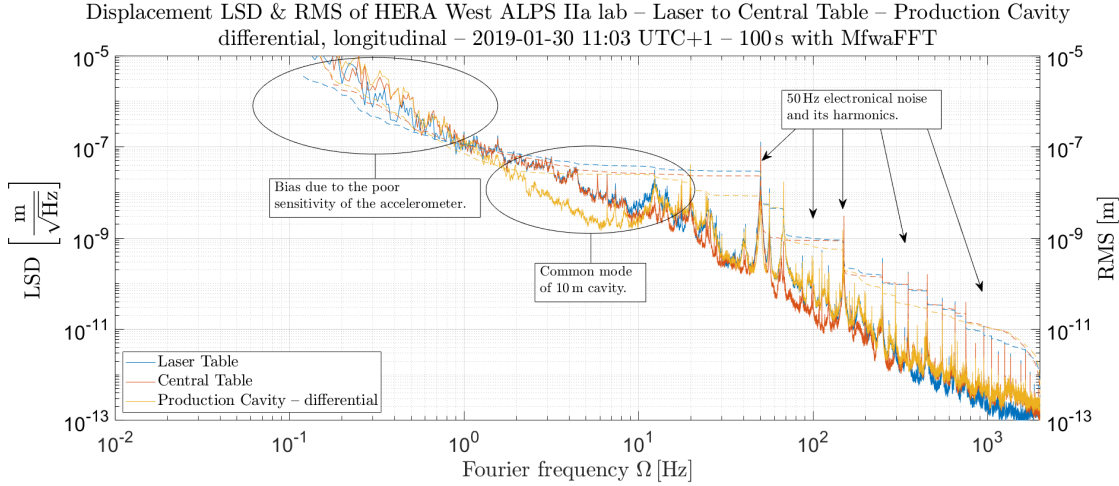


**Figure 4.25.:** Single displacement LSD & RMS of HERA West ALPS IIa laboratory Laser Table in longitudinal direction on 2019-01-30 at 11:03 UTC+1. Analysing characteristics: Kaiser window with a beta factor of 2.5 and 20% overlap; analysed with MfwaFFT with a *dod* of 12.

Here, nearly the same peculiarities as in the previous plot can be observed. This is owing to the concrete foundation used in the ALPS IIa laboratory. Only slight changes in the amplitudes or shifts in the frequency of the broad peaks between 10 Hz and 100 Hz become apparent. These can be ascribed to the different anchors of the optical tables (compare with 4.3.2.1).



Now, comparing the difference of the two simultaneously measured signals creates the relative signal of those locations. Hence, to represent the PC, the signal of the Central Table was subtracted from that of the Laser Table in the time domain and then analysed to obtain the displacement LSD and RMS. This is visualised in figure 4.26, where the blue line refers to the Laser Table, the red line to the Central Table, and the yellow line represents the differential seismic signal the PC would detect.



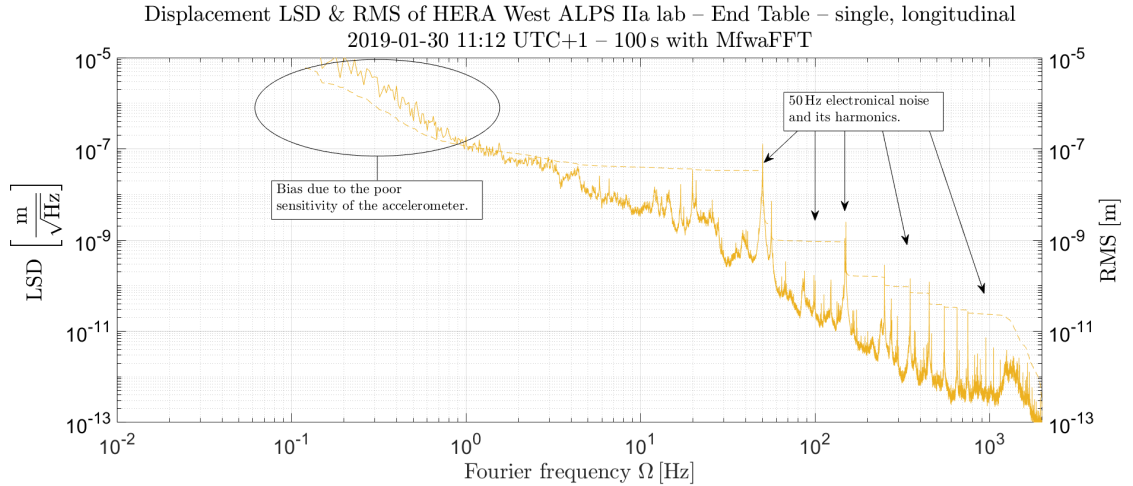
**Figure 4.26.:** Differential displacement LSDs & RMSs of HERA West ALPS IIa laboratory Laser to Central Table (PC) in longitudinal direction on 2019-01-30 at 11:03 UTC+1. Analysing characteristics: Kaiser window with a beta factor of 2.5 and 20% overlap; analysed with MfwaFFT with a *dod* of 12.

The differential signal assumes the value of the higher signal if the signals are independent. Whereas signals negate each other if they hit both sensors at the same time. This can be observed in the graph below 10 Hz. Thus, that effect is defined as a common mode. The lines below 1 Hz appear to mix again, which can be owing to the sensitivity of the accelerometer or the resolution of the oscilloscope (compare with 4.2.2.2).

The RMS, which determines the requirement, is dominated by the 50 Hz peak and its higher harmonics. Here, it is a combination of the narrow electronic and the wide mechanical noise peaks. The undamped pure seismic noise RMS, as it is shown here, is raised from  $10^{-10}$  m at 200 Hz up to  $8 \cdot 10^{-9}$  m at 50 Hz. That is a factor of 80 and therefore defines the most critical frequency range in the pure seismic noise of the PC. The peaks around 10 Hz again raise the RMS by a factor of 2, which should not be ignored either.

To obtain the relative signal of the RC, another measurement was carried out. Therefore, the data was acquired with 50 kHz over 100 s and analysed with MfwaFFT with a Kaiser window with a beta factor of 2.5 and 20% overlap in the same way as for the PC measurement. The single noise spectrum of the Central Table did not show any differences to the first measurement, whereas the displacement on the End Table is presented in figure 4.27.

The spectrum of the last table shows similar properties to the other single measure-



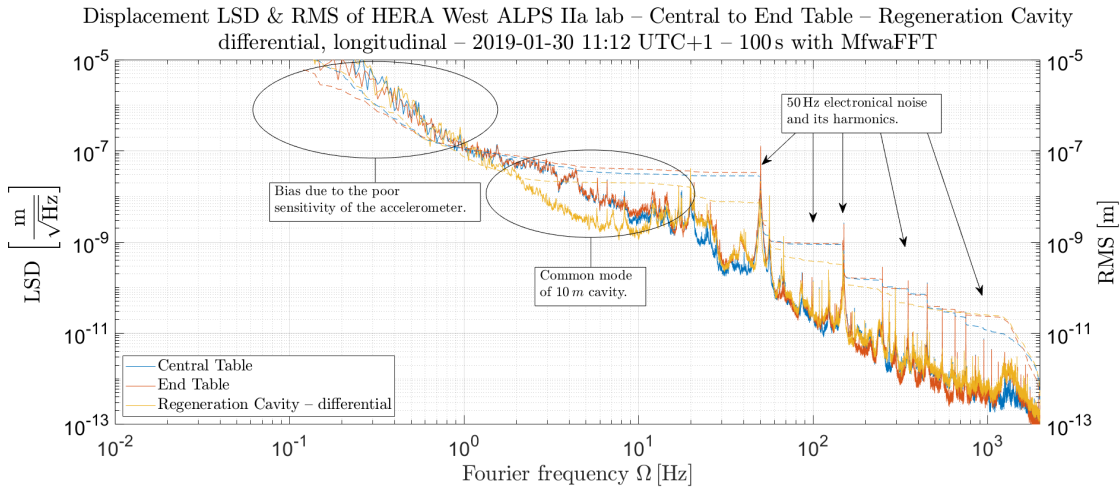
**Figure 4.27.:** Single displacement LSDs & RMSs of HERA West ALPS IIa laboratory End Table in longitudinal direction on 2019-01-30 at 11:12 UTC+1. Analysing characteristics: Kaiser window with a beta factor of 2.5 and 20% overlap; analysed with MfwaFFT with a *dod* of 12.

ments described above (compare with figures 4.24 and 4.25). Additionally, it shows a wide resonance above 1 kHz. This might be explained by the fact that the table is closest to the wall of the hall, which leads to a more stable ground and thus to a better transformation of the higher frequencies. On the other hand, it also leads to a lower vibration capability in the lower frequencies.

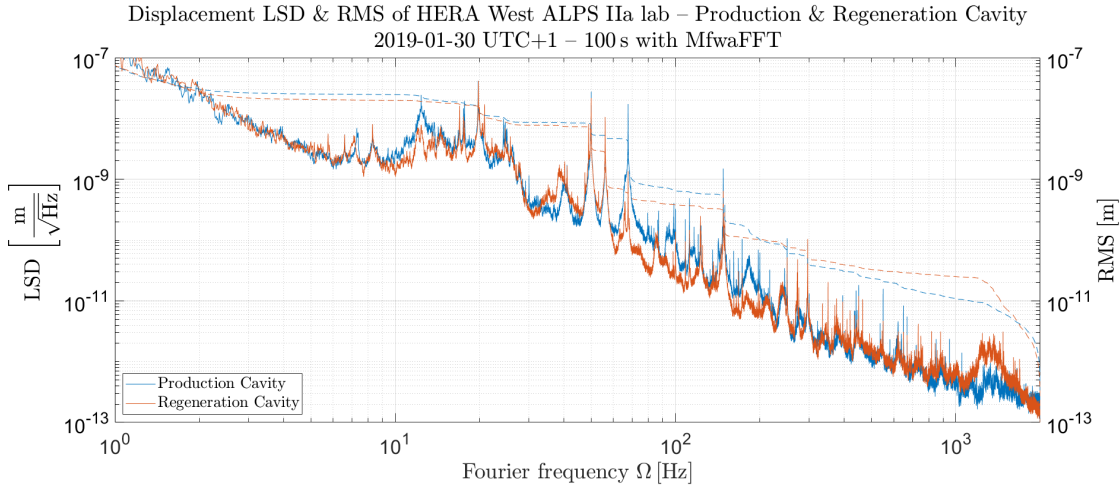
The differential signal of the RC then is visualised in figure 4.28, with the blue line referring to the Central Table, the red line to the End Table, and the yellow line to the differential signal of the RC.

Likewise to figure 4.26, the common mode is visible below 10 Hz and the combination of the narrow electronic and the wide mechanical noise peaks above 10 Hz affect the RMS. The most critical frequency range for the RC is defined from 150 Hz to 50 Hz by an increase of the RMS value of approximately 70.

For a better comparison both cavities are plotted in figure 4.29 in their valid frequency range from 1 Hz to 2,000 Hz. This figure represents the pure undamped seismic noise that affects the ALPS IIa optical cavities. In section 4.4 it is used to compare ALPS IIa with ALPS IIc.



**Figure 4.28.:** Differential displacement LSDs & RMSs of HERA West ALPS IIa laboratory Central to End Table (RC) in longitudinal direction on 2019-01-30 at 11:12 UTC+1. Analysing characteristics: Kaiser window with a beta factor of 2.5 and 20% overlap; analysed with MfwaFFT with a *dod* of 12.



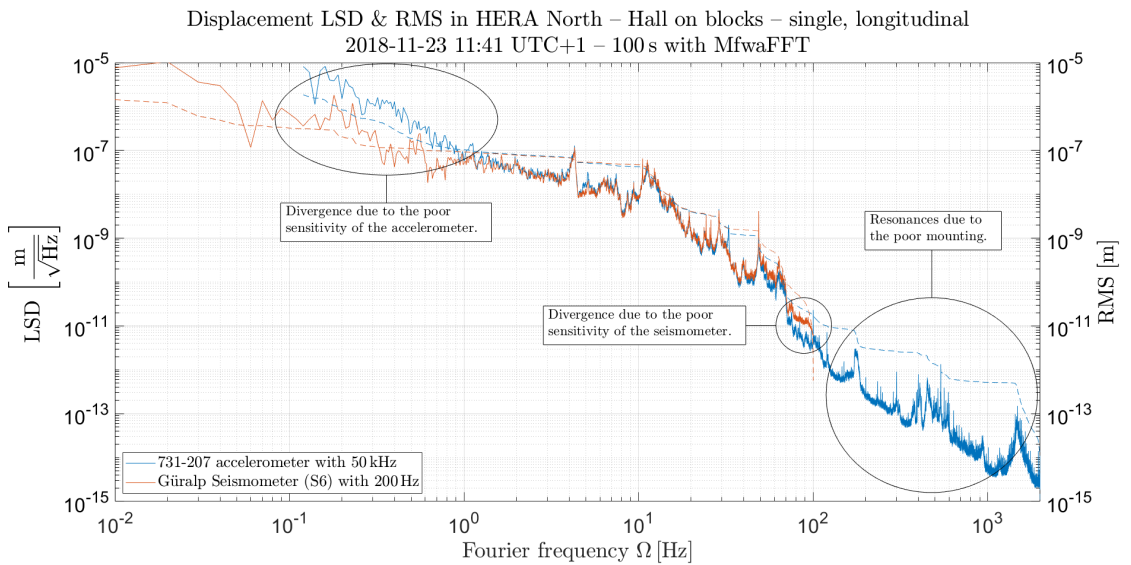
**Figure 4.29.:** Differential displacement LSDs & RMSs of HERA West ALPS IIa laboratory Production and Regeneration Cavity on 2019-01-30 UTC+1. Analysing characteristics: Kaiser window with a beta factor of 2.5 and 20% overlap; analysed with MfwaFFT with a *dod* of 12.

### 4.3.1.2. ALPS IIc site (HERA North)

Compared to ALPS IIa, the future ALPS IIc laboratory does not yet have an infrastructure as reported in section 3.1.5. Therefore, the measurements could only be taken from the floor of the hall or the tunnels and not from (or only close to) the final mirror positions. To obtain information for the final set-up, various transfer functions have to be applied. This will be explained in subsection 4.4.1. All measurements below were taken with the 731-207 accelerometer on ACC mode with an amplification of 100 and were acquired with the Tektronix Digital Phosphor Oscilloscope DPO7000 or with a Güralp Seismometer *S6* or *S7* with its own acquisition system (compare with 3.2.1.3) to achieve a broadband seismic noise spectrum.

In total, four different points were examined. These are the three positions of the future clean rooms, two approximately 100 m inside the tunnels<sup>6</sup> on the concrete tunnel elements and one in the hall between the tunnels – here, on stacked concrete blocks. The fourth is on the floor of the hall as a reference to the concrete blocks and its support structure.

Starting with a single measurement in the HERA North Hall in longitudinal direction, meaning measuring the vibration of the concrete blocks, where the central ALPS IIc clean room will be located. Figure 4.30 shows the displacement in two lines over the frequency. The blue line refers to the accelerometer data which was acquired with the oscilloscope with 50 kHz at 40 mV/div resolution, where the red line refers to the seismometer data acquired with 200 Hz.



**Figure 4.30.:** Single displacement LSDs & RMSs of HERA North Hall in longitudinal direction on 2018-11-23 at 11:41 UTC+1. Analysing characteristics: Kaiser window with a beta factor of 2.5 and 20% overlap; analysed with MfwaFFT with a *dod* of 12.

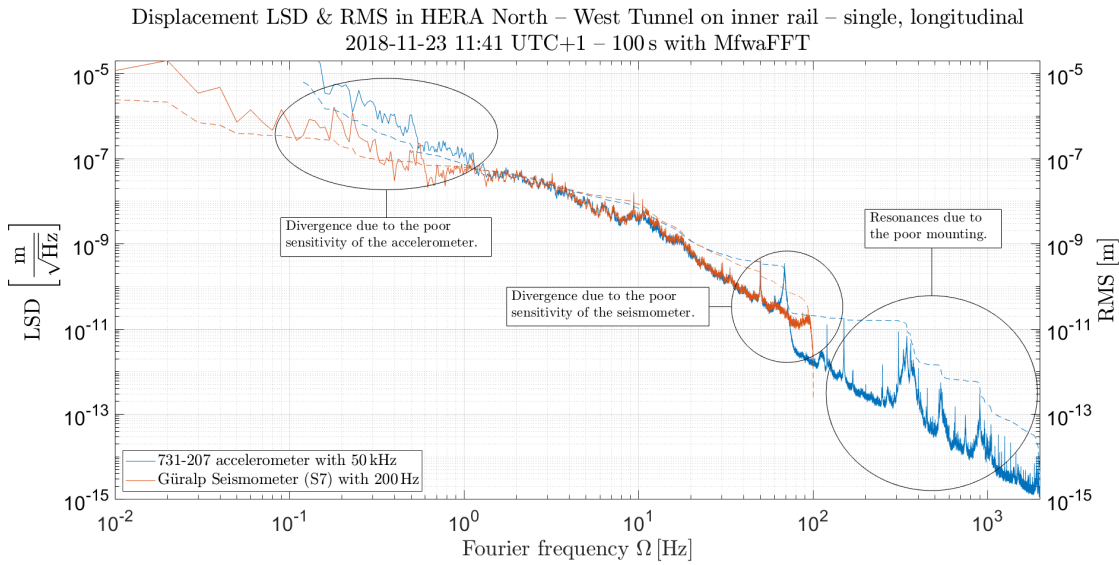
Compared to the specifications from table 3.2, the valid frequency range of the seis-

<sup>6</sup>At the time of the measurement, a cavity length of 100 m was assumed.

nometer ranges from 0.033 Hz to 100 Hz, whereas in the case of the accelerometer it ranges from 0.2 Hz to 1,300 Hz. In practice, the values vary from 0.01 Hz to 60 Hz for the seismometer and from 1 Hz to 2,000 Hz for the accelerometer due to the sensitivity of the instruments and the given noise level (compare with 4.2.1.2). The divergences pointed out in the figure thus can be explained by their valid frequency ranges. Therefore, below 2 Hz, only the data of the seismometer are reliable and above 60 Hz only those of the accelerometer (compare with 4.2.1.2).

Unfortunately, due to the low mass of the accelerometer, a rigid mounting would have been required, which could not be provided in the current state of the infrastructure. That is why the accelerometer data shows resonances above 100 Hz (compare subsection 4.2.2). Therefore, the peaks must be considered as a worst-case scenario, which can mask true seismic noise features but still can exclude higher noise in that region. Here, the frequency region between 2 Hz and 70 Hz shows congruent data. Furthermore, the peaks in this region can be interpreted as relevant seismic noise.

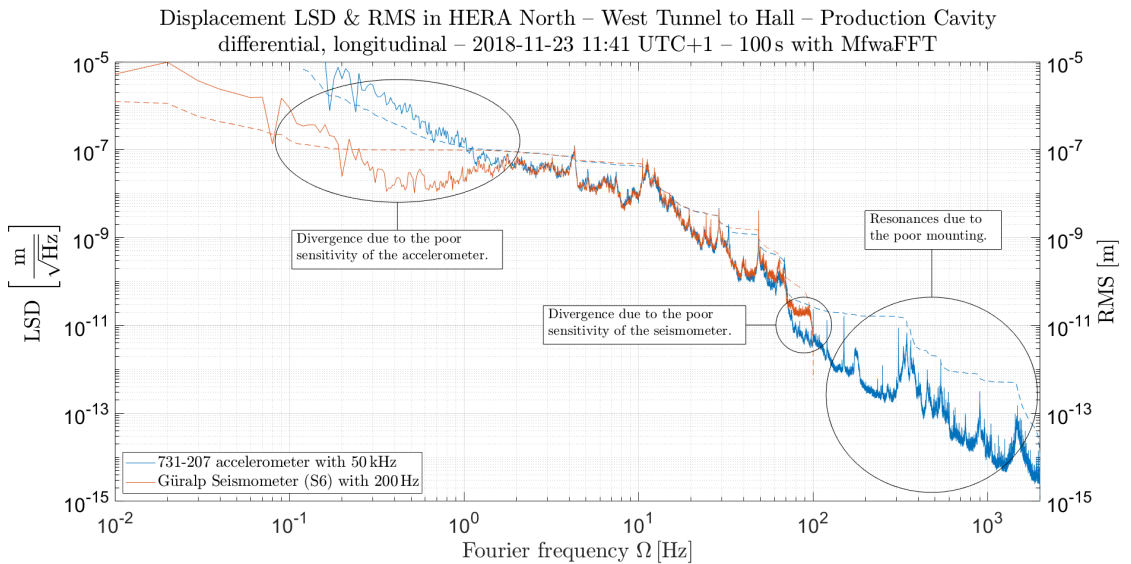
Likewise as for the ALPS IIa laboratory, the data will be compared with the simultaneously measured data from HERA North West Tunnel that is shown in figure 4.31. The outer clean rooms are built on concrete elements, whereas the optical table will be mounted into the tunnel floor, which is the quietest area available (compare subsection 3.1.5). For this, the measurements had to be as similar as possible to these conditions. Therefore, the instruments were placed as close as possible to the tunnel ring elements on the concrete to obtain a measurement relevant for later construction. The blue line again refers to the accelerometer whose data were acquired with the oscilloscope with 50 kHz sample rate at a resolution of 40 mV/div and the red line refers to the seismometer data acquired at 200 Hz.



**Figure 4.31.:** Single displacement LSDs & RMSs of HERA North West Tunnel in longitudinal direction on 2018-11-23 at 11:41 UTC+1. Analysing characteristics: Kaiser window with a beta factor of 2.5 and 20 % overlap; analysed with MfwaFFT with a *dod* of 12.

The peculiarities shown here are the same as those in the hall (see figure 4.30). Moreover, the seismic noise peaks detected above are not so pronounced here, indicating a more quiet location. This is due to the fact, that these peaks are attributable to human made seismic noise sources (see 2.2.2), which is mostly not dominant in the tunnels.

Hence, more of interest is the differential data of the hall and the tunnel. As the data was taken simultaneously, subtracting the signals in the time domain and afterwards creating the LSD and RMS will give a relative signal of the PC shown in figure 4.32.



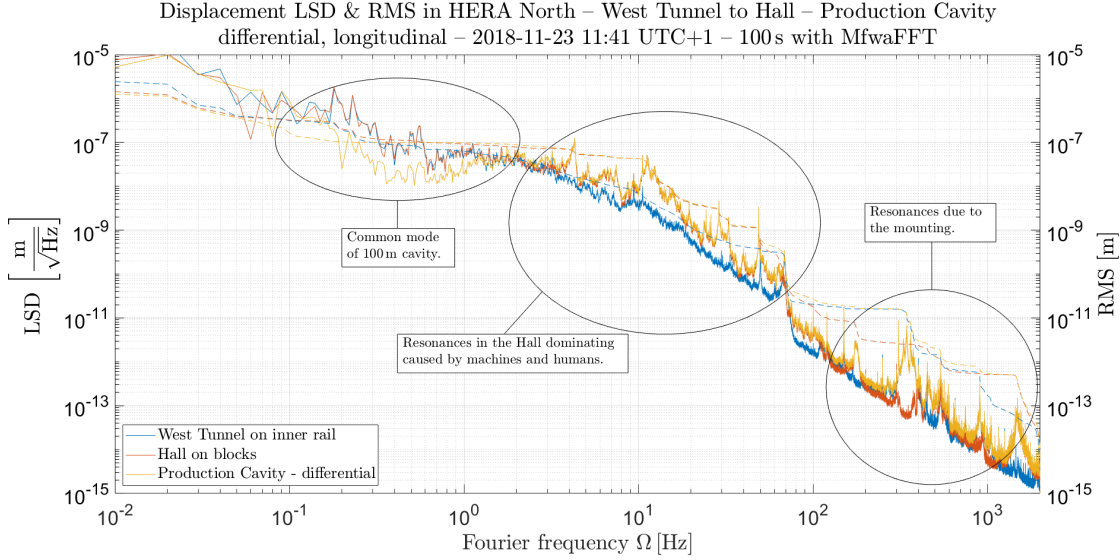
**Figure 4.32.:** Differential displacement LSDs & RMSs of HERA North West Tunnel to Hall in longitudinal direction on 2018-11-23 at 11:41 UTC+1. Analysing characteristics: Kaiser window with a beta factor of 2.5 and 20 % overlap; analysed with MfwaFFT with a *dod* of 12.

The figure represents the displacement that the PC would have to cope with. Any vibration experienced equally by both points will be ignored, as it would be in the case in the experiment. Again, the same peculiarities are displayed as before, but with a larger difference below 2 Hz. Also, the peaks in the frequency region between, here, 3 Hz and 70 Hz are present again.

In order to analyse the conditions in the hall, in the tunnels, and relative to each other, two techniques are used. First, the data of both measuring instruments are combined. Therefore, the data from the seismometer up to and from the accelerometer above 3 Hz is used to generate a ‘super-sensor’. Here, a smooth transition weighting of the sensors would have been possible as used in the MfwaFFT. This was omitted because of the lack of necessity and the simplicity of the measurement. Second, the differential signal is plotted together with its respective signals to reveal their relationship. This is visualised in figure 4.33.

The figure allows for three important statements. First, the differential signal is dominated by the higher signal except below 1 Hz. This indicates a common mode of both sites, which results in lower seismic noise than it would be the case if each one were

### 4.3. Seismic measurements on-site



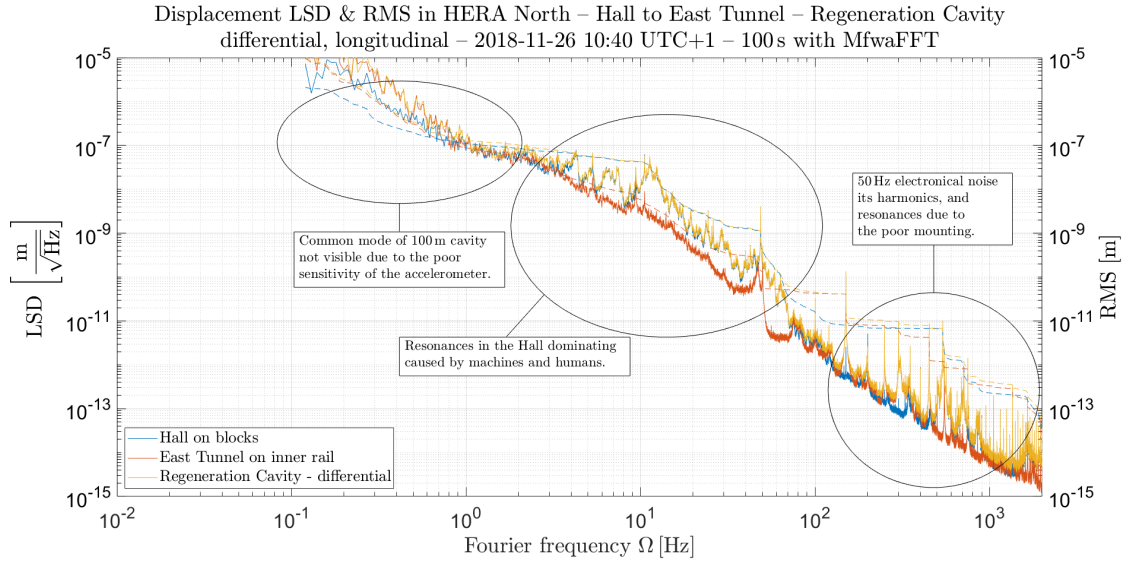
**Figure 4.33.:** Combined displacement LSDs & RMSs of HERA North, West Tunnel, Hall, and differential signal in longitudinal direction on 2018-11-23 at 11:41 UTC+1. Analysing characteristics: Kaiser window with a beta factor of 2.5 and 20% overlap; analysed with MfwaFFT with a *dod* of 12.

to be regarded separately. Compared to the ALPS IIa PC in figure 4.26 the common mode is lower by a factor of 10. This is due to the direct correlation of the different length of the optical cavities by a factor of 10. Second, it can be seen that the hall dominates the seismic noise in the range between 3 Hz and 100 Hz, especially at 4.3 Hz and between 10 Hz and 20 Hz. Here, the RMS value is raised by a factor of approximately 40 from 100 Hz to 50 Hz and again by a factor of approximately 70 from 30 Hz to 3 Hz. Therefore, it is defined as the crucial part. Third, the peaks defined as the worst-case scenario in the frequencies above 100 Hz have no significant influence on the RMS of the overall data and can therefore be neglected for the time being.

Assuming the seismic noise in both tunnels (west and east) is similar, only the accelerometer were used to determine the conditions in the East Tunnel. Figure 4.34 shows the displacement LSD and RMS of the hall in blue, the East Tunnel in red, and the differential signal of the RC in yellow.

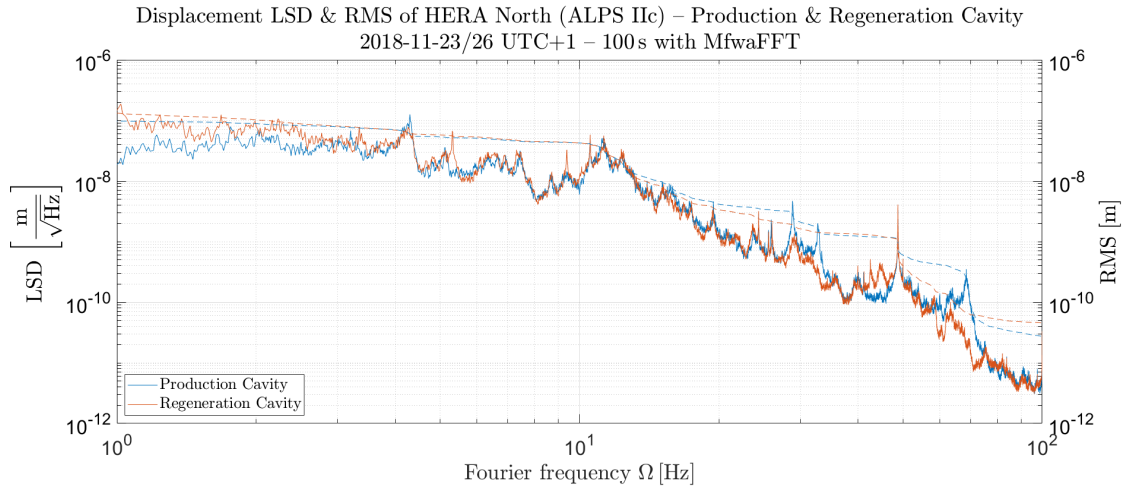
Again, three statements can be made. First, the common mode is not visible owing to the poor sensitivity of the accelerometers below 1 Hz, but it can be assumed to be in the same frequency range as in figure 4.33 by referring to the same distances and ground conditions. Second, for the RC, the seismic noise between 3 Hz and 80 Hz is dominated by the hall. Here the RMS value is increased by a factor of about 200. Third, the peaks above 100 Hz can again be interpreted as a worst-case scenario that has no significant effect on the overall RMS value.

Figure 4.35 compares the PC to the RC for the valid and at the same time crucial frequency range of 1 Hz to 100 Hz. Except minor discrepancies, the overall signal and RMS value are very similar. The figure reflects the pure undamped seismic noise that will



**Figure 4.34.:** Differential displacement LSDs & RMSs of HERA North Hall to East Tunnel in longitudinal direction on 2018-11-26 at 10:40 UTC+1. Analysing characteristics: Kaiser window with a beta factor of 2.5 and 20 % overlap; analysed with MfwaFFT with a *dod* of 12.

affect the ALPS IIc cavities. The comparison to the data from the ALPS IIa laboratory is made in section 4.4.

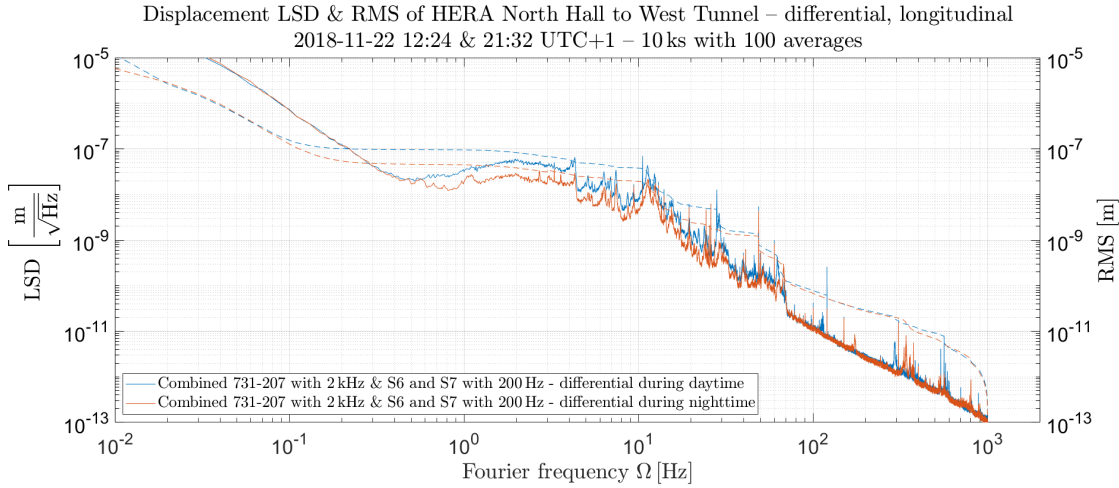


**Figure 4.35.:** Differential displacement LSDs & RMSs of HERA North (ALPS IIc) Production and Regeneration Cavity on 2018-11-23 and 2018-11-26 UTC+1. Analysing characteristics: Kaiser window with a beta factor of 2.5 and 20 % overlap; analysed with MfwaFFT with a *dod* of 12.



### Long-term measurements

Another subject of research is the different seismic noise during day and night, as it affects the data in the crucial frequency range between 1 Hz and 100 Hz. Therefore, two long-term measurements were carried out to identify the differences between day and night. Both were done with the accelerometer and the seismometer with the specifications as described above for a duration of 10,000 s. To simplify the analysis and decrease the computation time a simple mean over 100 averages was applied. The result is again stitched at 3 Hz and presented in figure 4.36.



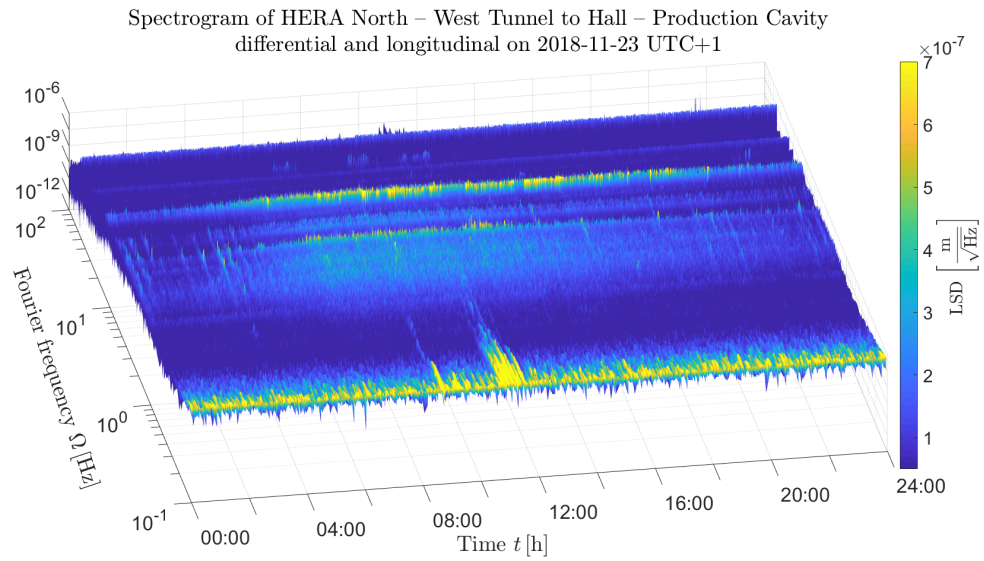
**Figure 4.36.:** Combined displacement LSDs & RMSs of HERA North Hall to West Tunnel in longitudinal direction on 2018-11-22 at 12:24 and 21:32 UTC+1. Analysing characteristics: Kaiser window with a beta factor of 2.5 and 20% overlap; analysed over 100 averages.

Here, the blue line refers to the daytime measurement, whereas the red line reflects the seismic noise at night. The difference in the seismic noise is approximately a factor of 2 between 0.6 Hz and 70 Hz. This can be explained by the noise emitted by traffic and workers during daytime (compare with 2.2.2.2).

Furthermore, another measurement was taken only with the seismometers to create a low-frequency spectrogram analysing the seismic noise for the duration of one day from 0.1 Hz up to 100 Hz. Figure 4.37 visualises the vibrations, acquired on the 23rd of November 2018 formed logarithmically over the frequency and linearly over the time, while the amplitude is presented logarithmically as well. The colour is used for better visualisation of the amplitudes. The analysis was averaged over 1 min samples, resulting in a fine pattern.

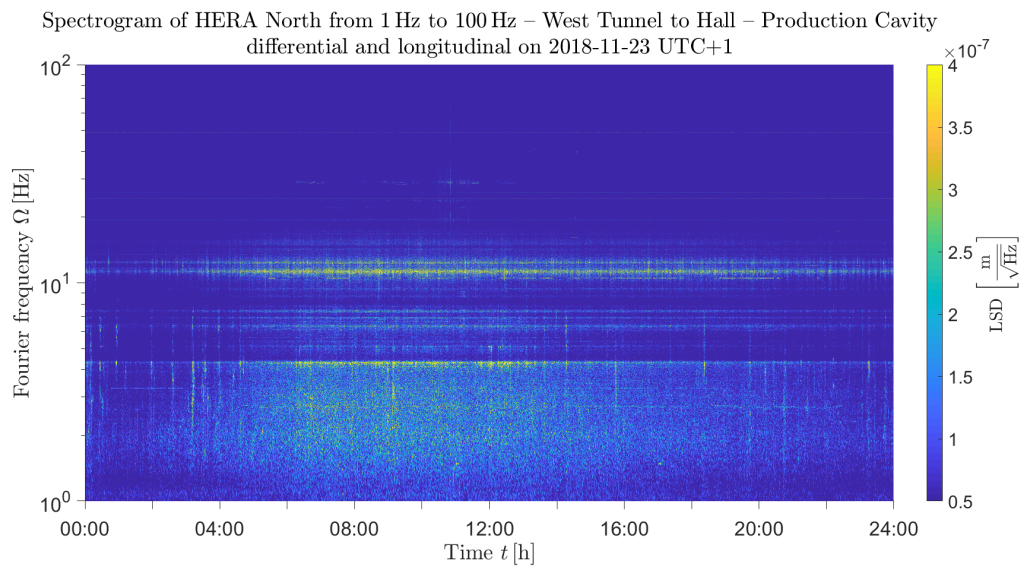
The bright blue or yellow peaks between 07:00 and 17:00 and between 1 Hz and 100 Hz indicate the working hours or the day/night shift as described in figure 4.36. Moreover, the plot shows an eruption around noon below 1 Hz that could be attributed to human work. Also, some frequency lines are visible throughout the day or for longer periods. These reflect persistent effects in the higher frequency range caused by air conditioners, ventilation, or other routine equipment present in HERA.

To focus more on the crucial frequencies between 1 Hz and 100 Hz another spectrogram



**Figure 4.37.:** Spectrogram of HERA North Hall to West Tunnel in longitudinal direction on 2018-11-23 UTC+1. Analysing characteristics: 1,440 averages (1 min) with a Kaiser window with a beta factor of 2.5 and 20 % overlap.

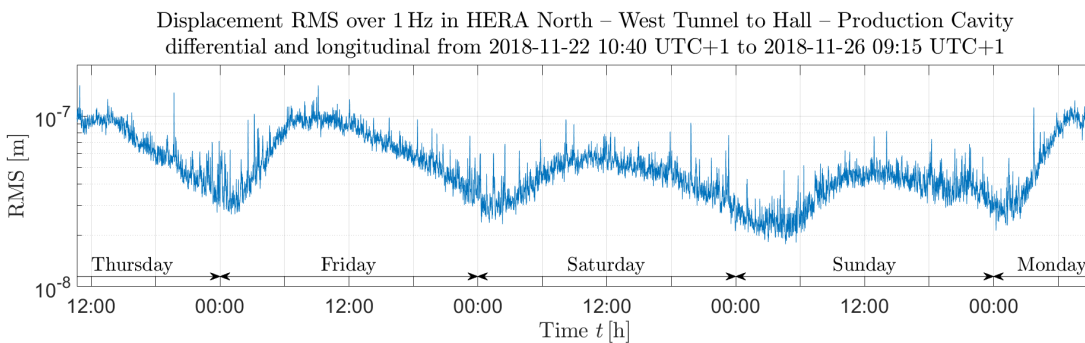
is shown in figure 4.38. It is plotted as a two-dimensional coloured map to achieve a better assignment of the peaks to the respective frequencies or times. Thus, every vertical line refers to an event in the time domain, whereas every horizontal line refers to a more permanent event at a specific frequency.



**Figure 4.38.:** Spectrogram of HERA North Hall to West Tunnel in longitudinal direction on 2018-11-23 UTC+1. Analysing characteristics: 1,440 averages (1 min) with a Kaiser window with a beta factor of 2.5 and 20 % overlap.

As mentioned and shown above, the peaks are more pronounced during daytime. Here, a direct correlation with the exact frequencies is possible, so that the most active seismic noise is defined in the range between 10 Hz and 20 Hz. Even if some frequencies are repeated, however, no continuous signal is recognisable. This indicates repetitive effects, e.g. a closing door, a passing vehicle, a used flush, or similar human-made vibrations. This frequency range is mainly assigned to traffic in the environment [2]. Another clear signal is present at approximately 4.3 Hz. It is visualised as a continuous line, which can be interpreted as a permanent effect. Last, there are three frequencies visible throughout the day between 6 Hz and 8 Hz.

Referring to the ALPS IIC requirements (compare with 3.1.4), the RMS value limits the allowable seismic noise. The frequencies below 1 Hz are not critical, assuming that they will be damped by the control loop (see subsection 4.4.3). Therefore, the RMS value at 1 Hz is examined, visualising the actual displacement that occurs at frequencies above 1 Hz. The data were analysed with 1 min samples over a period of approximately 4 days. Figure 4.39 shows the time-dependent RMS value over one weekend.

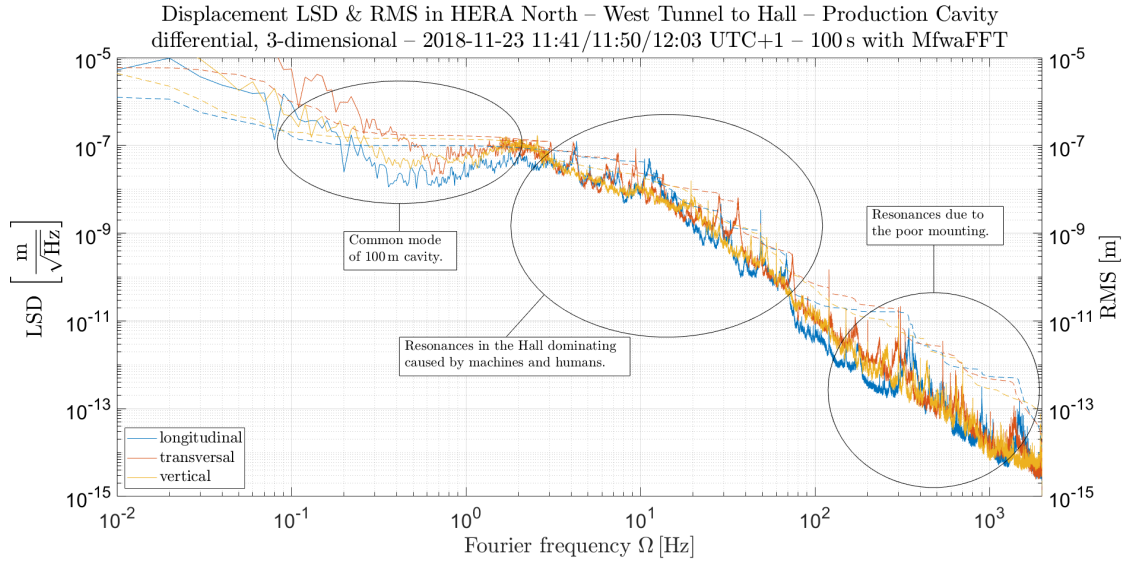


**Figure 4.39.:** Displacement RMS of HERA North, West Tunnel to Hall in longitudinal direction from 2018-11-22 at 10:40 UTC+1 to 2018-11-26 09:15 UTC+1. Analysing characteristics: 5676 averages (1 min) with Kaiser window with a beta factor of 2.5 and 20 % overlap.

The graph varies regularly from day to day, starting at approximately 02:00 UTC+1, reaching its peak at around 08:00 UTC+1, and then dropping off at about 12:00 UTC+1. The weekend indicates a more quiet environment, which is explained by the lack of noise caused during the normal working hours. Summing up, the RMS value at 1 Hz fluctuates between  $3 \cdot 10^{-8}$  m and  $2 \cdot 10^{-7}$  m during the week and between  $2 \cdot 10^{-8}$  m and  $7 \cdot 10^{-8}$  m on the weekend. This knowledge can be used to optimise and schedule data runs for ALPS IIC if the loop can not handle the seismic noise.

### 3D measurements and transfer functions

Furthermore, the three-dimensional seismic noise of the cavities has to be investigated. Figure 4.40 shows three simultaneously measured displacement LSDs and RMSs of differential measurements from the HERA Hall and West Tunnel. Again, the signal is combined from the seismometer and the accelerometer with the same instrumental settings as described previously.



**Figure 4.40.:** Combined displacement LSDs & RMSs of HERA North, West Tunnel to Hall in three-dimensional direction on 2018-11-23 at 11:41/11:50/12:03 UTC+1. Analysing characteristics: Kaiser window with a beta factor of 2.5 and 20% overlap; analysed with MfwaFFT with a *dod* of 12.

The longitudinal measurement, in blue, is the same as described in figure 4.33 and refers to the critical ALPS IIc requirements stated in 3.1.4. All lines display similar behaviour over all frequencies, with the vertical line, in yellow, showing a slightly flatter path, where the transversal, in red, has the highest seismic noise below 1 Hz. The differences mostly result from the larger noise in the hall. This can be explained by the existing construction in the hall, which results from resonances of the stacked concrete blocks and its support (compare with 3.1.5).

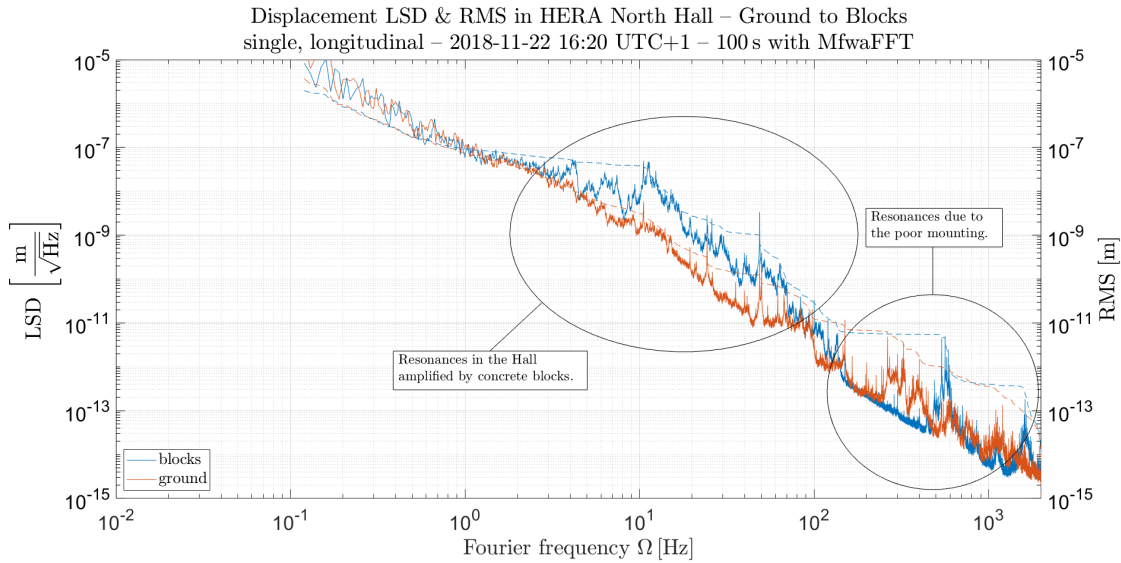
Consequently, these concrete blocks were examined. As mentioned above in 4.3.1.2, the fourth measuring point is on the floor of the hall, more precisely exactly below the concrete block construction at a free corridor. Here, as well as on the blocks, an accelerometer was placed to obtain the disparity in the seismic noise. Figure 4.41 shows an LSD and RMS of a longitudinal measurement, visualising the concrete block construction in blue and the ground of the hall in red.

Between 3 Hz and 80 Hz a clear difference can be seen as previously in the differential measurements from the hall to the tunnels (compare figures 4.33 and 4.34). Hence, it can be concluded that the vibrations in these frequencies are amplified by the resonances of the concrete blocks stacked in the hall or its support structure (compare with 2.1.1.2).

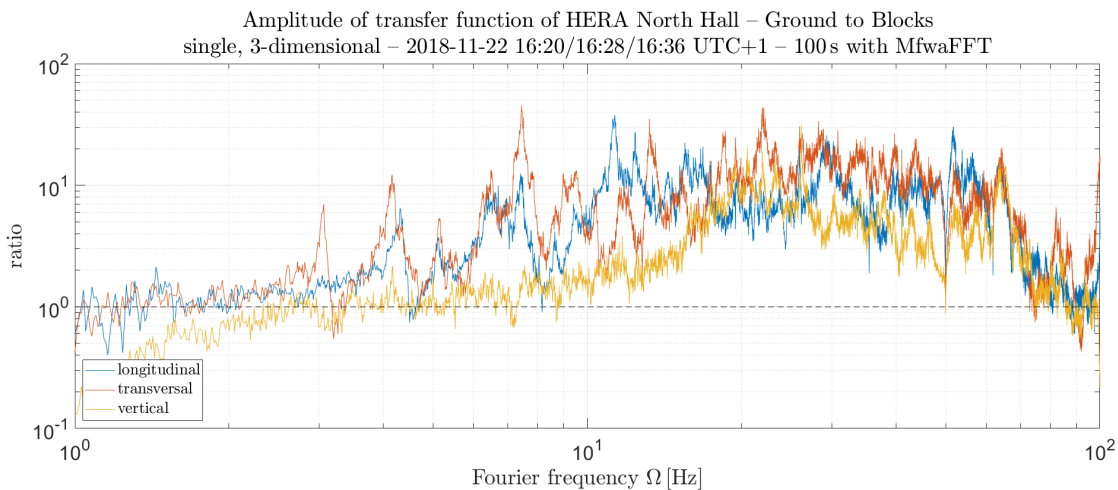
In order to gain a comprehensive understanding of the impact of the concrete blocks on seismic noise, all three dimensions were studied. Subsequently, a transfer function was formed in each case describing the effects on the seismic noise (compare with 2.1.4.3). Figure 4.42 visualises the amplitudes of these transfer functions from 1 Hz to 100 Hz.

The lines almost exclusively show a value greater than 1, resulting in an amplification of the seismic noise existing on the ground which is transferred to the concrete

### 4.3. Seismic measurements on-site



**Figure 4.41.:** Single displacement LSDs & RMSs of HERA North Hall on concrete blocks and ground in longitudinal direction on 2018-11-22 at 16:20 UTC+1. Analysing characteristics: Kaiser window with a beta factor of 2.5 and 20% overlap; analysed with MfwaFFT with a *dod* of 12.

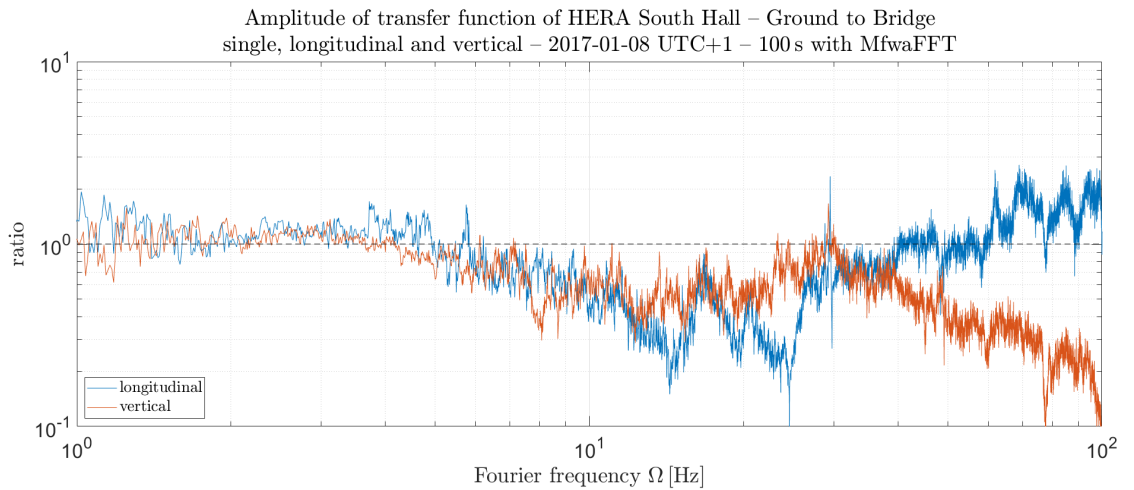


**Figure 4.42.:** Amplitude of transfer function of HERA North Hall on ground to concrete blocks in all three-dimensional directions on 2018-11-22 at 16:20/16:28/16:36 UTC+1. Analysing characteristics: Kaiser window with a beta factor of 2.5 and 20% overlap; analysed with MfwaFFT with a *dod* of 12.

blocks. The vertical direction, in yellow, shows a flatter amplification, especially in the frequencies below 20 Hz, probably because of a stiffer support of the concrete blocks in the vertical axis due to gravity.

### 4.3.1.3. Reference (HERA South)

As mentioned in 4.3.1, there is an existing bridge construction in HERA South to provide a stable connection between the tunnel entrances within the hall. In order to investigate this, a measurement was carried out with the accelerometer 731-207 in ACC mode with a gain of 100 and recorded with the Tektronix Digital Phosphor Oscilloscope DPO7000 at a sampling rate of 50 kHz for 100 s. The LSDs show similar data as those of HERA North. Therefore, figure 4.43 only shows the amplitudes of the transfer functions of the bridge construction to the ground of the hall. The blue line represents the longitudinal direction, while the red line shows the vertical.



**Figure 4.43.:** Amplitude of transfer function of HERA South Hall on ground to bridge construction in longitudinal and vertical direction on 2017-01-08 UTC+1. Analysing characteristics: Kaiser window with a beta factor of 2.5 and 20 % overlap; analysed with MfwaFFT with a *dod* of 12.

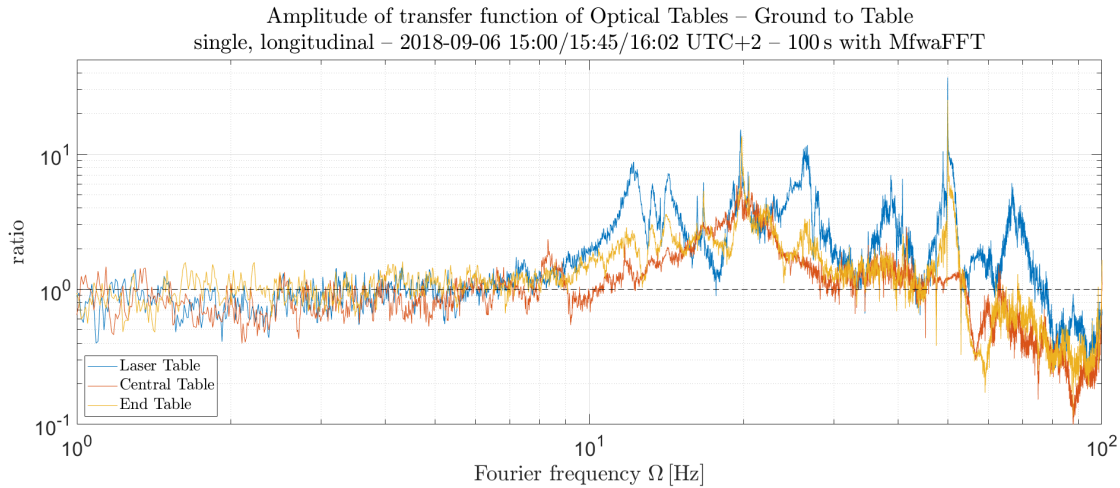
Contrary to figure 4.42, these transfer functions do not amplify the seismic noise in the critical frequency range between 1 Hz and 100 Hz, but have a damping effect. It is assumed that the resonances due to the stiff construction are in the range of a few kHz and therefore are not visible nor of interest here.

## 4.3.2. Optic-related components of the ALPS II experiment

The previous subsection described the ground conditions within the HERA ring accelerator (compare subsection 4.3.1). As mentioned in subsection 3.1.5, the infrastructure of the ALPS IIc set-up is not yet installed. Thus, to obtain a valid seismic noise level compared to the ALPS IIa laboratory, all major objects that transform seismic noise must be appraised in order to adapt the measurement point spatially to all interfering conditions. For this purpose, the optical tables used in each clean room and the CBB in the central clean room are evaluated in the following paragraphs.

#### 4.3.2.1. Optical tables

The three optical tables installed in the ALPS IIa laboratory are all slightly different but will be similarly incorporated into ALPS IIc. All tables (Laser Table (LT), Central Table (CT), and End Table (ET)) were examined to determine a transfer function representing the transformation from the ground motion to the excited motion on the table. Therefore, measurements with the 731-207 accelerometer were performed simultaneously on the table and on the floor for a duration of 100 s. The data were acquired at a sample rate of 50 kHz and the clean room flow boxes were deactivated. The result is shown in figure 4.44 where the blue line represents the LT, the red the CT, and the yellow the ET.



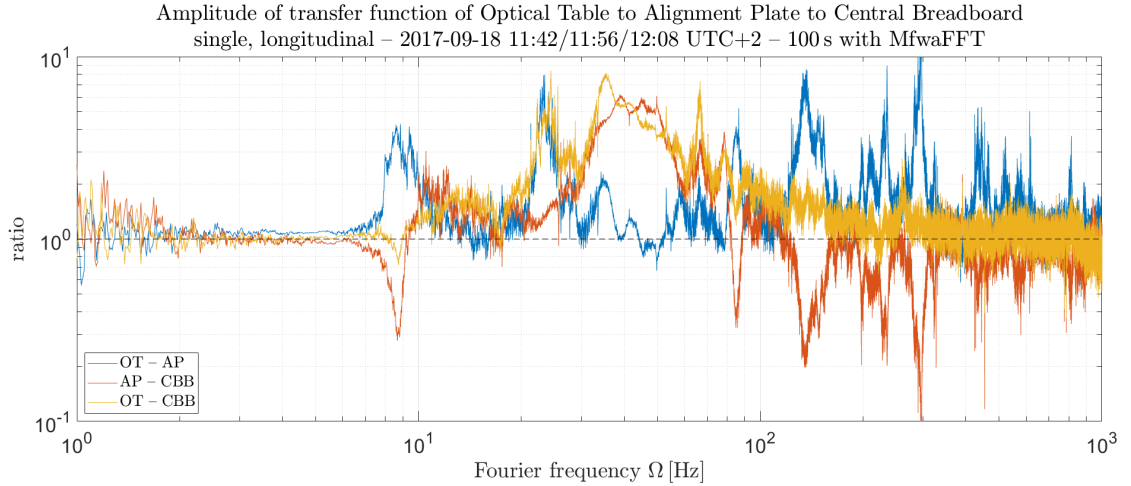
**Figure 4.44.:** Amplitude of transfer function of HERA West ALPS IIa lab ground to optical tables in longitudinal direction on 2018-09-06 15:00/15:45/16:02 UTC+2. Analysing characteristics: Kaiser window with a beta factor of 2.5 and 20% overlap; analysed with MfwaFFT with a *dod* of 12.

All three tables have their own resonances or internal noise sources which are visible in the figure. The LT (blue), for example, has the laser, a beam dump fan, and a cooling water flow which create vibrations on the table. Nevertheless, all tables amplify the seismic noise compared to the ground between 10 Hz and at least 50 Hz.

#### 4.3.2.2. CBB and mirror mountings

As mentioned in the previous subsection, the measurements were impossible to be carried out on the surface of the cavity mirrors, but as close to them as possible. Within the experimental set-up of ALPS IIa, the CBB being located in a vacuum tank was inaccessible for testing, but as it is decoupled from the vacuum tank, only the mountings to the Optical Table (OT) will transform seismic noise. Therefore, these and a construction called Alignment Plate (AP), which serves as an intermediate state to position the CBB when it is in the vacuum, were investigated. Hence, three measurements with the 731-207 accelerometer were performed simultaneously for a duration of 100 s from the OT

to the AP, from the AP to the CBB, and from the OT to the CBB. The sensors were screwed or clamped to the objects to allow for higher frequency evaluation. The data were acquired with the Tektronix Digital Phosphor Oscilloscope DPO7000 at 50 kHz. Figure 4.45 shows the amplitudes of the three transfer functions up to 1,000 Hz.



**Figure 4.45.:** Amplitude of transfer function of OT to AP to CBB in longitudinal direction on 2017-09-18 11:42/11:56/12:08 UTC+2. Analysing characteristics: Kaiser window with a beta factor of 2.5 and 20% overlap; analysed with MfwaFFT with a *dod* of 12.

The figure visualises that the AP amplifies some vibrations, which are then partially attenuated by the CBB. More precisely, the intermediate stage oscillates stronger than the outer ones. Since the inner cavity mirrors will be clamped directly to the CBB, only its transfer function to the optical table is of interest.

For ALPS IIc, the outer cavity mirrors located inside the tunnels will have 2" bezel mounts. Unfortunately, these could not be investigated with the existing sensors. With all the analyses made, the seismic noise can be spatially transformed from the measured ground point to the predicted mirror position (see subsection 4.4.1).

### 4.3.3. Associated noise sources

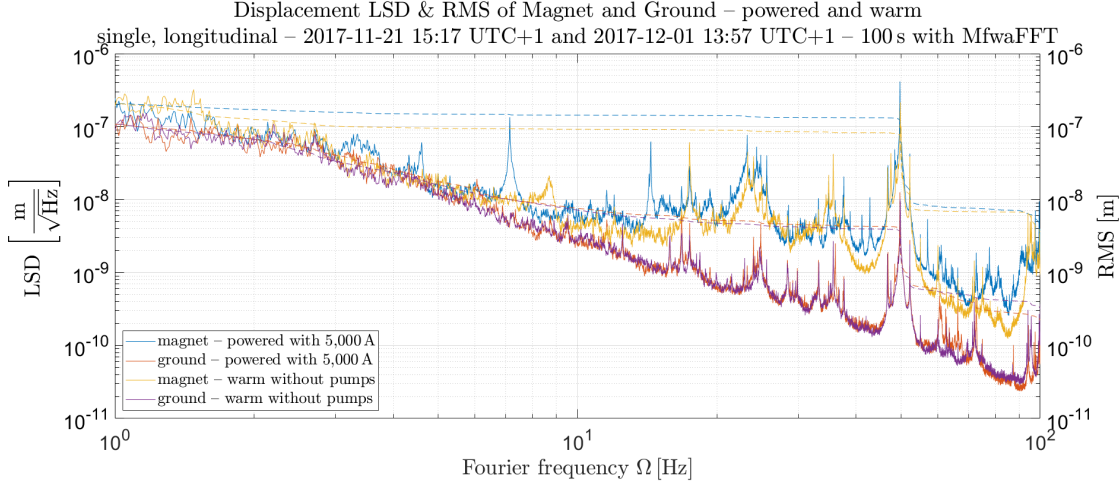
The following paragraphs present the examinations on internal noise sources that may induce additional vibrations to the system and will be present in ALPS IIc. The term ‘associated’ describes seismic noise sources that are obligatory in ALPS IIc but are not located within the clean rooms. Thus, the dipole magnets and the FFUs were investigated.

#### 4.3.3.1. Dipole magnet girders

As mentioned in subsection 3.1 twenty four HERA dipole magnets will be used to generate the magnetic field needed for the conversion of the photon into an axion and vice versa. These electromagnets are cooled by a cryogenic tube system and powered in the



superconducting state with at least 5,700 A. Therefore, a magnet was investigated in the warm as well as in the cooled, powered state. The measurements were performed on the flange of the magnet and simultaneously on the ground with two 731-207 accelerometer and the Tektronix Digital Phosphor Oscilloscope DPO7000 at 50 kHz over a duration of 100 s. Figure 4.46 shows the LSDs and RMSs from the magnet's flange and the ground. First, the magnet was cooled and powered with 5,000 A<sup>7</sup> and the second time in a warm state with all cooling and vacuum pumps deactivated.



**Figure 4.46.:** Displacement LSDs & RMSs of dipole magnet and nearby ground powered and warm in longitudinal direction on 2017-11-21 15:17 UTC+1 and 2017-12-01 13:57 UTC+1. Analysing characteristics: Kaiser window with a beta factor of 2.5 and 20 % overlap; analysed with MfwaFFT with a *dod* of 12.

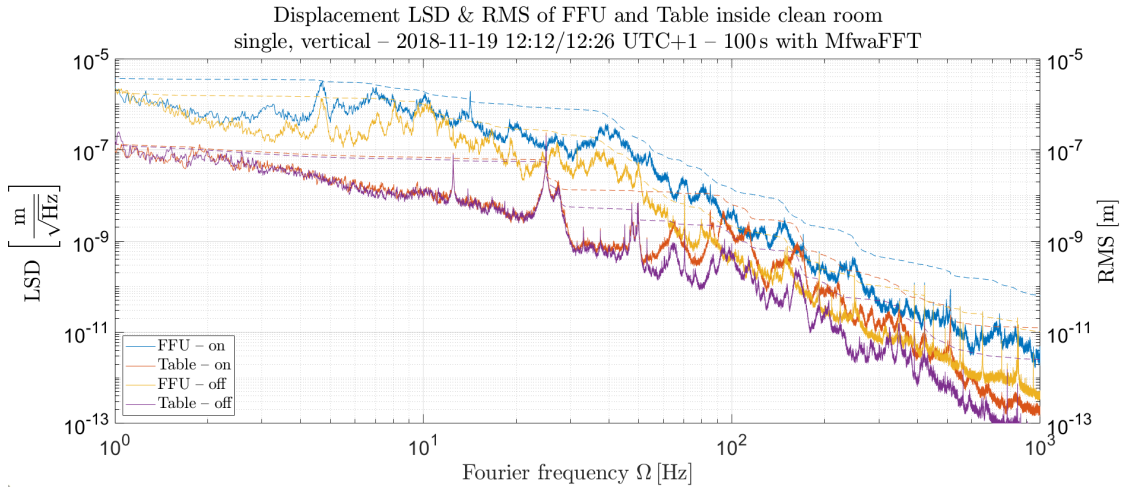
When comparing the seismic noise on the magnet (blue and yellow lines), there are some differences in the LSD. Besides the peak above 7 Hz and its first harmonic, the overall vibrations were slightly higher; resulting in an RMS value between 50 Hz and 2 Hz being a factor of 2 higher when the magnet is in use. Looking at the ground motion (red and magenta lines), no significant change is visible except for a small increase in the RMS value at 50 Hz. This indicates that the vibration of the magnets does not transfer to the floor and therefore does not affect the stability of the mirrors. Note that the measurement was performed on a single magnet and in an experimental hall. The conditions for ALPS IIc in the tunnel with all of the magnets could be different.

#### 4.3.3.2. Filter Fan Units

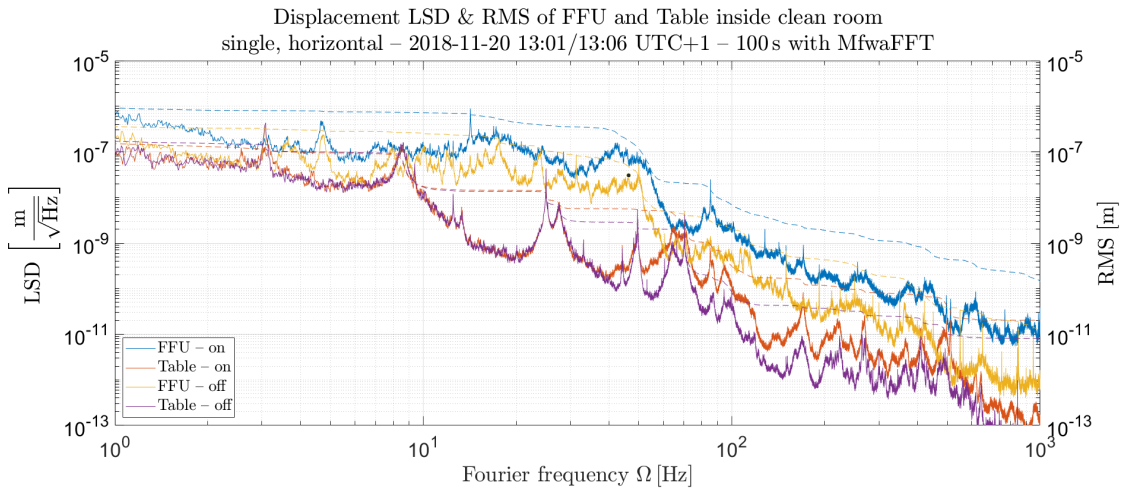
In ALPS IIa the airflow is ensured by the flow boxes mounted directly over the optical tables. Since this is not optimal and will not be the case for the ALPS IIc set-up, they were deactivated for the measurements. In ALPS IIc, FFUs will be inserted into the clean room ceiling to produce the most constant airflow possible. Similar FFUs were investigated in an experimental hall using two 731-207 accelerometers and the Tektronix

<sup>7</sup>The seismic noise does not differ at higher currents.

Digital Phosphor Oscilloscope DPO7000. The measurements were acquired at 50 kHz over a duration of 100 s. Therefore, one accelerometer was on top of the FFU, the other was in the clean room on a conventional table, while the FFU was once activated and once deactivated. Both, the vertical as well as a horizontal direction were examined. Figures 4.47 and 4.48 show the LSDs and RMSs for the vertical and a horizontal direction with the FFU.



**Figure 4.47.:** Displacement LSDs & RMSs of FFUs and a table inside the clean room in vertical direction on 2018-11-19 12:12/12:26 UTC+1. Analysing characteristics: Kaiser window with a beta factor of 2.5 and 20% overlap; analysed with MfwaFFT with a *dod* of 12.



**Figure 4.48.:** Displacement LSDs & RMSs of FFUs and a table inside the clean room in a horizontal direction on 2018-11-20 13:01/13:06 UTC+1. Analysing characteristics: Kaiser window with a beta factor of 2.5 and 20% overlap; analysed with MfwaFFT with a *dod* of 12.

Similar to the examination of the magnet, the seismic noise on top of the FFUs is raised across all frequencies when they are turned on, but will not induce vibrations

over solid objects to the tables. This can be seen by comparing the noise peaks on the blue line with the raised spots of the red one. More important is the change in the vibrations visible on the table over 50 Hz. It is represented as broadband noise, which can be assumed to be turbulent airflow. The RMS value at 100 Hz is approximately 5 times higher when the FFUs are activated. This applies to both the vertical and the horizontal direction, with the background noise more dominant in the vertical. Note that the accelerometers were not rigidly mounted as it would be required for an accurate measurement above 100 Hz and that an office table was used instead of an optical table. That is why the data must be considered as a worst-case scenario.

### 4.4. Filtering of signal

The following section discusses the filters and transformations of the data to project the analysed seismic noise to future ALPS configurations, e.g. ALPS IIc or JURA. First, the spatial transformations are explained in 4.4.1, then the low-pass filtering by the optical resonator in 4.4.2, and finally the high-pass filtering by the control loop in 4.4.3. Table 4.1 shows an overview of all filters and transformations used. Their implementation is presented in section 4.5.

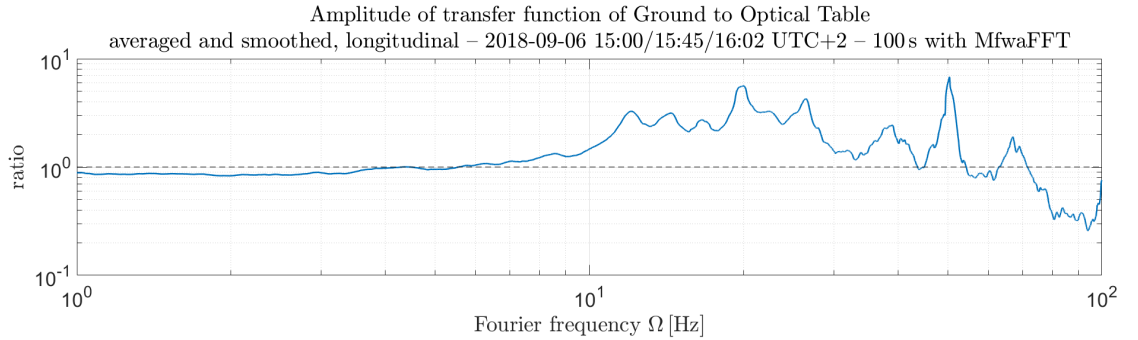
**Table 4.1.:** Overview of filters and transformations for adjusting the seismic noise data.

Type	Based on
optical table	measurements of the ALPS IIa optical tables – compare with 4.3.2.1
CBB	measurements of the AP and CBB – compare with 4.3.2.2
hall construction (optional)	measurements of the concrete blocks and bridge structure – compare with 4.3.1.2 and 4.3.1.3
low-pass filter	calculations of the cavity pole – compare subsection 3.1.4
suppression by the control loop	model of the control loop design – compare subsection 3.1.3

#### 4.4.1. Spatial transfer functions

With the results described in subsection 4.3.2, any spatial adjustment relevant for ALPS IIc can be made. This is a transformation from the measuring point on the ground to the optical tables for all three mirror positions. The measurements were described in 4.3.2.1 and the transfer functions presented in figure 4.44. Assuming that the table construction will be similar to the ALPS IIa set-up, a smoothed, arithmetic mean

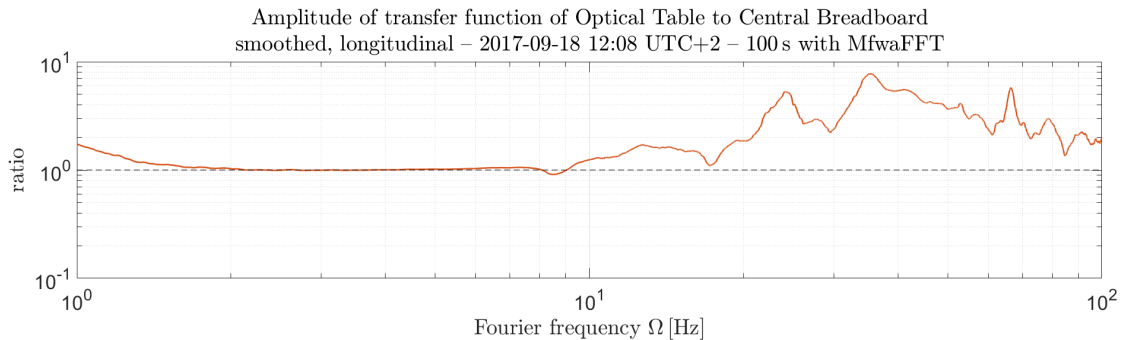
in the confident frequency range of the sensors from 1 Hz to 100 Hz was calculated and is shown in figure 4.49.



**Figure 4.49.:** Filtering model: smoothed and averaged amplitude of transfer function of HERA West ALPS IIa lab ground to optical tables in longitudinal direction on 2018-09-06 15:00/15:45/16:02 UTC+2. Analysing characteristics: Kaiser window with a beta factor of 2.5 and 20 % overlap; analysed with MfwaFFT with a *dod* of 12.

The model visualises some resonances of the tables between 9 Hz and 70 Hz that amplify the seismic noise. The transfer function can be multiplied by the data acquired at a position on the ground to simulate as if the data had been taken on an optical table. Note that the transformation is a simplified model, which should give an estimate of the not yet existing conditions and might not perfectly represent the real seismic noise signal.

As mentioned above, the CBB introduces a second transfer function that must be applied to the central clean room measurement discussed in 4.3.2.2 and presented in figure 4.45. Here, the transfer function from the optical table to the CBB was smoothed over the confident frequency range as shown in figure 4.50.

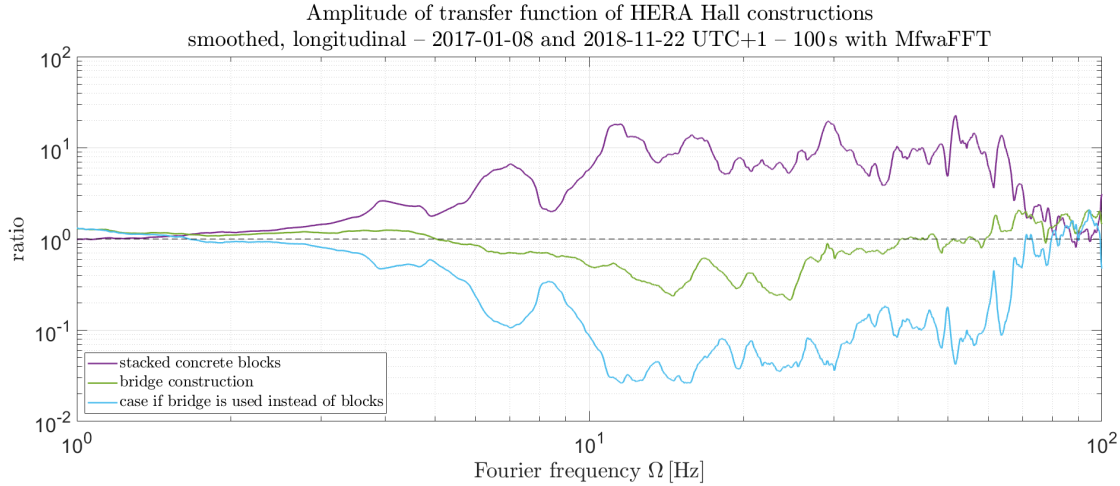


**Figure 4.50.:** Filtering model: smoothed amplitude of transfer function of optical table to CBB in longitudinal direction on 2017-09-18 12:08 UTC+2. Analysing characteristics: Kaiser window with a beta factor of 2.5 and 20 % overlap; analysed with MfwaFFT with a *dod* of 12.

Again, the transfer function shows resonances above 9 Hz that will raise the seismic noise level on the CBB. Since the CBB is the core of the ALPS II experiment with two clamped cavity mirrors, its displacement affects both cavities. Since the outer

cavity mirrors could not be examined, applying the transfer function of the CBB to the differential data as a worst-case scenario is a good estimate.

To reduce seismic noise on the CBB, the construction inside the HERA North Hall could be adapted to the bridge construction of the HERA South Hall. Therefore, two models resulting from the longitudinal measurements of 4.3.1.2 and 4.3.1.3 represented via figures 4.42 and 4.43 were calculated. The procedure was identical to the previous models. From this, a further model was derived, which describes the change in the design from using concrete blocks to a bridge construction. The single as well as the combined models are shown in figure 4.51.



**Figure 4.51.:** Filtering model: smoothed amplitude of transfer function of stacked concrete blocks, bridge construction, and the case if the bridge is used instead of the blocks in longitudinal direction on 2017-01-08 and 2018-11-22 UTC+1. Analysing characteristics: Kaiser window with a beta factor of 2.5 and 20 % overlap; analysed with MfwaFFT with a *dod* of 12.

The light blue line represents the case if the bridge construction were to be built in HERA North Hall instead of the stacked concrete blocks. The graph clearly shows an attenuation of seismic noise between 3 Hz and 80 Hz. Again, it has to be noted that the transfer functions are models and should be used as rough assumptions, especially for the latter case where multiple models are layered.

As mentioned in subsection 4.3.3, the influence of the magnets can be neglected as well as the airflow generated by the FFUs since the mirrors will be in vacuum and mounted on the optical table. Further filtering will be explained in the following subsections.

#### 4.4.2. Low-pass filter due to the cavity pole frequency

The cavities serve as low-pass filters for power and frequency fluctuations dependent on the cavity pole frequency, similar to an organ pipe for musical notes. This results in a transfer function like the one of an harmonic oscillator as described in 2.3.1.5, which can be determined by the cavity pole frequency  $f_p$  calculated from equations (3.9) (compare table 3.1) [45]:

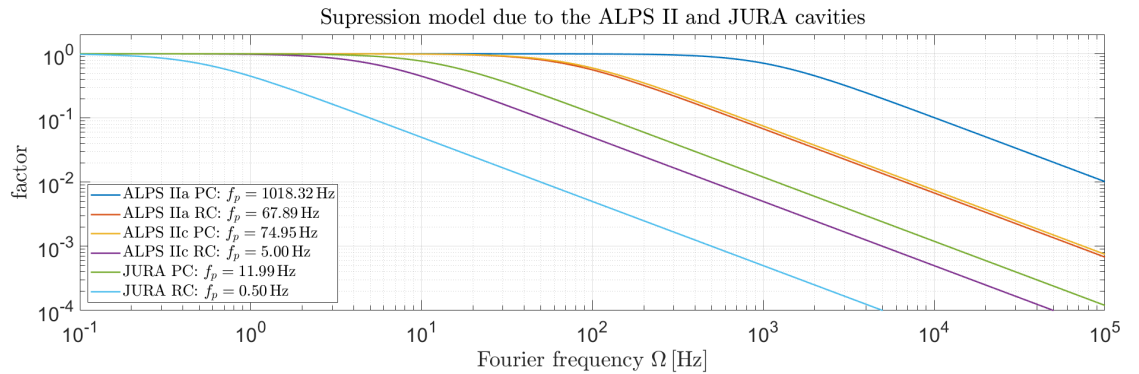
The cavity pole frequency  $f_p$  is used to calculate the low-pass filter  $low$  of the optical cavity for every Fourier frequency  $\Omega$  with small angle approximation as follows [45]:

$$low = 1 + i \cdot \frac{\Omega}{f_p} \quad \text{if } \Omega \ll f_{FSR} \quad (4.22)$$

A model for the magnitude and phase for the ALPS II and JURA cavity low-pass filters  $low$  can be found in figure D.1 in appendix D. Therefore, a seismic noise suppression model that can be used to calculate the influence on vibrations on the differential signals is more of interest (compare the measured data from subsection 4.3.1). This is defined by the inverted absolute value of the low-pass filter  $low$  as follows:

$$low_{supp} = \left| \frac{1}{1 + i \cdot \frac{\Omega}{f_p}} \right| \quad (4.23)$$

Figure 4.52 shows a model calculated from equation (4.23) for all (possible) cavities.



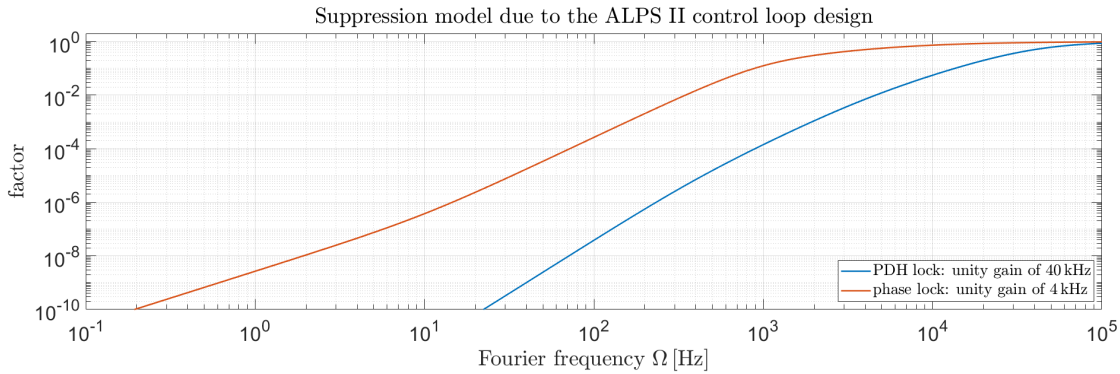
**Figure 4.52.:** Suppression model: inverted absolute value of the low-pass filter of the ALPS II and JURA cavities.

Since the length and finesse of the cavity affect the pole frequency, the PC of ALPS IIa is shown in dark blue on the far right, with the RC from JURA in light blue at the far left side of the figure. The latter has a suppression, starting at  $f_p = 0.50$  Hz, and a three orders of magnitude stronger suppression in the high-frequency region than the former. Furthermore, the low-pass filter attenuates the high-frequency laser noise induced by the high-power laser. The low-pass filter of the cavity is a physical phenomenon that benefits the conditions of LSW experiments.

### 4.4.3. Filter by the control loop

As described in subsection 3.1.3, the ALPS II experiment uses different feedback control schemes for locking both cavities. First, both are individually locked with the PDH technique with a unity gain of 40 kHz and then phase-locked together for the dual resonance condition with a unity gain of 4 kHz (compare subsection 3.1.3). For the former, a model with zeros at 40 Hz, 400 Hz, and 4 kHz, two integrators, two poles at 4 Hz, and one pole at 40 kHz [66] is used to act on the laser crystal. For the latter, a model with a unity gain of 4 kHz, two zeros at 1 kHz, two integrators, and one pole at 10 Hz [66] is used to act on one cavity mirror [58].

The resulting magnitude and phase of the control loop are shown in figure D.2 in appendix D. Similar to the low-pass filter due to the cavity pole, suppression models are defined from the inverted absolute value of the control loops. They express the impact on vibrations when the control loop is engaged.



**Figure 4.53.:** Suppression model: inverted absolute value of the ALPS II control loop.

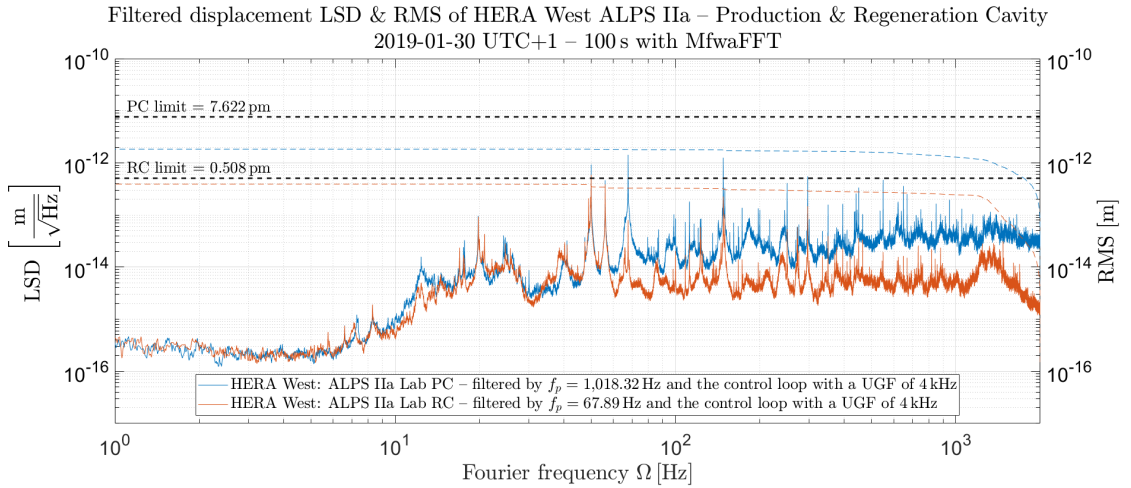
The overall control scheme is limited by its dynamic range as well as its slowest component. This is the PLL control by physically moving the mirror, represented by the red line. Thus, the control scheme can be used to suppress seismic noise below a frequency of 4 kHz.

## 4.5. Data evaluation

In the last section of this chapter, the measured seismic data of section 4.3 are transformed by the filters introduced in section 4.4 to compare the given conditions with the outlined requirements for the ALPS II and JURA experiments determined in table 3.1 in subsection 3.1.4. The filters and transformations are applied to the differential data representing the cavities for ALPS IIa and ALPS IIc, as well as for an assumption on JURA. The RMS value is subsequently calculated via the filtered signal. An example of how the filters gradually influence the differential seismic noise signal is shown in figure D.3 in appendix D.

### 4.5.1. Specifications for the ALPS IIa isolation

For ALPS IIa, the data from figure 4.29 attenuated by the suppression models of their cavities. The data can be plotted from 1 Hz to 2,000 Hz since only the 731-207 accelerometers were used that were screwed onto the optical tables and is presented in figure 4.54.



**Figure 4.54.:** Filtered differential displacement LSDs & RMSs of HERA West ALPS IIa laboratory Production and Regeneration Cavity on 2019-01-30 UTC+1. Analysing characteristics: Kaiser window with a beta factor of 2.5 and 20% overlap; analysed with MfwaFFT with a *dod* of 12. Filter characteristics: attenuated by the cavities with  $f_p = 1,018.32$  Hz for PC and  $f_p = 67.89$  Hz for RC and by the control loop with a unity gain frequency of 4 kHz.

Owing to the broadband seismic noise in the HERA West Hall and some noise peaks, especially around 50 Hz, the RC limit is just been met. This is visualised by the dashed lines in the figure, which are near the RMS boundary taken from table 3.1. Since ALPS IIa is designed to test and demonstrate the optical and the control scheme, it does not present a problem at that point.

### 4.5.2. Specifications for an ALPS IIc isolation

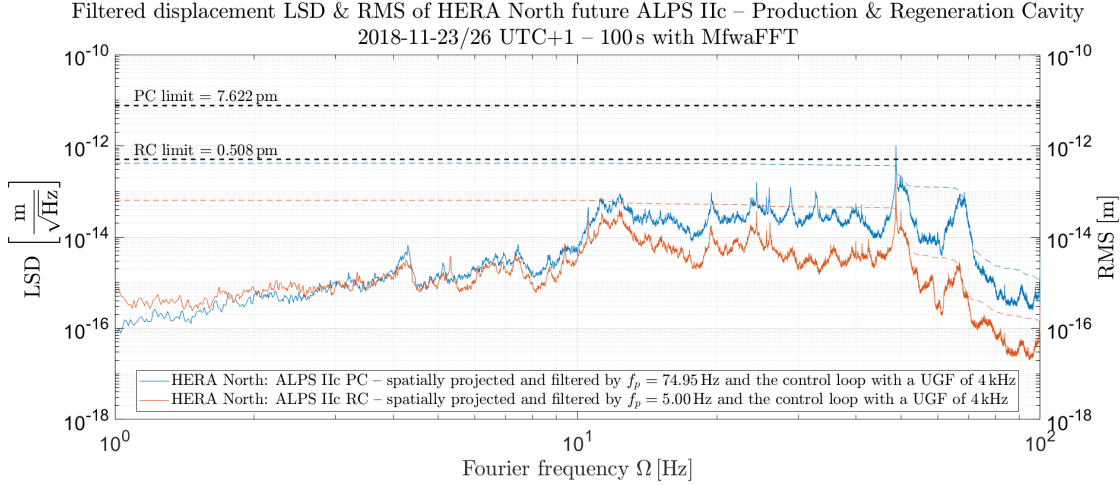
For ALPS IIc, the data must be spatially transformed onto the tables and onto the CBB as well as to the attenuation of the suppression models of the cavities and the application of the PLL control loop. Figure 4.55 shows this based on the data from figure 4.35 from 1 Hz to 100 Hz.

Both the PC and the RC limits are reached with a margin of almost one order of magnitude. Since the measurement is only a sample of 100 s, the data from figure 4.39 were also filtered with the same procedure to investigate seismic noise changes over several days. The resulting data is shown in figure 4.56.

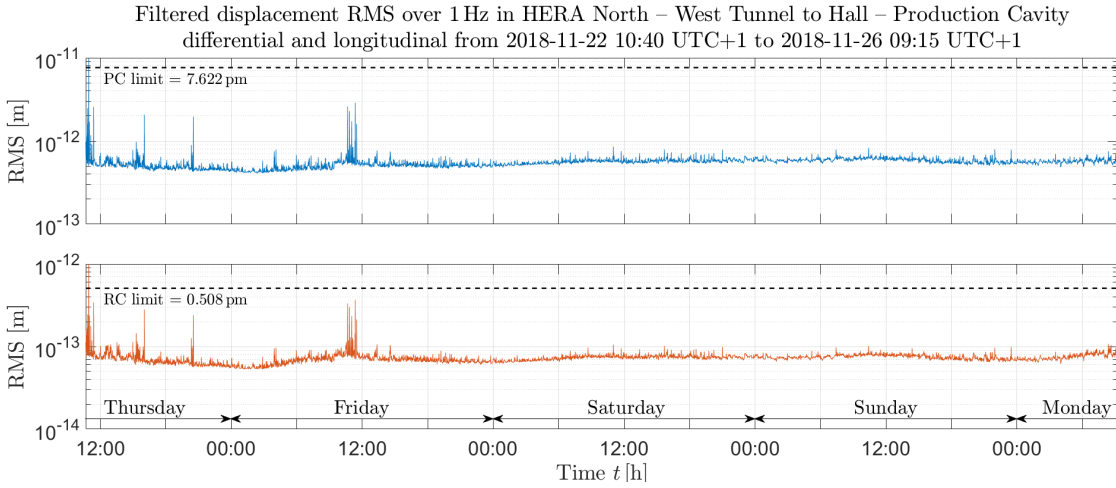
Except for a few outliers (due to workers that will not be present while ALPS IIc data is taken), the filtered RMS value down to 1 Hz does not exceed the limits. Thus, the results from figures 4.55 and 4.56 suggest that no seismic isolation is needed to meet the



## 4.5. Data evaluation



**Figure 4.55.:** Filtered differential displacement LSDs & RMSs of HERA North (ALPS IIc) Production and Regeneration Cavity on 2018-11-23 and 2018-11-26 UTC+1. Analysing characteristics: Kaiser window with a beta factor of 2.5 and 20% overlap; analysed with MfwaFFT with a *dod* of 12. Filter characteristics: attenuated by the cavities with  $f_p = 74.95$  Hz for PC and  $f_p = 5.00$  Hz for RC and by the control loop with a unity gain frequency of 4 kHz.



**Figure 4.56.:** Filtered displacement RMS of HERA North, West Tunnel to Hall in longitudinal direction from 2018-11-22 at 10:40 UTC+1 to 2018-11-26 09:15 UTC+1. Analysing characteristics: 5676 averages (1 min) with Kaiser window with a beta factor of 2.5 and 20% overlap. Filter characteristics: attenuated by the cavities with  $f_p = 74.95$  Hz for PC and  $f_p = 5.00$  Hz for RC and by the control loop with a unity gain frequency of 4 kHz.

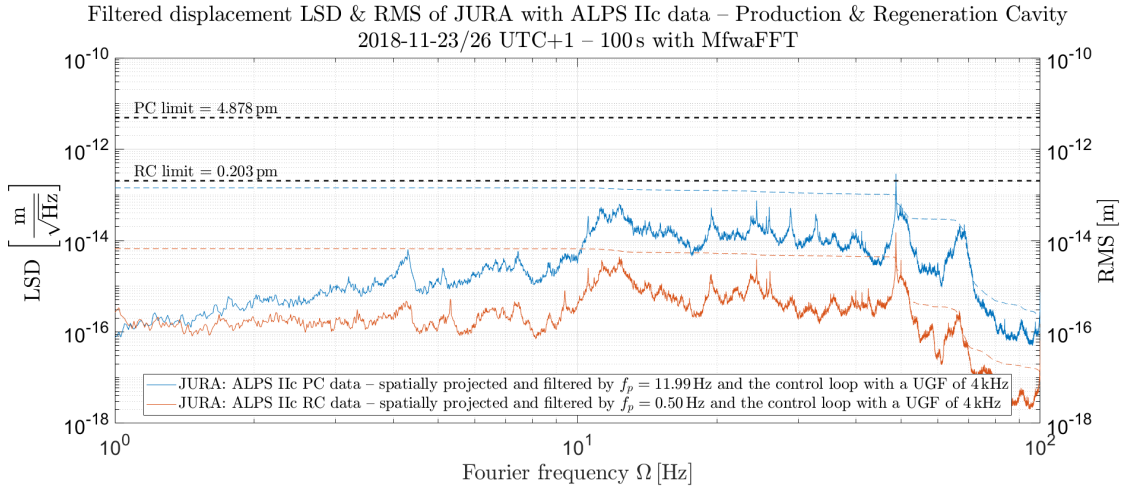
ALPS II requirement of a longitudinal offset of less than 7.622 pm for the PC and less than 0.508 pm for the RC!

In general, seismic measurements should be taken regularly during the construction of ALPS IIc. This is to especially observe the effects of the magnets and the FFUs in the final set-up. In addition, a detailed analysis should be carried out, as soon as the

optical tables are implemented in the clean rooms. This data then has to be compared to the results presented above.

### 4.5.3. Specifications for a JURA isolation

As an assumption, the data taken from the ALPS IIc site is projected onto the JURA specifications. Therefore, the identical procedure as for ALPS IIc was used, but on the JURA optics specifications of table 3.1. These are a cavity length of 500 m, a finesse of 12,500 for the PC and 300,000 for the RC [46]. The filtered LSDs and RMSs are shown in figure 4.57.



**Figure 4.57.:** Filtered differential displacement LSDs & RMSs of an assumption for JURA by the HERA North (ALPS IIc) Production and Regeneration Cavity data measured on 2018-11-23 and 2018-11-26 UTC+1. Analysing characteristics: Kaiser window with a beta factor of 2.5 and 20% overlap; analysed with MfwaFFT with a *dod* of 12. Filter characteristics: attenuated by the cavities with  $f_p = 11.99$  Hz for PC and  $f_p = 0.50$  Hz for RC and by the control loop with a unity gain frequency of 4 kHz.

In the figure the requirements are fulfilled. That is because the PLL control loop makes a significant contribution to the suppression of seismic noise. Considering actuating on larger optics, due to the divergence of the laser beam, and therefore larger inertial forces, it may not be wholly transferable from ALPS II to JURA. The assumption therefore is that accounting for the size of the larger experiment seismic isolation will be required.

In conclusion, a seismic isolation system will not be of primary importance for the achievement of the objectives of ALPS II. Therefore, the following chapter describes a seismic isolation concept as a backup system for the ALPS IIc experiment and as a basis for what is needed in the JURA experiment.

## 5. Development of seismic isolation systems

This chapter describes the development of a seismic isolation system. Section 5.1 introduces a procedure that explains the method of dealing with seismic noise or isolation problems. Following, two high-end state-of-the-art isolation concepts will be presented to give an outlook on modern isolation solutions in section 5.2. This basis was used to develop a seismic isolation model for possible damping of the ALPS II cavity mirrors. The simulations, constructions, and evaluations made for this are presented in section 5.3. The last section outlines a seismic isolation concept that could be applied to JURA in 5.4.

### 5.1. Procedure for handling seismic noise and isolation problems

The following section describes how to manage a seismic isolation problem. In most cases, the defined requirements limit the seismic noise to a maximum amplitude or a maximum RMS value at a particular frequency or in a specified frequency range, as in the case of the ALPS II experiment. These requirements can also be unknown especially in scientific research because technical solutions are not obviously available. The following subsections will describe how to solve the problem step by step, from the analysis of the seismic noise of the object under investigation over to the design of a possible isolation concept, to the final evaluation of the developed solution.

#### Seismic noise analysis

First, the object or system of examination and its parameters have to be determined. Before performing a seismic noise analysis, as described in chapter 4, the background conditions such as the frequency band, measurement points, the on-site environment, and the required accuracies, tolerances and limits must be defined. Therefore, suitable equipment for the measurement and acquisition of seismic noise have to be selected and evaluated. This can be done in a calibration and accuracy analysis (compare section 4.2). If a priori information is available, it can be used in the study for a more detailed modal analysis, for example, if it is known that a particular frequency is critical. The seismic noise analysis should cover three-dimensional and long-term or day-night effects, preferable under final conditions, always including a reference. The results can be used to evaluate the seismic situation, to design a seismic isolation system, and as input for a monitoring or feed-forward control scheme.

**CAD-Draft**

If an isolation system is required, a CAD draft must be created. It forms the common basis for the FEM simulation and the subsequent construction. Hence, the results of the seismic noise analysis are adopted to define the dimensions and material of the isolation to be used. The design should not contain details such as bore holes or surface treatments, instead focus more on dimensions, contact points and mechanical damping properties. It is useful to choose a CAD software that allows easy integration into a later FEM simulation.

**FEM simulation**

The FEM simulation, performed for example with ANSYS [40], is used to obtain a transfer function for the seismic isolation system under investigation and a response to the desired, applied excitation. Therefore, the correct definitions of the connections and the meshing of the objects are mandatory. To obtain an effective sequence, the following analyses should be built on each other.

In an FEM simulation, material properties such as the density or mechanical strengths are based on material characteristics that are fed into the system. These characteristics result from stress and load tests and therefore are based on real circumstances, including errors in the grain boundaries or in the crystal lattice. They can be found in table books [48, 49]. Thus, changing materials in an FEM simulation also change their characteristics, considering material uncertainties.

First the system has to be set to the correct conditions (“Static Structural” in ANSYS). Here, outer contact points are defined as well as standard earth gravity and possible pre-loads are applied to obtain resulting deformation and stress information. The pre-stressed model is then applied in a modal analysis (“Modal” in ANSYS) to obtain all modes with their associated frequencies. As no excitation is applied here, this step can therefore be considered as a preliminary analysis for further investigations.

In order to obtain a transfer function, as described in 2.1.4.3, a response to a defined excitation must take place over a certain frequency range (“Harmonic response” in ANSYS). Here, the decay rate for the damping of the object must be taken into account (compare subsection 2.1.2). Ideally, the result is similar to that of the harmonic oscillator (compare with 2.3.1.5). If the response of a measured excitation is pertinent, a spectra of it can be used to calculate the total deformation on the system (“Response spectra” in ANSYS).

Depending on the task, the results must be checked for their congruity, compared with existing results, or validated with an existing model. At this point, it is cost-efficient and easy to apply changes to the fundamental design.

**Design drawing, construction, and manufacture**

The next step is to create design drawings for the construction and later manufacturing. In the case of a sensitive experiment in physics, like the ALPS II experiment, the vacuum compatibility has to be fulfilled for each part. This prohibits the use of some materials, such as diffusing plastics, liquids, and ultra fine threads often used in optics. In addition,

details and tolerances have to be specified.

### Comparison of measurements to simulations

Subsequently, another seismic analysis, this time of the manufactured system has to be carried out. If not already undertaken, a comparison must be made with the FEM simulations. If deviations occur, they must be described and the simulation has to be adjusted. If requirements are no longer met, the process must be iterated until the results converge.

### Evaluation of seismic isolation

Finally, the seismic isolation system is evaluated in terms of general applicability, reusability, and cost. The results can then be implemented into an existing experiment or project.

## 5.2. State-of-the-art seismic isolation concepts

The following sections presents some high-end state-of-the-art seismic isolation concepts that are in use for the gravitational wave detectors Laser Interferometer Gravitational-Wave Observatory (LIGO) [16] and Virgo [27] located at the European Gravitational Observatory (EGO) as they require unprecedented seismic levels of isolation. The LIGO concept focuses on active control loops, whereby the Virgo concept centres more on passive isolations.

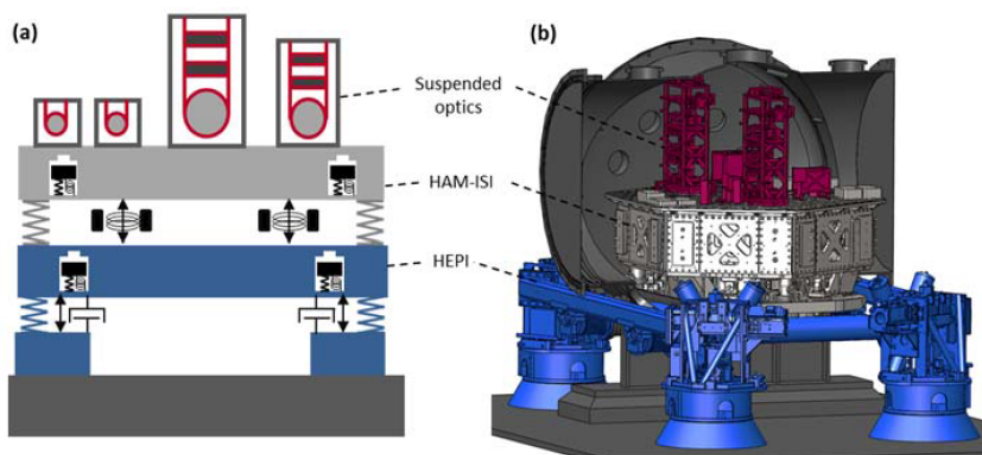
### 5.2.1. The LIGO system

Briefly explained in [51], LIGO developed a three staged passive-active isolation system to attenuate seismic noise to the attometre level. Parts of it are based on the results of the GEO600<sup>1</sup>. Figure 5.1 shows the isolation concept using the example of the Horizontal Access Modules (HAM). The blue stage indicates the Hydraulic External Pre-Isolator (HEPI) for low-frequency suppression or pre-positioning of the vacuum chamber. The grey area represents the Internal Seismic Isolators (ISI) in combination with the HAM chamber. The suspended optics are indicated on top in red [51].

In the final set-up, the HEPI is only used as an alignment and support stage. The first isolation is made by suspension springs of the HAM-ISI stage that passively suppresses seismic noise above the resonant frequency (compare with 2.3.1.5). Furthermore, relative sensors in combination with actuators actively control the stage accounting for the support at low frequencies via a feedback loop. In addition, inertial sensors provide feedback and feed-forward control of the ISI (compare subsection 2.3.2). Therefore, all six Degrees Of Freedom (DOF) can be controlled independently [51]. The last stage includes a triple-coupled pendulum, which is vertically suspended. The first two pendulums are controlled via Another Optical Sensor Electromagnetic Motors (AOSEMs) which act as non-contact sensors and actuators at the same time to adjust the optics more accurately

---

<sup>1</sup>The GEO600 is ground-based interferometric gravitational wave detector located near Hanover: <http://www.geo600.org/>



**Figure 5.1.:** LIGO seismic isolation system at the example of the HAM camber – conceptual (a) and CAD (b) design – taken from [51].

with respect to its frame. The three staged passive-active isolation system allows LIGO to operate the mirrors within an accuracy of a few attometres [15].

### 5.2.2. The VIRGO system

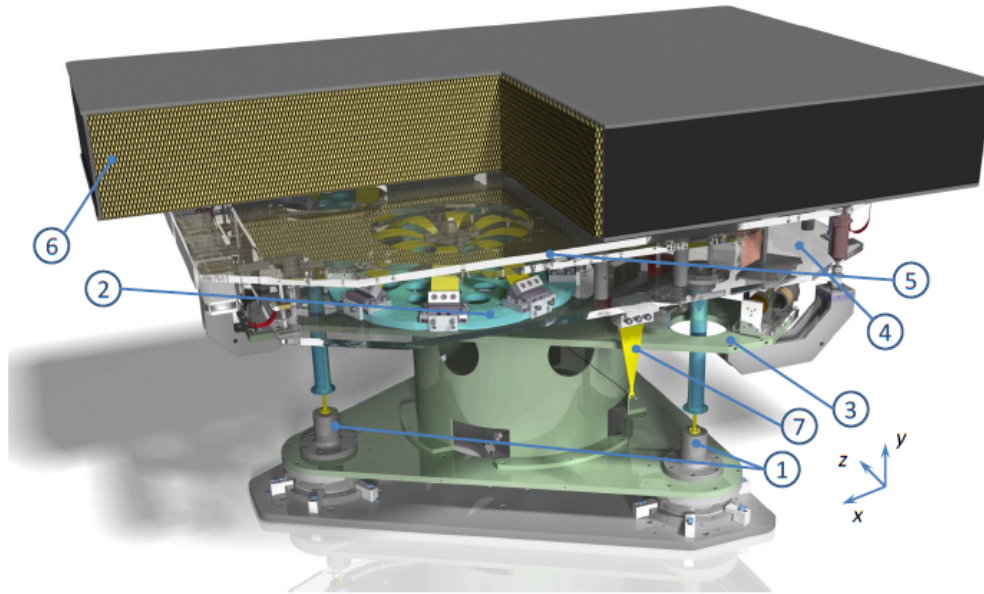
The Virgo collaboration developed the External Injection Bench Seismic Attenuation System (EIB-SAS) for seismic isolation of the Advanced Virgo based on the principles of the HAM-ISI. The system uses Inverted Pendulums (IPs) and Geometric Anti-Spring (GAS) filters (compare subsection 2.3.1) to tune seismic noise at low-frequencies. Figure 5.2 shows the EIB-SAS as a conceptual design [10].

The GAS filters' natural frequency can be tuned to below 400 mHz to allow a lower unity-gain-frequency of the control system. Their resonance frequencies are attenuated with the Linear Variable Differential Transformers (LVDTs), geophones, and feedback controls. Therefore, the EIB-SAS allows relatively small dimensions for seismic isolation in all DOF [10, 8].

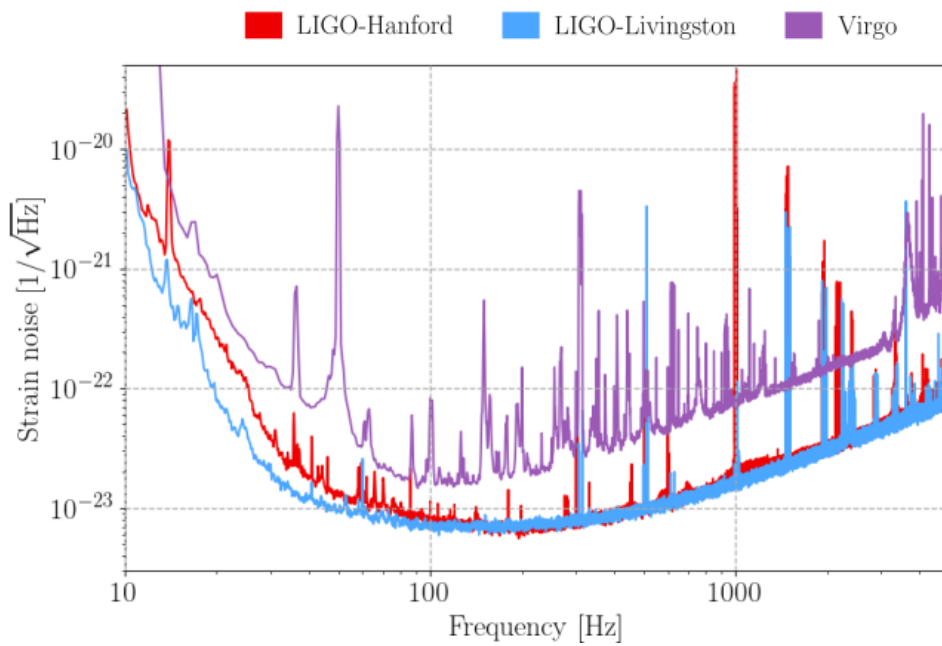
These high-end seismic isolation systems can reach sensitivities at the attometre level. This is visualised in the example of an LSD showing the strain noise<sup>2</sup> of the LIGOs and the Virgo interferometers.

The achieved sensitivity is one millionth of the sensitivity required for the ALPS II experiment. A seismic isolation system for the ALPS IIc or JURA experiment can therefore be less complex.

<sup>2</sup>Strain noise is the normalised displacement by being divided by the length of the cavity – here 4 km.



**Figure 5.2.:** Schematic of the EIB-SAS with three inverted pendulums (1), GAS filters (2), a LVDT platform (3), a springbox (4), a top-plate (5), an optical bench (6), and a tilt stabiliser (7) for seismic noise suppression at low-frequencies [10].



**Figure 5.3.:** Strain noise LSD achieved at O2 observing run of LIGOs and VIRGO cavities – taken from [27].

### 5.3. Development of a seismic isolation system

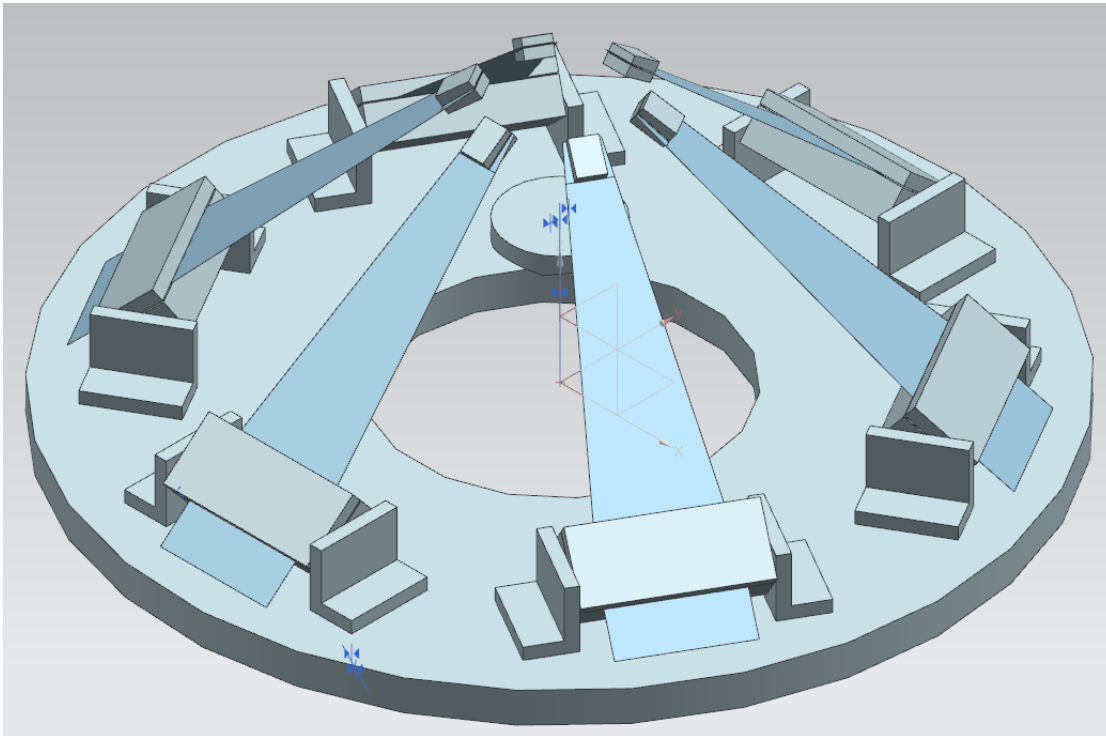
Chapter 4 concludes that ALPS IIc does not require a seismic isolation system to meet its requirements. This is true if all the assumptions made were correct. Hence, a seismic isolation concept was developed as a backup system for ALPS IIc and as a baseline for JURA. As described in section 5.1 the seismic noise analysis is used as a basis for the development. Here, frequencies between 1 Hz and 100 Hz have been shown as critical and thus have to be damped. Therefore, the concept of the IP and the GAS were modified to develop a seismic isolation system with very low natural frequencies to meet the ALPS IIc or JURA requirements if seismic noise increases or the control loop does not work as expected. In a first step, a test model was developed to enable different pendulum lengths and weights as well as small dimensional and angular changes. The aim was to test whether the methods of the systems shown above are applicable to the ALPS requirements. Therefore, a simulation must be performed and compared with measurements on an existing model. For this purpose, a cost-effective suppression of low-frequency seismic disturbances in small dimensions should be made possible.

#### 5.3.1. CAD draft of a test model

The dimensions of the test model were defined to be at a maximum  $400\text{ mm} \times 400\text{ mm} \times 400\text{ mm}$  to easily fit inside a vacuum tank. Since the most complex part of the Virgo EIB-SAS is the vertical isolating GAS filter, it was examined in more detail. Figure 5.4 shows a model named Spider, a simplified version of the GAS filter with only 200 mm in diameter.

The draft allows for FEM simulation and sets the basis for construction. The baseplate is rigidly mounted with a frame and acts as a fixed support for the model. The pendulum wire is attached to the centre of the so-called keystone, which represents the suspended optics. Six spring blades are used to dampen the vertical vibrations which can be mounted in a flexible angle (and position) on the baseplate and also with an increment of  $5^\circ$  on the keystone. The length of the pendulum determines the natural frequency of the damping in the horizontal (compare with equation (2.89)), wherein the stiffness of the spring blades together with the applied mass define the vertical damping (compare with equation (2.94)). Since the length of the wire is inversely proportional to the natural frequency, the maximum length possible is chosen. The calculation for the vertical natural frequency on the other hand is not as trivial. The stiffness depends on the load applied to the system, the material properties, the thickness, the length, and the angle of the spring blades. For a low natural frequency, a low stiffness is desired. Therefore, a spring steel (7C27Mo2) and again the maximum length for the spring blades were selected. Different loads, different blade thicknesses, and slightly different blade lengths and angle settings for vertical damping were tested in the FEM simulation.

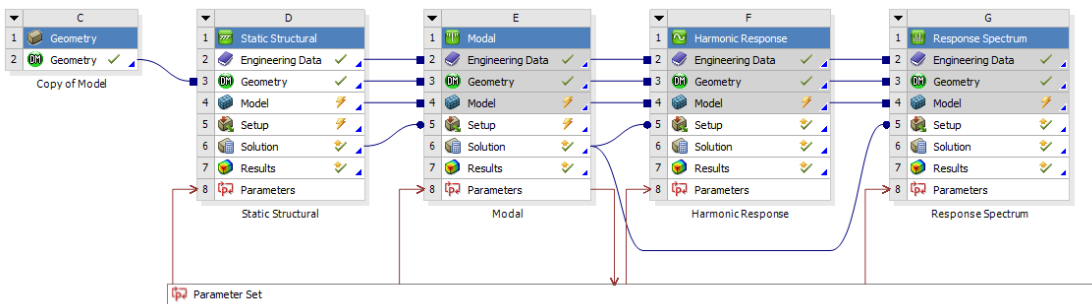




**Figure 5.4.:** Schematic of the Spider with the blades mounted to the outside blocks without bending them.

### 5.3.2. FEM simulations

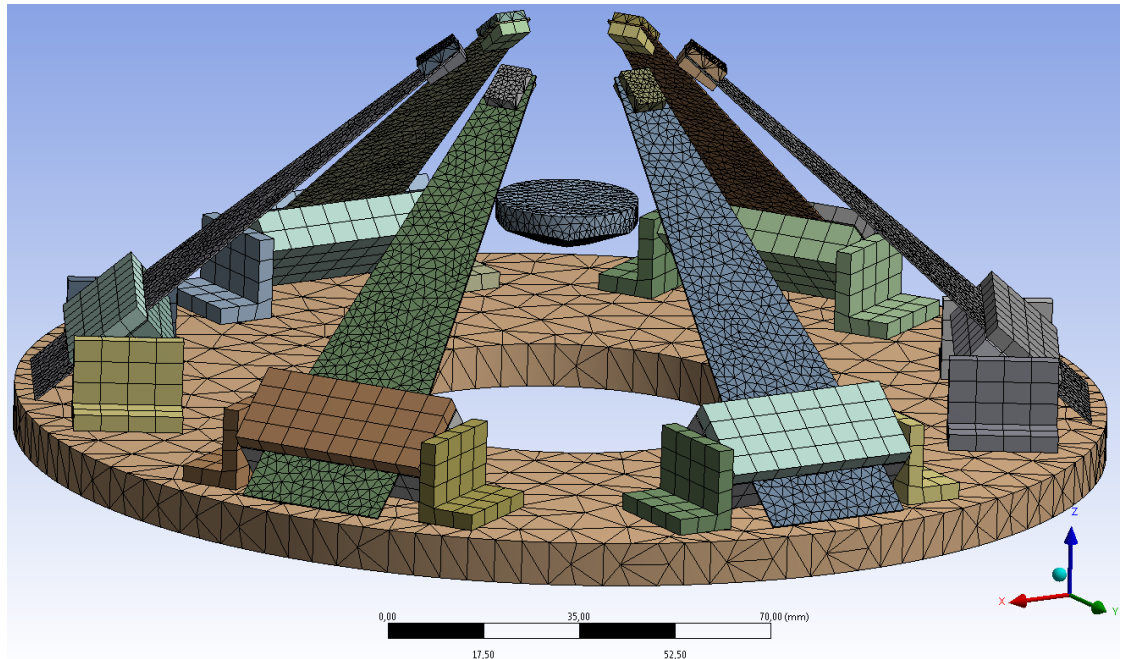
As described in subsection 3.2.3 ANSYS was used to execute the FEM simulation. To obtain a transfer function and a response for a given excitation of the Spider isolation system, all the steps from the FEM simulation mentioned in section 5.1 were carried out. Figure 5.5 shows an overview of all the steps defining the optimal specifications for the Spider.



**Figure 5.5.:** Overview of steps of the FEM simulation carried out to define the optimal specifications for the Spider.

The parameter set varies the blade thickness and the load applied to the keystone. The blade thickness ranges from 0.18 mm to 0.40 mm in 0.02 mm increments and the load from 0.3 kg to 6.4 kg in 0.1 kg or with more detail in 0.02 kg increments. Those results are shown later.

The geometry of figure 5.4 was used in “Static Structural” of ANSYS to calculate the total deformation and equivalent stress of the system under the bending forces and gravity. On the keystone an angle of  $30^\circ$  was used, whereas on the baseplate nearly  $45^\circ$  was applied. A mesh was selected that concentrates on the critical areas at or around the spring blades. This is visualised in figure 5.6.



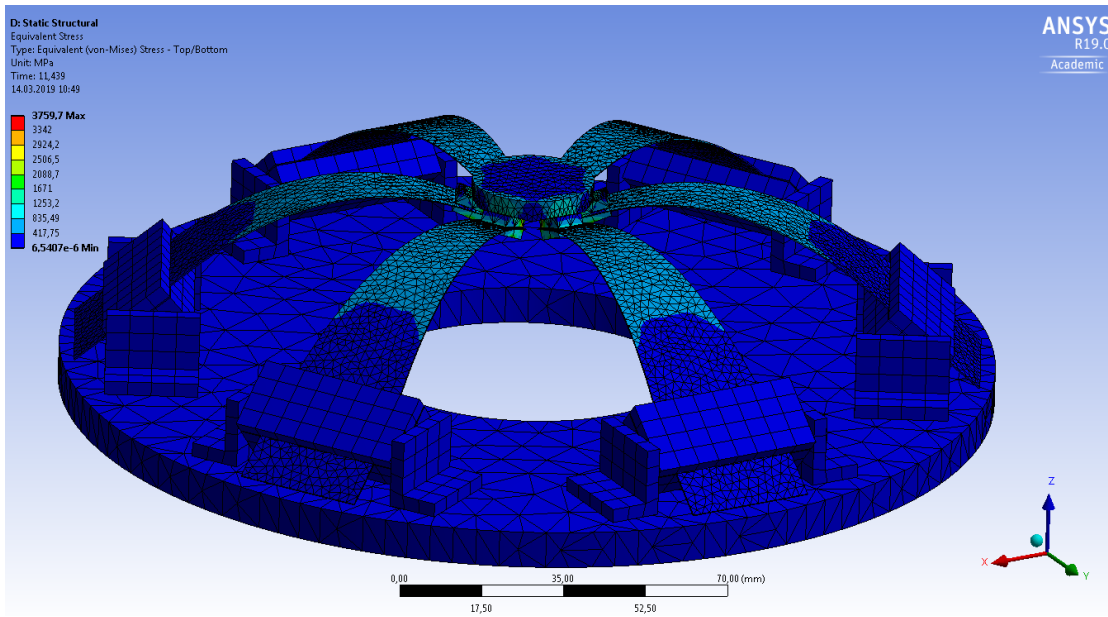
**Figure 5.6.:** Geometry of Spider imported into ANSYS with an applied mesh.

The “Static Structural” verifies whether the system would withstand the pre-deformation with the given parameters. If the blade thickness is too thin and the load too heavy, the system collapses. A working example is shown in figure 5.7 with a blade thickness of 0.30 mm and an applied load of 2.3 kg.

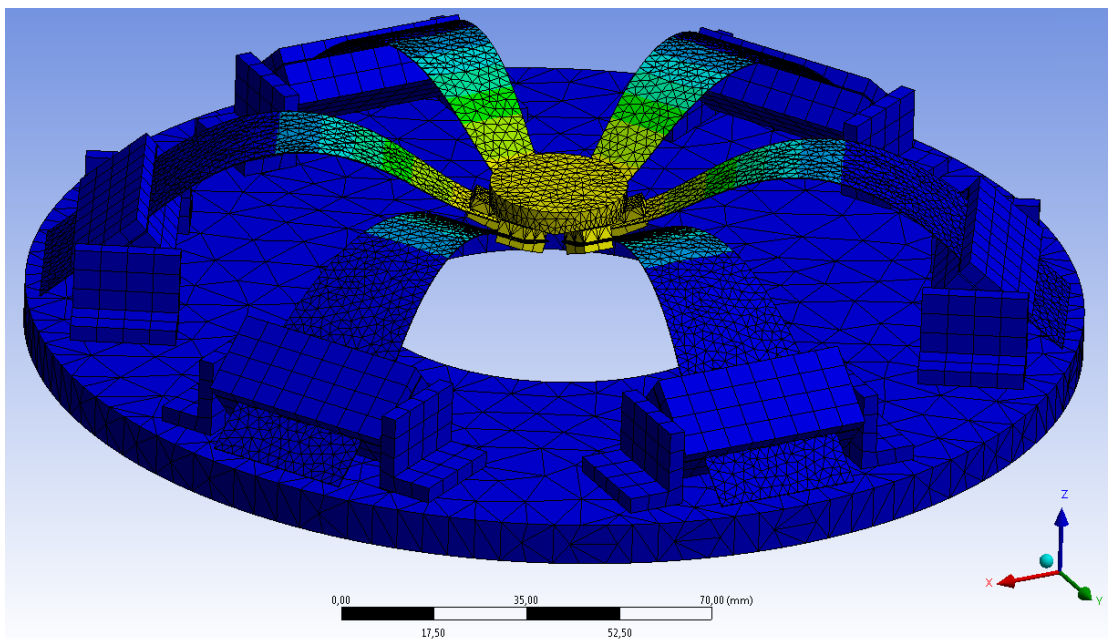
The colours indicates the equivalent stress, where the blades reach their maximum at approximately 900 MPa. Note that the spring steel has a tensile ultimate strength of 1,763 MPa, which is almost four times higher than that of ordinary steel. Therefore, it can withstand these forces.

These results are used to perform “Modal” simulation. Here, the Spider was excited from 0 Hz to 4,000 Hz, twice as high as the frequency band which was to be examined later, to find all the relevant modes. In total 47 modes were found. An example is shown in figure 5.8 with the first mode (first natural frequency of the system) at 5.9 Hz. Again, a blade thickness of 0.30 mm and a load of 2.3 kg were applied.

### 5.3. Development of a seismic isolation system



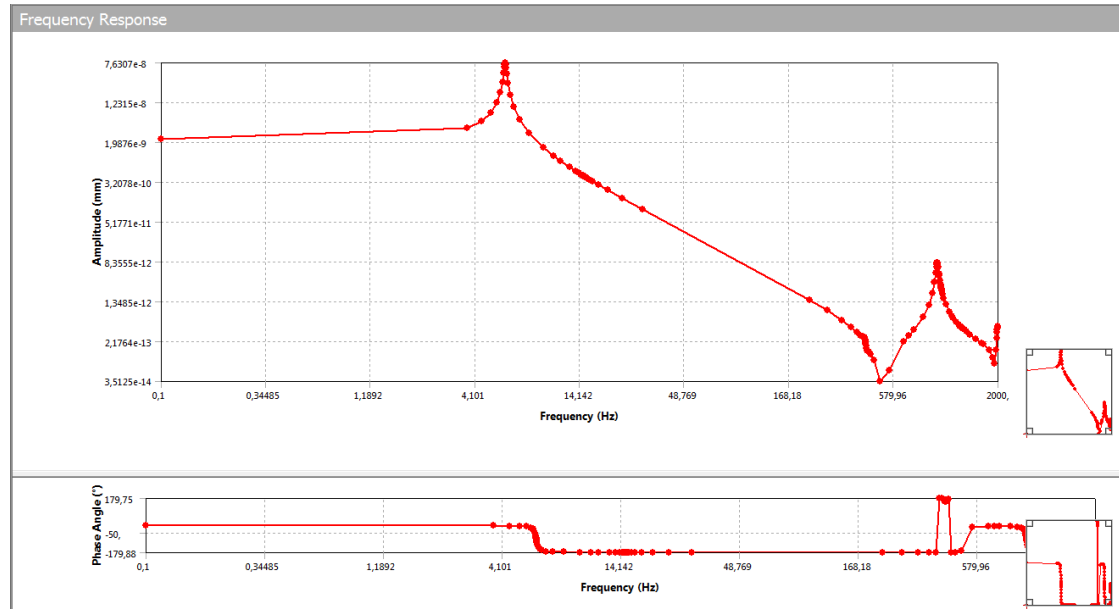
**Figure 5.7.:** “Static Structural” simulation of ANSYS showing the equivalent stress of the Spider with a blade thickness of 0.30 mm and a load of 2.3 kg.



**Figure 5.8.:** “Modal” simulation of ANSYS showing the first mode of the Spider with a blade thickness of 0.30 mm and a load of 2.3 kg.

Based on the information gained from “Static Structural” and “Modal” a “Harmonic Response” simulation was executed. The results from “Modal” were used to sensibilise

the algorithm for the correct modes. For the excitation a vertical oscillating force of 1 N (comparable to the measured results in chapter 4) from 0.1 Hz to 2,000 Hz was applied to the baseplate. Figure 5.9 shows the frequency response with an assumed decay rate of  $\{\beta\} = 0.015$  as a Bode plot.



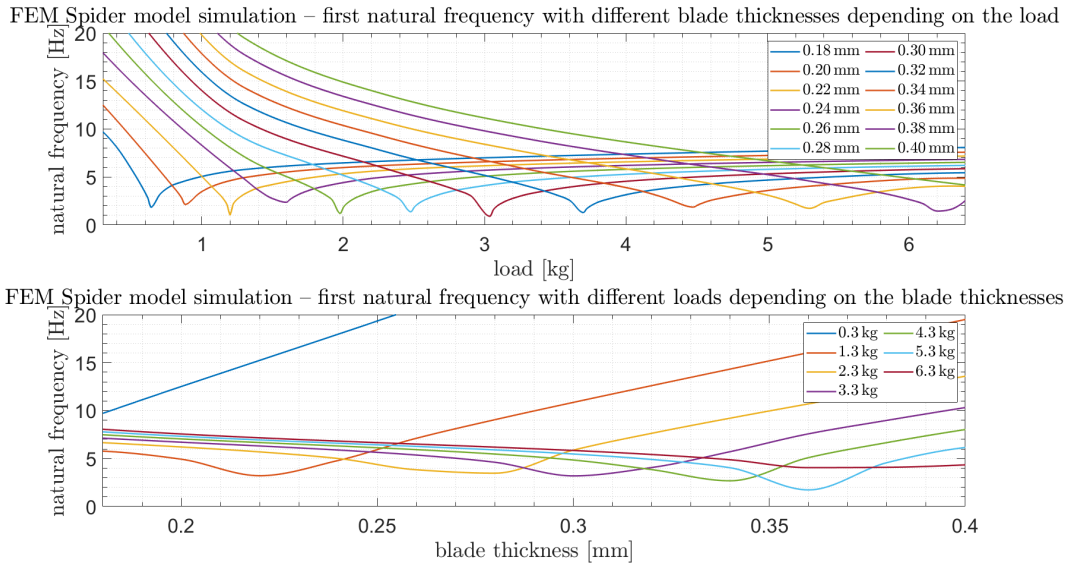
**Figure 5.9.:** Frequency response in vertical direction with an excitation of 1 N at the baseplate and a decay rate of  $\{\beta\} = 0.015$  as Bode plot of the Spider with a blade thickness of 0.30 mm and an applied load of 2.3 kg.

The figure shows the effect of the first mode at 5.9 Hz and some higher modes (see figures E.1 and E.2 in appendix E) at 418 Hz and 979 Hz. To examine the effect of different blade thicknesses and loads, a parameter-based simulation was performed. The results depending on the blade thickness or the load are shown in figure 5.10.

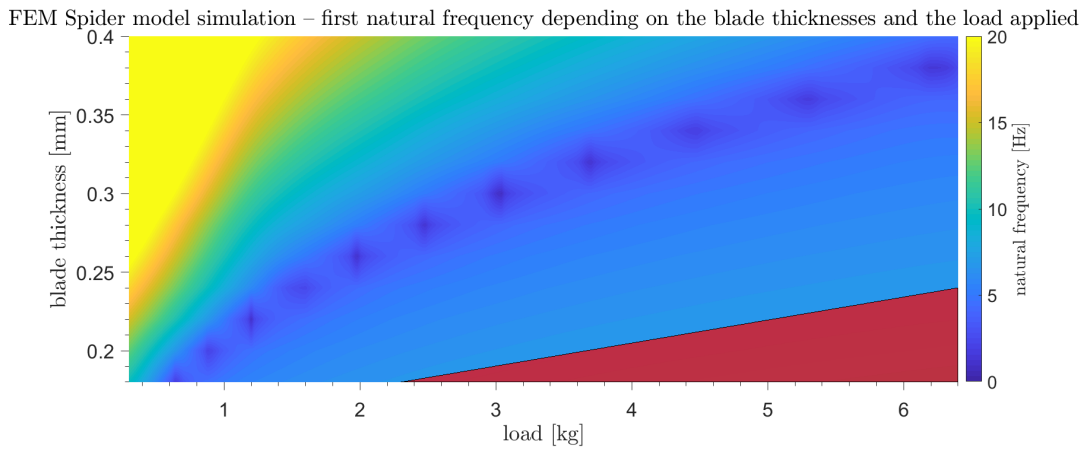
For better clarity, figure 5.11 shows the two-dimensional effect in a coloured plot, with blue indicating low and yellow high frequencies. The red area represents the region where the system collapses due to the combination of thin blade thickness and heavy load.

To obtain the total displacement of the keystone, a “Response Spectrum” was carried out. Therefore, a given measured excitation (RMS in units of acceleration) from HERA North Hall (compare with figure 4.40) was applied to the baseplate with an assumed decay rate of  $\{\beta\} = 0.015$ . This is shown in figure 5.12.

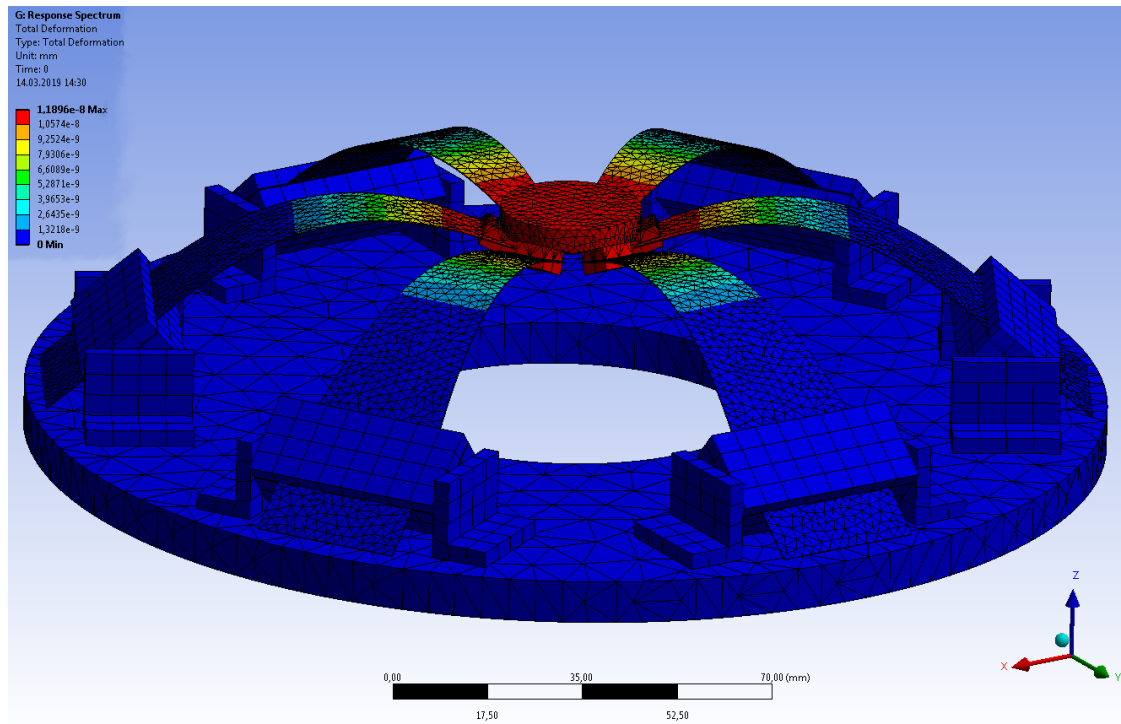
The figure indicates a total displacement of less than 12 nm with a total RMS of more than 1  $\mu\text{m}$ , which refers to a suppression of a factor of approximately 100. Unfortunately, ANSYS only outputs one number over the entire frequency range and no frequency-dependent deformation results.



**Figure 5.10.:** Parameter-based “Modal” simulation of ANSYS showing the first mode of the Spider with different blade thickness depending on the load from 0.3 kg to 6.4 kg (upper) and with different loads depending on the blade thickness from 0.18 mm to 0.40 mm (lower).



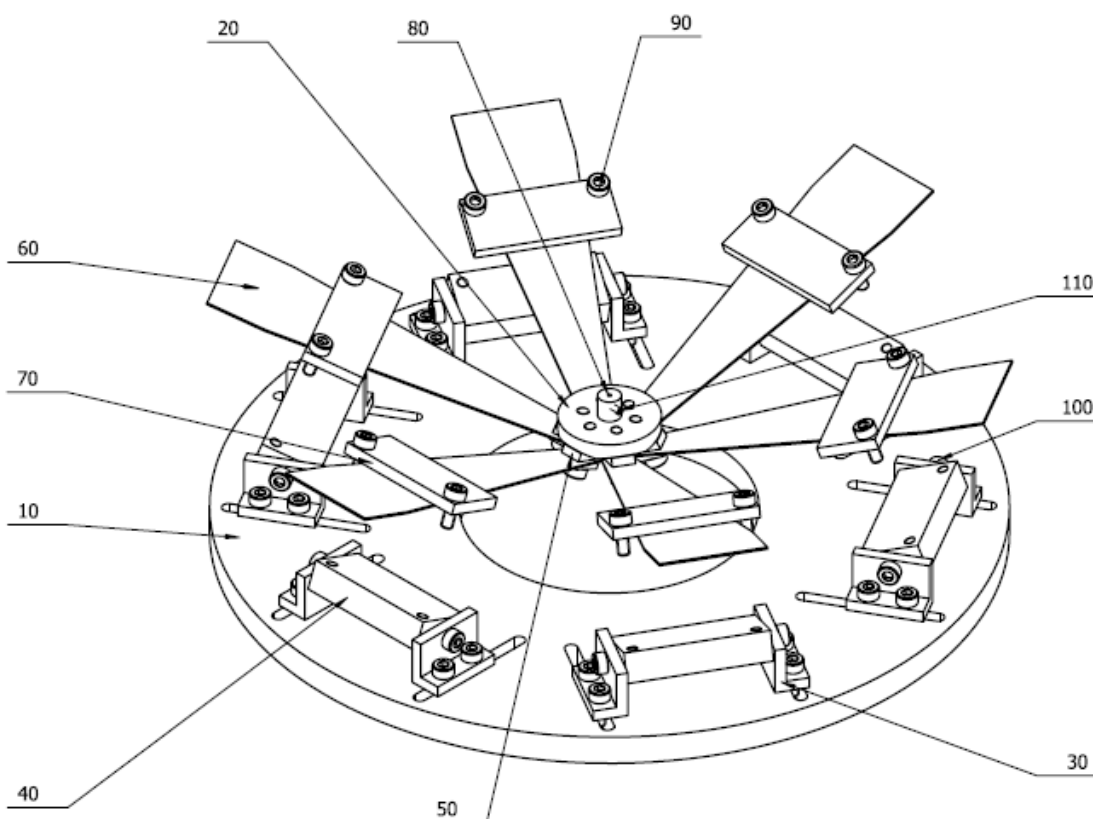
**Figure 5.11.:** Parameter-based “Modal” simulation of ANSYS showing the first mode of the Spider with a blade thickness from 0.18 mm to 0.40 mm and an applied load from 0.3 kg to 6.4 kg with the red area indicating the system collapse.



**Figure 5.12.:** “Response Spectrum” simulation of ANSYS showing the total displacement of the Spider with a blade thickness of 0.30 mm and an applied load of 2.3 kg with a measured excitation from the HERA North Hall applied.

### 5.3.3. Design drawing

The designed and simulated Spider model was manufactured according to the technical drawing of figure 5.13. Here, M3 size cylinder head screws, nuts in the baseplate, and a socket for tightening the pendulum wire with two threaded pins are included. Except for the blades, the model is made out of aluminium because it is lightweight, easy to work with, and compatible for vacuum.



**Figure 5.13.:** Technical assembly drawing of Spider with base plate (10), keystone (20), angle brackets (30), tiltable blocks (40), wedges (50), spring blades (60), fixation plates (70), socket (80), and screws (90) – (110) with the blades mounted to keystone.

The manufactured components were assembled with the option of different blade thicknesses from 0.10 mm to 0.50 mm and additional 1 kg weights that can be applied to the system. These components were tested to verify the results of the FEM simulation. Figure 5.14 shows a photograph of the manufactured Spider including three spring blades.



**Figure 5.14.:** Photograph of the Spider including three spring blades.

#### 5.3.4. Evaluation and validation

The Spider was examined on a RK Rose + Krieger<sup>3</sup> profile frame. Two 731-207 accelerometers were used to register the oscillation on the baseplate and on the suspension point. The data was acquired with the Tektronix Digital Phosphor Oscilloscope DPO7000 with a sample rate of 50 kHz. The suspension point is defined by the end of a 1 m long guitar string, which is fixed in the socket hanging downwards. The sensor with its mounting block has a total weight of 0.3 kg and was suspended from the Spider together with 1 kg weights. Thus, loads with a weight from 0.3 kg to 5.3 kg were applied with a blade thickness of 0.30 mm. This was chosen because it allows the largest load range (compare with figure 5.11). The LSDs with their RMSs of the vertical measurements are plotted in figure 5.15 along with the data from figure 5.9.

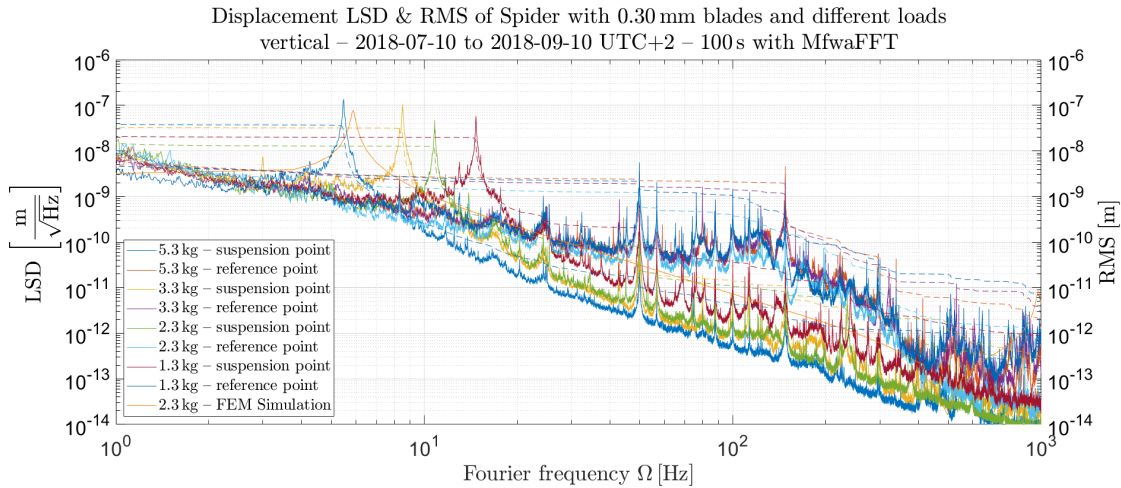
The data shows a significant dependence of the first mode with the applied load, as equation (2.94) indicates. For comparison with the frequency response of the FEM simulation from “Harmonic Response” (compare with figure 5.9), transfer functions from the suspension point to the reference point were performed and visualised in figure 5.16 along with the normalised data from figure 5.9.

The line shape is the same as the simulation shows, but with slightly different specifications. A direct comparison can be made with a blade thickness of 0.30 mm and a load

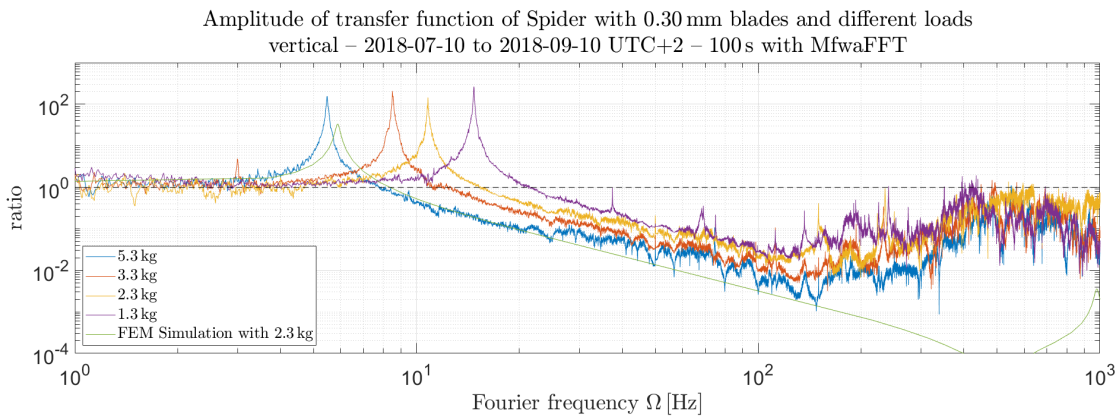
<sup>3</sup>Phoenix Mecano AG, RK Rose+Krieger GmbH produces profile assemble structures: <https://www.rk-rose-krieger.com/deutsch/produkte/modul-technik/>



### 5.3. Development of a seismic isolation system



**Figure 5.15.:** Displacement LSDs & RMSs of Spider with 0.30 mm blades with different loads in vertical direction on 2018-07-10/13/23 and 09-10 at 15:31/13:21/11:28/11:21 UTC+2. Analysing characteristics: Kaiser window with a beta factor of 2.5 and 20% overlap; analysed with MfwaFFT with a *dod* of 12.



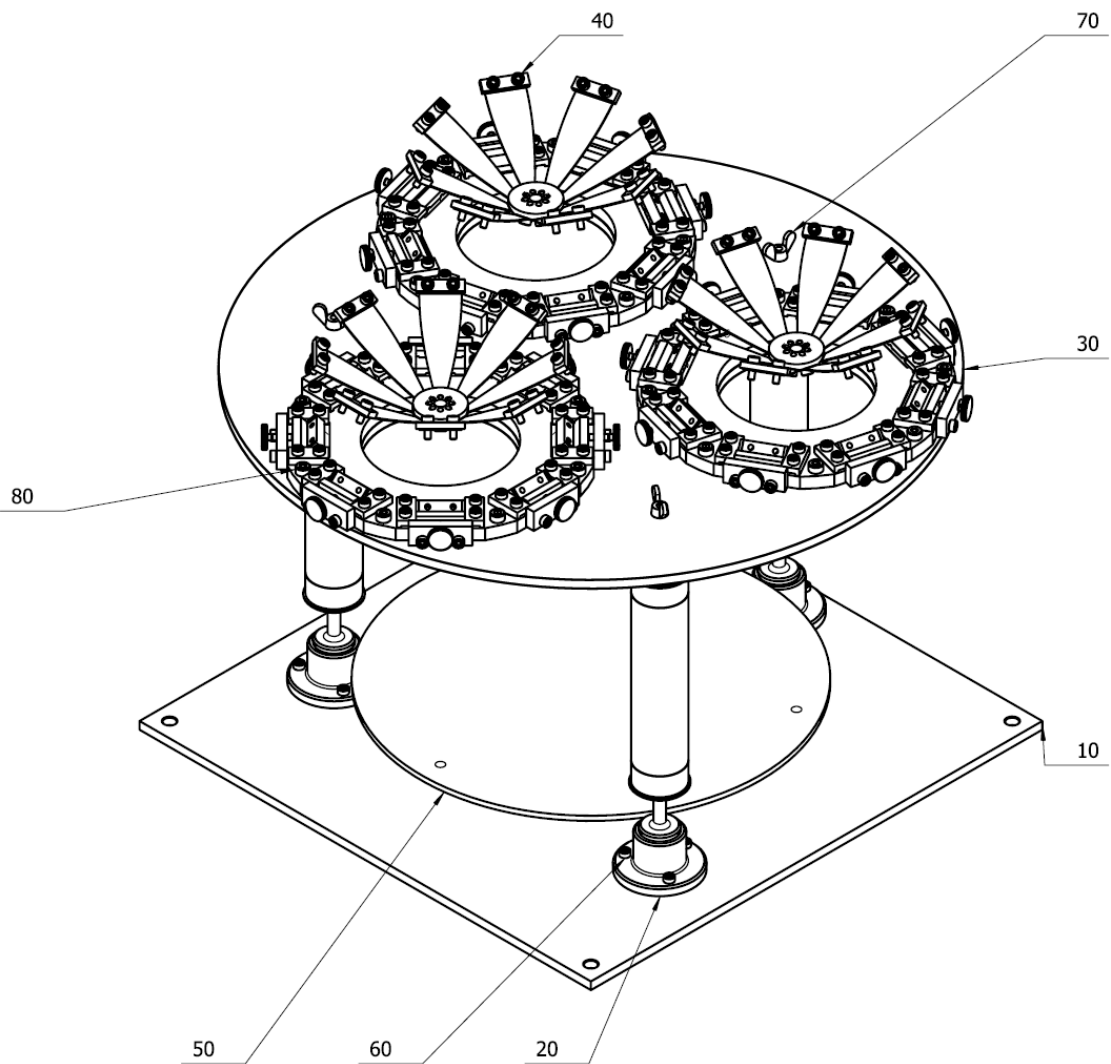
**Figure 5.16.:** Amplitude of transfer function of Spider with 0.30 mm blades with different loads in vertical direction on 2018-07-10/13/23 and 09-10 at 15:31/13:21/11:28/11:21 UTC+2. Analysing characteristics: Kaiser window with a beta factor of 2.5 and 20% overlap; analysed with MfwaFFT with a *dod* of 12.

of 2.3 kg. Here, the natural frequency varies from 5.9 Hz in the simulation to 10.8 Hz in the measurement. This is approximately a factor of 2, which can be considered as a good result. The discrepancy occurs due to not perfectly rotationally symmetric alignment and imperfect contact regions in the real measurement.

As a result a more detailed version of a seismic isolation model can be designed as a concept for ALPS IIc or JURA. This will be explained in the following section.

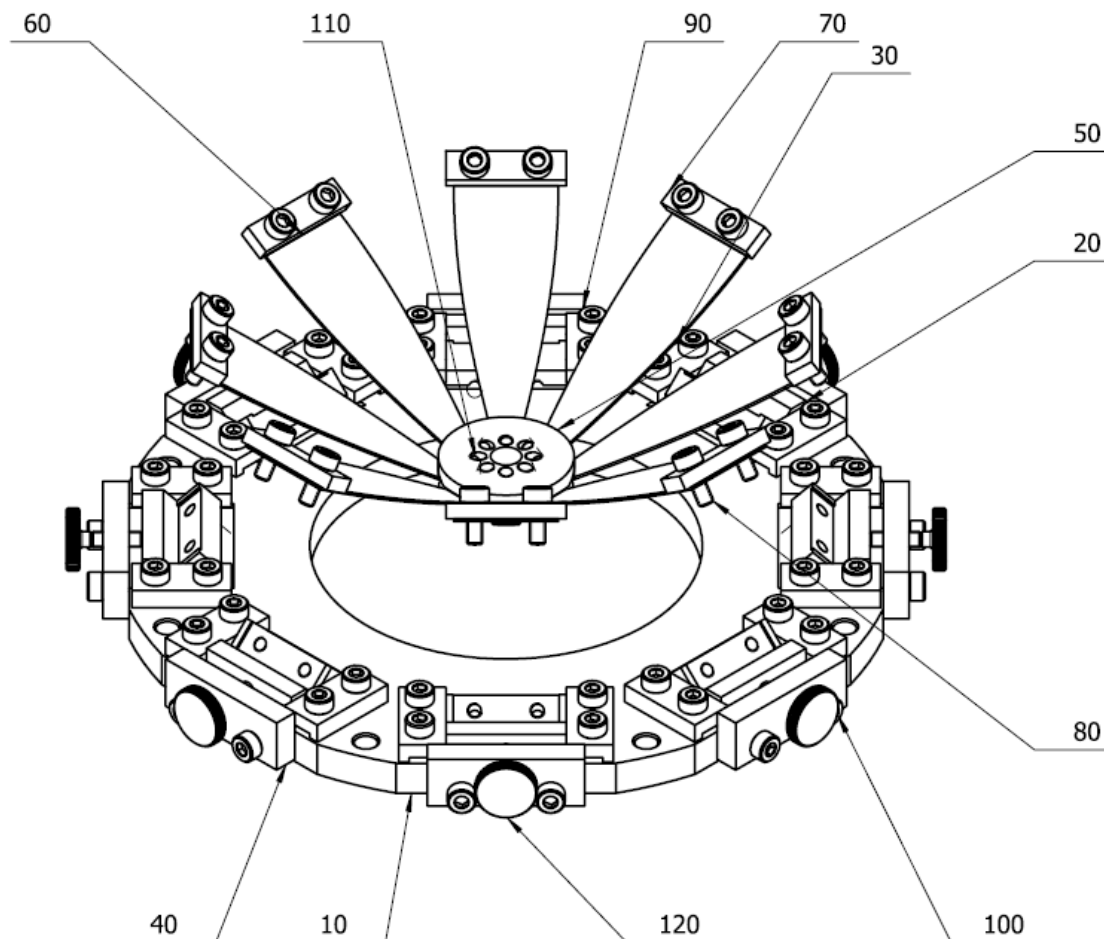
## 5.4. Seismic isolation concept for ALPS IIc and JURA

Based on the EIB-SAS [10], the results of the FEM simulation, and the measurements on the Spider, a seismic isolation concept called Seismic Isolation Non-Unified Systems (SINUS) was developed. It had to fulfil the same dimensions as mentioned above to be a maximum  $400\text{ mm} \times 400\text{ mm} \times 400\text{ mm}$  for it to easily fit inside the vacuum tank. Therefore, vacuum-compatible materials, boreholes, and threads had to be used. Figure 5.17 shows a technical assembly drawing of the SINUS. It contains a base plate, that represents the optical table, three IPs (compare with 2.3.1.3), three further developed Spiders, and a swinging plate that can accommodate the mirror.



**Figure 5.17.:** Technical assembly drawing of SINUS with base plate (10), inverted pendulums (20), upper plate (30), Spiders (40), swinging plate (50), and screws and nuts (60) to (90) – based on [10].

The upper plate has a diameter of 350 mm and the maximum height does not exceed 260 mm. The results from the FEM analysis were used to further develop the vertical isolation of the Spider. In SINUS three of these are arranged in a circle with an offset of  $60^\circ$  from the IPs. The arrangement was chosen because of the stability of the overall system. In addition, the Spiders now make use of the anti-spring effect (compare with 2.3.1.4). The new Spider design is visualised by the assembly drawing of the Spider for SINUS in figure 5.18.

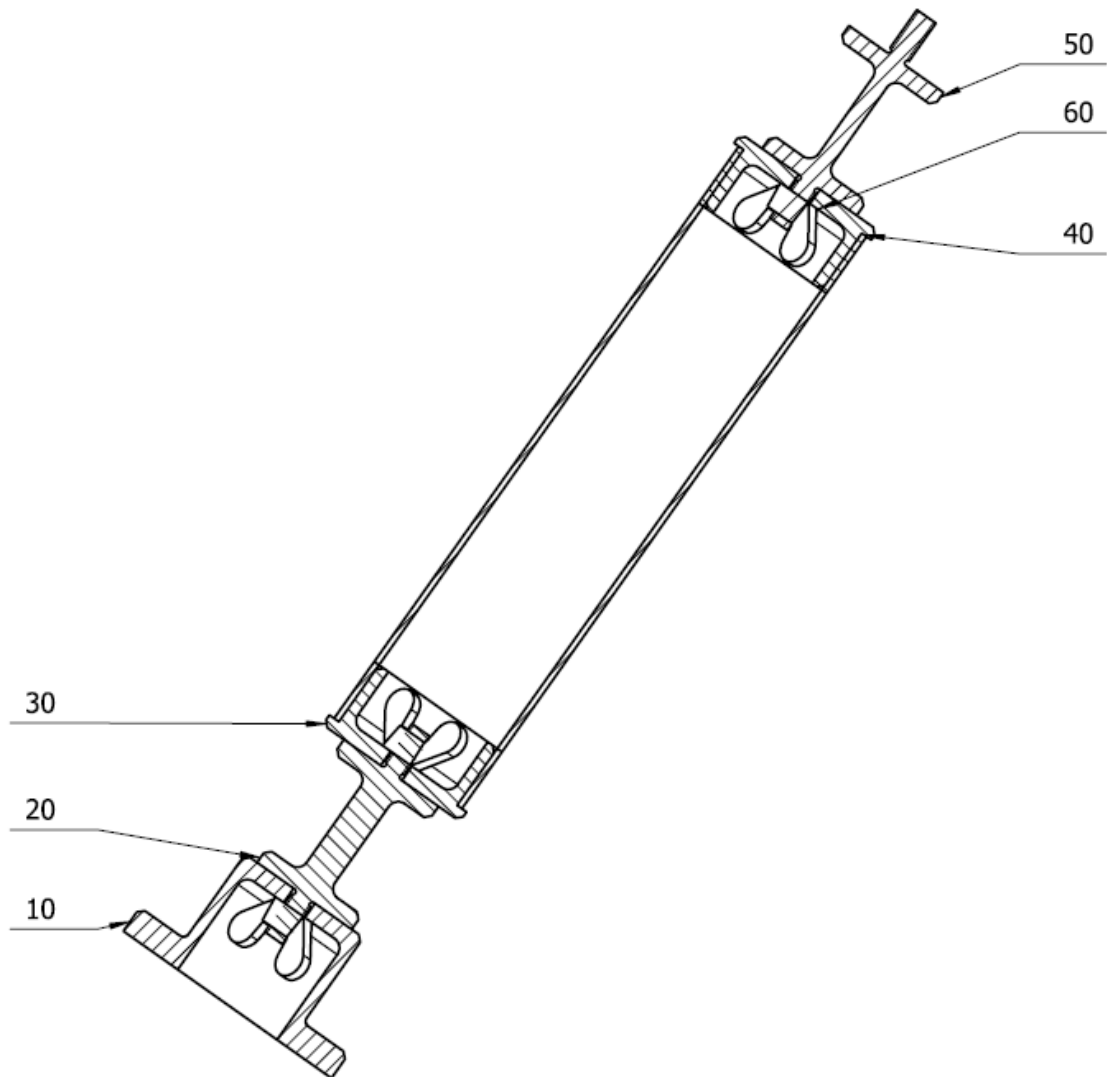


**Figure 5.18.:** Technical assembly drawing of Spider for SINUS with base plate (10), blocks (20), clamps (30), pre-load plates (40), keystone (50), spring blades (60), fixation plates (70), cylinder head screws (80) to (110), and knurled screw (120) – based on [10].

The thickness and pitch of the spring blades are determined by the results of the FEM analysis and its evaluation in subsection 5.3.4. A total weight of up to 10 kg, including the swinging plate, can be loaded on the three Spiders with a blade thickness of 0.30 mm. The blades were mounted with a pitch of  $33^\circ$  on the keystone and  $45^\circ$  on the blocks. The anti-spring effect is introduced by the knurled screws labelled as (120) in figure 5.18. They allow a pre-load force on the spring blades, which reduces

their natural frequency according to equation (2.99). Note that these forces should be applied rotationally symmetric. In addition, to allow the spring blades even more stress, Marval18 (X2NiCoMo18-8-5) is defined for the spring steel [18].

For horizontal noise suppression, an inverted pendulum effect (compare with 2.3.1.3) was used in addition to the simple pendulum of the suspension wires. Its principle is based on the IP of the EIB-SAS [10]. Figure 5.19 shows a technical assembly drawing of the designed IP for the SINUS.

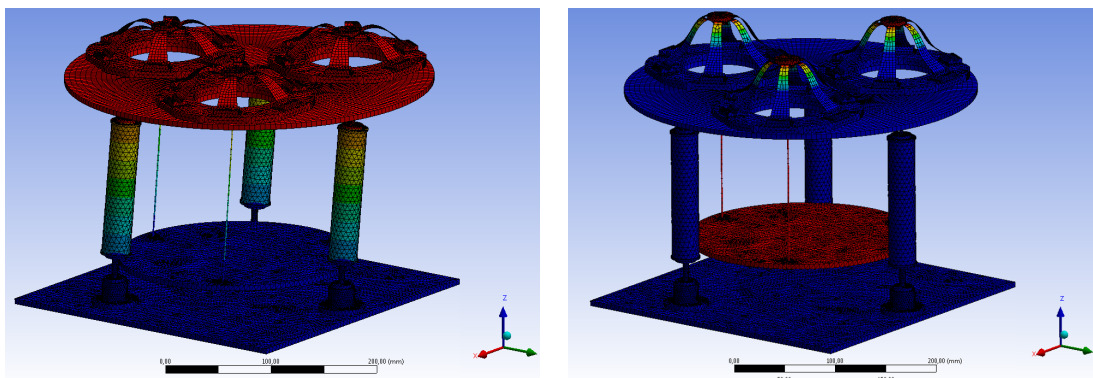


**Figure 5.19.:** Technical assembly drawing of IP for SINUS with foot (10), lower flex (20), tube connectors (30), tube (40), upper flex (50), wing screw (60) – based on [10].

The foot can be mounted onto an optical table and the tube simply defines the height of the frame. More interesting are both flexes (20) and (50) in the figure. These define

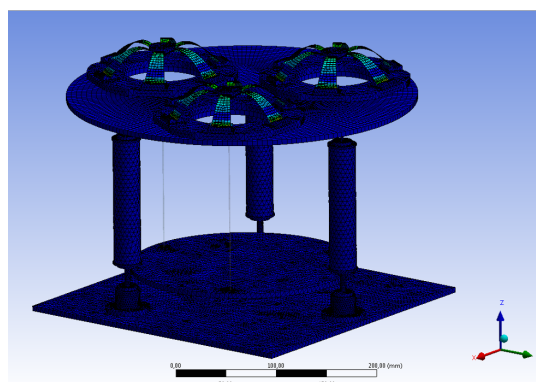
the pivot points that decrease the spring constant  $k$  from equation (2.97) used to lower the natural frequency of the IP (compare with 2.3.1.3). More specifically, the lower flex has a wider diameter than the upper flex and therefore determines the spring constant  $k$ . The upper flex only serves to counteract the resulting tilting effect. A list of all technical drawings for the SINUS can be found in appendix F.

Same as described above, an FEM analysis was performed on a simplified model of the SINUS. Figure 5.20 shows stress and main modes of the SINUS. The blue areas indicate no movement or stress, where the red ones represent the maxima.



(a) “Modal” showing the seventh mode of the SINUS at 17.58 Hz.

(b) “Modal” showing the tenth mode of the SINUS at 23.147 Hz.



(c) “Static Structural” showing the equivalent stress of the SINUS.

**Figure 5.20.:** FEM analyses of ANSYS showing stress and main modes of the SINUS.

Even without tuning the results based on the load nor applying a pre-force the first natural frequencies are acceptable. In the longitudinal direction, referring to the IPs, the first harmonic is set at 17.58 Hz. In the vertical direction, referring to the Spider, the first harmonic is at 23.147 Hz. Both results can be further improved for future work, e.g. for the implementation in an experiment like JURA.



## 6. Conclusion

Seismic noise analysis and the development of a seismic isolation concept for the ALPS II and JURA experiments have been completed. All three research hypotheses were confirmed in chapters 4 and 5. The first hypothesis concerning the understanding of wide frequency ranged data in the modal analysis was proven by the development of the MfwaFFT explained in section 4.1. The second hypothesis dealing with the transformation of the measured data from the ALPS IIa laboratory to the ALPS IIc set-up was validated by the application of the filters in section 4.4 and the evaluation in section 4.5. The third hypothesis referring to the state-of-the-art seismic isolation concepts were confirmed by the development of SINUS, the seismic isolation concept for ALPS II and JURA, in section 5.4.

More time or more advanced technical equipment would have yielded more detailed results. However, as the ALPS II experiment is already under construction and budget planning is tight, the measurements had to be completed in time. The results of the work may hopefully be considered useful for further work on the ALPS II experiment and possibly also for general scientific research.

### 6.1. Summary

When examining the frequencies of vibrations and resonances, which apply on a system like the ALPS II experiment the Fourier transform as a method of modal analysis is applied. Here, signals are broken down from the time domain to enable analyses in the frequency domain. Only then is it possible to discern the harmful frequencies for which appropriate damping measures can be developed.

The problems of an FFT are that like a map of the real-world details might get lost in the conversion process. The correct application of the parameters, for instance choosing the fitting window function, is therefore paramount to obtain a discernible result. Current methods already provide fairly adequate results, but these can be either subject to interpretation (compare with 4.1.2.1) or result in reduced amplitude accuracy (compare with 4.1.2.2). The newly developed MfwaFFT on the other hand creates a specific number of differently averaged FFTs continuously over all possible frequencies with a corresponding and differentiable window function as weight. The method can be used to analyse signals over several orders of magnitude without the need of a priori information of the data. So while a very high degree of accuracy in the resulting FFT can be claimed, another advantage is its objectivity during its calculation. This makes it attainable for future and third party analysis.

As an outcome, MfwaFFT produced highly accurate FFTs of the measurements of the pervading seismic noise on-site in the HERA ring accelerator, which is described fully in

chapter 4. Through the obtained data, it can be concluded that the ALPS II experiment does not require seismic isolation to achieve the overall sensitivity target thanks to the successfully developed active feedback control. This should provide a great asset for the experiment as one problem less to worry about.

In addition, considering a follow-up LSW experiment like JURA, a seismic isolation concept was developed (compare section 5.4). The SINUS concept is based on state-of-the-art seismic isolation concepts of modern gravitational wave interferometers and serves as a backup system for the ALPS II experiment and as a basis for a seismic isolation system for the JURA experiment.

## 6.2. Outlook

The results of a seismic noise analysis could be improved by correcting the frequency-dependent response. Furthermore, sensitivity-dependent weighting of different coupled sensors could increase the detected dynamic range. In addition, newly developed devices such as optomechanical acceleration sensors can be used for this purpose.

Regarding the current state of the site, results of the seismic noise analysis concluded in chapter 4 should be verified regularly with seismic measurements during and after completion of the construction phase of the ALPS II experiment. This is especially true for the magnet string and the FFUs as explained in subsection 4.3.3. Furthermore, detailed analyses should be carried out, as soon as the optical tables are implemented in the clean rooms (compare section 4.5).

The seismic isolation system presented in section 5.4 can be manufactured at any time if needed. Nevertheless, further simulations and adjustments on the construction can be made based on new information.

In addition, since the ALPS II experiment uses high finesse optical cavities to increase its sensitivity, it is limited by seismic noise as explained in section 3.1. To compensate for mechanical vibrations caused by seismic noise signals, a feed-forward control scheme can be applied to the present control scheme (compare with 2.3.2.2), e.g. for the ALPS II experiment. The idea is to place a seismometer at each cavity mirror (in the case of ALPS, one at the in-coupling PC mirror, one at the CBB, and one at the out-coupling RC mirror). If an accurate transfer function of the mirror mountings is available, the seismometers can be fixed onto the optical table as close as possible to the mirrors inside the vacuum vessel. The gained and adjusted information can then be fed into the control loop of the experiment to combine the feedback with the feed-forward signal (compare with 2.3.2.4). The seismometers serve as a monitoring system for seismic noise and pre-isolation feed-forward sensors for the control. This feed-forward loop could compensate for slow control and stabilise the current control design in a frequency range between 10 mHz and 2 kHz to enable long-term measurements at the ALPS II experiment.



# Appendices



## A. Notation key for documentation

*[acquisition device]\_[seismometer (+specs)]\_[location (+specs)]\_[date]\_[time]\_[sample rate]\_[measurement time]\_[additional information]*

The eight individual elements use acronyms with the following meaning:

1. acquisition device:

- *AL*: data acquired with the **ALAZAR** card
- *SA*: data acquired with the **Spectrum Analyser**
- *SC*: data acquired with the oscillo**SCO**pe
- *SC2*: data acquired with the oscillo**SCO**pe with compressed information

2. seismometer:

- *Ctrl*: **C**ontrol signal of the cavity
- *S6*: Güralp **S**eismometer CMG-6TD – internal number **6**
- *S7*: Güralp **S**eismometer CMG-6TD – internal number **7**
- *L4*: **L-4C** geophone
- *L22*: **L-22D** geophone
- *PZT*: 731-207 accelerometer (**P**ie**Z**oelec**T**ric-Sensor)
  - *XG*: **G**ain setting of P702B power unit/amplifier
    - \* *X1*: gain of **1**
    - \* *X10*: gain of **10**
    - \* *X100*: gain of **100**
  - *atI*: **I**ntegrator stage of P702B power unit/amplifier
    - \* *atA*: turned off – **A**CC-mode: output is in V/g
    - \* *atV*: turned on – **V**EL-mode: output is in V/in/s
  - *onPS*: **P**ower **S**upply of P702B power unit/amplifier
    - \* *onAC*: powered by AC
    - \* *onDC*: powered by DC
  - **Note**: E.g. *PZTX100atAonAC* would refer to the 731-207 accelerometer with amplifier settings as follows: gain of 100 and integrator turned off (AC mode).

3. location:

- *H2*: **H**all **2** - MEA measuring hall
  - *atRef*: on 1,000 kg **R**eference block
- *HN*: **H**ERA North – refers to the (future) ALPS IIc set-up
  - *atP*: defines the **P**osition at HERA North
    - \* *atC*: **C**entral in the hall

- \* *atE*: **E**ast tunnel
  - \* *atW*: **W**est tunnel
  - *onB*: defines the base (in the tunnels)
    - \* *onB*: concrete **B**locks
    - \* *onG*: **G**round of the hall
    - \* *onGirder*: (blue) magnet **G**irder
    - \* *onInRail*: **I**nnner tram **R**ail
  - *HS*: **H**ERA **S**outh
    - *atP*: defines the **P**osition at HERA South
      - \* *atB*: **B**ridge in hall
      - \* *atG*: **G**round of hall
      - \* *atE*: **E**ast tunnel
  - *HW*: **H**ERA **W**est – refers to the ALPS IIa laboratory
    - *atT*: defines the optical **T**able
      - \* *atT*: table in optics lab
      - \* *atA*: table **A**, also 1 or laser table LT
      - \* *atB*: table **B**, also CBB or CB
      - \* *atC*: table **C**, also 3 or end table ET
      - \* *atD*: table **D**, also 2 or central table CT
      - \* *atGT*: at **G**round next to optical table *T*
    - *w/woF*: status of the **F**low boxes in the clean rooms
      - \* *wF*: **w**ith flow boxes turned on
      - \* *woF*: **w**ithout flow boxes turned on
  - **Note**: The position will also contain the information if the measurement is a differential one. Then there are two *tables* or *locations* mentioned connected with a '**m**', e.g. *HNatConBmWonInRail* would refer to an differential measurement between the hall on the concrete blocks minus the western tunnel on the inner tram rail in HERA North.
4. date shown as **yyyy-mm-dd**
  5. time shown as **hh-mm** UTC+1/2 (depending on daylight-saving time; most relevant for long-term measurements)
  6. sample rate, e.g. *50kHz* refers to a sample rate of 50 kHz
  7. measurement time, e.g. *10s* refers to a measurement time of 10 s
    - in the case of *SA*: a frequency range of the spectrum or maximum frequency beginning at 0 Hz is given, e.g. *800Hz* would mean linear spaced Fourier frequencies from 0 Hz to 800 Hz
  8. additional information:
    - direction referring to the (future) laser beam (optional)
    - resolution of the oscilloscope (optional)

---

**Note:** e.g. *SC2\_PZTX100atAonAC\_HN at ConB\_2018-11-23\_11-41\_50kHz\_100s\_ longitudinal\_40mV* would refer to a measurement acquired with the oscilloscope that was stored compressed with the 731-207 accelerometer with a gain of 100 on ACC mode and external power supply in HERA North Hall on the concrete blocks at 23<sup>rd</sup> November 2018 at 11:41 UTC+1 sampled with 50 kHz over 100 s in longitudinal direction with a resolution of 40 mV/div.



## B. MATLAB code 'Method of frequency-weighted and averaged FFT'

```
function[Info, M, errr, fm, xm, win] = CalculateDetail2(y, Fs, detail, ...
    Measure, Confident, x)
% CalculateDetail(y, Fs, detail, Measure, Confident, x)
% Calculates detail FFT
% 'y'          y-values
% 'Fs'         sample frequency
% 'detail'     desired deree of detail
% 'Measure'    type of measure used
% 'Confident'  use only confident data
% 'x'         x-values --> only for spectrogram

dod = detail{1};

% define time steps
div = 10;
sec = int32(length(y)/Fs) * div;

% calculate possible averages
jj = 1;
for j = 1:sec
    if mod(sec,j) < 0.1
        iteration(jj) = j;
        jj = jj+1;
    end
end

% define steps to go for
steps = round(1:(length(iteration)-1)/(dod-1):length(iteration));
if length(steps) > length(iteration)
    disp('Note: Level of detail higher than possible');
    steps = 1:length(iteration);
end
if isempty(steps)
    disp('Note: Level of detail lower than possible');
    steps = 1;
```

```

end
%steps = [8 14 20 26 31 36];
iteration = iteration(steps);

l = length(iteration);
Hz = sec / 10;
Hz = (double(Hz) ./ double(iteration)).^-1;
Info = [l {iteration} Hz];

clearvars steps sec Hz

% calculate FFT of steps
Nx = size(y,1)./double(iteration);
for j = 1:l
    w = kaiser(Nx(j),2.5);
    noverlap = Nx(j)*0.2;
    nfft = Nx(j);
    [P{j}, pf{j}, er{j}] = pwelch(y, w, noverlap, nfft, Fs, ...
        'ConfidenceLevel', 0.95);
    er{j} = sqrt(er{j});
    er2{j}(:,1) = min(er{j}, [], 2);
    er2{j}(:,2) = max(er{j}, [], 2);
    er{j} = er2{j};
    P{j} = sqrt(P{j}*NENBW_K(j)); % as LSD
    if Confident
        [pf{j}, P{j}, er{j}] = ConfidenceInterval(pf{j}, P{j}, ...
            Measure, er{j});
    else
        pf{j}(1) = [];
        P{j}(1,:) = [];
        er{j}(1,:) = [];
    end
end
clearvars y Measure

% windowing / weight function
f = pf{1};
win = zeros(size(f,1),1);
for j = 1:l
    if j == 1
        win(:,j) = 1;
    else
        from = find(f>10*Info{3}(j),1);
        to = find(f>20*Info{3}(j),1);
    end
end

```



---

```

        win_size_freq = 10*Info{3}(j);
        window = zeros(to-from+1,1);
        for i = from:to
            window(i-from+1) = 0.5*(1-cos(pi*(f(i)/(win_size_freq)-1)));
        end
        win(from:to,j) = window;
        win(to:end,j) = 1;
    end
end

% interpolate data
PP = zeros(size(f,1),1);
for j = 1:l
    PP(:,j) = interp1(pf{j},mean(P{j},2),f);
    err{j} = interp1(pf{j},er{j},f);
    err_min(:,j) = err{j}(:,1);
    err_max(:,j) = err{j}(:,2);
end
errr(:,1) = min(err_min, [], 2);
errr(:,2) = max(err_max, [], 2);
clearvars P er* -except errr

% convolution
Norm = sum(win,2);
PPP = PP .* win;

% trimming of the end
PPP = PPP(find(~isnan(PP(:,2)),1):find(~isnan(PP(:,end)),1,'last'),:);
errr = errr(find(~isnan(PP(:,2)),1):find(~isnan(PP(:,end)),1,'last'),:);
f = f(find(~isnan(PP(:,2)),1):find(~isnan(PP(:,end)),1,'last'),:);
Norm = Norm(find(~isnan(PP(:,2)),1):find(~isnan(PP(:,end)),1,'last'),:);
win = win(find(~isnan(PP(:,2)),1):find(~isnan(PP(:,end)),1,'last'),:);
clearvars PP

% average all steps together
PM = nansum(PPP,2) ./ Norm;
clearvars PPP Norm
fm = f(any(PM,2),:);
M = PM(any(PM,2),:);
errr = errr(any(PM,2),:);
win = win(any(PM,2),:);
xm = 0;

end

```



## C. Calibration charts

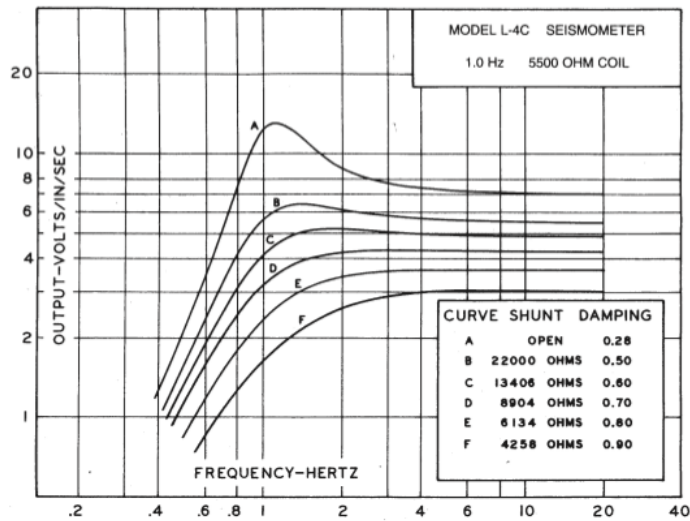


Figure C.1.: Calibration chart of the L-4C horizontal geophone – taken from the data sheet [47].

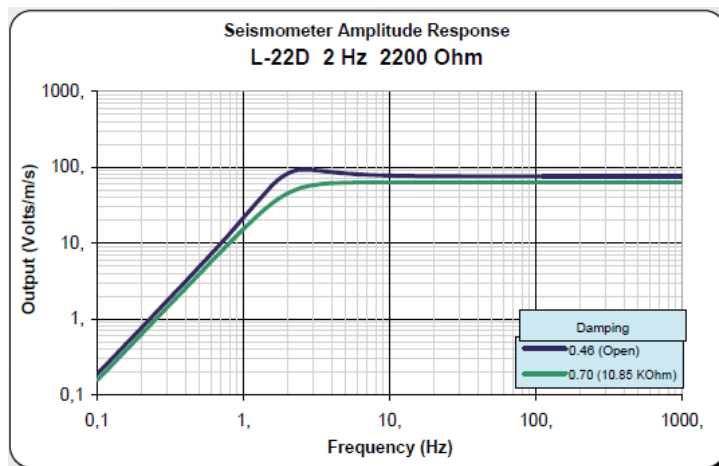
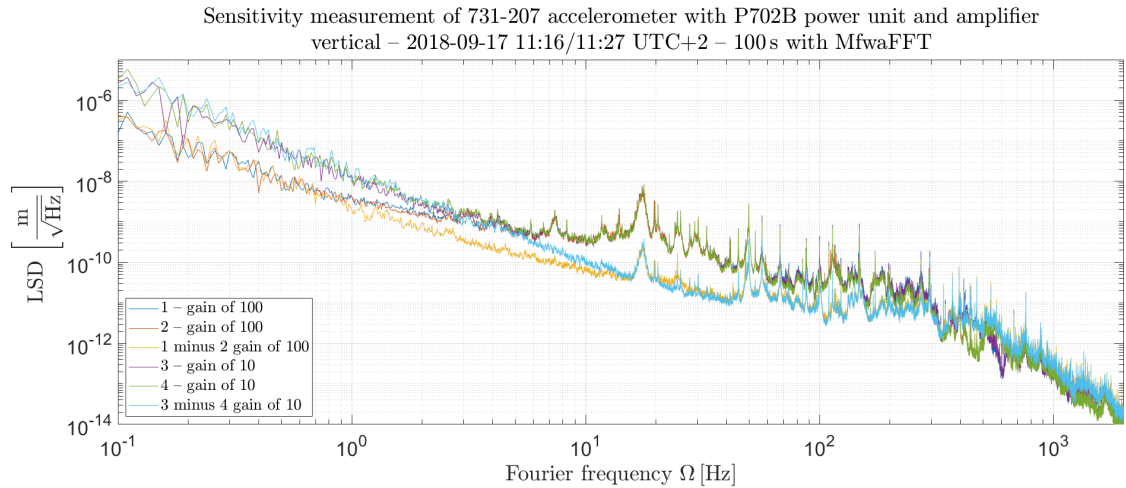
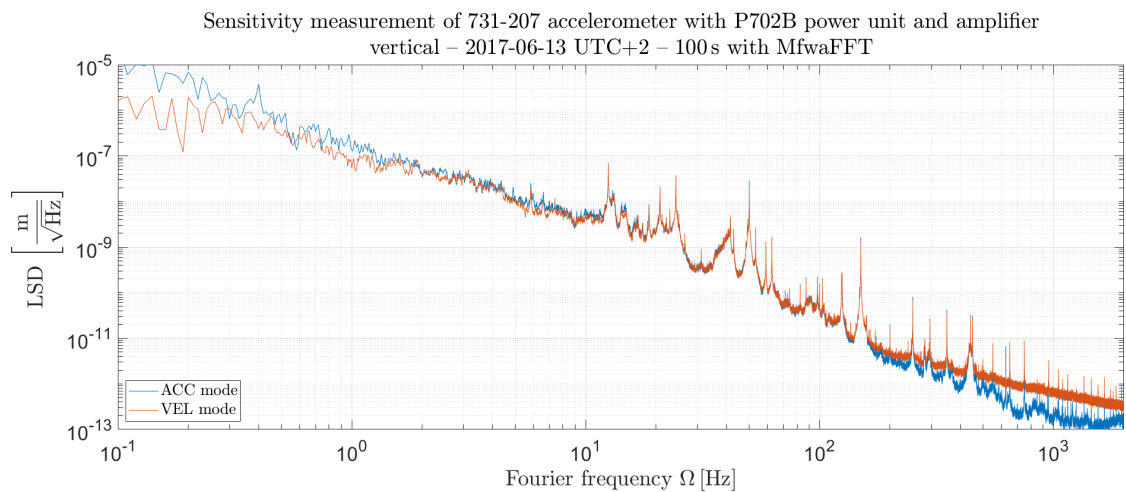


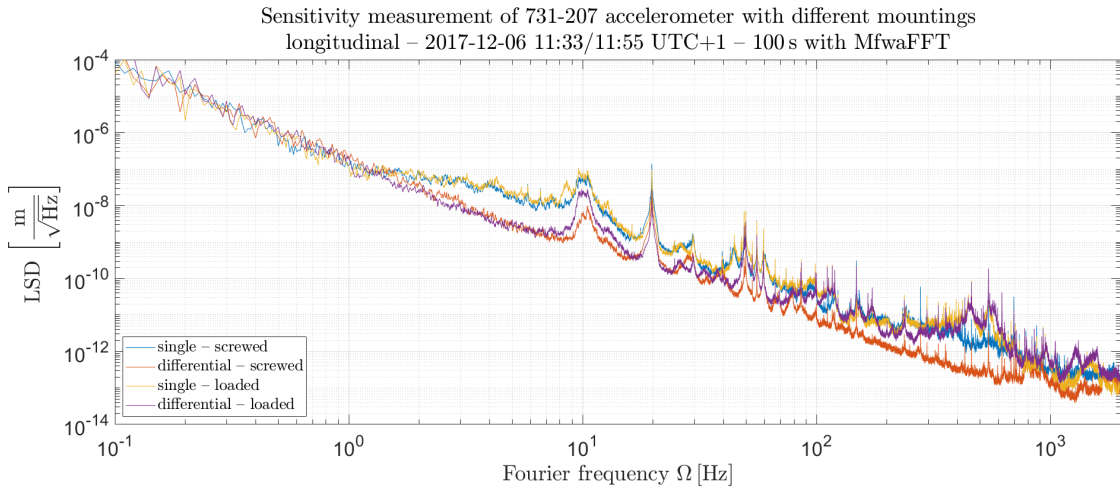
Figure C.2.: Calibration chart of the L-22D vertical geophone – taken from the data sheet [64].



**Figure C.3.:** Sensitivity measurement of 731-207 accelerometer with P702B power unit and amplifier – displacement LSDs of table measurements (single and differential) in vertical direction on 2018-09-17 at 11:16/11:27 UTC+2. Analysing characteristics: Kaiser window with a beta factor of 2.5 and 20 % overlap; analysed with MfwaFFT with a *dod* of 12.



**Figure C.4.:** Sensitivity measurement of 731-207 accelerometer with P702B power unit and amplifier – displacement LSDs of table measurements in longitudinal direction on 2017-06-13 UTC+2. Analysing characteristics: Kaiser window with a beta factor of 2.5 and 20 % overlap; analysed with MfwaFFT with a *dod* of 12.



**Figure C.5.:** Sensitivity measurement of 731-207 accelerometer with different mountings in longitudinal direction on 2018-12-06 11:33/11:55 UTC+1. Analysing characteristics: Kaiser window with a beta factor of 2.5 and 20% overlap; analysed with MfwaFFT with a *dod* of 12.



## D. Filter functions

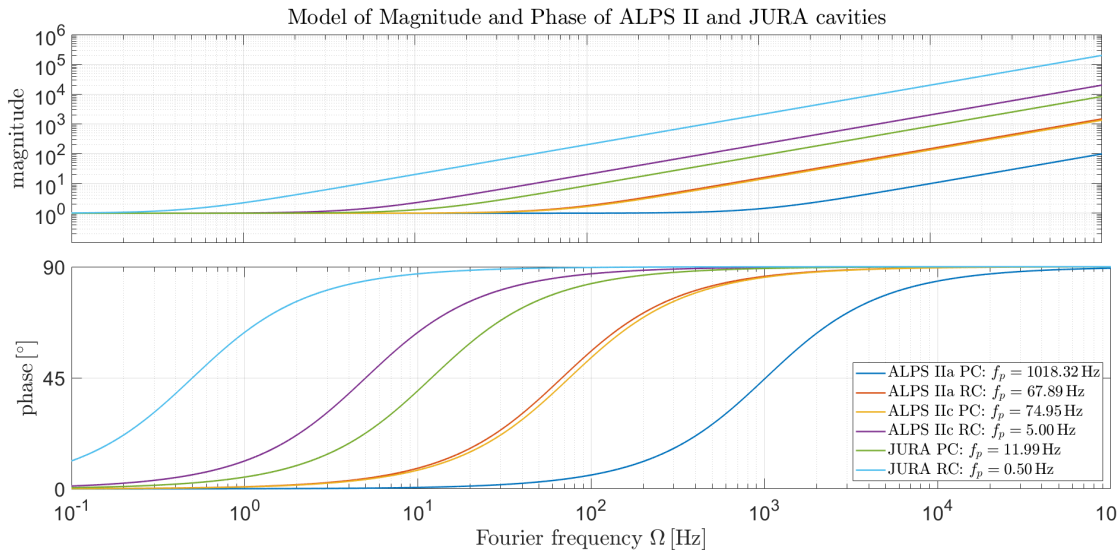


Figure D.1.: Model of magnitude and phase for the ALPS II and JURA cavities.

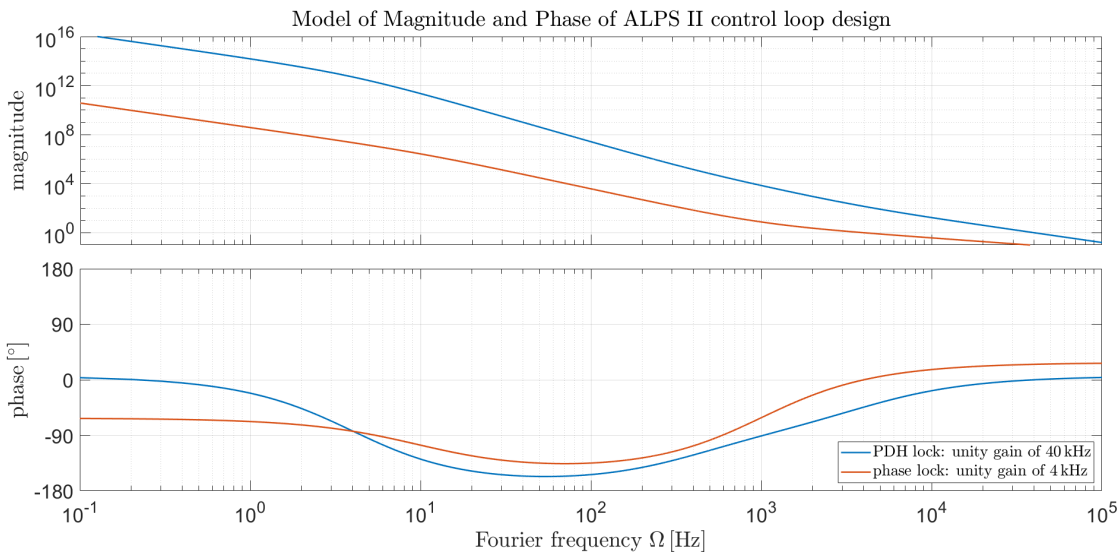
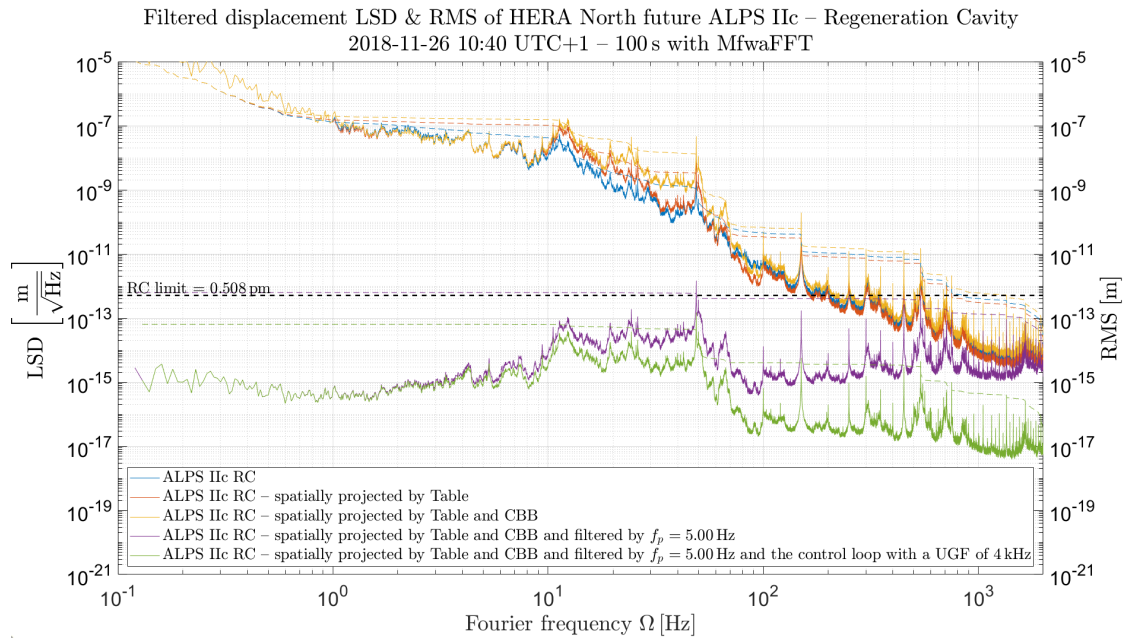


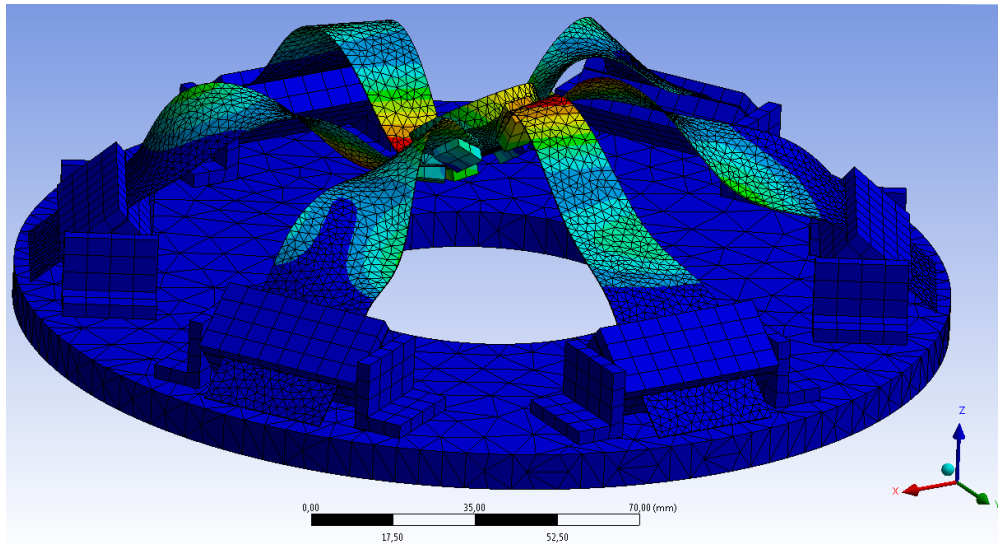
Figure D.2.: Model of magnitude and phase for the ALPS II and JURA cavities.



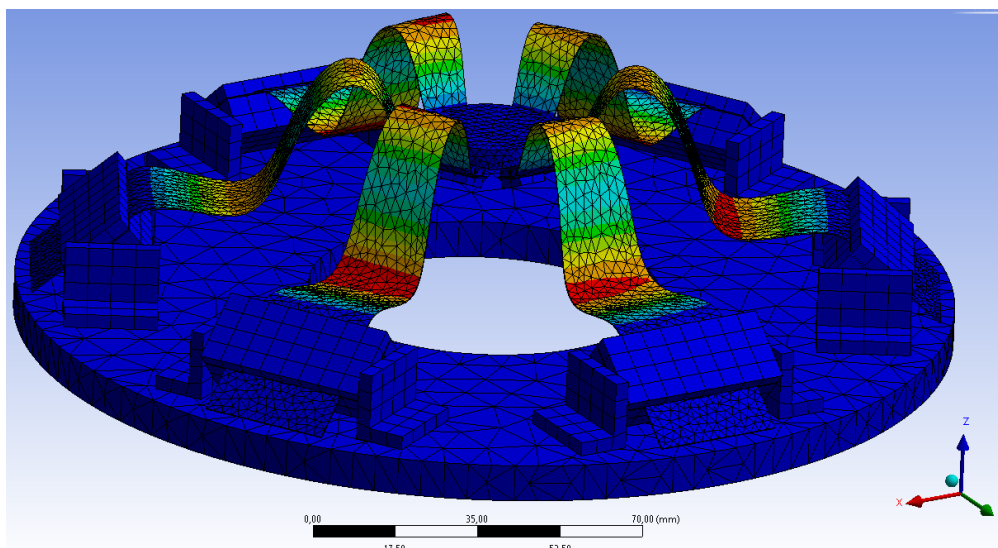
**Figure D.3.:** Example showing the effect of several filters applied to the differential signal to attenuate the seismic noise and compare its RMS value to the given requirements.



## E. FEM simulation



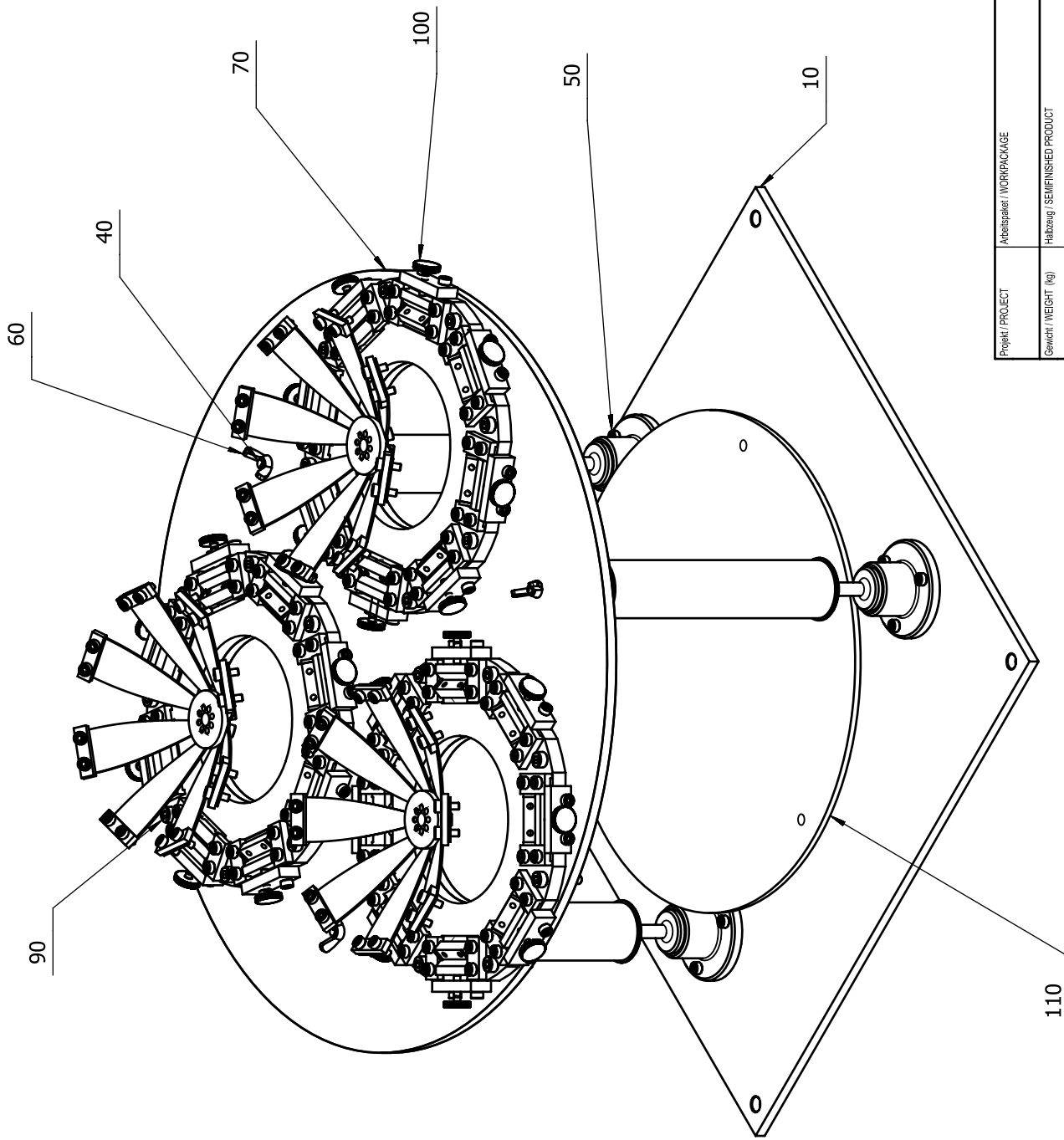
**Figure E.1.:** “Modal” simulation of ANSYS showing the fourth or fifth mode at 418 Hz of the Spider with a blade thickness of 0.30 mm and an applied load of 2.3 kg.



**Figure E.2.:** “Modal” simulation of ANSYS showing the sixth mode at 979 Hz of the Spider with a blade thickness of 0.30 mm and an applied load of 2.3 kg.




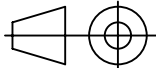
## **F. Technical drawings for SINUS**

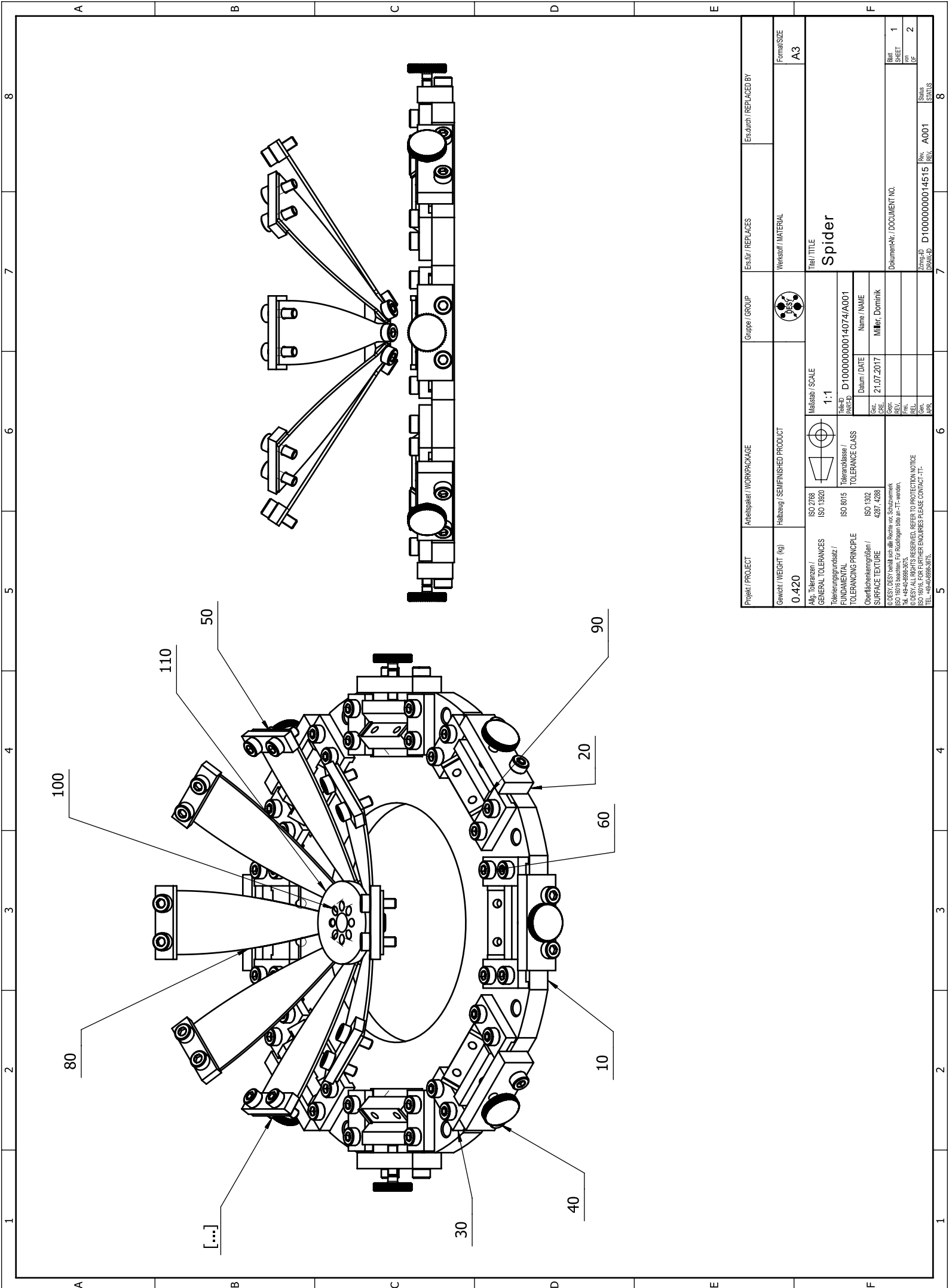


Projekt / PROJECT	Arbeitspaket / WORKPACKAGE	Gruppe / GROUP	Ersatzteil / REPLACES	Ersatzstück / REPLACED BY
Gewicht / WEIGHT (kg)	Hilfszeug / SEMIFINISHED PRODUCT		Werkstoff / MATERIAL	Formgröße
5.504	ISO 2768 ISO 13320			A3
Allg. Toleranzen / GENERAL TOLERANCES	Maßstab / SCALE			
ISO 8015	1:2			
Toleranzgrundsatz / FUNDAMENTAL TOLERANCING PRINCIPLE	Toleranzklasse / TOLERANCE CLASS	Teil-ID / PART-ID	Datum / DATE	
ISO 1302	ISO 1302	D10000000014050/A001	21.07.2017	
Oberflächenkenngrößen / SURFACE TEXTURE	ISO 4287, 4288	Name / NAME		
		Miller, Dominik		
<small>© DESY GESY bewahrt sich alle Rechte vor. Schutzmarke ISO 10716 beachten. Für Rückfragen bitte an -IT- wenden. TEL. +49-430368-3875. FAX. +49-430368-3876. WWW.DRESS-DE.COM. ALLES RECHTEN ERHALTEN. PLEASE CONTACT IT-1. TEL. +49-430368-3875.</small>				
Dokument-Nr. / DOCUMENT NO.		Blatt / SHEET		
D10000000014517		1		
Rev. / REV.		von / OF		
A001		2		
Status		8		

Pos. No.	Titel Title	Element-ID Item-ID	Stk. Qty.	Werkstoff Material	Halbzeug/Bemerkungen Semi-Finished Product/Remarks
10	Base_Plate	D10000000014022/A001	1	EN AW-5083 (AlMg4,5Mn0,7)	
40	IP	D10000000014059/A001	3		
50	Zylinderschraube ISO 4762 M3x8 1.4301	D10000000014052/A001	9	1.4301 (X4CrNi18-10)	
60	Reyher 882159400040000 Flügelmuttern, kleine "amerikanische" Form R 88215 M4 1.4301	D10000000014062/A001	3	1.4301 (X4CrNi18-10)	
70	Upper_Plate	D10000000014069/A001	1	EN AW-5083 (AlMg4,5Mn0,7)	
80	Sechskantmutter ISO 4032 M4 1.4301	D10000000014133/A001	24	1.4301 (X4CrNi18-10)	
90	Zylinderschraube ISO 4762 M4x20 1.4301	D10000000014132/A001	24	1.4301 (X4CrNi18-10)	
100	Spider	D10000000014074/A001	3		
110	Swinging_Plate	D10000000014135/A001	1	EN AW-5083 (AlMg4,5Mn0,7)	



Projekt / PROJECT		Arbeitspaket / WORKPACKAGE		Gruppe / GROUP		Ers.für / REPLACES		Ers.durch / REPLACED BY			
Gewicht / WEIGHT (kg)		Halbzeug / SEMIFINISHED PRODUCT				Werkstoff / MATERIAL		Format/SIZE			
5.504								A4			
Allg. Toleranzen / GENERAL TOLERANCES		ISO 2768 ISO 13920				Maßstab / SCALE		<b>SINUS_ALPS_IIa</b>			
Toleranzungsgrundsatz / FUNDAMENTAL TOLERANCING PRINCIPLE		ISO 8015				1:1					
Oberflächenkenngrößen / SURFACE TEXTURE		ISO 1302 4287, 4288		Toleranzklasse / TOLERANCE CLASS		Teile-ID PART-ID				Dokument-Nr. / DOCUMENT NO.	
						D10000000014050/A001					
				Datum / DATE		Name / NAME					
				21.07.2017		Miller, Dominik					
				Gepr. CRE.							
				Frei. REL.							
				Gen. APR.							
© DESY. DESY behält sich alle Rechte vor. Schutzvermerk ISO 16016 beachten. Für Rückfragen bitte an -TT- wenden, Tel. +49-40-8998-3675. © DESY. ALL RIGHTS RESERVED. REFER TO PROTECTION NOTICE ISO 16016. FOR FURTHER ENQUIRIES PLEASE CONTACT -TT- TEL. +49-40-8998-3675.				Zchnng.-ID DRAW-ID		D10000000014517		Rev. REV. A001		Status STATUS	
										Blatt SHEET 2 von OF 2	

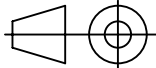


Projekt / PROJECT	Arbeitspaket / WORKPACKAGE		Gruppe / GROUP	Ersch./ REPLACES		Erschlich / REPLACED BY	
Gewicht / WEIGHT (kg)	0.420			Werkstoff / MATERIAL		Formgröße	
Allg. Toleranzen / GENERAL TOLERANCES Toleranzgrundsatz / FUNDAMENTAL TOLERANCING PRINCIPLE Oberflächentexturen / SURFACE TEXTURE	ISO 2768 ISO 13320 ISO 8015 ISO 1302 4287, 4288			Maßstab / SCALE 1:1		Formgröße	
Toleranzklasse / TOLERANCE CLASS Datum / DATE 21.07.2017 Name / NAME Müller, Dominik		Teil-ID / PART-ID D10000000014074/A001		Dokument-Nr. / DOCUMENT NO. D10000000014515		Blatt / SHEET von / OF 1 / 2	
© DESY. DESY bleibt sich alle Rechte vor. Schutzmerk ISO 9016 beachten. Für Rückfragen bitte an -IT- wenden. TEL. +49-4249-693-3875. © DESY. ALL RIGHTS RESERVED. REFER TO PROTECTION NOTICE FOR FURTHER ENQUIRIES PLEASE CONTACT -IT- TEL. +49-4249-693-3875.						Status A001 8	

Pos. No.	Titel Title	Element-ID Item-ID	Stk. Qty.	Werkstoff Material	Halbzeug/Bemerkungen Semi-Finished Product/Remarks
[...]	Zylinderschraube ISO 4762 M3x8 1.4301	D10000000014052/A001	16	1.4301 (X4CrNi18-10)	
10	Spider_Base	D10000000014073/A001	1	EN AW-5083 (AlMg4,5Mn0,7)	
20	PreLoad_Plate	D10000000014123/A001	8	EN AW-5083 (AlMg4,5Mn0,7)	
30	Clamp	D10000000014116/A001	16	EN AW-5083 (AlMg4,5Mn0,7)	
40	Zylinderschraube ISO 4762 M3x12 1.4301	D10000000014127/A001	16	1.4301 (X4CrNi18-10)	
50	Blade_Fixation	D10000000014122/A001	8	EN AW-5083 (AlMg4,5Mn0,7)	
60	Zylinderschraube ISO 4762 M3x10 1.4301	D10000000014125/A001	32	1.4301 (X4CrNi18-10)	
70	Rändelschraube DIN 653 M3x12 1.4301	D10000000014136/A001	8	1.4301 (X4CrNi18-10)	
80	Blade	D10000000014070/A001	8	Marval18 (X2NiCoMo18-8-5)	
90	Block	D10000000014072/A001	8	EN AW-5083 (AlMg4,5Mn0,7)	
100	Zylinderschraube ISO 4762 M3x6 1.4301	D10000000014131/A001	8	1.4301 (X4CrNi18-10)	
110	Keystone	D10000000014129/A001	1	EN AW-5083 (AlMg4,5Mn0,7)	

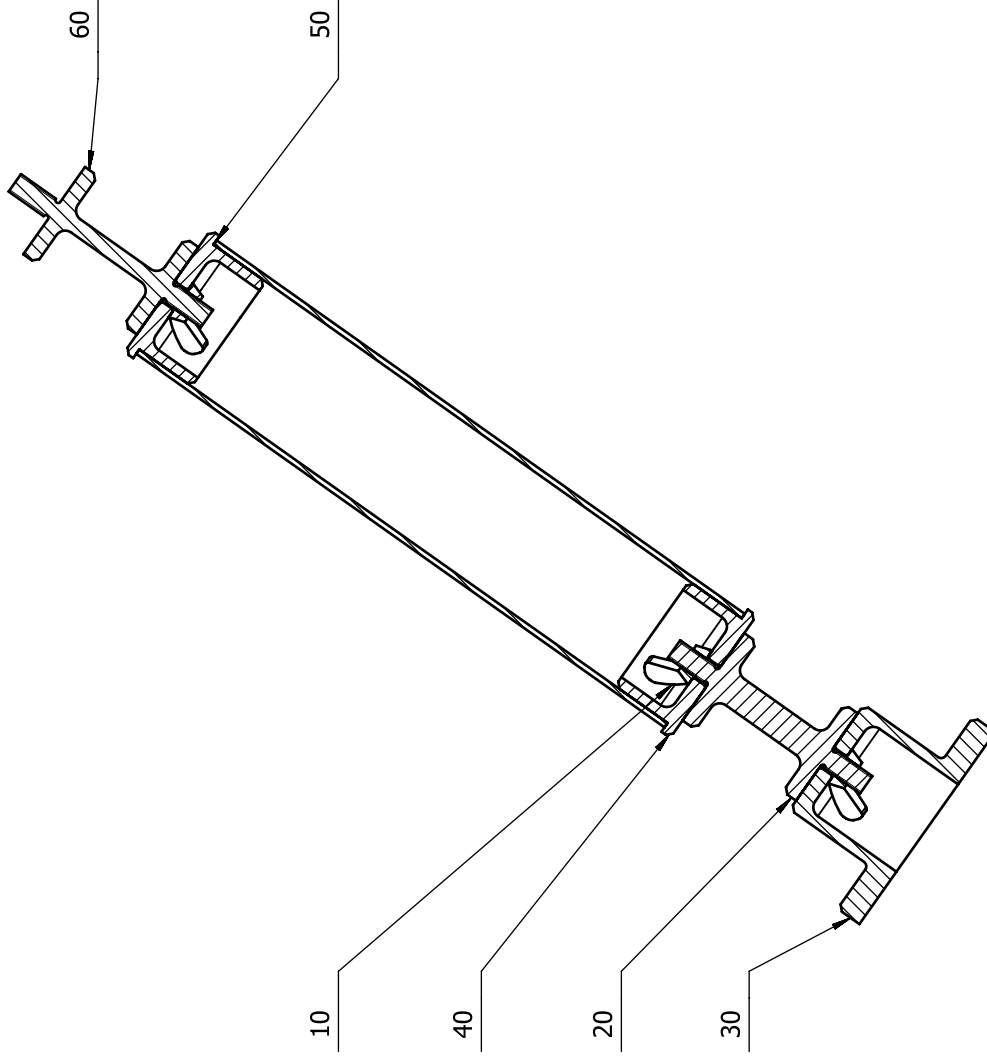
Projekt / PROJECT	Arbeitspaket / WORKPACKAGE	Gruppe / GROUP	Ers.für / REPLACES	Ers.durch / REPLACED BY
-------------------	----------------------------	----------------	--------------------	-------------------------

Gewicht / WEIGHT (kg)	Halbzeug / SEMIFINISHED PRODUCT		Werkstoff / MATERIAL	Format/SIZE
0.420				A4

Allg. Toleranzen / GENERAL TOLERANCES	ISO 2768 ISO 13920		Maßstab / SCALE		Titel / TITLE
			1:1	Spider	
Tolerierungsgrundsatz / FUNDAMENTAL TOLERANCING PRINCIPLE	ISO 8015	Toleranzklasse / TOLERANCE CLASS	Teile-ID PART-ID		D10000000014074/A001
Oberflächenkenngrößen / SURFACE TEXTURE	ISO 1302 4287, 4288		Datum / DATE	Name / NAME	
			Gez. CRE.	21.07.2017	Miller, Dominik
			Gepr. REV.		
			Frei. REL.		
			Gen. APR.		
© DESY. DESY behält sich alle Rechte vor. Schutzvermerk ISO 16016 beachten. Für Rückfragen bitte an -TT- wenden, Tel. +49-40-8998-3675. © DESY. ALL RIGHTS RESERVED. REFER TO PROTECTION NOTICE ISO 16016. FOR FURTHER ENQUIRIES PLEASE CONTACT -TT- TEL. +49-40-8998-3675.					Dokument-Nr. / DOCUMENT NO.
					Blatt SHEET
					2
					von OF
					2
			Zchng.-ID DRAW-ID	D10000000014515	Rev. REV.
				A001	Status STATUS



A-A



Projekt / PROJECT	Arbeitspaket / WORKPACKAGE		Gruppe / GROUP	Ersatz / REPLACES	Ersatzlich / REPLACED BY
Gewicht / WEIGHT (kg)	0.122			Werkstoff / MATERIAL	Formgröße A3
Allg. Toleranzen / GENERAL TOLERANCES	ISO 2768 ISO 13920				
Toleranzgrundsatz / FUNDAMENTAL TOLERANCING PRINCIPLE	ISO 8015		Teil / TITLE IP		
Oberflächenkenngrößen / SURFACE TEXTURE	ISO 1302 4287, 4288		Maßstab / SCALE 1:1		
<small>DESY/DESY beschließt sich für Rechte von Schutzrechten ISO 10716 bezogen. Für Rückfragen bitte an -IT- wenden. TEL: +49-40-6968-3875. FAX: +49-40-6968-3876. WWW: www.desy.de MAIL: ip@desy.de TEL: +49-40-6968-3873.</small>			<small>FORM ID: D10000000014059/A001</small> <small>Name / NAME: Müller, Dominik</small> <small>Datum / DATE: 20.07.2017</small> <small>Skizze: [ ]</small> <small>Gezeichnet: [ ]</small> <small>Geprüft: [ ]</small> <small>Freigegeben: [ ]</small> <small>APPROV: [ ]</small>		
<small>DESY/DESY beschließt sich für Rechte von Schutzrechten ISO 10716 bezogen. Für Rückfragen bitte an -IT- wenden. TEL: +49-40-6968-3875. FAX: +49-40-6968-3876. WWW: www.desy.de MAIL: ip@desy.de TEL: +49-40-6968-3873.</small>			<small>Dokument-Nr. / DOCUMENT NO.:</small> <small>Skizze-Nr. / SKETCH NO.:</small> <small>Form-Nr. / FORM NO.:</small> <small>Rev. / REV.:</small> <small>Status:</small>		

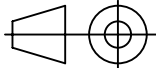
Blatt / SHEET	1
von / OF	2
Form-Nr. / FORM NO.	A001
Rev. / REV.	
Status	



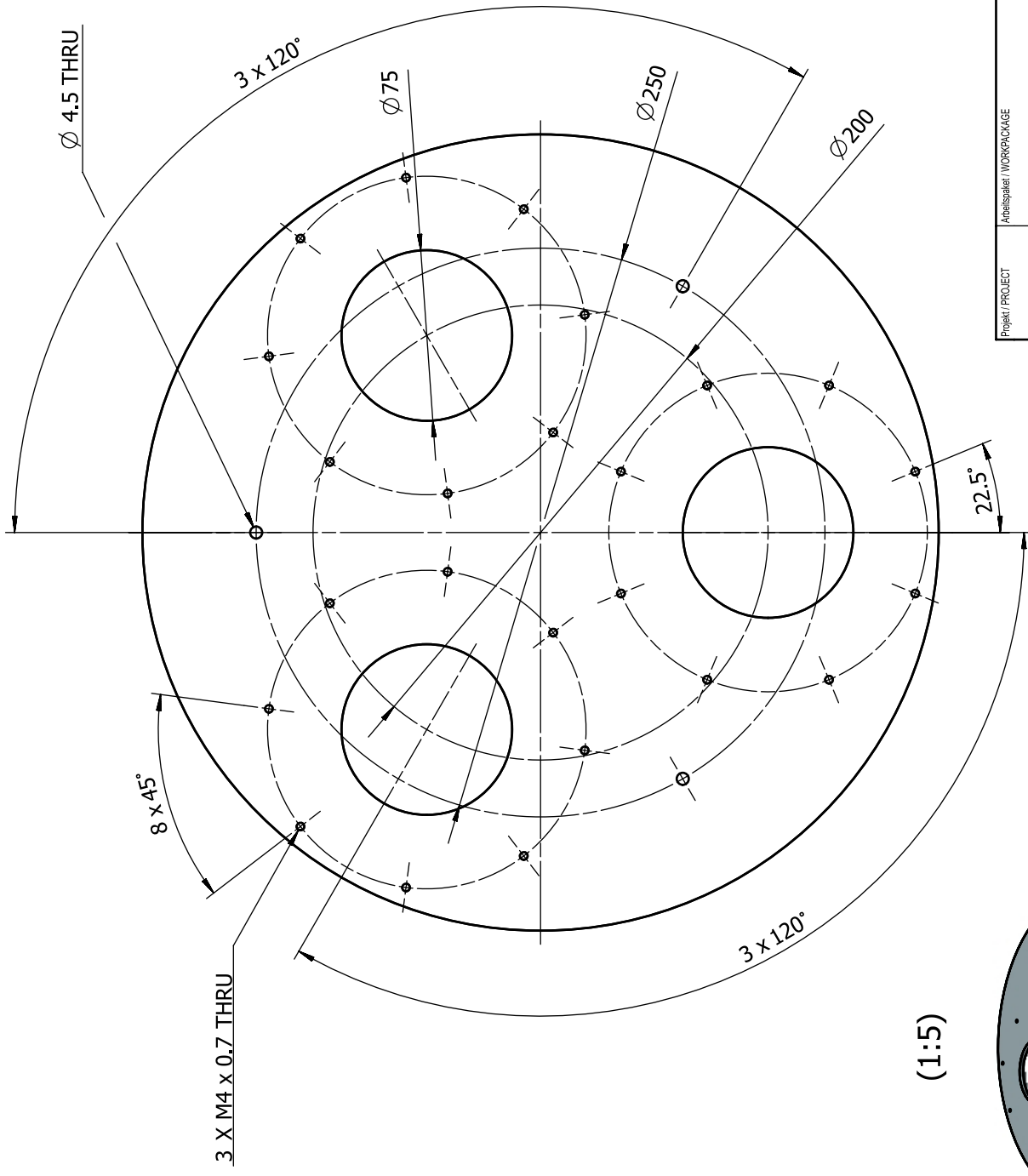
Pos. No.	Titel Title	Element-ID Item-ID	Stk. Qty.	Werkstoff Material	Halbzeug/Bemerkungen Semi-Finished Product/Remarks
10	Reyher 882159400040000 Flügelmuttern, kleine "amerikanische" Form R 88215 M4 1.4301	D10000000014062/A001	3	1.4301 (X4CrNi18-10)	
20	Lower_Flex	D10000000014058/A001	1	Marval18 (X2NiCoMo18-8-5)	
30	IP_Foot	D10000000014051/A001	1	EN AW-5083 (AlMg4,5Mn0,7)	
40	Tube_Connector	D10000000014061/A001	2	1.4404 (X2CrNiMo17-12-2)	
50	Tube	D10000000014063/A001	1	EN AW-5083 (AlMg4,5Mn0,7)	
60	Upper_Flex	D10000000014067/A001	1	Marval18 (X2NiCoMo18-8-5)	

Projekt / PROJECT	Arbeitspaket / WORKPACKAGE	Gruppe / GROUP	Ers.für / REPLACES	Ers.durch / REPLACED BY
-------------------	----------------------------	----------------	--------------------	-------------------------

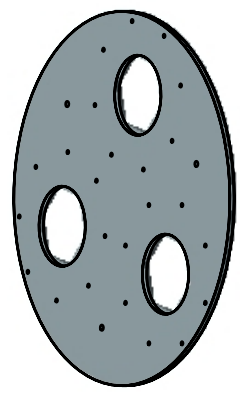
Gewicht / WEIGHT (kg) <b>0.122</b>	Halbzeug / SEMIFINISHED PRODUCT		Werkstoff / MATERIAL	Format/SIZE <b>A4</b>
---------------------------------------	---------------------------------	---	----------------------	--------------------------

Allg. Toleranzen / GENERAL TOLERANCES ISO 2768 ISO 13920		Maßstab / SCALE <b>1:1</b>		Titel / TITLE <b>IP</b>
		Toleranzklasse / TOLERANCE CLASS	Teile-ID PART-ID <b>D10000000014059/A001</b>	
FUNDAMENTAL TOLERANCING PRINCIPLE ISO 8015		Datum / DATE	Name / NAME	Dokument-Nr. / DOCUMENT NO.
Oberflächenkenngrößen / SURFACE TEXTURE ISO 1302 4287, 4288		Gez. CRE. 20.07.2017	Miller, Dominik	
		Gepr. REV.		
© DESY. DESY behält sich alle Rechte vor. Schutzvermerk ISO 16016 beachten. Für Rückfragen bitte an -TT- wenden, Tel. +49-40-8998-3675. © DESY. ALL RIGHTS RESERVED. REFER TO PROTECTION NOTICE ISO 16016. FOR FURTHER ENQUIRIES PLEASE CONTACT -TT- TEL. +49-40-8998-3675.		Gen. REL.		Blatt SHEET von OF <b>2</b>
	Gen. APR.		Zchnng-ID DRAW-ID <b>D10000000014466</b>	Rev. REV. <b>A001</b>
				Status STATUS



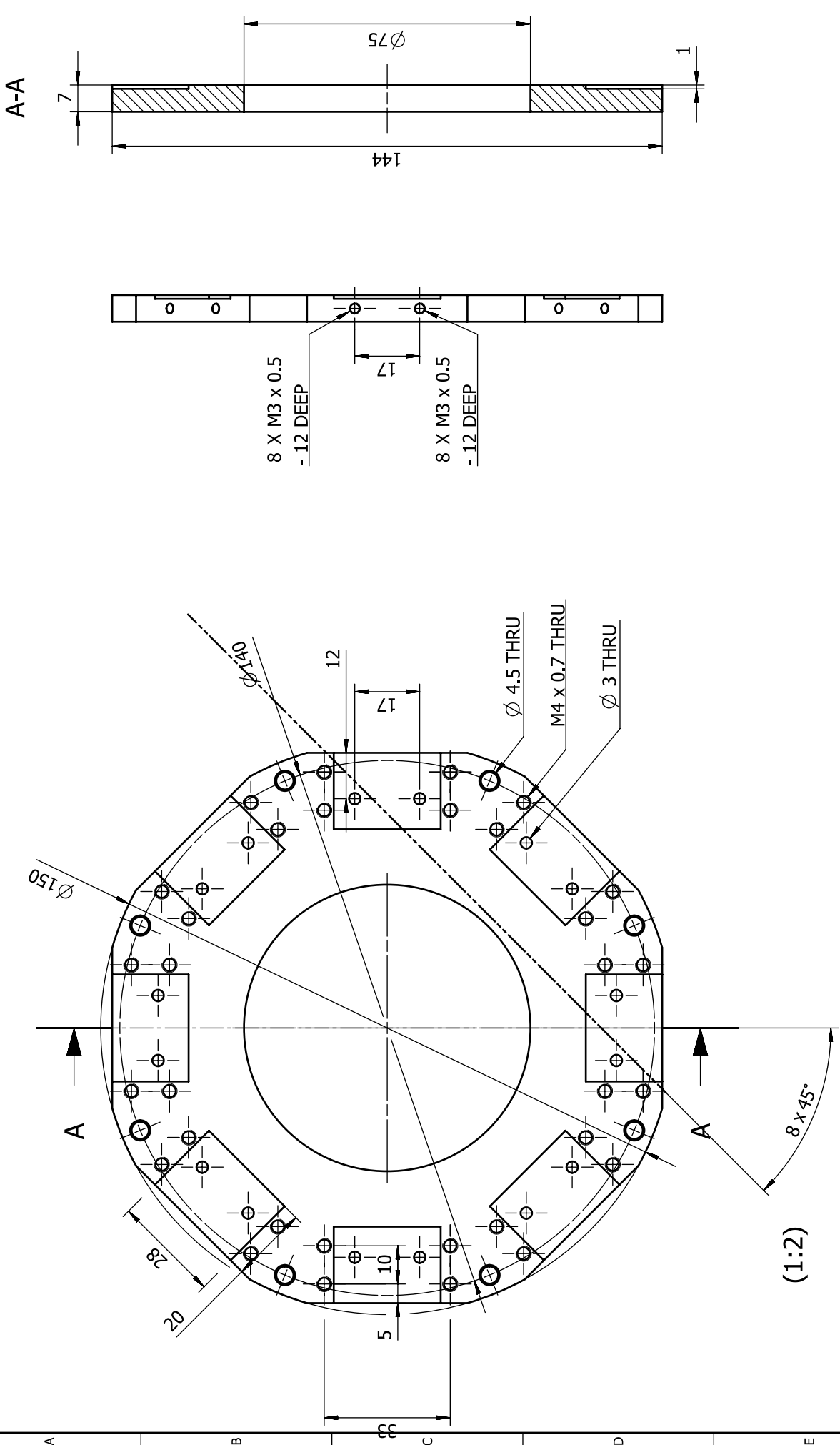


(1:5)



Projekt / PROJECT	Arbeitspaket / WORKPACKAGE	Gruppe / GROUP	Esstüch / REPLACES	Erstlich / REPLACED BY
Gewicht / WEIGHT (kg)	Hilfszeug / SEMIFINISHED PRODUCT		Werkstoff / MATERIAL	Formgröße
2.236	ISO 2768 ISO 13320		EN AW-5083 (AlMg4,5Mn0,7)	A3
Allg. Toleranzen / GENERAL TOLERANCES	ISO 8015	Titel / TITLE		
Toleranzgrundsatz / FUNDAMENTAL TOLERANCING PRINCIPLE	ISO 1302	Upper_Plate		
Maßstab / SCALE	ISO 4287, 4288	Teil-ID / PART-ID		
1:2		D10000000014069/A001		
Toleranzklasse / TOLERANCE CLASS		Name / NAME		
		Miller, Dominik		
Oberflächenkenngrößen / SURFACE TEXTURE		Datum / DATE		
		20.07.2017		
		Zust. / STATE		
		Gepr. / CHECKED		
		Rev. / REV.		
		Dokument-Nr. / DOCUMENT NO.		
		D10000000014487		
© DESY / DESY bleibt sich alle Rechte vor. Schutzmarke ISO 9016 beachten. Für Rückfragen bitte an -IT- wenden. TEL. +49-40-899-3875. FAX. +49-40-899-3876. WWW.DESY-DESY.DE		Zust. / STATE		Rev. / REV.
		A001		A001
		Blatt / SHEET		1
		von / OF		1
		Status		



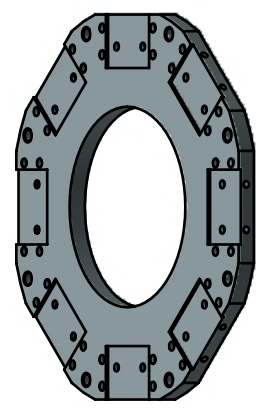


A-A

8 X M3 x 0.5  
- 12 DEEP

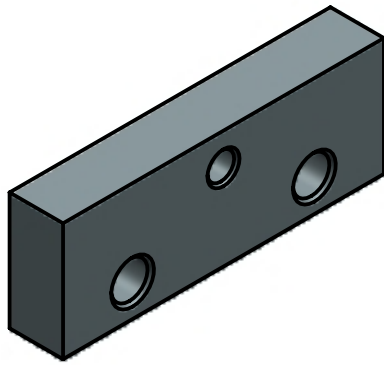
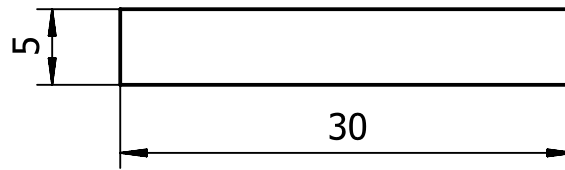
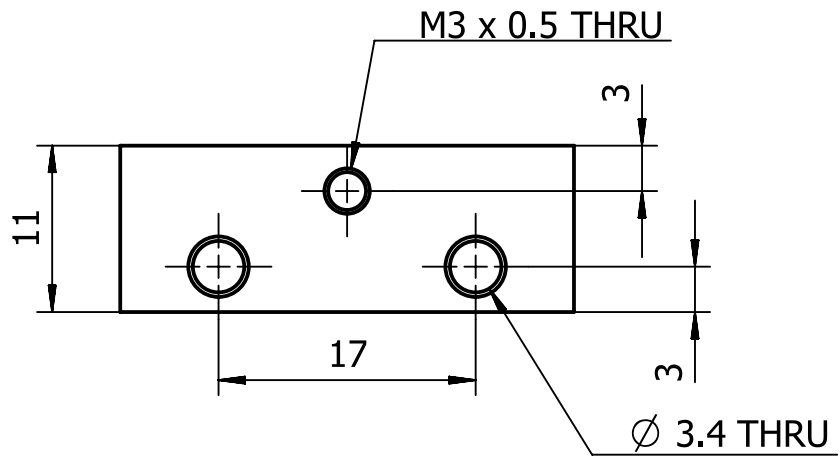
8 X M3 x 0.5  
- 12 DEEP

(1:2)



Projekt / PROJECT	Arbeitspaket / WORKPACKAGE	Gruppe / GROUP	Ersatzteil / REPLACES	Ersatzteil / REPLACED BY
Gewicht / WEIGHT (kg)	Hilfszeug / SEMIFINISHED PRODUCT		Material / MATERIAL	Formel / SIZE
0.214	ISO 2768 ISO 13320	D10000000014073/A001	EN AW-5083 (AlMg4.5Mn0.7)	A3
Allg. Toleranzen / GENERAL TOLERANCES	ISO 8015	Teil-ID / PART-ID	Titel / TITLE	
Toleranzgrundsatz / FUNDAMENTAL TOLERANCE CLASS	ISO 1302	Datum / DATE	Spider_Base	
Toleranzgrundsatz / FUNDAMENTAL TOLERANCE CLASS	ISO 1302	20.07.2017	Name / NAME	
Oberflächenkenngrößen / SURFACE TEXTURE	4287, 4288	Gepr. / PREP.	Miller, Dominik	
<small>         © DESY. DESY bleibt sich alle Rechte vor. Schutzmarke ISO 9016 beachten. Für Rückfragen bitte an "IT" wenden. TEL. +49-40-899-3875. FAX. +49-40-899-3876. WWW.DESY-DESY.DE. E-MAIL: DESY@DESY.DE. TEL. +49-40-899-3875.       </small>				
<small>         ALL RIGHTS RESERVED. REFER TO PROTECTION NOTICE FOR FURTHER INFORMATION. PLEASE CONTACT "IT".       </small>				
<small>         Dokument-Nr. / DOCUMENT NO.       </small>				
<small>         Blatt / SHEET       </small>				
<small>         von / OF       </small>				
<small>         Status       </small>				
<small>         Rev. / REL.       </small>				
<small>         A001       </small>				
<small>         D10000000014489       </small>				
<small>         Scale       </small>				
<small>         8       </small>				

A  
B  
C  
D  
E



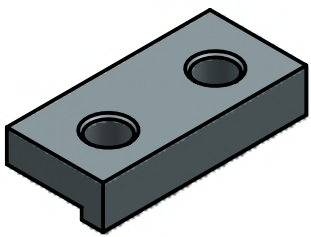
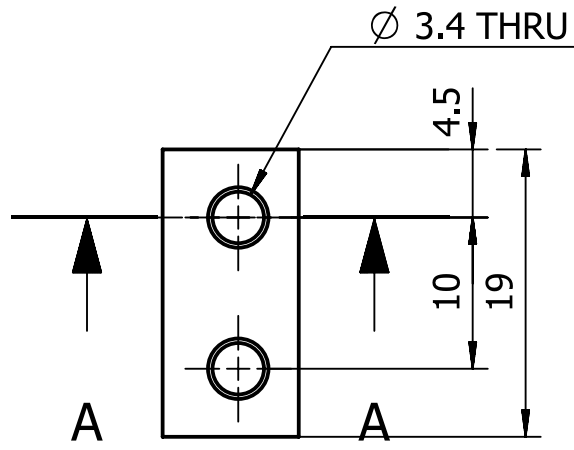
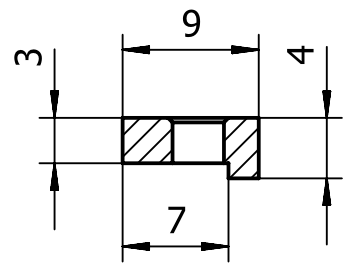
Projekt / PROJECT		Arbeitspaket / WORKPACKAGE		Gruppe / GROUP		Ers.für / REPLACES		Ers.durch / REPLACED BY			
Gewicht / WEIGHT (kg) <b>0.004</b>		Halbzeug / SEMIFINISHED PRODUCT				Werkstoff / MATERIAL <b>EN AW-5083 (AlMg4,5Mn0,7)</b>			Format/SIZE <b>A4</b>		
Allg. Toleranzen / GENERAL TOLERANCES ISO 2768 ISO 13920				Maßstab / SCALE <b>2:1</b>		<b>PreLoad_Plate</b>					
Tolerierungsgrundsatz / FUNDAMENTAL TOLERANCING PRINCIPLE ISO 8015				Toleranzklasse / TOLERANCE CLASS							
Oberflächenkenngößen / SURFACE TEXTURE ISO 1302 4287, 4288		Teile-ID / PART-ID <b>D10000000014123/A001</b>		Datum / DATE 20.07.2017		Name / NAME Miller, Dominik		Dokument-Nr. / DOCUMENT NO.			
© DESY. DESY behält sich alle Rechte vor. Schutzvermerk ISO 16016 beachten. Für Rückfragen bitte an -TT- wenden, Tel. +49-40-8998-3675. © DESY. ALL RIGHTS RESERVED. REFER TO PROTECTION NOTICE ISO 16016. FOR FURTHER ENQUIRIES PLEASE CONTACT -TT- TEL. +49-40-8998-3675.		Gez. CRE.		Gen. APR.		Zchnng-ID / DRAW-ID <b>D10000000014494</b>		Rev. REV. <b>A001</b>		Status STATUS	
		Blatt SHEET 1		von OF 1							

1 2 3 4

A  
B  
C  
D  
E  
F

1 2 3 4

A-A

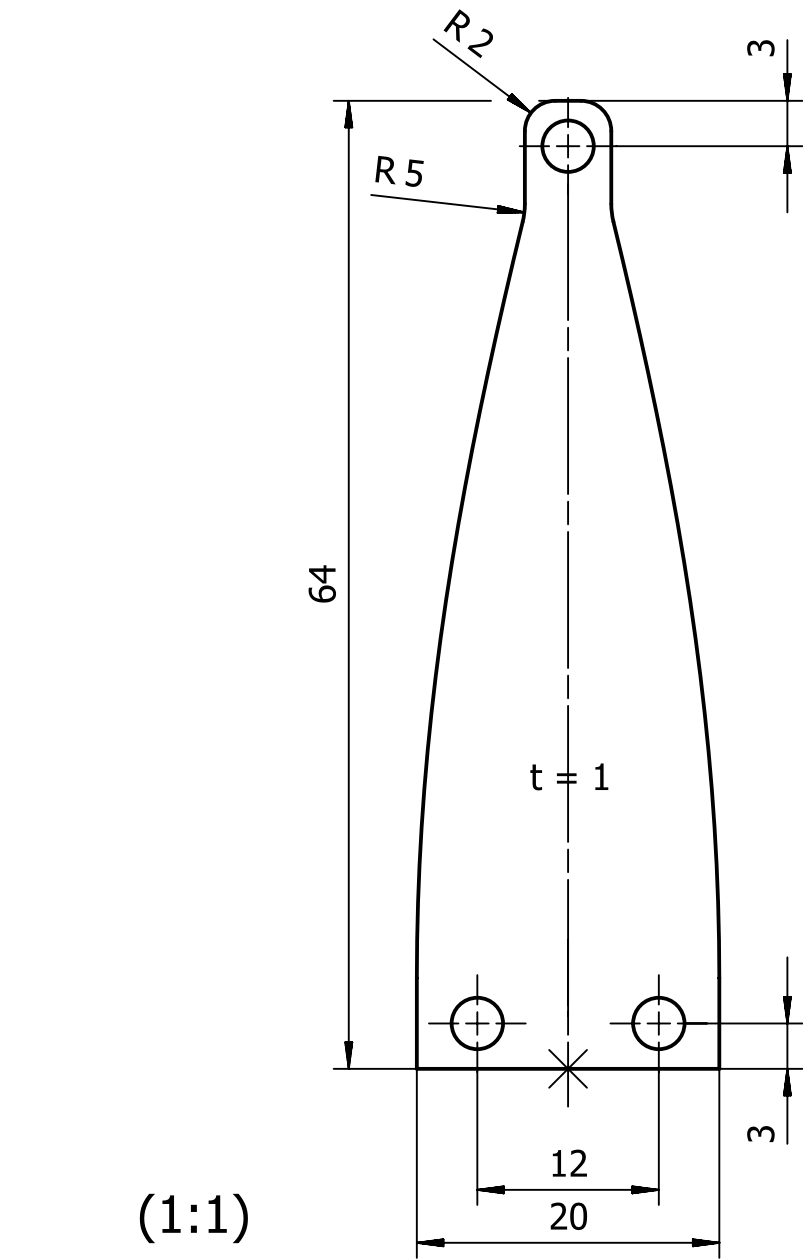


Projekt / PROJECT		Arbeitspaket / WORKPACKAGE		Gruppe / GROUP		Ers.für / REPLACES		Ers.durch / REPLACED BY	
Gewicht / WEIGHT (kg) <b>0.001</b>		Halbzeug / SEMIFINISHED PRODUCT				Werkstoff / MATERIAL <b>EN AW-5083 (AlMg4,5Mn0,7)</b>			Format/SIZE <b>A4</b>
Allg. Toleranzen / GENERAL TOLERANCES ISO 2768 ISO 13920				Maßstab / SCALE <b>2:1</b>		Titel / TITLE <b>Clamp</b>			
Tolerierungsgrundsatz / FUNDAMENTAL TOLERANCING PRINCIPLE ISO 8015				Toleranzklasse / TOLERANCE CLASS					
Oberflächenkenngrößen / SURFACE TEXTURE ISO 1302 4287, 4288				Datum / DATE 20.07.2017		Name / NAME Miller, Dominik		Dokument-Nr. / DOCUMENT NO.	
© DESY. DESY behält sich alle Rechte vor. Schutzvermerk ISO 16016 beachten. Für Rückfragen bitte an -TT- wenden, Tel. +49-40-8998-3675. © DESY. ALL RIGHTS RESERVED. REFER TO PROTECTION NOTICE ISO 16016. FOR FURTHER ENQUIRIES PLEASE CONTACT -TT- TEL. +49-40-8998-3675.				Gez. CRE.				Blatt SHEET 1	
				Gen. APR.				von OF 1	
				Zchnng-ID / DRAW-ID <b>D10000000014491</b>		Rev. REV. <b>A001</b>		Status STATUS	

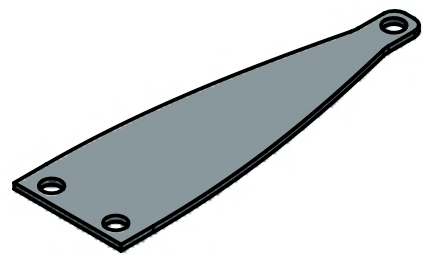
1 2 3 4





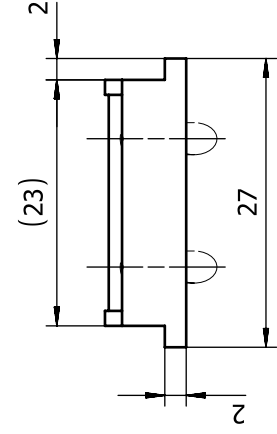


(1:1)

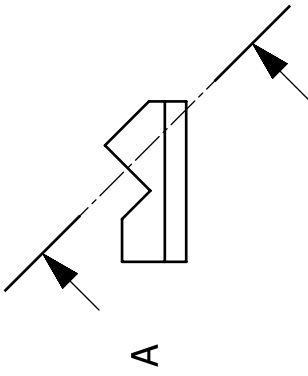
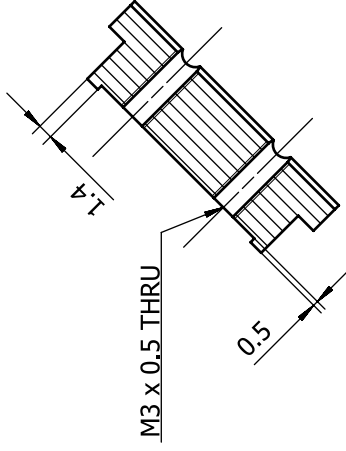


X	Y
0	10.000
5	9,920
10	9.681
15	9.288
20	8.746
25	8.064
30	7.254
35	6.327
40	5.299
45	4.187
50	3.007

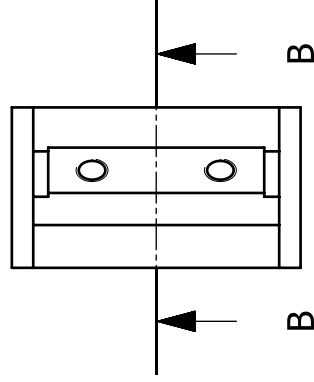
Projekt / PROJECT		Arbeitspaket / WORKPACKAGE		Gruppe / GROUP		Ers.für / REPLACES		Ers.durch / REPLACED BY					
Gewicht / WEIGHT (kg)		Halbzeug / SEMIFINISHED PRODUCT				Werkstoff / MATERIAL Marval18 (X2NiCoMo18-8-5)			Format/SIZE A4				
Allg. Toleranzen / GENERAL TOLERANCES ISO 2768 ISO 13920				Maßstab / SCALE 2:1		Titel / TITLE <b>Blade</b>							
Tolerierungsgrundsatz / FUNDAMENTAL TOLERANCING PRINCIPLE ISO 8015				Toleranzklasse / TOLERANCE CLASS									
Oberflächenkenngrößen / SURFACE TEXTURE ISO 1302 4287, 4288				Teile-ID / PART-ID D10000000014070/A001		Datum / DATE 20.07.2017		Name / NAME Miller, Dominik					
© DESY. DESY behält sich alle Rechte vor. Schutzvermerk ISO 16016 beachten. Für Rückfragen bitte an -TT- wenden, Tel. +49-40-8998-3675. © DESY. ALL RIGHTS RESERVED. REFER TO PROTECTION NOTICE ISO 16016. FOR FURTHER ENQUIRIES PLEASE CONTACT -TT- TEL. +49-40-8998-3675.				Gez. CRE.		Gen. APR.		Dokument-Nr. / DOCUMENT NO.		Blatt SHEET 1 von OF 1			
				Frei. REL.				Zchnng-ID / DRAW-ID D10000000014492		Rev. REV. A001		Status STATUS	



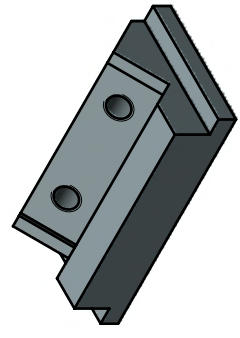
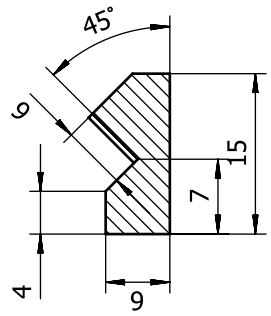
A-A



A



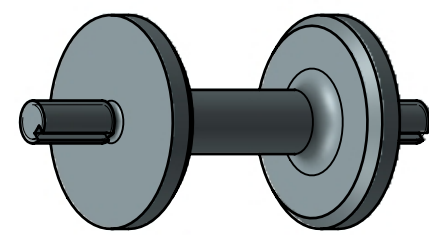
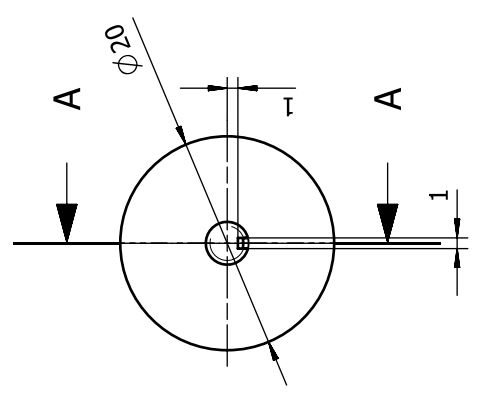
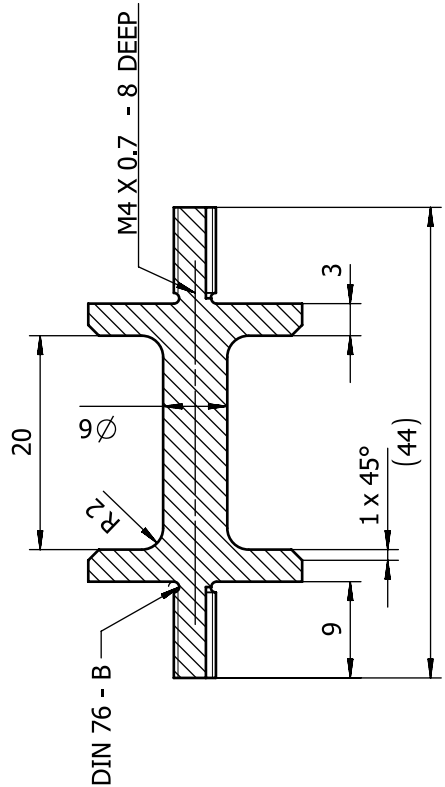
B-B



Projekt / PROJECT	Arbeitspaket / WORKPACKAGE	Gruppe / GROUP	Erstellt / REPLACES	Erstlich / REPLACED BY
Gewicht / WEIGHT (kg)	Holzzeug / SEMIFINISHED PRODUCT		Wechsel / MATERIAL	Formgröße
0.005	ISO 2768 ISO 13320		EN AW-5083 (AlMg4,5Mn0,7)	A3
Allg. Toleranzen / GENERAL TOLERANCES	ISO 8015	Maßstab / SCALE	Teil / TITLE	
Toleranzgrundsatz / FUNDAMENTAL TOLERANCING PRINCIPLE	ISO 1302	2:1	Block	
ISO 1302	4287, 4288	Teil-ID / PART-ID		
ISO 1302	4287, 4288	D10000000014072/A001		
Oberflächenkenngrößen / SURFACE TEXTURE		Datum / DATE	Name / NAME	
		20.07.2017	Miller, Dominik	
<small>© DESY. DESY behält sich alle Rechte vor. Schutzmerkmal ISO 9016 beachten. Für Rückfragen bitte an -IT- wenden. TEL. +49-40-8998-3875. WWW.DESY-DESY.DE</small>		<small>Dokument-Nr. / DOCUMENT NO.</small> <small>Stapel-Nr. / STACK NO.</small> <small>Form-Nr. / FORM NO.</small> <small>Rev. / REV.</small> <small>Status</small>		
		<small>D10000000014490</small> <small>A001</small> <small>8</small>		



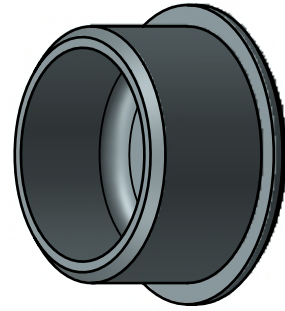
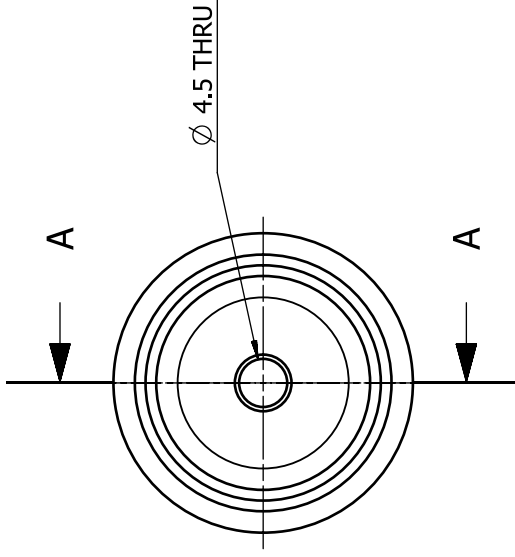
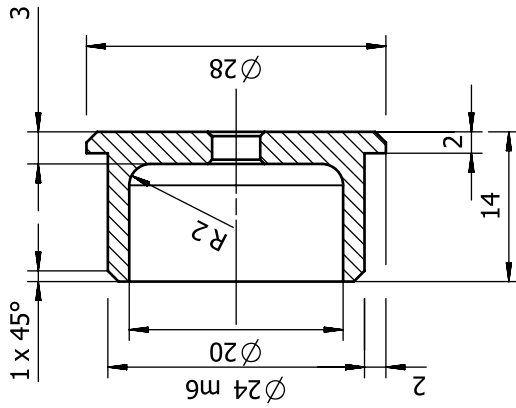
A-A




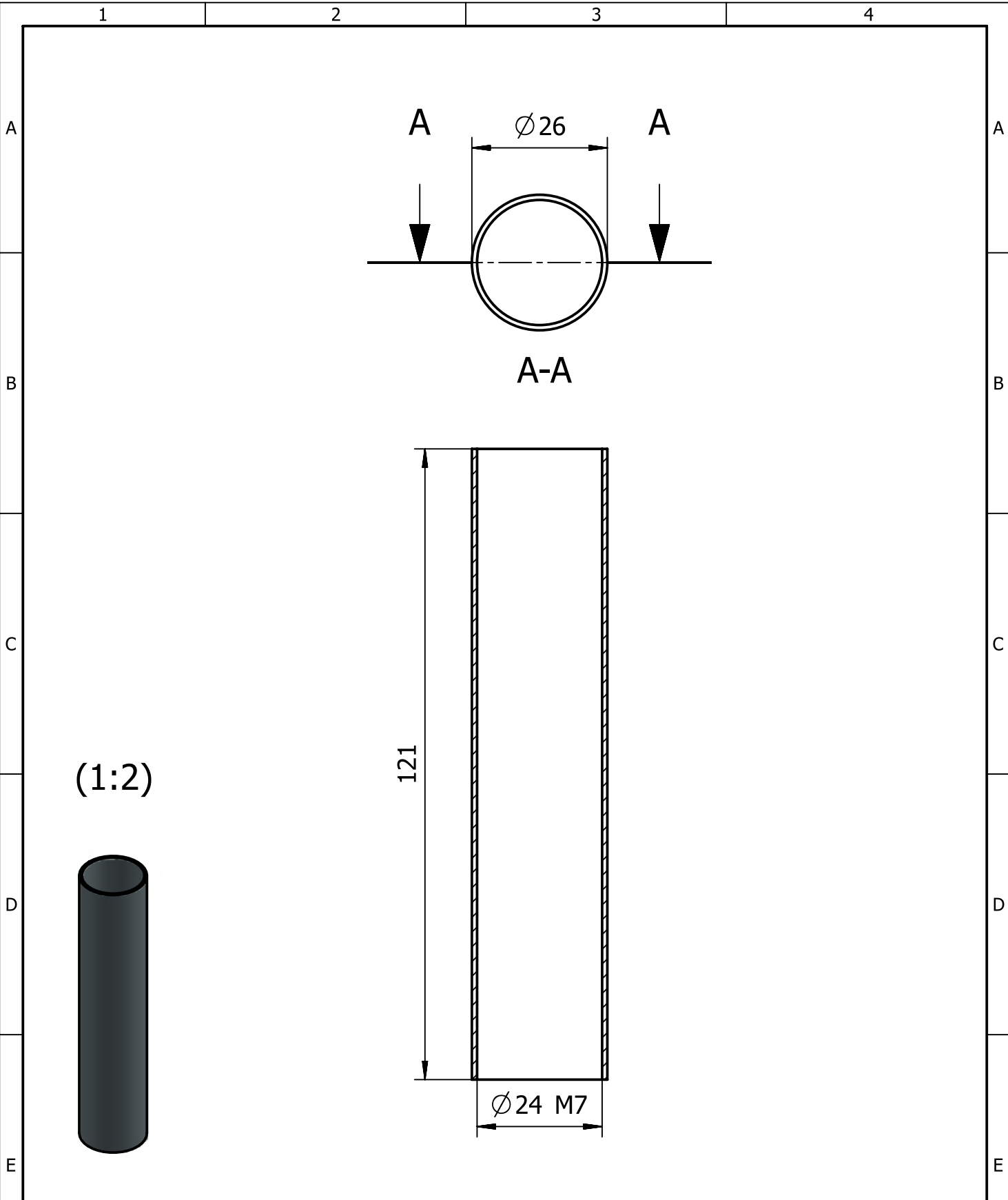
Projekt / PROJECT	Arbeitspaket / WORKPACKAGE	Gruppe / GROUP	Ersch./ REPLACES	Erschlich / REPLACED BY
Gewicht / WEIGHT (kg)	Holzzeug / SEMIFINISHED PRODUCT		Werkstoff / MATERIAL	Formgröße
Allg. Toleranzen / GENERAL TOLERANCES	ISO 2768		Marval18 (X2NiCoMo18-8-5)	A3
Toleranzgrundsatz / FUNDAMENTAL TOLERANCING PRINCIPLE	ISO 13320		Teil / TITLE	
Oberflächenkenngrößen / SURFACE TEXTURE	ISO 8015	Messstab / SCALE		
	ISO 1302	2:1		
	4287, 4288	Teil-ID / PART-ID		
		D10000000014056/A001		
		Datum / DATE		
		20.07.2017		
		Name / NAME		
		Miller, Dominik		
		Dokument-Nr. / DOCUMENT NO.		
		Blatt / SHEET		
		1		
		von / OF		
		1		
		Status		
		PREL.		
		REL.		
		APR.		
		Druck-Nr. / PRINT NO.		
		A001		
		Druck-Nr. / PRINT NO.		
		D10000000014462		
		Blatt / SHEET		
		8		



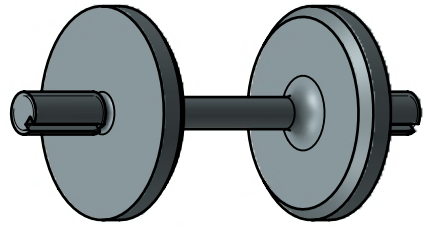
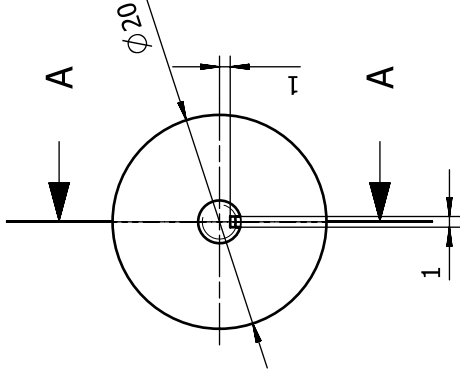
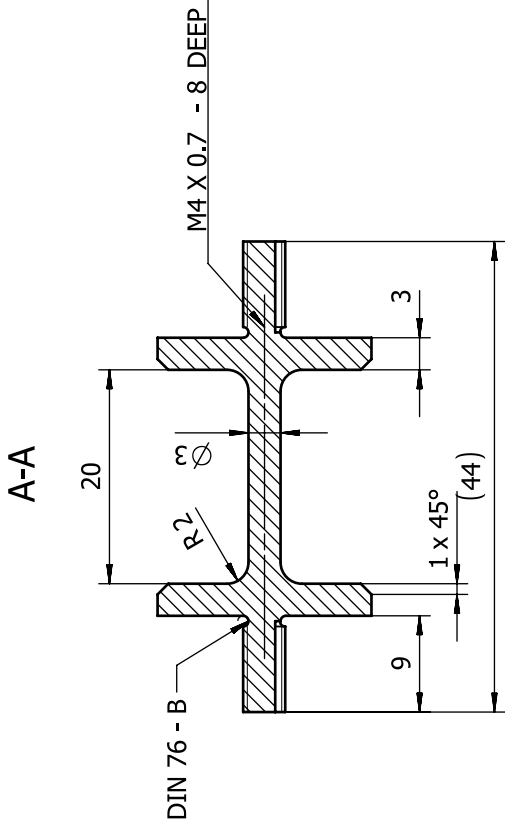
A-A



Projekt / PROJECT	Arbeitspaket / WORKPACKAGE		Gruppe / GROUP	Ersatz / REPLACES		Ersichtlich / REPLACED BY	
Gewicht / WEIGHT (kg)	0.025			Werkstoff / MATERIAL		Formgröße	
Allg. Toleranzen / GENERAL TOLERANCES	ISO 2768 ISO 13320			1.4404 (X2CrNiMo17-12-2)		A3	
Toleranzgrundsatz / FUNDAMENTAL TOLERANCING PRINCIPLE	ISO 8015		Teil-ID / PART-ID		D10000000014061/A001		Maßstab / SCALE 2:1
Oberflächenkenngrößen / SURFACE TEXTURE	ISO 1302 4287, 4288		Datum / DATE		20.07.2017		
TOLERANCE CLASS TOL. 49-42-38-375			Name / NAME		Miller, Dominik		Dokument-Nr. / DOCUMENT NO. D10000000014460
ISO 8015 beachten. Für Rückfragen bitte an -IT- wenden. © DESY. ALL RIGHTS RESERVED. REFER TO PROTECTION NOTICE FOR FURTHER ENQUIRIES PLEASE CONTACT IT- TEL. +49-424-880-3273			Zust. / STATE		A001		
			Zust. / STATE		A001		Blatt / SHEET
			Zust. / STATE		A001		von / OF
			Zust. / STATE		A001		1
			Zust. / STATE		A001		1
			Zust. / STATE		A001		8



Projekt / PROJECT		Arbeitspaket / WORKPACKAGE		Gruppe / GROUP		Ers.für / REPLACES		Ers.durch / REPLACED BY	
Gewicht / WEIGHT (kg) <b>0.026</b>		Halbzeug / SEMIFINISHED PRODUCT				Werkstoff / MATERIAL <b>EN AW-5083 (AlMg4,5Mn0,7)</b>			Format/SIZE <b>A4</b>
Allg. Toleranzen / GENERAL TOLERANCES ISO 2768 ISO 13920				Maßstab / SCALE <b>1:1</b>		Titel / TITLE <b>Tube</b>			
Tolerierungsgrundsatz / FUNDAMENTAL TOLERANCING PRINCIPLE ISO 8015				Toleranzklasse / TOLERANCE CLASS					
Oberflächenkenngrößen / SURFACE TEXTURE ISO 1302 4287, 4288				Datum / DATE 20.07.2017		Name / NAME Miller, Dominik		Dokument-Nr. / DOCUMENT NO.	
© DESY. DESY behält sich alle Rechte vor. Schutzvermerk ISO 16016 beachten. Für Rückfragen bitte an -TT- wenden, Tel. +49-40-8998-3675. © DESY. ALL RIGHTS RESERVED. REFER TO PROTECTION NOTICE ISO 16016. FOR FURTHER ENQUIRIES PLEASE CONTACT -TT- TEL. +49-40-8998-3675.				Gepr. / CRE.				Blatt / SHEET 1	
				Frei. / REL.				von / OF 1	
				Gen. / APR.				Zchnng.-ID / DRAW.-ID <b>D10000000014461</b>	
						Rev. / REV. <b>A001</b>		Status / STATUS	



Projekt / PROJECT	Arbeitspaket / WORKPACKAGE		Gruppe / GROUP	Ersch./ REPLACES		Ersch./ REPLACED BY	
Gewicht / WEIGHT (kg)	0.017			Material / MATERIAL		Formgröße	
Allg. Toleranzen / GENERAL TOLERANCES	ISO 2768 ISO 13920			Marval18 (X2NiCoMo18-8-5)		A3	
Toleranzgrundsatz / FUNDAMENTAL TOLERANCING PRINCIPLE	ISO 8015 ISO 1302		Teil-ID / PART-ID		D10000000014067/A001		Maßstab / SCALE <b>2:1</b>
Oberflächenmignößen / SURFACE TEXTURE	4287, 4288		Datum / DATE		20.07.2017		
GDESY GESY bewältigt sich alle Rechte von Schutzmerkmalen. ISO 10716 beachten. Für Rückfragen bitte an -IT- wenden. GDESY ALL RIGHTS RESERVED. REFER TO PROTECTION NOTICE FOR MORE INFORMATION. PLEASE CONTACT IT- TEL.: +49-44-366-3675.			Name / NAME		Miller, Dominik		
			Dokument-Nr. / DOCUMENT NO.		Upper_Flex		
			Zust./ REV.		A001		
			Status / STATUS		8		



# Bibliography

- [1] ALPS – DESY. <https://alps.desy.de/>. Accessed: 2019-02-25.
- [2] S. Achilles and P. Kortsch. Messbericht zu den Bodendynamischen Untersuchungen – PETRA III Experimentiergebäude im DESY Forschungszentrum Hamburg. Technical report, GuD – Geotechnik und Dynamik Consult GmbH, November 2005.
- [3] ATS9416 – 100 MS/s 16 channel PCIe Digitizer. AlazarTech, September 2018.
- [4] ATS9626 – 250 MS/s 16-Bit DC-coupled PCI Express Digitizer with user-programmable FPGA. AlazarTech, September 2018.
- [5] Stanislav Babak and other. LISA Data Analysis Status. Technical report, LISA Mission Science Office, May 2009.
- [6] Robin Bähre et al. Any light particle search II – Technical Design Report. *JINST*, 8, 2013.
- [7] Noemie Alice Chloe Bastion. *The cryogenic photon detection system for the ALPS II experiment: characterization, optimization and background rejection*. PhD thesis, Universität Hamburg, 2016.
- [8] Mark Gerrit Beker. *Low-frequency sensitivity of next generation gravitational wave detectors*. PhD thesis, Vrije Universiteit, June 2013.
- [9] E. D. Black. An introduction to Pound-Drever-Hall laser frequency stabilization. *American Journal of Physics*, 69:79–87, January 2001.
- [10] Mathieu Blom. *Seismic attenuation for Advanced Virgo*. PhD thesis, Vrije Universiteit Amsterdam, December 2015.
- [11] Anton Braun. *Grundlagen der Regelungstechnik – Kontinuierliche und diskrete Systeme*. Carl Hanser Verlag GmbH & Co. KG, 2005.
- [12] Prof. Dr.-Ing. Carsten Burmeister. Regelungstechnik. FH Wedel - University for applied science, 2014.
- [13] Zachary Ronald Dylan Thomas Bush. *Coherent detection of ultra-weak electromagnetic fields using optical heterodyne interferometry*. PhD thesis, University of Florida, 2018.

- 
- [14] Goutam Chatraborty, Takuja Kamiyama, Hideyuki Takahashi, and Tetsuo Kinoshita. An Efficient Anomaly Detection in Quasi-Periodic Time Series Data A Case Study with ECG. *Time Series Analysis and Forecasting – Selected Contributions from ITISE 2017*, pages 147–157, 2018.
- [15] Giacomo Ciani et al. HAM Auxiliary Suspensions Final Design. Technical report, July 2013. LIGO-T1000338-v4.
- [16] LIGO Scientific Collaboration. <https://www.ligo.org/>. Accessed: 2019-03-22.
- [17] Marijana Cosovic, Slobodan Obradovic, and Emina Junuz. Deep Learning for Detection of BGP Anomalies. *Time Series Analysis and Forecasting – Selected Contributions from ITISE 2017*, pages 95–113, 2018.
- [18] Steel MARVAL18 X2NiCoMo18-8-5. Aubert & Duval, 22, rue Henri-Vuillemin - 92230 Gennevilliers - France.
- [19] K Desch et al. A European Strategy Towards Finding Axions and Other WISPs. December 2018.
- [20] Klaus Ehret et al. Resonant laser power build-up in ALPS: A 'Light-shining-through-walls' experiment. *Nucl.Instrum.Meth.*, A612:83–96, 2009.
- [21] Klaus Ehret, Maik Frede, Samvel Ghazaryan, Matthias Hildebrandt, Ernst-Axel Knabbe, et al. New ALPS results on hidden-sector lightweights. *Phys.Lett.*, B689:149–155, 2010.
- [22] Prof. Dr. Jacob Flury. Methods and Applications of Physical Geodesy. Institut für Erdmessung, Leibniz Universität Hannover, 2016.
- [23] Iris EDU Incorporated Research Institutions for Seismology. How Does a Seismometer Work? *Education and Outreach Series*, (7):1.
- [24] Oliver Gerberding, Felipe Guzman Cervantes, John Melcher, Jon Pratt, and Jacob Taylor. Optomechanical reference accelerometer. 2015.
- [25] Peter W. Graham, Igor G. Irastorza, Steven K. Lamoreaux, Axel Lindner, and Karl A. van Bibber. Experimental Searches for the Axion and Axion-Like Particles. *Ann. Rev. Nucl. Part. Sci.*, 65:485–514, 2015.
- [26] Karl-Heinz Grothe and Jörg Feldhusen. *Dubbel: Taschenbuch für den Maschinenbau*. Springer Verlag, Heidelberg, 23 edition, 2011.
- [27] VIRGO Group. <http://www.virgo-gw.eu/>. Accessed: 2019-03-22.
- [28] Peter R.W. Gumert and Karl-August Reckling. *Mechanik*. Vieweg, Baunschweig, Wiesbaden, 2 edition, 1987.
- [29] Güralp Systems Limited, Aldermaston RG7 8EA, England. *CMG-6TD, Operator's guide, Document No. MAN-T60-0002*, September 2015.

- [30] Fredric Joel Harris. On the Use of Windows for Harmonic Analysis with the Discrete Fourier Transform. *Proceedings of the IEEE*, 66(1):51–83, January 1978.
- [31] G. Heinzl, A. Rüdiger, and R. Schilling. Spectrum and spectral density estimation by the Discrete Fourier transform (DFT), including a comprehensive list of window functions and some new at-top windows. Technical report, Max-Planck-Institut für Gravitationsphysik (Albert-Einstein-Institut), 2002.
- [32] Erik Hennes and Mark Beker. Pushing the Advanced VIRGO Interferometer to the limit. *Mikroniek*, 53(4):5–11, October 2013.
- [33] Ekbert Hering, Rolf Martin, and Martin Stohrer. *Physik für Ingenieure*. Springer Verlag, Heidelberg, 10 edition, 2007.
- [34] Ekbert Hering and Karl-Heinz Modler. *Grundwissen des Ingenieurs*. Fachbuchverlag Leipzig, 13 edition, 2002.
- [35] Otto Heunecke, Heiner Kuhlmann, Walter Welsch, Andreas Eichhorn, Hans Neuner, Michael Möser, Gerhard Müller, and Harald Schlemmer. *Handbuch der Ingenieurgeodäsie: Auswertung geodätischer Überwachungsmessungen*. Wichmann, 2 edition, 2013.
- [36] Martin Hewitson. eLISA: <https://www.elisascience.org/ltpda/usermanual/usermanual.html>. Accessed: 2019-02-13.
- [37] Modal Analysen. HGL Dynamics - Dynamic Vibration Solution, 2012.
- [38] Reza Hodajerdi. *Production Cavity and Central Optics for a Light Shining through a Wall Experiment*. PhD thesis, Universität Hamburg, 2014.
- [39] Prof. Dr. Heiner Igel. Seismology. Geophysik, Universität München, 2017.
- [40] ANSYS Inc. <https://www.ansys.com/>. Accessed: 2019-03-22.
- [41] iZOTOPE. <https://www.izotope.com/en/blog/mastering/multiband-compression-basics-izotope-mastering-tips.html>. Accessed: 2019-03-12.
- [42] J. Michael Jacob. *Industrial Control Electronics*. Pearson College Div, 1988.
- [43] Todd Kozlowski. Control and Alignment of the ALPS IIc Experiment, March 2019.
- [44] Todd Kozlowski, Dominik Miller, Rikhav Shah, and Richard Smith. Any Light Particle Search II. unpublished poster, February 2019.
- [45] Patrick Kwee. Charakterisierung von Lasersystemen für Gravitationswellendetektoren, September 2005.

- 
- [46] Axel Lindner, Andrzej Siemko, Herman Ten Kate, and Benno Willke. A future option for searching axion-like particles through light-shining-through-a-wall experiments: JURA (Joint Undertaking on Research for Axion-like particles). internal note, July 2018.
- [47] Mark Products L-4 Seismometer. Sercel, November 2001.
- [48] Wilhelm Matek, Dieter Muhs, Herbert Wittel, Manfred Becker, and Dieter Janasch. *Roloff/Matek Maschinenelemente – Normung, Berechnung, Gestaltung*. Viewegs Fachbücher der Technik, 15 edition, 2001.
- [49] Wilhelm Matek, Dieter Muhs, Herbert Wittel, Manfred Becker, and Dieter Janasch. *Roloff/Matek Maschinenelemente – Tabellen*. Viewegs Fachbücher der Technik, 15 edition, 2001.
- [50] MathWorks. <https://de.mathworks.com/products/matlab.html>. Accessed: 2019-03-12.
- [51] Fabrice Matichard et al. Seismic isolation of Advanced LIGO: Review of strategy, instrumentation and performance. *Class. Quant. Grav.*, 32(18):185003, 2015.
- [52] Wilcoxon Research model 731-207, Ultra low frequency seismic accelerometer. Meggitt Sensing Systems, May 2012.
- [53] Wilcoxon Research model P702B, General purpose power unit and amplifier. Meggitt Sensing Systems, February 2012.
- [54] Erwin Meyer and Dieter Guicking. *Schwingungslehre*. Fridr. Vieweg + Sohn GmbH, 1974.
- [55] Dominik Miller and Thorsten Stoye. Grundlagen der Schwingungslehre. unpublished, April 2018.
- [56] Rüdiger Mitdank. Stehende Welle. Institut für Physik, Humboldt-Universität zu Berlin: <http://people.physik.hu-berlin.de/~mitdank/dist/scriptenm/stehendew.htm>. Accessed: 2018-12-10.
- [57] Dr. Rod Nave. Driven Oscillator. Department of Physics and Astronomy, Georgia State University: <http://hydrogen.physik.uni-wuppertal.de/hyperphysics/hyperphysics/hbase/oscdr.html>. Accessed: 2018-11-23.
- [58] Members of the ALPS collaboration. private communication.
- [59] Jan Hendrik Pöld and Hartmut Grote. ALPS II – design requirement document. internal note, February 2019.
- [60] Witold Pedrycz, Shyi-Ming Chen, and Ronald R. Yager. *Time Series Analysis, Modeling and Applications – A Computational Intelligence Perspective*. Springer-Verlag Berlin Heidelberg, 1 edition, 2013.

- [61] Andreas Ringwald. Exploring the Role of Axions and Other WISPs in the Dark Universe. *Phys.Dark Univ.*, 1:116–135, 2012.
- [62] Ignacio Rojas, Héctor Pomares, and Olga Valenzuela. *Time Series Analysis and Forecasting: Selected Contributions from ITISE 2017 (Contributions to Statistics)*. Springer Verlag, 2018.
- [63] Dr.-Ing. Akbar Schabanloui. Geo-Kinematics And Geo-Dynamics. Institut für Erdmessung, Leibniz Universität Hannover, 2017.
- [64] Geophone Specifications. Sercel Inc. - U.S.A., February 2018.
- [65] Anthony E. Siegman. *Lasers*. Stanford University, 1986.
- [66] Aaron Spector and Guido Mueller. Control and Alignment Conceptual Design for TES and HET Designs. internal note, October 2018.
- [67] FFT Spectrum Analyzers – SR785 - 100 kHz two-channel dynamic signal analyzer. Stanford Research Systems.
- [68] Akiteru Takamori. *Low Frequency Seismic Isolation for Gravitational Wave Detectors*. PhD thesis, University of Tokyo, 2002.
- [69] Robert Taylor. *Journal of Time Series Analysis*. John Wiley & Sons Ltd, 2019.
- [70] Digital Phosphor Oscilloscopes, DPO7000 Series Datasheet. Tektronix, Inc., May 2016.
- [71] Yongning Wang and Ruey S. Tsay. Clustering Multiple Time Series with Structural Breaks. *Journal of Times Series Analysis*, 40, November 2019.
- [72] Christoph Weinsheimer. *Light-Shining-through-a-Wall – Searching for Axion-Like Particles with the OSQAR and ALPS II experiment*. PhD thesis, Johannes Gutenberg Universität, Mainz, December 2017.
- [73] Mitchell M. Withers et al. High-Frequency Analysis of Seismic Background Noise as a Function of Wind Speed and Shallow Depth. *Bulletin of the Seismological Society of America*, 86(5):1507–1515, October 1996.
- [74] Hristo Zhivomirov. A Method for Colored Noise Generation. *Romanian Journal of Acoustics and Vibration*, 14(1):14–19, January 2018.
- [75] Tingyi Zhu and Dimitris N. Politis. HigherOrder Accurate Spectral Density Estimation of Functional Time Series. *Journal of Times Series Analysis*, 40, May 2019.



# Acknowledgements

Above all, I would like to thank my beloved fiancée, Charlotte Kaiser, for her energetic support and loving affection. For all the encouragement, motivation, and backing that kept me on track in times of trouble, for all the patience and peace you gave me when I had doubts, and of course for all your infinite love, which was ultimately the greatest and most important motivation of all!

A special thanks to Thomas Kaiser for his enormous help. Without you, the linguistic correctness and understanding of this work would not be on the current level. Thank you for your accuracy and precision in each comment as well as the will to understand every detail. I was overwhelmed by the effort and diligence you invested in me.

No less thanks to all my family, who guided me on my path and supported me in every situation. Only with your parental care, help, and assistance could I have reached the point where I stand now and look upon a confident future.

I am thankful to Dr. Axel Lindner and Thorsten Stoye for their comments, ideas, advice, and support during the past years. Of course not to forget that together with Andreas Ringwald you made the job possible for me. I would also like to thank my mentor Thomas Adams for his helpfulness, energetic ideas, and dedicated support. You were more than just supervisors for me; your interest in my life and your far-reaching counselling have made you role models who I will not forget.

At this point, I would like to thank my Ph. D. supervisor Prof. Dr.-Ing. Jakob Flury for your positive attitude towards my work and kindness towards me. Also, with the assistance of Prof. Dr.-Ing. Ingo Neumann and Prof. Dr. rer. nat. Hartmut Grote, I like to say “Thank you” for the work and commitment in supporting my Ph. D. thesis.

Furthermore, many thanks also to the entire ALPS group. Thank you for accepting me so warmly and helping me getting used to physics. Thank you also for every answered question, every comment about my work, and every minute you have invested in me. I have always felt comfortable in this working group and enjoyed the time I spent with you very much.

Finally, I would like to thank all the people who made this work possible. Thank you for your support at work, at sports, or in private life – this has made my time much easier and enjoyable.

*“You now know that vibrations affect us all, so enjoy the good ones!”*  
– Dominik Miller





# Dominik Miller

## Lebenslauf

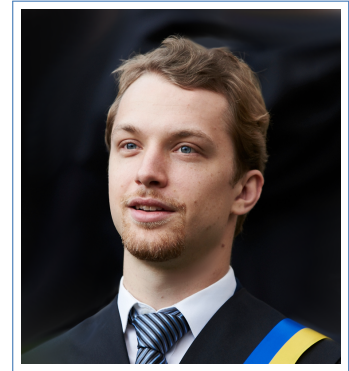
Müggenkampstraße 79  
20257 Hamburg  
Deutschland

☎ +49 (0)40 8998 4598

📞 +49 (0)163 144 74 15

✉ dominik.miller@desy.de

\* 6. März 1991 in Hamburg



### Berufserfahrung

seit 01/2016      Wissenschaftlicher Mitarbeiter am DESY – ALPS II Experiment

### Master Thesis

Titel      *Kooperatives Verhalten mobiler, autonomer Robotereinheiten*

Betreuer      Prof. Dr. Mike Schmitt

Beschreibung      Entwicklung einer Gruppenarchitektur und Software für das kooperative Verhalten von mobilen, autonomen Robotereinheiten im Bezug auf Anwendungsfallorientierten Szenarien

### Studium

04/2016 – heute      **Promotionsstudium: Geodäsie und Geoinformatik, Leibniz Universität Hannover**, Titel der Dissertation.

Seismic noise analysis and isolation concepts for the ALPS II experiment at DESY

10/2013 – 09/2015      **M. Sc. Wirtschaftsingenieurwesen (Technik), Fachhochschule Wedel**, Note 1.3.

13/12/2013      **Innovationspreis 2013, Rotary Club Wedel.**

Verleihung für besonders innovative Arbeiten

27/09/2013      **Hochschulpreis 2013, Fachhochschule Wedel.**

Beste Abschlussarbeit im Bereich Wirtschaftsingenieurwesen

10/2010 – 09/2013      **B. Sc. Wirtschaftsingenieurwesen, Fachhochschule Wedel**, Note 1.6.

### Studienbegleitende Tätigkeiten

11/2013 – 08/2014      Werkstudententätigkeit bei der APOS GmbH

### Praktika

02/2011 – 04/2011      Technisches Grundpraktikum bei ADT-Thiede

03/2013 – 08/2013      Betriebspraktikum bei der APOS GmbH

---

## Sonstige Tätigkeiten

2005 – 2010	Bereitstellungsdienst als Schul-Sanitäter am Gymnasium Rissen (ehrenamtlich)
10/2007 – heute	Judovereinstrainer im Rissener Sportverein e.V. & VEJAS Hamburg e.V.
11/2014 – 01/2015	Leitung einer Taekwondo AG an der Grundschule Windmühlenweg (ehrenamtlich)

---

## Methodenkompetenz

Communication Skills	Erweiterung sozialer Kompetenzen
Führungskräftetraining	videoanalytische Aufbereitung von HR Situationen/Fallbeispielen
Judo C-Trainer	psycho- und physiotekhnische Didaktik
Judo B-Trainer	Leistungssportspezifische Trainingsmethoden für Jugendliche
Kreativitätstechniken	Methoden zur Produktivitätssteigerung
Projektmanagement in der Praxis	Fallbeispiele anhand eines typischen Projektes als Workshop
Tutor für Analysis & Höhere Analysis	wöchentliche Vorbereitung für Kommilitonen
Verhandlungsführung	Fokus auf Empathie und kommunikativer Kompetenz

---

## EDV-Kenntnisse

Betriebssysteme	Windows, OS X, Linux
Anwendungen	Microsoft Office (Excel, Word, Power Point, Outlook, Project und Visio); Microsoft Visual Studio, Microsoft Expression (Blend 4); CAD (NX 10, Pro Engineer 5), CAM(G-Codes, WinNC Sinumerik, Shopmill); ERP-System (SAP), OLAP, BEx Analyzer, SPSS Modeler; ARIS
Programmierung	MATLAB, C#, C, C++, Visual Basic, SQL, GPSS/H
Datenbanken	Oracle

---

## Sprachen

Englisch	Fließend in Wort und Schrift
Italienisch	Grundlagen in Wort und Schrift
Französisch	Grundlagen in Wort und Schrift
Japanisch	Grundlagen in Wort und Schrift

---

## Sportliche Aktivitäten

seit 10/1998	Judo
2004 – 2009	Volleyball
seit 10/2006	Standard- und Lateintanz
seit 02/2011	Taekwondo

---

## weitere Interessen

technische Innovationen, Sport im Allgemeinen, Fotografie, Motorsport, gemeinsames Kochen und Lesen

Hamburg, den 21. März 2019

# Eidesstattliche Erklärung

Hiermit erkläre ich:

- die Regeln der geltenden Promotionsordnung zu kennen und eingehalten zu haben und mit einer Prüfung nach den Bestimmungen der Promotionsordnung einverstanden zu sein,
- die Dissertation selbst verfasst zu haben, keine Textabschnitte von Dritten oder eigener Prüfungsarbeiten ohne Kennzeichnung übernommen und alle von ihr oder ihm benutzten Hilfsmittel und Quellen in seiner oder ihrer Arbeit angegeben zu haben,
- Dritten weder unmittelbar noch mittelbar geldwerte Leistungen für Vermittlungstätigkeiten oder für die inhaltliche Ausarbeitung der Dissertation erbracht zu haben,
- die Dissertation noch nicht als Prüfungsarbeit für eine staatliche oder andere wissenschaftliche Prüfung eingereicht zu haben,
- keine gleiche oder eine in wesentlichen Teilen ähnliche Arbeit bei einer anderen Hochschule sowie keine andere ähnliche Abhandlung als Dissertation eingereicht zu haben,
- damit einverstanden zu sein, dass die Dissertation auch zum Zwecke der Überprüfung der Einhaltung allgemein geltender wissenschaftlicher Standards genutzt wird, insbesondere auch unter Verwendung elektronischer Datenverarbeitungsprogramme.

Hamburg, den 25. März 2019

---

Ort, Datum

---

Unterschrift



# Wissenschaftliche Arbeiten der Fachrichtung Geodäsie und Geoinformatik der Leibniz Universität Hannover

*(Eine vollständige Liste der Wiss. Arb. ist beim Geodätischen Institut, Nienburger Str. 1, 30167 Hannover erhältlich.)*

- Nr. 324 WU, Hu: Gravity field recovery from GOCE observations (Diss. 2016)
- Nr. 325 XU, Xiangyang: Terrestrial Laser Scanning for the Generation and Calibration of Finite Element Models (Diss. 2016)
- Nr. 326 SAYYAD, Muhammad Naeem Shahzad: Joint use and mutual control of terrestrial laser scans and digital images for accurate 3D measurements (Diss. 2016)
- Nr. 327 SCHACK, Lukas: Object-based matching of Persistent Scatterers to Optical Oblique Images (Diss. 2016)
- Nr. 328 REICH, Martin: Global Image Orientation from Pairwise Relative Orientations (Diss. 2016)
- Nr. 329 KLINGER, Tobias: Probabilistic multi-person localisation and tracking (Diss. 2016)
- Nr. 330 SCHMIDT, Alena: Markierte Punktprozesse für die automatische Extraktion von Liniennetzen in Rasterdaten (Diss. 2016)
- Nr. 331 HOFMANN, Franz: Lunar Laser Ranging - verbesserte Modellierung der Monddynamik und Schätzung relativistischer Parameter (Diss. 2017)
- Nr. 332 BRIEDEN, Phillip: Validierung von GOCE-Gravitationsgradienten in Kreuzungspunkten und Zukunftsperspektiven der Satellitengradiometrie (Diss. 2017)
- Nr. 333 VON GÖSSELN, Ilka: Simulationsbasierte Effizienzoptimierung von Messprozessen am Beispiel der tachymetrischen Netzmessung (Diss. 2017)
- Nr. 334 HOFMANN, Sabine: Potential von LiDAR Mobile Mapping für hochgenaue Karten (Diss. 2017)
- Nr. 335 ALBERT, Lena: Simultane Klassifikation der Bodenbedeckung und Landnutzung unter Verwendung von Conditional Random Fields (Diss. 2017)
- Nr. 336 NIEMEYER, Joachim: Verwendung von Kontext zur Klassifikation luftgestützter Laserdaten urbaner Gebiete (Diss. 2017)
- Nr. 337 EGGERT, Daniel: Effiziente Verarbeitung und Visualisierung von Mobile Mapping Daten (Diss. 2017)
- Nr. 338 FITZNER, Daniel: Estimation of Spatio-Temporal Moving Fields at High Resolution (Diss. 2017)
- Nr. 339 CZIOSKA, Paul: Meeting point locations for shared rides (Diss. 2018)
- Nr. 340 FEUERHAKE, Udo: Erfassung von Trajektorien und Erkennung von Bewegungsmustern (Diss. 2018)
- Nr. 341 HUANG, Hai: Bayesian Models for Pattern Recognition in Spatial Data (Habil. 2018). (Nicht im Layout unserer Schriftenreihe erschienen, sondern als Heft DGK Reihe C, Heft 751)
- Nr. 342 BOCK, Urs Fabian: Dynamic Parking Maps from Vehicular Crowdsensing (Diss. 2018)
- Nr. 343 KRAWINKEL, Thomas: Improved GNSS Navigation with Chip-scale Atomic Clocks (Diss. 2018)
- Nr. 344 GOSWAMI, Sujata: Understanding the sensor noise in the GRACE range-rate observations by analyzing their residuals (Diss. 2018)
- Nr. 345 ZHANG, Yin: Expected Utilities for Decision Making and Steering of Measurement Processes (Diss. 2018)
- Nr. 346 SCHLICHTING, Alexander: Fahrzeuglokalisierung durch Automotive Laserscanner unter Verwendung statischer Merkmale (Diss. 2018)
- Nr. 347 RÖTH, Oliver: Extraktion von hochgenauer Fahrspurgenometrie und -topologie auf der Basis von Fahrzeugtrajektorien und Umgebungsinformationen (Diss. 2018)
- Nr. 348 NEELMEIJER, Julia: Observing Inter- and Intra-Annual Glacier Changes and Lake Loading Effects from Synthetic Aperture Radar Remote Sensing (Diss. 2018)
- Nr. 349 HOBERG, Thorsten: Conditional Random Fields zur Klassifikation multitemporaler Fernerkundungsdaten unterschiedlicher Auflösung (Diss. 2018)
- Nr. 350 SCHILLING, Manuel: Kombination von klassischen Gravimetern mit Quantensensoren (Diss. 2019)
- Nr. 351 MILLER, Dominik: Seismic noise analysis and isolation concepts for the ALPS II experiment at DESY (Diss. 2019)

*Die Arbeiten werden im Rahmen des wissenschaftlichen Schriftenaustausches verteilt und sind nicht im Buchhandel erhältlich. Der Erwerb ist zu einem Stückpreis von € 25,00 bei den herausgebenden Instituten möglich.*